Process Characterisation for Electrochemical Machining

David Clifton

PhD Thesis

The University of Edinburgh

2001

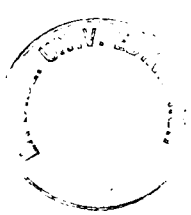

Statement of Primary Achievement

The basis of a technique for in-line process characterisation of ECM has been established. This technique has been applied to map out parameter interdependence in the form of the C-function. This mapping is achieved within a single characterisation trial taking only a few minutes to complete, thus avoiding the need for extensive iterative trials, as has previously been the case. This approach has been made possible through the novel application of ultrasonic time-of-flight data to the direct measurement of erosion parameters.

Abstract

Electrochemical machining is a process that has the potential to machine complex full-form shapes at high production rates. The effective economic utilisation of this process, however, has been impeded by the iterative trial and error approach that is often required to generate process specifications for any one machining set-up. This approach arises due to the incompleteness of models used to describe the complex physical, chemical and hydrodynamic parameter interdependencies. Such interdependence results in non-ideal effects that distort the transfer geometry between the tool shape and the required workpiece form. In this thesis a semi-empirical characterisation strategy, aimed at mapping out parameter interdependence through a single characterisation trial, is proposed. This approach has been realised through the development of a segmented tooling assembly that enables the probing of spatial parameter sensitivities and through the development of a distributed gap measurement system. The combined use of these systems, in the form of the characterisation cell assembly, has enabled detailed parameter mappings to be carried out within a procedure taking only a few minutes to complete. The concept of the C-function expression is introduced as a means of representing parameter independence generated by the characterisation trials. This expression represents non-ideal effects as a spatial series, discretised along intervals of flow path length, with coefficients representing the sensitivity of gap size to primary process variables. Characterisation trials have been carried out using both titanium and nickel based alloys machined using chloride and nitrate based electrolytes. The method has also been applied to an analysis of one of the recently developed titanium aluminide alloys. These trials have identified a range of parameter interdependencies. Most significantly these have included observation of a previously unknown phenomenon, termed electrochemical hysteresis, and a range of spatial characteristics in the dependencies between current density, flow velocity and gap size. The use of the C-function as a means of representing these characteristics is demonstrated by extrapolating characterisation data to shape prediction for a 2-D double-cosine profile.

Acknowledgements

I would like to thank the many people who have helped me, either directly or indirectly, to complete the work of this thesis. Derek Jardine and Bob Gustard, the technicians working on project, who have guided and contributed to the design of equipment and experimental set-ups. Special thank also to Derek for the construction of my inverted computer frame ("the ladder") which enable me to continue the write-up, in a horizontal orientation, when my back wasn't up to letting me sit at a keyboard. Thanks go to Kirstin Eley, an undergraduate student, who spent one of her summer holidays helping me carry out some of the general characterisation trials. Thanks to James McClennan and Paul Howarth, both postgraduate students, who helped monitor system parameters during some of the C-function characterisation trials (at times the ECM system required three operators!). Specific thanks go to Paul for acting as the "human servo" by manually controlling the voltage when the automatic system wasn't working properly. Andy Mount and George Alder are thanked for their contribution to the development of current-time solutions and analysis of the tool design problem, respectively. Andy and George are also thanked for many useful discussions on general aspects of the project. Alan Cannon, of Rolls-Royce plc, is thanked for many useful discussions and for supplying the material for trial test pieces. Mike Yardley, of Doncasters plc, is thanked for lending the project some of the experimental equipment and also for many useful discussions on the industrial application of ECM. Frank Mill, my supervisor, is thanked for guidance and for making many useful comments on the draft manuscript. Thanks to the Isle of Arran for acting as a hideaway during some periods of this write-up (three weeks in a caravan). And finally, a special thanks and love, to my mother for support and for the loan of her flat as a hideaway during parts of the write-up, and also to my girlfriend, Pam, for her support and understanding during the long hours of my absence whilst I was slaving over (and under!) my computer.

Notation

A	area of electrode (both tool and workpiece) (m^2)
a	matrix notation for ε (gm mol^{-1})
C	C-function (m^2 sec^{-1})
F	the Faraday (C)
f	tool feed rate (mm sec^{-1})
G	average molecular mass of the workpiece (gm mol^{-1})
g	mass of workpiece surface dissolved by charge q (gm)
I	total current (A)
J	current density (A cm^{-2})
k	k-parameter (m^2 sec^{-1})
L	flow path length (mm)
l	flow path interval (integer)
m	discrete flow path index (integer)
M	total number of intervals in flow path discretisation (integer)
n	valency or number of electrons transferred per dissolving metal atom (dimensionless)
r_p	the resistivity of the pure electrolyte (ohm.m)
r_e	the resistivity of gas-electrolyte phase (ohm m)
t	time (sec)
U	electrolyte flow rate (l min^{-1})
V	applied voltage (V)
V_0	portion of the applied voltage required at the electrode interfaces to drive the machining process (V)
Vol	volume of material dissolved in unit time (mm^3)
w	is the width of the tool and workpiece electrodes (mm)
y	thickness of the workpiece (perpendicular to the workpiece surface) (mm)
z	gap between the electrodes (perpendicular to the planar electrode surfaces) (mm)
z_∞	gap between the electrodes (perpendicular to the planar electrode surfaces) at equilibrium (mm)
κ	electrolyte conductivity (S cm^{-1})
ρ	density of the workpiece material (g cm^{-3})
dy/dt	erosion rate (mm min^{-1})
δ_x	thickness of gas-electrolyte phase (mm)
ε	electrochemical equivalent of workpiece (gm mol^{-1})

Subscripts

∞	value as time approaches infinity
i	initial value (value at time designated as initial time for fitting purposes)
0	value at time zero
x	condition at co-ordinate x
m	condition at index m

ABBREVIATIONS

ECM *electrochemical machining*

ACFM *alternating current field measurement*

EDM *electrode discharge machining*

LDVT *linear differential voltage transducer*

ROV *remote operated vehicle*

Table of Contents

Table of figures

Aims and preface

The general aims of this work can be summarised as follows:

- ***To develop a characterisation strategy for the measurement and representation of process interdependencies which are applicable over the wide range of practical ECM process conditions***

- ***To be able to implement such a strategy without the need for repeated exhaustive trials***

- ***To consider the application of parameter characterisation/representation to general 2-D profiles***

The work of this thesis is presented in the following form:

In chapter one the early history of ECM developments is outlined. This includes a discussion on the general areas of application and competitiveness of this process. The limitations and problems associated with ECM are then considered in the context of the aims of this thesis. Chapter two provides a general description of the electrolysis process and provides the theoretical basis for ECM planar dynamics from which a means to parameterise the ECM process is developed. Past and recent work in ECM relevant to the work in this thesis is reviewed in a Chapter three. This review begins by describing work from which basic machineability data has been modelled with both inclusion and exclusion of non-ideal effects. An overview of the work of others on tool design, ECM process simulation and methods for representing parameter sensitivities is also given. The theoretical developments of current-time and gap-time analysis leading to the concept of the C-function representation of parameter interdependence are detailed in Chapter four. Chapter five describes the development of the experimental ECM equipment and characterisation cell systems. General planar and segmented characterisation trials are described in Chapter six. Chapter six also reports on measurements of the fundamental parameters, and spatial decomposition of these parameters, for a range of selected material/electrolyte systems. Chapter six concludes with a discussion on the need for the measurement of gap-time data to resolve certain ambiguities in fundamental relationships. The development of an ultrasonic gap measurement system is described in Chapter seven. Chapter eight describes the application of the ultrasonic gap measurement system, in combination with the segmented tooling system, to produce distributed two-point C-function representations of parameter interdependence. Application of the C-function representations to 2-D profiles is also presented in Chapter eight. The thesis concludes with a short section describing the conclusions and intended future directions.

CHAPTER:

1 Introduction and general background

This Chapter begins with an introduction and justification of the work presented in this thesis and then provides an outline of the early history of ECM developments. This is put into context of today's manufacturing requirements with a discussion on the general areas of application and competitiveness of the ECM process. Specialist applications in cases where ECM has no realistic competition are also outlined. The limitations and problems associated with ECM are then considered and the Chapter concluded with a discussion on the aims of this thesis in the context of making ECM more generally applicable.

1.1 Introduction

The fundamental basis of electrochemical machining is the removal of metal through anodic dissolution. The basic arrangement is in the form of an electrolytic cell with the tool biased as the cathode and the workpiece biased as the anode. An electrolyte solution is directed through the gap between the workpiece and the tool. Applying a machining voltage causes the flow of an electrolysis current producing dissolution of the anodic workpiece surface. To ensure that dissolution occurs in a controlled predetermined way, the tool is then traversed to maintain close proximity to the workpiece surface as erosion takes place. Unlike many competing metal machining processes ECM can machine a material irrespective of hardness and is able to produce complex shapes at relatively high removal rates. The process has the potential to produce a high quality machined surface free from residual stresses or microstructural damage.

The economic utilisation of ECM has been impeded by the iterative approach that is often required to generate process specifications for any one machining set-up. This approach arises due to the incompleteness of models used to describe the complex physical, chemical and hydrodynamic parameter interdependencies. Such interdependence results in non-ideal effects that distort the transfer geometry between the tool shape and the required workpiece form. The most significant consequence of this is that producing a required tool design and parameter selection for a give ECM set-up (required workpiece shape and material) is often achieved through trial and error iterations. The development costs required for any one production set-up can therefore be prohibitively expensive in many applications. As a result the process currently finds application primarily for specialist components in high technology industries such as aerospace, automotive and medical where the high cost of production can, to some extent, be offset against the high level of investment already incurred.

In an attempt to facilitate the wider application of this process much of the current research effort is directed to examining, understanding and modelling the tool to workpiece transfer function. The primary direction of most of this work is aimed towards the modelling of the electric field distribution for purposes of tool design and/or process simulation. The application of such techniques has required certain ideal assumptions to be made about the insensitivity of certain parameter relationships. In many practical machining situations such assumptions have a very limited range of applicability and as a result much of the current modelling strategies only provide a first order approximation. Improving the accuracy of these approaches will be achieved through an improved understanding and/or measurement of primary parameter interrelationships. Much of the past effort on characterising these interrelationships has been carried out using indirect measurements over a limited range of conditions. Such characterisations are carried out thorough

use of time-consuming parameter mapping trials carried out to generate a look-up database to relate process parameters and variables. Such databases are very limited and do not in general resolved parameter interdependence to the detail and range required for automated process simulation and/or tool design requirements. The work described in this thesis is directed to addressing the problem of ECM process characterisation through the development of a system in which parameter interdependence can be readily and automatically resolved and represented.

1.2 A brief history of ECM

The use of anodic dissolution as a means of removing large amounts of material for machining was first proposed as a patent in 1929 by Gmseff (British patent No 335 003). It was not till the early 1950s that ECM was applied to a limited degree in specific applications such as the sharpening of carbide tipped drills and for the removal of broken, hardened steel drill bits. The Battelle Memorial Institute, in the United States, pioneered the extension of process usage to more complex shapes by the development a prototype system for the machining of gas-turbine blades. In the United Kingdom, Rolls-Royce plc adapted these machines to apply the process, for the first time, to the mass production of gas-turbine blades. In the late 1950s the American company, Anocut Engineering, started to build and market ECM machines designed for general purpose use. The market for these systems was, however, limited to specialist applications. Soon after, the British company, TI Healy Ltd, started to produce its own range of ECM machines. In Europe, AEG Elotherm became involved in the ECM market and started to produce purpose built modular machines providing a current capacity of up to 400,000 Amps. In recent years, a spin-off company from TI Healy (who are no longer in business), Electrochemical Machining Services ltd, began work offering sub-contractor machining facilities in ECM.

Electrochemical Machining Services Ltd and AmChem plc (now owned by the Doncaster's Group) are today the UK's two remaining companies of a significant size that still offer ECM sub-contractor facilities. Anocut Engineering plc remain one of the market leaders in the manufacture of ECM systems. In Britain several small ECM service companies still operate carrying out limited production runs using ECM equipment of their own.

The dominant usage of the process is still to be found in aerospace industries. In particular, Rolls-Royce plc remain one of the world's leading users and developers of the process. The following subsection provides an example of one of the main application areas for this process at Rolls-Royce.

1.2.1 The development of the 360° ECM process

In 1978 engineers at Rolls-Royce's Advanced Manufacturing Unit, at Filton Bristol, set about to produce what was to become one of the world's most advanced and effective ECM production

operations. The aim was to produce compressor blades using ECM as the primary manufacturing process. Up until that time the blades had been manufactured using a series of processes centred around precision forgings and combining pinch rolling, milling, grinding and extensive hand finishing operations. The aim of the new initiative, which is described in detail by Atkey [1], was to reduce machining costs and improve production efficiency through the development of a fully automated compressor blade production facility. In particular, since ECM'ed components rarely require any finishing operations, Rolls-Royce were aiming to eliminate the high expense of hand finishing operations. By the mid-1980s the programme had resulted in an automated ECM production sequence producing full-form blades from titanium and nickel alloy bar, at a rate of over 2500 per week. The technique developed, which has now been patented by Rolls-Royce plc, known as a 360 degree ECM, forms both the convexed and concave sides of the airfoil in a single pass tooling set-up. The system utilises a sequence of four, six axis, pick-and-place industrial robots to manipulate the components through the machining operations. Prior to the application of ECM the blade's root (the *fir tree* feature at the blades base) is first formed by broaching. The root is then used as a location slot to facilitate accurate position of the pre-form when setting up to generate the airfoil surfaces by ECM. A total of four ECM machines are used in parallel in order to keep up with the throughput from the broaching stage. As an indication of the scale of this operation, the electrolyte tanks feeding each of the ECM stations has a capacity of 40,000 gallons.

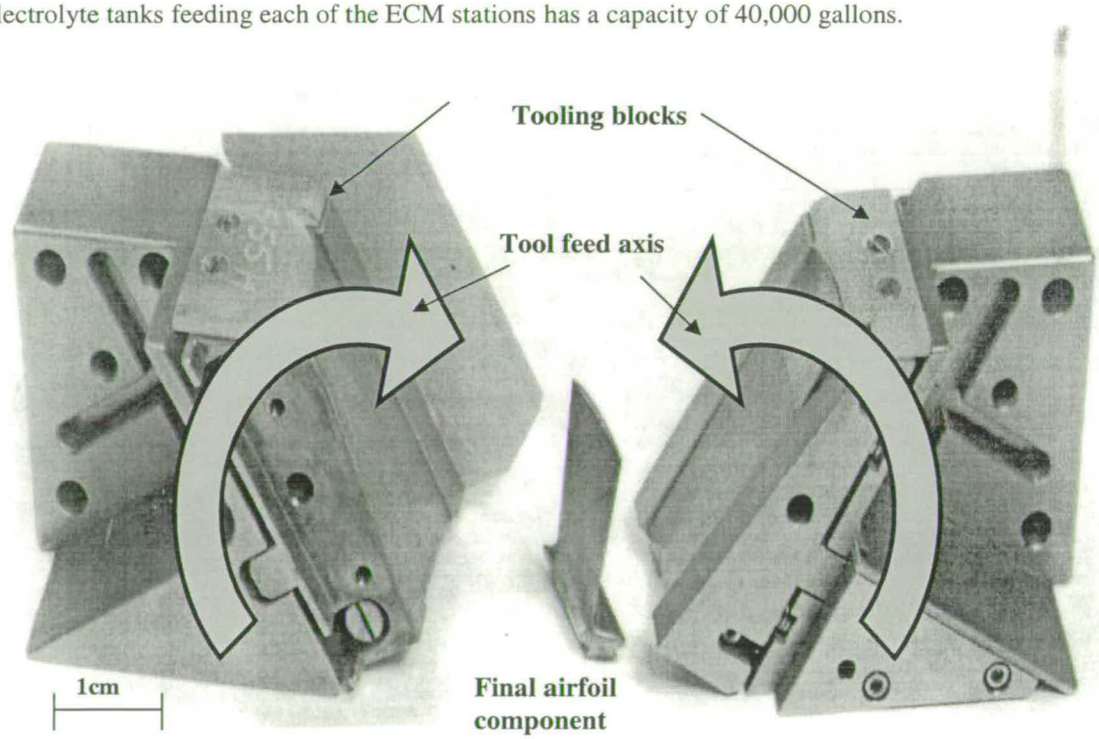

Figure 1.2-1: Shows Rolls-Royce's 360 degree ECM set-up (reproduced with permission from Rolls-Royce plc)

Figure 1.2-1 shows the tooling position and relative motion of Rolls-Royce's 360 degree ECM set-up. A compressor blade manufactured by this method is shown in Figure 1.2-2.

As well as being cost-effective, the 360 degree ECM process enables blade designs to be machined to a specification that was previously unachievable with other machining methods. Most significantly, because of the low force associated with the ECM process these blades can be made very thin thus improving aerodynamic performance. An additional advantage is that the pre-form can be smaller in size providing material savings of around 30% when compared to the forgings that had been previously used.

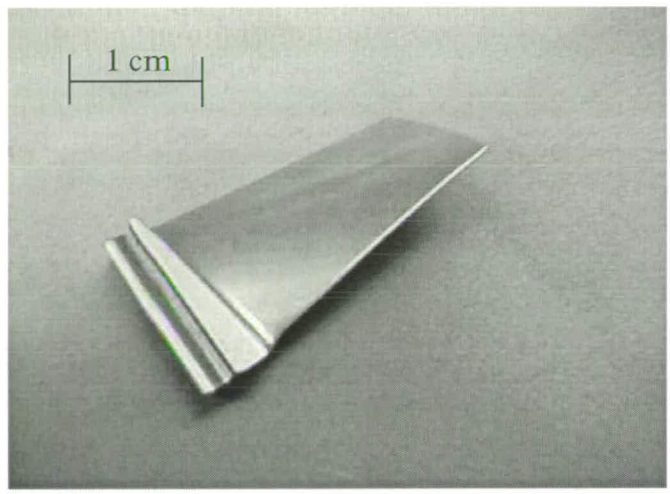

Figure 1.2-2: A compressor blade manufactured by the 360 degree ECM process

1.3 Competitiveness of the general application of ECM

The selection of a manufacturing process will be dependent upon making economic comparison with other competing processes able to achieve the same or similar components or features. Examples of specific cases where ECM can be readily and efficiently applied are as follows:

- Irregular shaped cavities with features running along a single axis. ECM has particular advantages when deep cavities are required since conventional tools will often have access limitations at greater depths. In the specific case of hole drilling, conventional twist drills are not usually suitable to machine holes with depth to diameter ratios greater than ten to one. The drilling of the holes with significantly greater length/diameter ratios will often results in drill breakage. This is not usually a significant problem for ECM.

- Holes and other features required in fragile and/or thin and delicate components. In these cases the high cutting forces associated with conventional machining could break or distort the components. This is not usually a problem for ECM where the "cutting forces" are those associated with the electrolyte supply pressure and are not usually excessive.

- Machined surfaces that are required to be stress free or highly polished. Unlike the case for most conventional machining techniques ECM can produce a high quality surface in a single pass operation (typically 0.5 –1.5 R_a).

When considering the wider application of ECM more specific comparisons must be made with conventional stock removal processes, such as turning and milling, and also with non-conventional processes, in particular electro discharge machining (EDM).

The volumetric removal rate that can be achieved by ECM is in the region of 10 to 20 $cm^3\ min^{-1}$ for large area die sinking operations. This is typically 5 to 10 times greater than rates achieved by EDM and it is comparable to rates achieved by conventional processes when being applied to soft materials when machining relatively simple shapes. However, in applications where the required geometry becomes more complex and/or the material being machined is hard, then conventional processes, in general, have reduced rates of machining. This is because the cutter, which is usually fixed in size (and usually small for increasingly complex shapes), will have to repeatedly traverse the same contour. In such cases ECM will often have an economic advantages in terms of overall production rates. As the hardness of the material increases then the overall cost of machining, by conventional means, increases. The overall cost being dependent on a trade-off made between the rate of tool wear and the achievable volumetric removal rate. For difficult to cut materials such as a titanium and nickel based superalloys, the options for conventional machining become limited. The removal rates achieved are generally low and tool wear can be prohibitively high. The recent introduction of high speed machining (HSM) has, to some extent, reduced this problem.

The main application general area that could see potential expansion for ECM is into production applications that are currently carried out using EDM. ECM and EDM processes are often thought of as being similar in that they both have the ability to produce complex shapes, with multiple features, using single tooling configurations operating along a single axis. For example, a component with through holes, a pocket feature and a contoured recess might be conventionally machined using a combination of milling and drilling. In the case of both ECM and EDM such a component could be machined using a single pass, single axis tooling set-up.

Over the past two decades EDM, has developed into a technology with £850 million pound world market and a regular growth rate of 2-3% [2], in die and mould manufacture. A similar potential for applying the ECM process, as a general purpose, high yield, method of producing components to a high quality, has not yet been fully realised. There are some specific reasons for this which will be detailed in at the next section. However, it is worth noting that there have already been many examples of where ECM has been used as an effective replacement for EDM operations. Several of

these examples have been detailed by Goyer [3] in a review of the ECM process. For example, Goyer provides details of a case study on an automotive company who produced hardened steel dies to produce parts for a gearbox assembly. This die had previously been manufactured using an EDM sinking operation. The production time for the die was around 150 hours. This time included hand finishing which was required to remove the EDM'ed recast layer. After assessing the possibilities of using the ECM process the company purchased an off-the-shelf ECM system. The operation was then carried out in only 35 hours by a sequence in which the die block was roughened out by ECM, followed by a short EDM operation to achieve the final tolerance, and finally finished by ECM to remove the recast layer. Goyer makes the point that switching to ECM for the main machining phase also saved on tooling costs since ECM tools do not wear out.

A further example given by a Goyer illustrates another aspect of the advantages of ECM over EDM. This concerned the machining of a sequence of curved sockets into the outer circumference of a stainless steel shroud ring. EDM had originally been considered to machine these pockets. However, in production trials, the estimated cost of the operation was too high (at around $270 dollars per ring) and the surface finish obtained which was in the region of 4.5 microns R_a was considered unacceptably high. By employing ECM to cut the slots the cost of the producing the ring was cut by around 55 per cent (to $114 per ring) and the surface finish was improved to acceptable levels of around 0.8 microns R_a.

1.4 Specialist applications of ECM and applications to modern materials

The above discussion concerned the competitiveness of the ECM process in cases where alternative competing technologies already existed. It is however worth noting there are a few specialist cases where ECM can be applied where there are no other realistic alternatives, or in cases where the need to be able to machine newly development difficult to cut materials has led to improved competitiveness of the ECM process.

The recent introduction of titanium aluminide intermetallics is an example of this later case. These alloys offer low density, high stiffness, good creep resistance and high strength at a wide range of temperatures [4,5]. In addition, these materials offer good oxidation and hot corrosion resistance [6]. Such characteristics make titanium aluminide a potentially important material in respect of weight savings in high performance components operating at high temperatures. The alloy is therefore of particular interest in aerospace application as a replacement to heavier nickel and iron based alloys [7]. These and other potential applications have led to an increasing requirement to define the overall processing route for such alloys. As part of this route, forging and casting methods will enable initial

production of components to pre-form shape. More accurate, secondary operations will then be required to produce the final required component accuracy. Some work has already been carried out to examine properties of the machining of this alloy using single point cutting [8] grinding [9] and high speed machining [10]. However, such mechanical techniques are often limited in terms of surface integrity effects [8] and the formation of surface hardened layers [9]. Work has also been carried out to characterise the machineability of this alloy using EDM [11]. In this case EDM was found to produce micro-cracking, due to thermal recasting and white layers on the machined surface. The application of ECM, to this material could potentially offer improved characteristics over EDM and mechanical machining techniques. This will be explored as part of the work in this thesis.

Examples of cases where realistic alternatives are very limited include the production of turbine blade cooling holes. Such holes enable jets of gaseous coolant to be passed through the body of a blade and out through further holes on the leading and trailing edges of the blade to form a protective cooling envelope. Such blades can operate in surrounding temperatures that would otherwise cause melting of the blade material. Cooling holes can be formed during the investment casting of a blade using ceramic core inserts during the production of low specification blades. However in the case of higher specification blades the ECM process can be applied, using tools in the form of fine tubing, to produce these holes to the required specification. Figure 1.4-1 shows an example of these holes machined by ECM through a Pegasus turbine blade. In the case of single crystal blades holes can be produced by ECM without affecting the overall single crystal integrity. Thermal techniques such as laser drilling and EDM are unacceptable in this case since thermal re-casting would disrupt the integrity of the otherwise single crystal structure.

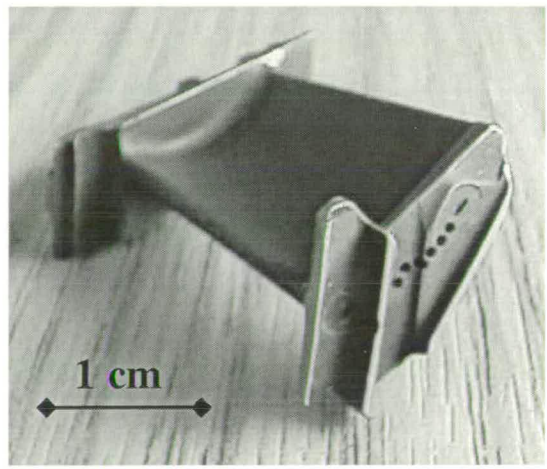

Figure 1.4-1 Pegasus turbine blade with axial cooling hole produced by ECM

Defect sampling/assessment operations are a further example where ECM can be applied in cases where conventional means will not readily provide a realistic solution. Such operations are often carried out on welded structures when a defect is found. These operations are carried out, in part, to

remove the defect to prevent further growth, but also in some cases to obtain a sample of the defect for subsequent analysis. Such analysis can often provide an estimate of the residual life of a structure or be used to provide information about whether the defect was introduced at the time of manufacture or has arisen during service.

Although grinding operations can be used for defect removal, it has been reported [12] that this method can impart additional stress at the machined site and this will often produce a residual surface which is prone to further crack growth. The use of grinding operations will in general destroy the defective section of the weld material and therefore sampling the defect by grinding cannot readily be achieved. This is especially true when the defective weld is in a relatively inaccessible location, such as in subsea situations.

Although not considered a direct part of the work of this thesis, this author has pioneered a project directed to the development of ECM for defect sampling and removal. A brief overview of the work is given here (for details see [13] as appended in Appendix A1).

This work has involved the development and application of an integrated sampling tool/non-destructive testing (NDT) system which provides the potential to undertake a weld inspection, carry out removal of the defective zone, and achieve validation of the repair, all within a single deployment operation (applied for the particular case of subsea use). ECM is applied to removal of the defect zone in combination with the Alternating Current Field Measurement (ACFM) NDT system which is used to ensure that the defect has been completely removed.

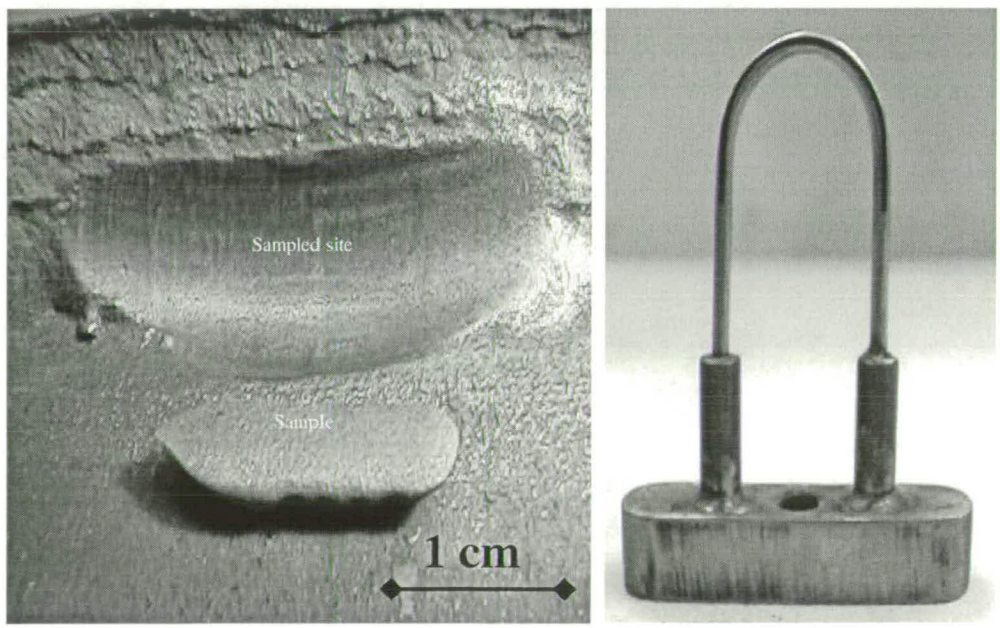

Figure 1.4-2: Sampled site in welded toe section and removed sample (on left) and "U-shaped" ECM sampling tool (on right)

The ECM sampling tool bit consists of a section of tubing shaped with the outer cutting face forming an approximate inverse of the required sample site profile. This has commonly been a "U" shaped section of the form shown in Figure 1.4-2 (right). The tube is slotted around the forward facing cutting surface to enable the supply of electrolyte into the active cutting zone in the direction of feed. The integrated ECM tooling/ACFM system is shown operating, in position on a tubular weld section, during submersed operation in a test tank (Figure 1.4-3). The sampled site and recovered sample are shown in Figure 1.4-2 (left).

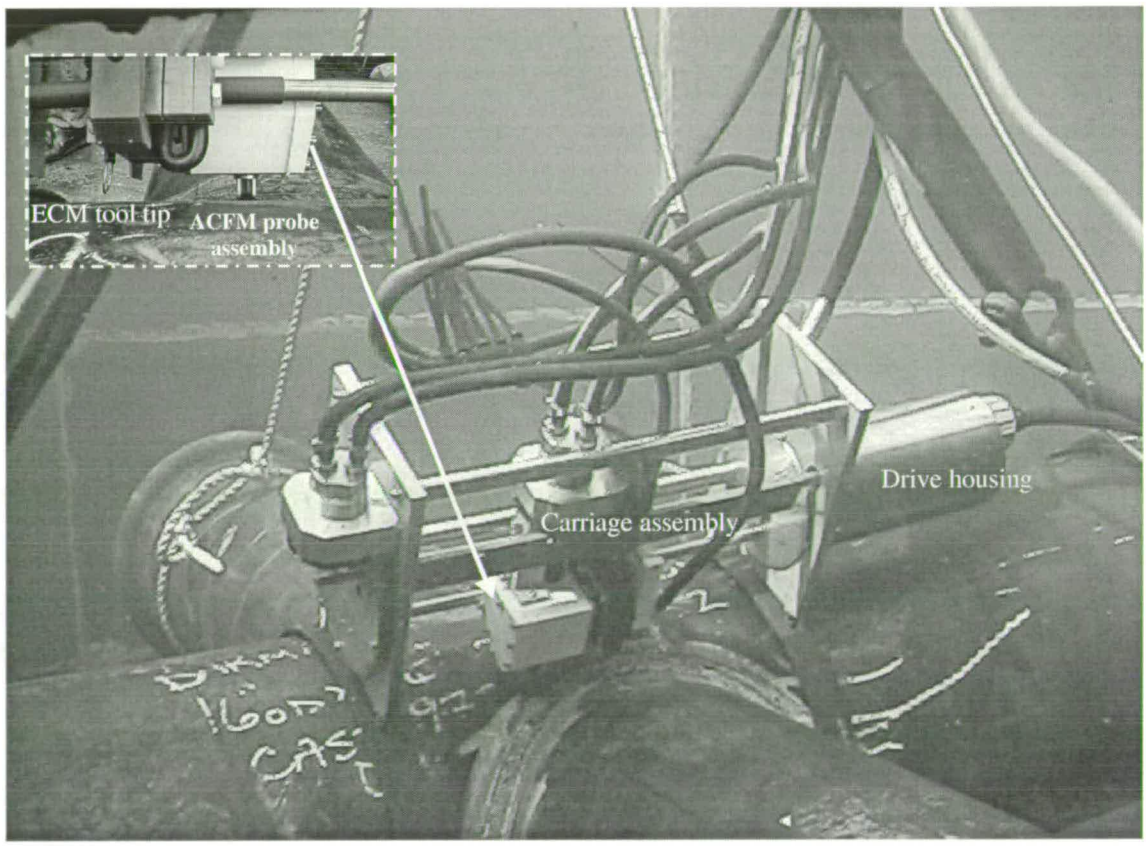

Figure 1.4-3:ECM/ACFM system during submersed operation in test tank with insert showing close-up of ECM tool (in retracted position) and ACFM probe (in deployed position) aligned at the weld toe

The application of ECM to this operation has the advantage that additional stress will not be imparted into the machined zone and that the surface at the sampled site after machining will be of high structural integrity. Also, because the process is essentially forceless it can readily be applied without the use of bulky mechanisms. Thus the system readily lends itself to Remote Operated Vehicle (ROV) deployed operations. Furthermore, unlike grinding, the ECM system, by using

flexible tools with minimal cutting areas, enables samples of the defective zone to be retained for subsequent metallurgical analysis.

1.5 Problems associated with ECM

Before discussing the problem associated with ECM in the context of today's manufacturing requirements, it is worth noting, as discussed by De Barr [14], that to some extent the expansion of ECM may have been impeded by the initial success of early applications. De Barr points out that the initial application of ECM in the manufacture of airfoil blades led to an acceleration of effort for shaping geomerties that could be regarded as relatively simple in the context of an ECM operation. This is because an airfoil profile enables tooling configurations to be designed with relatively simple single pass, single axis feed paths. Such configurations also lend themselves to provide electrolyte flow paths that are inherently uniform. De Barr makes the point that in wider ranging application, such as general purpose die and mould production, then the tooling configuration, and more specifically, the required electrolyte flow paths, would often be much more complicated. In many cases, multi-axis feed configurations and/or multiple pass tooling would be required and more than one electrolyte inlet outlet port arrangement would have to be simultaneously employed. This complexity would require more detailed tooling and process parameter developments than those that would otherwise have been avoided in the case of ECM applied to airfoil shapes. De Barr's point is that if work had been started on modelling complexities in ECM at the onset, then wider application in present day manufacturing may have been realised.

In the context of present-day manufacturing requirements, several related reasons can be identified to explain the limited usage of ECM. The most immediate reason can be equated with a general ignorance within manufacturing industry as to the possible usefulness and potential applications of the process. This was emphasised by Mike Yardley, the technical manager of AmTech plc, who, in a recent conversation with the author of this thesis, stated that many of his customers "simply lacked a general appreciation of the processes capabilities".

This problem was further illustrated in a recent series of seminars/short courses on advanced machining processes that were run and organised at Edinburgh University. As part of the series, the author of this thesis was involved in the organisation of a one-day seminar on ECM and EDM. About 20 people attended the course. What became very apparent during this course was, not only that there was a high level of interest in the ECM process, but also that there was a high level of ignorance about its possibilities (the level of interest in the EDM process was obviously lower because its potential was well understood).

In one particular case, an engineer from a well known manufacture of valves and flow controllers brought along examples of the cast body of one of their stainless steel valve systems. This part was manufactured from an initial casting of the valve assembly followed by the use of EDM to machine the valve seat to the required shape and surface finish. A high quality surface was required in order to decrease the flow path turbulence in the region of the valve seat. However, the company were not happy with the performance of their valves. At high flow levels, high turbulence occurred and this resulted in pitting, probably due to cavitation, in the region of the valve seat. In many cases this pitting was so severe that only after a short time of use the valve would not seal properly when closed. To address this problem the company were carrying out hand finishing of the flow channel in order to reduce turbulence and prevent cavitation. This secondary operation was an expensive bottleneck in their production process. The engineer was at the course because had been told that modern EDM systems were capable of producing much better surfaces than the older system which the company were currently using. He was told that this was true but that the removal rate, when using the polishing capabilities of EDM, would be extremely low, and that ECM may offer a better option for this type of operation.

This engineer had not heard of the ECM process prior to this course. It was pointed out to him that ECM could be used, not only to finish the valve flow path, but also to achieve the bulk-removal. The engineer was then put in touch with the ECM company, EMS Ltd, in Coventry, who carried out a short feasible study on the valve. This proved to be successful and EMS were awarded a series of rolling contracts to machine the valves.

This example serves to illustrate that, to at least some extent, a lack of knowledge about ECM (or even no knowledge about the process's existence) has impeded its wider application. However, even engineers who are familiar with ECM may find themselves deterred when considering implementation of the process. The reasons for this can be grouped into four categories, which are discussed individually in the following sub-sections.

1.5.1 Expensive set-up costs

When compared to EDM for example, the ECM process can be expensive to set up. Since most machines today are purpose-built it is difficult to obtain prices for general purpose ECM machines. However, Kellock [15] reviewed some prices in 1982 and concluded that prices, for a 10,000A machine, which would be capable of removing material at a rate of 16 cm^3/min, were in the region of £200k. Lower removal rates, of in the region of 3cm^3/min, could be achieved with a system costing around £32,000. At the time, the cost of an EDM machine (although achieving a lower removal rate) would be around half this value, and this is probably the situation today. Kellock points out that the production of ECM machines in greater numbers would inevitably lead to reduced prices.

1.5.2 Environmental aspects of ECM

Gaseous products need to be removed from the machining zone and extracted to outside the factory. Hydrogen, the main gaseous product, can be explosive under certain conditions. There may be concern that certain metals and electrolyte combinations could produce toxic gaseous by-products. Solid products of machining, usually hydroxides or oxides of the metal being machined, need to be disposed of. This can be a particular concern if the composition of the product is not known. Overall these aspects have given the process a "difficult-to-manage" image.

Environmental concerns about the application of the process will to some extent be offset if a clearer understanding of the chemical species involved is developed. This is currently the subject of collaboration between the author of this thesis and the Chemistry Department at Edinburgh University. The results of this investigation will be reported in a thesis [16] scheduled to be completed in October 2002.

1.5.3 Poor Accuracy

ECM is not usually thought of as a process for achieving good accuracy. These limitations are in practice due to limits on machine construction compromises and process control trade-offs. Goyer [3] for example gives the tolerances obtained for the machining of blades on a steam turbine drum, as ±0.05mm. DeBarr (Page 17, [14]) quotes typical and readily achievable tolerances as in the region of ±0.04mm for ECM and compares this to tolerances readily achieved for EDM, as a four-fold improvement to around ±0.01mm. Wilson [17] a former Development Engineer with a Rolls-Royce plc, indicates that tolerances obtained using ECM can be as good as ±0.01mm in some applications. Wilson points out that such tolerances should be achievable with machines made to greater rigidity and using close control of machining parameters and appropriate electrolyte selection.

An illustration of what can be achieved when using high rigidity set-ups, is provided by a recent project carried out by the author of this thesis. This work involved the ECM finishing of tensile test specimen in titanium aluminide material. The tooling, shown in Figure 1.5-1 was a static arrangement formed from two segments which fully enclosed the pre-form specimen. Positioning of the workpiece centrally between the upper and lower tool segments was achieved using a micrometer pin arrangement as shown in Figure 1.5-2. In order to achieve high accuracy in the dissolution interval an electronic timer with an resolution of one micro seconds was used to control the power on cycle. Calibration trials were carried out to determine the relationship between the power on duration of the envelope that would be removed for a given initial diameter of the preform. During the production runs tolerances of ±0.005mm were readily achieved.

Because this example of ECM uses a static tooling arrangement in a form which could be readily assembled to provide high rigidity, it can be thought of as representative of a near ideal ECM configuration. This example does however illustrate that ECM tolerances can be very good (competitive with EDM), and that achieving such tolerances are dependent upon the design of tooling configurations and process control, rather than any fundamentals of the process.

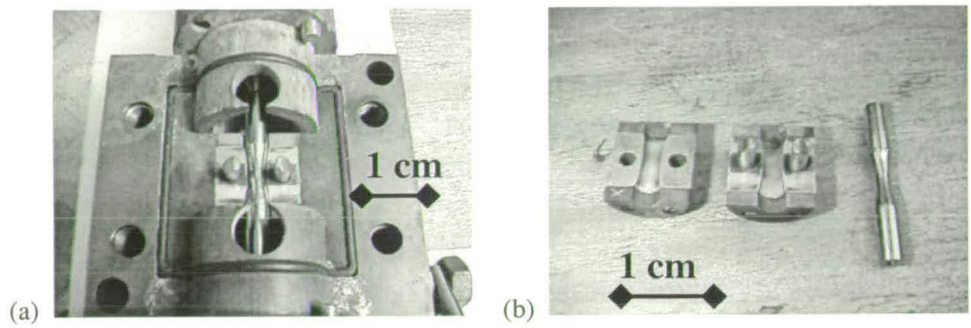

Figure 1.5-1: (a) cell arrangement for machining of tensile test specimens and (b) split tooling and pre-form workpiece

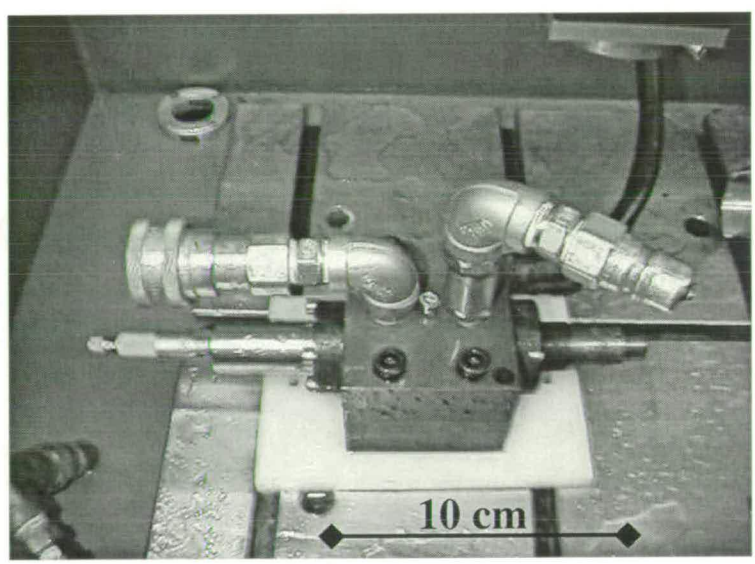

Figure 1.5-2: Cell and alignment system for ECM finishing of tensile test specimens; an application in which high accuracy can be achieved by ECM

1.5.4 The need for iterative methods for tool design and parameter selection

In general, for an EDM production set-up, the tooling can simply be designed as the inverse of the required workpiece shape. This is not the case with ECM where a direct inverse tool design is not suitable for most practical applications. Consequently, designing a tool form through iterative trial-

and-error methods is a time-consuming process that often makes the use of ECM prohibitively expensive.

Mike Yardley (technical manager of AmTech plc) has stated that the tool design problem represents the most significant challenge impeding the current advancement of the process. Alan Cannon, a development engineer for Rolls-Royce plc, agrees with this. He has described the tool design process as being one in which many trial and error iterations are required using general rule of thumb guidelines. Within Rolls-Royce several months can be spent achieving the required component tolerance and surface reproducibility. Because of this Alan Cannon has stated that ECM is generally only used when other alternatives have been exhausted. This is often only the case for particularly difficult to machine materials or when a particular ECM technology is already well-established such as the 360° airfoil manufacturing system as described in section 1.1.

Further discussion on the way in which ineffectiveness of tool design procedures and parameter selection have impeded the advancement of ECM is discussed by Jain et al. [18, 19] and Nilson et al. [20].

1.6 Chapter overview and conclusions

The discussion above has indicated that although ECM finds many specialist applications, several aspects associated with the process's implementation impede its expansion. Set-up costs are likely to remain high, but these will be offset by the high rate of production that can be realised. Environmental concerns could be overcome, at least to some extent, through work, currently in progress, aimed towards a better understanding of the chemical species involved. Realising high accuracy will be achieved by improvements in tooling rigidity and through improved control and understanding of process interrelationships (this aspect is been indirectly addressed in this thesis). The primary challenge, however, is the need to avoid the iterative approach currently employed for tool design and process parameter selection. The process characterisation strategy developed in this work is aimed at achieving a significant component in the realisation of this. This strategy is based upon ECM planar dynamics. Therefore, before detailing the process characterisation methodology of the thesis, the following chapter provides an overview of the basis of the approach evolved in subsequent chapters.

CHAPTER:

2 Theoretical Background

This chapter provides the basic theoretical background that will be developed in later chapters to form the basis of the C-function characterisation strategy of this thesis. This theory develops from a fundamental description of the electrolysis process to give a theoretical description of ECM planar dynamics. This representation provides basic relationships between process variables and parameters.

2.1 Electrochemistry of anodic dissolution

During the ECM process the workpiece is biased as the anode with respect to a cathodic tool. Electrolyte is directed to flow at high velocities through the gap between the tool surface and the workpiece surface. The tool is positioned close to the surface to be machined, but not touching, and is traversed and/ or sunk to initiate high current electrolysis and remove material to the required form.

Electrolysis can he defined as the production of chemical change by the passage of an electric charge thorough an electrolyte. In an electrolyte, positive and negative ions (usually made up from ionic salts dissolved in water) become the carriers of electric charge between the tool cathode and the workpiece anode. In ECM the chemical change is the dissolution of the workpiece material (anodic dissolution) which produces material removal from the workpiece surface atom by atom. Each atom being released as electrons are removed from the ionic bond to neighbouring atoms. The resultant free atom then becomes positively charged and moves away from the workpiece along the gradient of the electric field (resulting from the applied electric potential) towards the tool. Faraday's laws of electrolysis determine the rate at which dissolution occurs. Faraday's laws can be expressed as a simple proportionality between the mass of material released from the anodic workpiece and the quantity of electric current (charge) that passes through the electrolyte, as follows:

$$g \propto q\varepsilon$$

Equation 2.1-1

Where g is the mass of workpiece surface that is dissolved by a quantity, q, of electric charge passing through the cell arrangement.

ε, known as the electrochemical equivalent of the workpiece material, can be defined as a ratio of the average valency of dissolution, n, to the average atomic weight of the constituent elements making up a particular alloy, G. Thus:

$$\varepsilon = \frac{G}{n}$$

Equation 2.1-2

More specifically, in this work (see Appendix A2 for computation details), when alloy constituents are being considered, ε is represented using matrix notation, so that the total electrochemical equivalent for any one material/alloy is defined by:

$$\varepsilon = \sum_{i=0}^{I} \left(\frac{a_{i,0}}{a_{i,1}} \right) a_{i,2}$$

Equation 2.1-3

Where $a_{i,j}$ is a three column matrix with one row for each of the alloying elements of the material composition. Columns $a_{i,0}$, $a_{i,1}$, $a_{i,2}$, representing the atomic weight, the valency of dissolution and the percentage composition, respectively.

For example, the commonly used aerospace alloy, In718, which is one of the main alloys to be used throughout the trials in this thesis, has an elemental composition as shown in Table 2.1-1.

Element	Fe	Al	Mn	Co	Cr	Cu	Mo	Ni	Si	Ti
Atomic weight, $a_{i,0}$	55.9	27.0	54.9	58.9	52.0	63.5	95.9	58.7	28.1	47.9
% composition (by weight) , $a_{i,2}$	23.5	0.48	0.22	0.17	18.16	0.02	2.96	53.3	0.01	1.02

Table 2.1-1: Elemental composition (nominal) and atomic weights for In718 alloy*

For the purposes of this illustrative example, it is assumed that the valency of dissolution is three for each element of the alloy (i.e. $a_{i,1}$ = 3.0 for i = 0 to I Equation 2.1-3), then the electrochemical equivalent can be calculated according to Equation 2.1-3, as : 19.2 gm.mol^{-1}.

The constant of proportionality for Equation 2.1-1 is 1/F, the Faraday, equal to 96,500 Coulombs (or 26.8 Ah). Thus for a mass of material removed, g by the quantity of current, *I.t* (I amps flowing for a time period of t seconds), then:

$$g = vol.\rho = \frac{It\varepsilon}{F}$$

Equation 2.1-4

Vol. is of the volume of material with an average density of ρ dissolved in time t.

---

* Material Specification AMS 5596H Haynes International, Kokomo, Indiana, USA

With reference to Equation 2.1-4, it can be seen that the quantity of electricity I.t, will be equal to the constant, F, for the specific condition that g = ε. In this case $F = I.t$ and the mass of material dissolved by the passage of each Faraday of charge will be the electrochemical equivalent for that particular workpiece. It can therefore be seen that the mass of material removed will be sensitive to the value of ε. However, before this sensitivity can be discussed in detail, the concept of what is often referred to, as "process efficiency" in ECM, needs to be considered and clearly defined in the context of the work of this thesis.

In Equation 2.1-4 the rate of metal removal was defined in terms of Faraday's laws where, in the general definition, the current passing between the electrodes was said to bring about the chemical change of anodic dissolution. However, under certain conditions current can be "consumed" by other possible mechanisms. The production of oxygen for example has been observed to occur [21] to differing degrees depending on conditions. The total current passing between the electrodes is then the total of that taking part in anodic dissolution and oxygen production. A common way to express this is by defining a current efficiency, as follows:

Current efficiency (%) = (actual metal removal rate / theoretical metal removal rate) x 100%

The theoretical removal rate being that as defined by Equation 2.1-4 with the assumption that the passage of current produces only anodic dissolution. The definition of current efficiency defines the fraction of current "consumed" by metal dissolution, J_d relative to the total current passed between the electrodes, J, thus:

$$\textit{Current efficiency (\%)} = J_d/J \times 100\%$$

Using this definition for efficiency requires that further clarification be made concerning the definition of the rate of metal removal according to Equation 2.1-4. Firstly, the parameter ρ must refer only to the density of material within the anode that is consumed by dissolution. Thus the value of ρ must be reduced in cases where the total density includes workpiece constituents that do not take part in the electrolysis process. Such constituents would be for example, carbon in the case of iron and steel, or for example, carbides or other particulates, in the case of composite materials. Such components will, in general, just "fall-out" of the anode as the metallic base is eroded. Although in most cases the relative contribution of these non-electrolysed constituents will be small, and can therefore be neglected, their existence should be included in any efficiency calculation where maximum accuracy is required.

A second point in relation to efficiency should also be made. From examination of Equation 2.1-4 it can be seen that a change in valency, n (a constituent of ε), will also lead to an apparent change in

efficiency. Although it would be reasonable to include this parameter within the definition of current efficiency (this is the approach taken by many, for example [22]), in this thesis the term efficiency is used only in the context that the value of n is known. In practice this means that the efficiency can only be accurately stated if any deduction about the value of n is correct. Achieving this would be difficult in many cases since on the anode surface different discrete values of n may be occurring. This situation would lead to a non-integer value for the average value of n, and accurate determination of this value would be difficult unless accurate assumptions or determination of the efficiency could be made.

The use of chemical analysis in some cases could be used to determine the dissolution valency. However, such techniques can be complicated by the fact that these products can be modified by further reactions (with oxygen in the electrolyte for example) and this could lead to an implied average valency different from the actual valency of dissolution.

Ultimately then, if absolute clarification is maintained, it is probably not realistic to be confident about any statement about the dissolution efficiency, without also being confident about the value of valency. However, if a certain value of valency is assumed then the efficiency can be quoted in this context. Or if the efficiency value is assumed then the valency can be stated in this context. In this thesis, unless otherwise stated, this latter approach is taken where the apparent valency is assuming 100% current efficiency.

2.2 ECM planar dynamics

The characterisation strategy developed in this thesis is based upon a configuration consisting of a plane parallel tool eroding a plane parallel workpiece, as illustrated in Figure 2.2-1. The basic equations, initially detailed by Tipton [23, 24], are briefly reviewed here in the context of general characterisation.

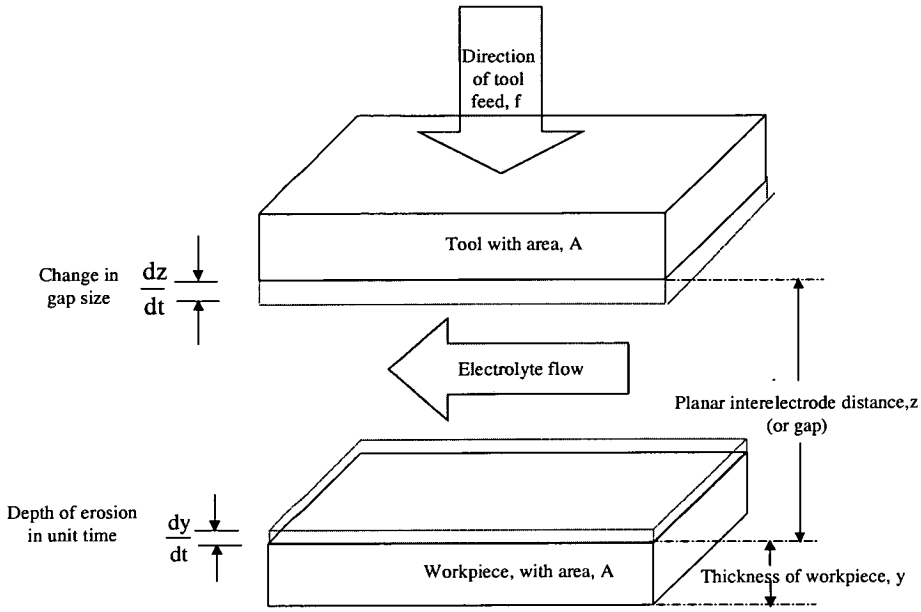

Figure 2.2-1: Notation for Planar ECM System

z, is the gap size[†] and dz/dt is the change in gap size, in the direction of tool feed, per unit time.

y, is the height of the workpiece and dy/dt is the amount by which the height of the workpiece is eroded per unit time.

To consider the case of ECM planar dynamics the following "ideal-system" assumptions are made:

- For any one electrolyte workpiece system the value of ε, the electrochemical equivalent, is considered as a constant and not sensitive to other process parameters.

- V_0, the overpotential sum required to drive the reaction at the electrodes, is constant and not sensitive to other process parameters.

[†] Between many different authors in ECM there appears to be some confusion as of the use of the term gap size which is sometimes used as a replacement term for the inter-electrode gap (IEG), and also visa-versa. In this thesis the term IEG will be used as the term for a complete description of the geometric form of the gap between the tool face and the workpiece surface. Thus the term IEG may be used to describe some profile in 2-D, or it may simply refer to the case of a constant gap along the length of a planar tool workpiece configuration (in which case gap size and IEG are equivalent). The term gap size will be used to refer to the specific case of a particular measurement at a particular point between the tool face and the workpiece surface.

- The conductivity, κ, of the electrolyte is constant and not sensitive to other process parameters.

It can readily be seen that the erosion rate, dy/dt is given by the mass removal per unit time (from Equation 2.1-4) as:

$$\frac{dy}{dt} = \frac{J\varepsilon}{\rho F}$$

Equation 2.2-1

where J is the current density, I/A.

For a constant value of tool feed rate f equilibrium conditions will be reached when the change in height of the workpiece will be equal to f. Thus the change in position of the tool face relative to the workpiece surface will remain unchanged so that z is a constant and equal to z_∞, J will become J_∞, and f will be equal to the erosion rate, thus:

$$f = \frac{J_\infty \varepsilon}{\rho F}$$

Equation 2.2-2

By substitution of G/n for ε (Equation 2.1-2)and rearranging Equation 2.2-4 an expression for calculating the valency at equilibrium can be formulated, as:

$$n = \frac{J_\infty G}{fF\rho}$$

Equation 2.2-3

Also, the current density, J, can be expressed in terms of the voltage available to drive the current through the electrolyte, $V\text{-}V_0$; the conductivity of the electrolyte, κ, and the gap size, z, as:

$$J = \frac{(V - V_o)\kappa}{z}$$

Equation 2.2-4

Combining Equation 2.2-2 and Equation 2.2-4 and rearranging gives an expression for the gap at equilibrium, z_∞ as:

$$z_\infty = \frac{\kappa(V - V_0)\varepsilon}{\rho F f}$$

Equation 2.2-5

Computation of the gap at equilibrium according to Equation 2.2-5 can be substituted back into Equation 2.2-4 to give the expression for the machining current density at equilibrium, as follows:

$$J_\infty = \frac{\kappa(V - V_0)}{z_\infty}$$

Equation 2.2-6

Equation 2.2-4, Equation 2.2-5 and Equation 2.2-6 will be used later in this thesis to examine process relationships under conditions of equilibrium. However, further insight can be gained by examining and developing more general dynamic equations, as follows:

In the general case, with reference to Equation 2.2-1 it can be readily seen that the change in gap size, dz/dt, is given by:

$$\frac{dz}{dt} = \frac{dy}{dt} - f$$

Equation 2.2-7

Where from Equation 2.2-4 and Equation 2.2-5 :

$$\frac{dy}{dt} = \frac{\kappa\varepsilon(V - V_0)}{\rho F z}$$

Equation 2.2-8

Now based on "ideal-system" assumptions (stated above), κ, ε and V_0 are considered as constant (F is a constant by definition) and ρ is constant based on the assumption of workpiece homogeneity, then an erosion constant, k (or k-parameter), can be defined for a set value of V, as:

$$k = \frac{\kappa\varepsilon(V - V_0)}{\rho F}$$

Equation 2.2-9

Equation 2.2-8 combined with Equation 2.2-7 can now be written:

$$\frac{dz}{dt} = \frac{k}{z} - f$$

Equation 2.2-10

Equation 2.2-10 is the time dependent description of ECM planar dynamics and can be confirmed by setting the equilibrium condition that the change in gap, $dz/dt=0$, when $z \rightarrow z_\infty$ and Equation 2.2-10 becomes:

$$f = \frac{k}{z_\infty}$$

Equation 2.2-11

Thus confirming Equation 2.2-5. The physical significance of the k-parameter can be seen in Equation 2.2-11 in that it defines the value of z_∞ for any given value of the set parameter f. The k-parameter will also provide a basis for a description of the geometric transfer characteristics between the tool and a workpiece at equilibrium conditions. This aspect is to be developed further in chapter 4 and will become the basis of the characterisation trials described in Chapter 6 and the C-function characterisations given in Chapter 8.

2.3 General "ideal" characterisation relationships and sensitivities

The sensitivity of the planar gap parameter, z, to changes in the k-parameter, can be examined by application of the equations outlined in section 2.2. Such an examination will provide an indication of the sensitivity of tool to workpiece transfer characteristics to the variation in each or a combination of the constituent machineability parameters of n, κ and V_0.

The most significant dependencies are:

- Gap size against machining voltage
- Gap size against feed rate
- Gap size against valency
- Gap size against conductivity

These relationships have been computed, using Mathcad worksheets (see Appendix A3), for the example case of machining a In718 alloy with an elemental composition as given in Table 2.1-1.

Nominal machineability parameters have been assumed for the example case of these initial calculations as follows:

$n = 3.0$
$\kappa = 20\ S\ m^{-1}$
$V_0 = 5.0\ V$

For this system and applying Equation 2.1-3 gives a value for the electrochemical equivalent, ε, of $0.019\ kg\ mol^{-1}$.

The dissolution constants of the Faraday and ρ for In718 are:
$F = 9.648\ A\ s\ mol^{-1}$
$\rho = 8.23 \times 10^3\ kg\ m^{-3}$ (as measured)

and set machining parameters are:

$V = 25\ V$
$f = 1.667 \times 10^{-5}\ m\ s^{-1}$ ($1.0\ mm\ min^{-1}$)

For these conditions the *k*-parameter is calculated according to Equation 2.2-9 as $1.064 \times 10^{-8}\ m^2\ s^{-1}$.

A fundamental machineability relationship is the dependency of the equilibrium gap upon the machining voltage for a fixed feed rate and the sensitivity of this dependency upon overpotential. This can be determined for ideal conditions applied to a planar configuration using Equation 2.2-5. Figure 2.3-1 shows the plot of this dependency for a voltage varying from 5 V to 25 V and an overpotential variation of ±10% about a mean value of 5 V.

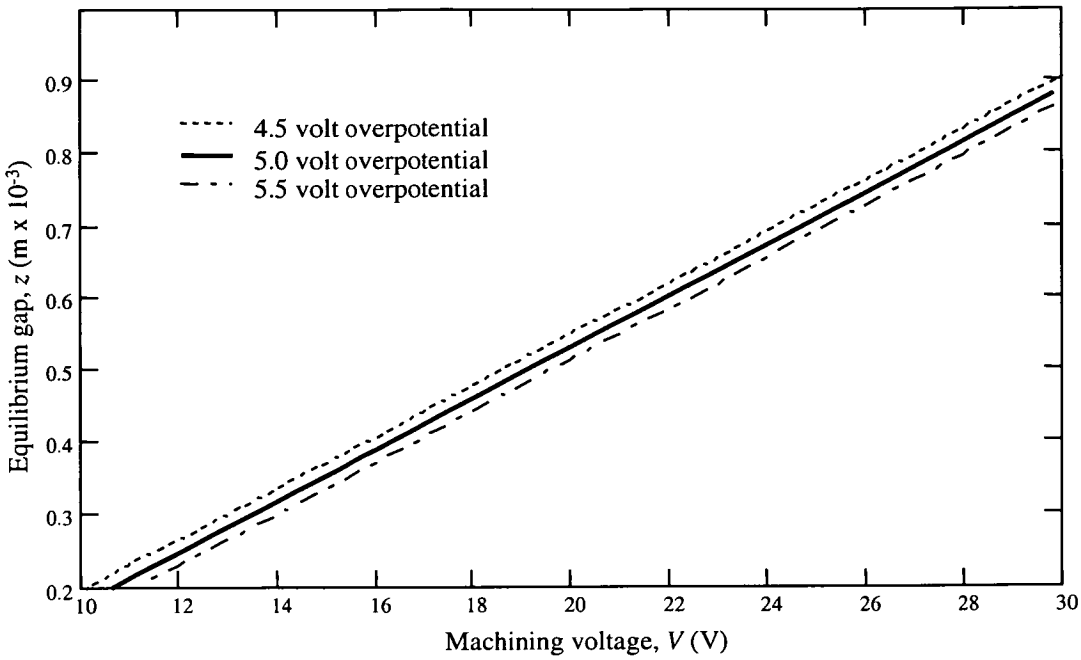

Figure 2.3-1: Sensitivity of equilibrium gap to machining voltage and overpotential

From Figure 2.3-1 and Equation 2.2-5 the equilibrium gap will vary by $\pm 0.02 \times 10^{-3}$ m for a variation in the overpotential of ±10%.

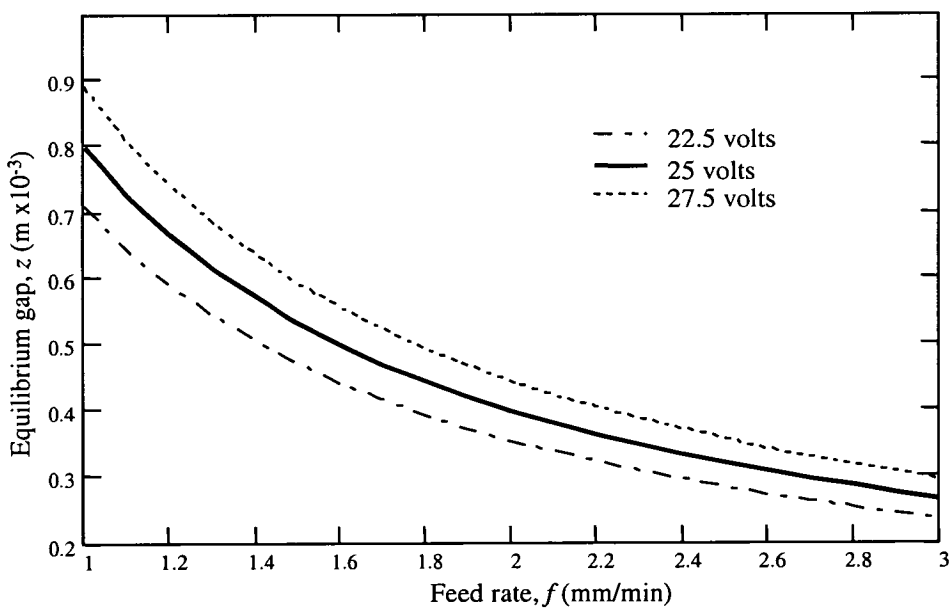

Figure 2.3-2: Sensitivity of equilibrium gap to a 10% change in machining voltage at feed rates of 1.0 to 3 mm/min

Equation 2.2-5 can be plotted for a voltage range of ±10% around a mean of 25 V over a feed rate range of 1.0 to 3 mm/min (shown in Figure 2.3-2) and over a valency range of 2 to 4 at a fixed feed

rate of 1 mm/min (shown in Figure 2.3-3). These plots illustrate that the sensitivity of the equilibrium gap to a change in the machining voltage and/or valency is more significant with decreasing feed rates. At a fixed feed rate of 1.0 min/min then the equilibrium gap will change by ±0.09mm for a ±10% change in machining voltage. From Figure 2.3-3 it can be seen that valency increment/decrement of ±1 will produce a change in the machining gap of typically 0.3mm (this sensitivity will be greater at lower values of valency).

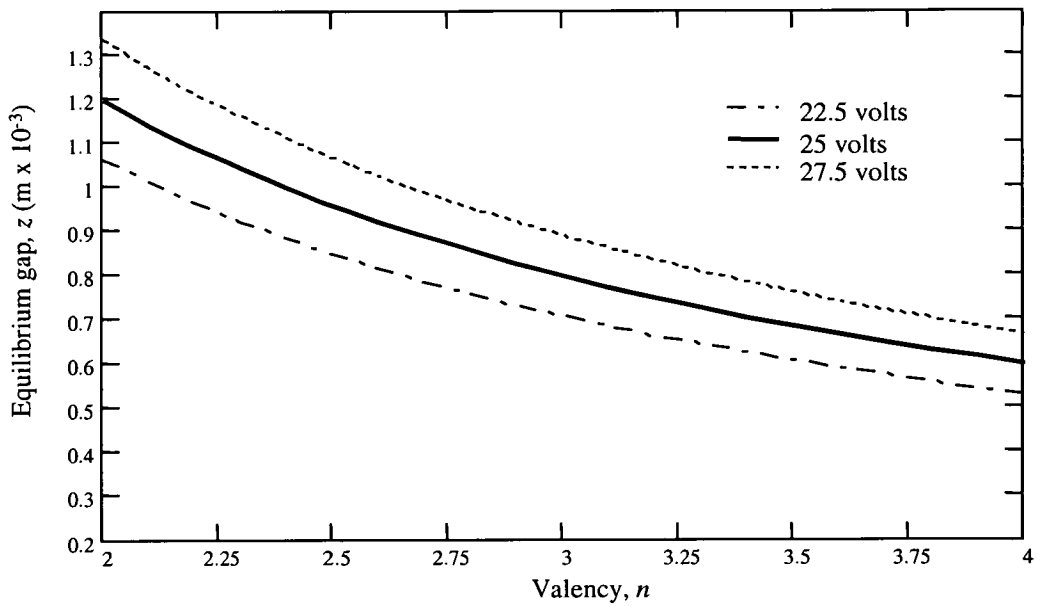

Figure 2.3-3: Sensitivity of equilibrium gap to a 10% change in machining voltage for a valency range of 2 to 4

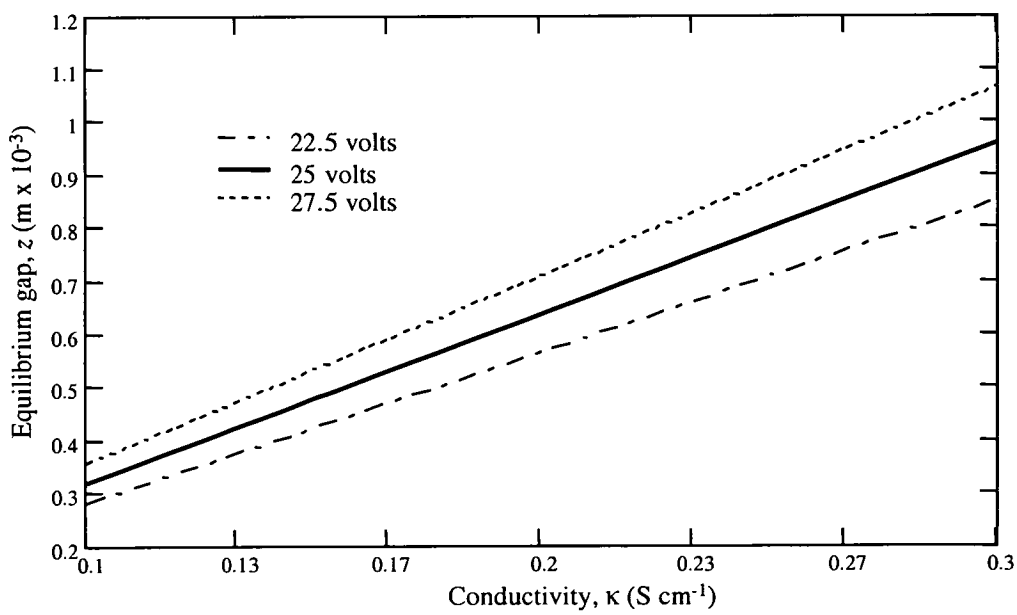

Figure 2.3-4: Sensitivity of equilibrium gap to a 10% change in machining voltage over a conductivity range of 0.1 to 0.3 S cm^{-1}

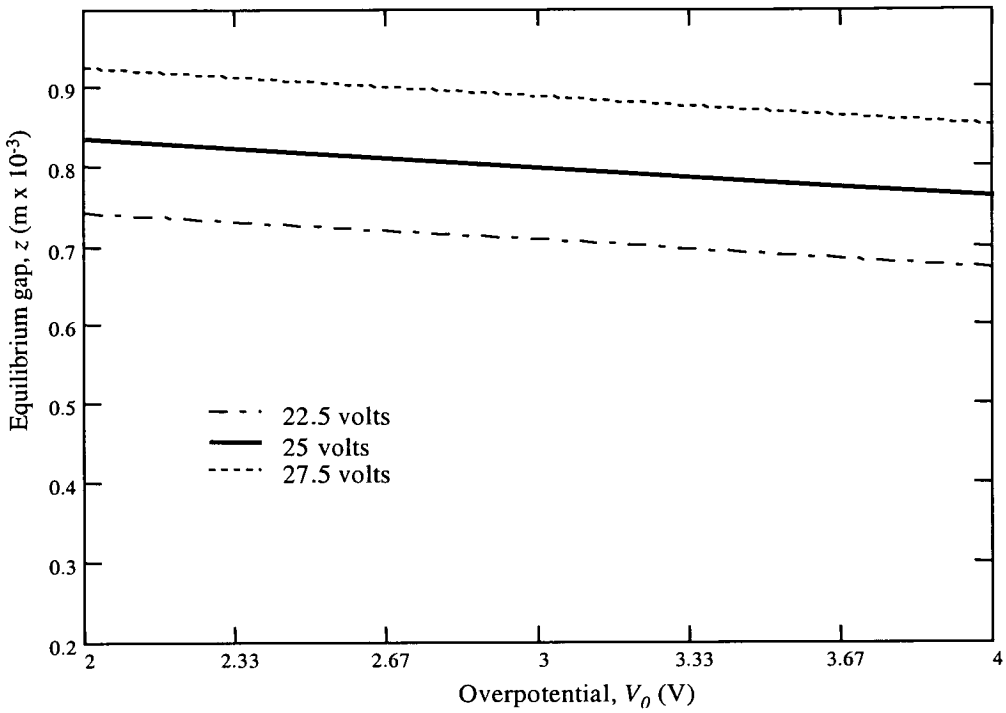

Figure 2.3-5: Sensitivity of equilibrium gap to a 10% change in machining voltage over an overpotential range of 2 to 4 V

Equation 2.2-5 is plotted over a conductivity range of 0.1 to 0.3 S cm^{-1} and an overpotential range of 2 to 4 V in Figure 2.3-4 and Figure 2.3-5 respectively. The sensitivity of the equilibrium gap to machining voltage will be higher for increasing values of conductivity. An increase/decrease in the gap conductivity of 0.1 S cm^{-1} will increase/decrease the gap size by 0.55mm (Figure 2.3-4). An increase/decrease in the value of overpotential of 1 V will increase/decrease the gap size by 0.036mm (Figure 2.3-5).

2.4 Chapter Overview and conclusions

This chapter has provided a theoretical background to describe ECM process relationships for the case of a planar tool/workpiece configuration. Within this theory a machineability parameter, the k-parameter, is defined as an assemble of ECM machineability constants. This treatment has also enabled determination of the sensitivity in the gap parameter to the primary machineability

constants. These sensitivities will be used to provide a determination as to the relevance of certain parameter relationships in the data discussed in chapter 6 and 8.

In chapter 4, the theoretical background of this chapter will be extended to provide current-time and gap-time process descriptions, from which the value for the k-parameter can be directly determined. The theory of this chapter will also be extended to develop the concept of C-function characterisation.

Before outlining these developments, the discussion of the following chapter, considers the work of others who have been working in the areas of process characterisation, process simulation and tool modelling.

Chapter:

3 Literature review

This chapter presents a review of work carried out between the 1960s and the present day on what can be broadly defined as characterisation of electrochemical machining. This work can be subdivided into investigations which model ECM under what can be termed ideal conditions and other work which examines the cases where the effect of non-ideal conditions are examined. Although this thesis is concerned with the direct measurement of machineability functions, it is of use to review the work of others who have attempted to determine analytical and semi-analytical descriptions of ECM. This review serves to illustrate the inherent complexities involved in such approaches and therefore leads to a justification of the partial empirical solution, described in this thesis. This chapter also includes a review of work carried out on process simulation and tool design in ECM. Although in this thesis such work is not directly developed, it is useful to assess the current state of progress since the characterisation strategy developed here will be configured as input to such systems.

Notation used for equations developed by other authors is the same as that used in the quoted publications but only in cases where symbols are referred to parameters not already used in this thesis. Otherwise the notation used throughout the rest of this thesis is used for these relationships.

3.1 ECM planar dynamics

The basic equations for ECM planar dynamics, first detailed by Tipton in [23], have been described in chapter 2. An initial assumption in this basic model was that ideal conditions exist within the IEG. That is, the conductivity of the electrolyte is constant and that the valency and overpotential are fixed constants which are insensitive to changes in machining parameters. The following reviews work, primarily using analytical description, directed to examining the cases when this assumption becomes inaccurate.

This section is divided into three subsections dealing individually with gap resistivity, overpotential and valency dependencies.

3.1.1 Gap resistivity/conductivity dependencies

As an additional part of the study in [23], in order to consider the dependency on conductivity distribution with temperature, Tipton calculates the approximate relationship between the inlet temperature, *T(0)*, and the temperature at a position *x*, *T(x)*, where *x* is a co-ordinate variable representing the position along a planar flow field. That is; $x = 0$ at the flow inlet side of the IEG and increases with flow path length. The basis of Tipton's model is to assume that the only significant contribution to heating within the gap is Joule heating due to the passage of the electrolysing current through the electrolyte. That is, heat generated due to viscous friction and heat lost by conduction through the electrodes, is ignored. The temperature gradient within the electrolyte, *dT/dx*, can thus be expressed as:

$$\frac{dT}{dx} = \frac{\kappa(V - V_0)}{v_0 \rho_e c y_0^2}$$

Equation 3.1-1

Where v_0 is the velocity of the electrolyte at the inlet, and ρ_e and c are the density and specific heat capacity of the electrolyte respectively.

Tipton then assumes a linear dependency of κ with T, as follows:

$$\kappa(x) = \kappa_0[1 + \alpha(T(x) - T_0)]$$

Equation 3.1-2

Where κ_0 and T_0 are the ambient (i.e. inlet) conductivity and ambient temperature respectively and α is the specific conductance of the electrolyte.

Combining Equation 3.1-1 and Equation 3.1-2 and solving the resulting differential equation, yields:

$$T(x) - T_0 = \frac{1}{\alpha}\left[e^{\alpha A \kappa_0 x} - 1\right]$$

Equation 3.1-3

Where: $A = \dfrac{\kappa(V - V_0)^2}{\nu_0 \rho_e c y_0^2}$

Thus the temperature, and as a consequence the electrolyte conductivity, is predicted to rise exponentially along the gap as the co-ordinate x increases.

Tipton also shows that the current density distribution, J(x), can be deduced by substitution of Equation 3.1-2 into Equation 2.2-4 and solving the resultant equation to give:

$$J(x) = \frac{(V - V_0)\kappa_0 e^{\alpha A \kappa_0 x}}{z_0}$$

Equation 3.1-4

Plotting Equation 3.1-4 for a range of values for the flow rate Q (calculated from ν_0 a constituent of the constant A in Equation 3.1-4) provides a visualisation of the magnitude and variation of parameters of importance (Figure 3.1-1).

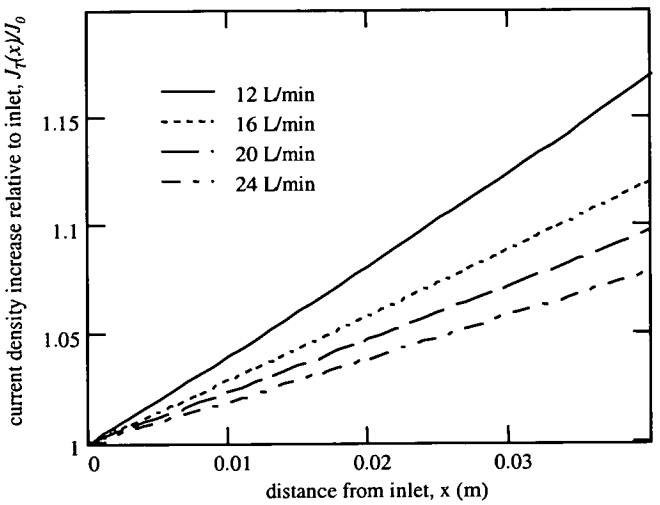

Figure 3.1-1: Current density increase relative to inlet considering only temperature effects (plot as per Equation 3.1-4 from [23])

Equation 3.1-4 will describe the initial situation, at the start of machining, in the case of plane parallel electrodes. As machining proceeds the self-compensating characteristics of the process will take effect (according to the dynamics described by Equation 2.2-10). Thus at the far end of the flow field, where the conductivity is higher, the current density will also be greater than at the inlet. This will cause an initial high rate of dissolution, which will cause an opening out of the gap at this point. After a certain duration a steady state situation is reached in which the value of current density is constant along the length of the gap (since the anode shape is now invariant this must be the case). For this condition Tipton shows that the temperature gradient along the gap is given by:

$$\frac{dT}{dx} = \frac{(V - V_0)J}{\nu \rho_e c z_{0\infty}}$$

Equation 3.1-5

Where $z_{0\infty}$ is the equilibrium gap at the flow inlet side.

The RHS of Equation 3.1-5 is a constant (with the assumption of ideal conditions) and therefore the temperature increases at a linear rate with x. As a consequence the gap at equilibrium will vary in proportion to the specific conductivity of the electrolyte, which for the case of temperature effects alone (Tipton does not consider other factors which affect conductivity although he acknowledges that gaseous products will have an effect in reducing conductivity) is given by:

$$z(x) = z_0 + z_0 \alpha \Delta T(x)$$

Equation 3.1-6

Where ΔT is the temperature rise at the co-ordinate x relative to the inlet temperature.

Several workers have since detailed the limitations and range of applicability of such basic models. Clark [25] has shown through incorporation of a linear array of bead thermistors, along the length of a planar IEG, that for many process conditions, the temperature rise along the gap cannot only be attributed to the effects of Joule heating. Clark found that for conditions of increasing current density the actual temperature rise increased at an increasing rate resulting in a distorted taper in the IEG at equilibrium (a linear taper is predicted by Tipton's analysis). Clark suggested that in addition to resistive heating, increased resistivity due to the accumulation of hydrogen and localised evolution of steam bubbles occurred. It is suggested that such bubbles, which form due to boiling within very localised turbulent voids, have properties of very high resistivity. Once these begin to form then the additional heating within these areas cause a runaway effects, resulting in increasing gap tapers towards the exit end of the flow fields.

Hopenfeld and Cole [26] have examined the hydrodynamic and thermodynamic mechanisms in ECM. In particular, this study has detailed the distribution of electrolyte conductivity, for the case of a planar IEG, through examining the influence of an accumulation of non-conducting gaseous products along the axis of electrolyte flow. Their work has demonstrated that at any one point in the IEG, for fixed conditions of flow, that the relationship between the current density and applied voltage, for a range of gap sizes typical to ECM (0.4 to 0.8 mm) is linear, and therefore obeys Ohm's Law. When the flow velocity is varied, from 0.2 l/min to 5 l/min, the conductivity increases at a decreasing rate until reaching a fixed constant value above 5 l/min. This variation in global current density is attributed to an averaging of variations in local effective conductivity. The primary cause of such local variations results from gaseous evolution within the IEG. The quantity of gaseous products relative to the local percentage of electrolyte, known as the *void fraction* (defined in Equation 3.1-9 below), is shown to increase with current density and decrease as the flow velocity increases. Hopenfeld and Cole's photographic results confirm this by illustrating how the void fraction thickness increases along the length of the flow path in the direction of flow. These results, however, only illustrate a very narrow range of ECM conditions.

Within the Hopenfeld and Cole model, illustrated in Figure 3.1-2, the gap resistivity is defined as a sum of two components; r_p the resistivity of the pure electrolyte, and r_e the resistivity of gas-electrolyte phase. For an overall gap thickness of z, and thickness of the gas-electrolyte phase of δ_x (in Hopenfeld's model it is assumed that δ_x increases linearly along the gap and equals z at the end

of the flow field), Ohm's law can be applied to compute the potential drop through the two phase mixture as:

$$V - \Delta V = r_e \delta_x i_x + (z - \delta_x) r_p i_x$$

Equation 3.1-7

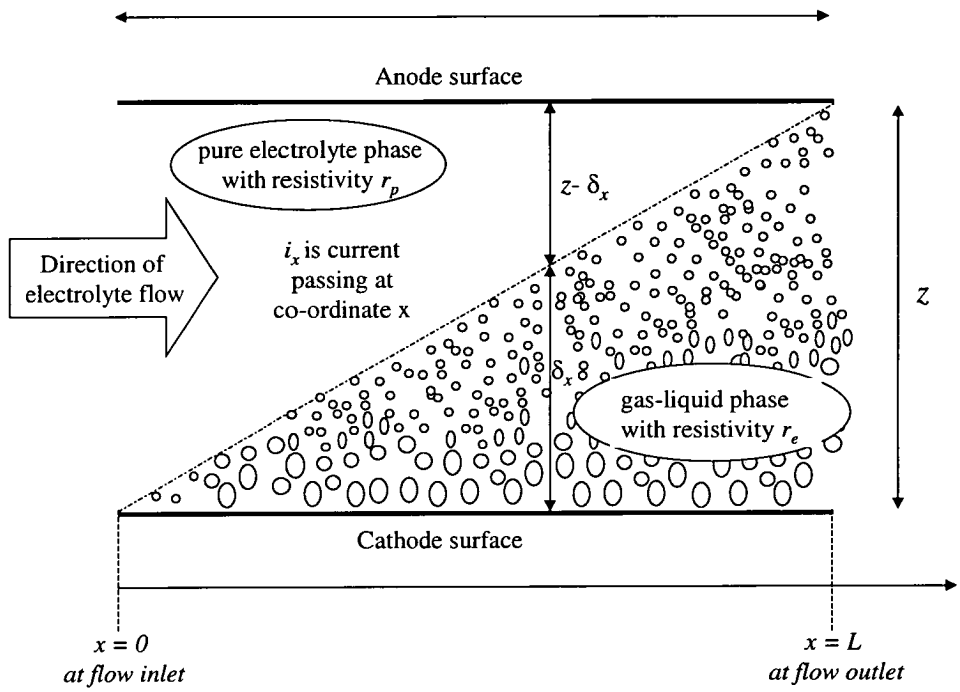

Figure 3.1-2: Two-phase model of the IEG in ECM

Although r_p can be readily determined, the value of r_e is estimated by a Hopenfeld and Cole using an empirical approximation developed by Rue [27], as follows:

$$r_e = r_p (1 + 1.5\alpha_x)$$

Equation 3.1-8

The parameter α_x, is the void fraction parameter mentioned above, which at any point along the flow path length describes the ratio of the volume of gas Q_g, to the volume of liquid Q_l, as follows:

$$\alpha_x = \frac{\beta}{1+\beta}$$

Equation 3.1-9

Where $\beta = Q_g / Q_l$.

Hopenfeld and Cole determined the mass of gas produced per coulomb of charge and use this to integrate the void fraction parameter into the model. However, since Hopenfeld and Cole's model does not include a determination of temperature or pressure distribution (Hopenfeld and Cole acknowledge that this would be very complex) or the way in which these factors will determine the volume occupied by the gas, an experimentally determined constant, $\overline{C}$ is introduced into the model. Then from Equation 3.1-7, Equation 3.1-8, and Equation 3.1-9, and the experimentally determined value for $\overline{C}$, Hopenfeld and Cole developed a semi-analytical expression for the local current density i_x, expressed as a ratio of the current density at the inlet, i_0, as follows:

$$\frac{i_x}{i_0} = \left[\frac{3(V - \Delta V) x w \overline{C}}{r_p z Q} + 1 \right]^{-\frac{1}{2}}$$

Equation 3.1-10

Thus, the Hopenfeld model predicts a fall off in local current density (to the power of –0.5) as the distance along the flow path length increases. The amount by which current density is reduced, at any one point, increases as the flow volume (and hence the flow velocity) decreases.

This non-uniformity in current density distribution predicted by Equation 3.1-10 will, once equilibrium has been established, produce a taper in the gap size with a profile proportional to the current density distribution function. Hopenfeld and Cole point out that the degree to which this taper will occur, can be reduced by adjustment of one or several process parameters. For example increasing Q and/or z or decreasing V and/or κ will reduce the taper. However, only an increase in Q would reduce the taper without incurring a corresponding overall decrease in the current density and therefore the mass removal rate from the workpiece. Since this would be undesirable in most production situations, Hopenfeld and Cole suggest that high values of Q will be the best method by which geometric accuracy can be held relatively insensitive to overall machining conditions.

In [26], Hopenfeld and Cole do not include an analysis of how the electrolyte conductivity (and hence the local current density) will be affected by the temperature rise along the gap due to Joule heating as discussed by Tipton. However, in a subsequent work [28] they extend their analysis to

equilibrium conditions and addressed some of the simplifying assumptions that had previously been made. They carried out a detailed study of the consequences of variations in the gap resistivity on the gap geometry. This extended generalised model, by use of a numerical solution, addresses equilibrium modelling with consideration of the effect of variation in pressure, temperature, and electrolyte velocity. Gap resistivity measurements are made by computing, according to ohms law, the gradient of the linear fit to the product J.z (at the centre of the flow path) and the voltage, V. Repeating this for a range of flow rates enabled Hopenfeld and Cole to map out the gap resistivity/ flow rate dependency. Their measurements indicated an increase in the specific conductivity with increasing flow rates, in approximate accordance with their model. They attributed this trend to a reduction in void fraction with increasing flow velocity. These measurements confirmed that the gap at equilibrium tapers towards the downstream end of the flow path and that this taper increases with decreasing flow rates. This relationship is in reasonable correspondence with their model at certain combinations of parameters but shows poor correspondence in some cases. Hopenfeld and Cole attribute these differences to measurement errors.

When considering the effects of temperature rise along the gap (absent in their previous work) Hopenfeld and Cole conclude that the increase in conductivity, due to Joule heating of electrolyte alone, underestimates the actual measured temperature rise. They do not provide an explanation for this. They also conclude that the decrease in conductivity due to void fraction formation is more pronounced than the increase in conductivity due to heating effects for any one value of current density. Thus for the flow rate range in Hopenfeld and Cole's experiments, conductivity variation due to void fraction formation is the dominant factor affecting the gap taper.

The models of Tipton and Hopenfeld and Cole were extended further in a study by Thorpe and Zerkle [29]. In this investigation, Thorpe and Zerkle, in contrast to the semi-numerical solution developed by Hopenfeld and Cole, produce a direct analytical solution to describe ECM dynamics. Thorpe and Zerkle also address some of the "unwarranted" simplifying assumptions made by Hopenfeld and Cole. Most significantly they address the heterogeneous nature of gap dynamics, by allowing for the possibilities that the various layers (i.e. gaseous-electrolyte, hydroxide-sludge, and pure electrolyte phases) do not necessarily move through the gap at the same velocity). Their model includes, for example, a slip ratio, σ_g, defined as the ratio of the velocity of the gas-electrolyte to the velocity of the pure electrolyte, v_g/v_e. Other slip ratios are included to describe the interactions between other phases.

A significant feature of the work of Thorpe and Zerkle is that they reduce the complex problem of ECM dynamics down to three algebraic and one differential equation. The equilibrium gap function being expressed in a compact notation, as follows :

$$\frac{z(x)}{Z_0} = \frac{1+Bx}{(1+Ax)^d}$$

Equation 3.1-11

Where A is a constant representing void fraction effects and B a constant representing temperature effects:

The usefulness of this representation becomes apparent for the condition, $A = B$ with the exponent $d = 1$, which leads to the condition $z(x) = z_0$ in Equation 3.1-11. That is, the gap along the length of the flow channel is constant. Thus A=B, d=1 is the criterion for the effect of conductivity increase, due to Joule heating, to be equal and opposite to the decrease in conductivity due to void fraction formation. Whether this condition is realistically achievable is not discussed by Thorpe and Zerkle. They then go on to plot Equation 3.1-11 for several different values of d. They note that Hopenfeld and Cole used a value of d of 1.5 (equation 25 in [28]) and that a better fit to experimental data (Thorpe and Zerkle use the experimental data of Hopenfeld and Cole and do not carry out any of their own experiments) is obtained if d is increased to 2.0 (compare Figure 2 in [29] with Figure 6a in [28]).

In their conclusions, Thorpe and Zerkle point out that because of the heterogeneous nature of transfer effects in ECM (particularly the distribution of void along an axis parallel to the direction of feed) then it is unlikely that a full analytical description of gap dynamics will be achievable. They point out that a detailed understanding of the gas slip ratio is one of the primary outstanding requirements for the implementation of a full model. They do however point out that their own analytical model could be force fitted to experimental data, to obtain the value of n and hence modelled ECM dynamics as a semi-analytical/empirical strategy

The work of Tipton, Hopenfeld and Cole, together with Thorpe and Zerkle all make certain simplifying assumptions particularly about the linearity and homogeneity of temperature and pressure distribution within the gap. The testing of such assumptions through experimental validation is considered difficult to achieve, due to the small dimensions, and high pressures and temperature gradients involved in an ECM system. However, a few studies have been directed to provide a least some indications of the variation and complexity of the parameter functions involved. For example, Pramanik et al.[30] carried out a series of measurements on the pressure distribution in a case of a planar parallel electrode configuration, 100 mm long by 40 mm width. In Pramanik's arrangement the electrolyte is supplied through a centrally located supply orifice. The pressure is measured using a multi-tube manometer arranged so that each individual tube can access points within the gap at 3 mm intervals. Pramanik et al report on pressure variations for gap values in a range of 0.1 mm to 0.75 mm and for electrolyte flow volumes in a range of 12 to 35 L/min. Their

results exhibit a general trend of an increase in pressure towards the centre of the flow field and then a decrease towards the exit (as would be expected assuming that the flow exits the gap to ambient pressure). A significant feature of their results is the observation that a small sharp pressure drop, to slightly below ambient, occurs a few millimetres into the flow field. This feature was noted over the full range of gaps and flow volumes used in their trials. There is no detailed explanation or analysis of these results.

A limitation of the experimental set-up of Pramanik et al. is that they use a centrally situated supply orifice (that is flow in two directions from a central position). Such a configuration is likely to be more prone to erroneous flow effects than say, for example, single axis flow through a planar configuration. Also, the work was carried out using gap conditions such that the electrolyte pressure do not exceed the measuring range of the manometer of only 260 mm of Hg (34 kPa or .34 Bar). Such pressures are very small compared to the range normally associated with the ECM process, 300 kPa being more typical. In the case of these more realistic pressures some of the effects noted by Pramanik et al would possibly not occur since the volume occupied by gaseous products would be reduced and this would have the effect of smoothing out possible flow anomalies. These results to however serve to illustrate the complex nature of phenomena that may be occurring and that any simplification used in models may limit their range of application.

A further assumption in the works of Tipton, Hopenfeld and Cole, and Thorpe and Zerkle is that the only thermal effect considered to occur is that of a Joule heating of the electrolyte (this assumption is implicit in Equation 3.1-5). Heat losses from the gap through the tool via conduction are ignored. However, as Jain and Murugan point out [31], the tools used in ECM are usually made from materials with a high thermal conductivity, such as copper and brass. The thermal loss through the tool could therefore be significant.

To investigate this possibility Jain and Murugan developed a finite element model in which heat transfer through the electrodes is considered. Their analysis was developed for a plane parallel electrode arrangement and uses experimental results obtained by Bhatia [PhD thesis 1971, India Institute of Technology, Bombay]. By incorporating an array of thermocouples along the tool surface, Jain and Murugan were able to make comparisons between theory and empirical results.

Their investigation showed that for tool materials of low thermal conductivity, such as stainless steel, temperature gradients show close correlation to theory developed by neglecting conduction through the electrodes. However when they compared the same theory for tooling made of a good thermal conductor, such as copper, they observed significant deviation from the theory. Although, when the basic theory was modified to include heat flow through the electrodes they reported close correlation to the data for the cases of high conductivity tools. They pointed out, however, that significant discrepancies still exist between theory and experiment. These discrepancies are

particularly pronounced at the exit and inlet ends of the flow field. Jain and Murugan do not give a detailed explanation for them. However, they do make the point that their model was constructed with several simplifying assumptions, not least that heat losses through conduction were considered as being uniaxial (i.e. no consideration was made of heat losses through the inlet and outlet ports). Furthermore, the effect of void fraction was neglected, and that the valency and efficiency were assumed to be constant.

3.1.2 Overpotential dependencies

Sensitivity of the overpotential with the type of electrolyte used in the dissolution process is common. Examples of this will be provided in chapter 7. However overpotential values can also be sensitive to process parameters when using a single electrolyte composition. For example, Landolt [32], carried out trials using a copper anode and a 1M sulphuric acid electrolyte. Over a current density range with a maximum of 39 Acm^{-2}, Landolt observed Tafel behaviour (i.e. a logarithmic sensitivity of overpotential with current density). Davydov et al. [33] report similar dependencies during dissolution of nickel in nitrate electrolytes. Such effects are small, in the region of 0.1V over an order of magnitude increase in current density, and can therefore often be neglected in ECM applications. However, there have been reports of change in overpotential of between discrete values. For example, Mount et al [34] report a transition in the overpotential when machining a nickel based alloy (In718) in a chloride electrolyte. In this case a transition from $V_0 = 3.2$ to $V_0 = 5.1$ occurred as the machining voltage was increased from 14 V to around 16 V.

3.1.3 Current efficiency and valency dependencies

When reviewing the work of others it is sometimes not clear whether a change in dissolution efficiency and/or a change in valency state is occurring (see section 2.1 for discussion on this ambiguity). For details on the electrochemical aspects of these phenomenon see [35]. In terms of empirical materials characterisation, however, it is only the relationship between the dissolution current and the rate of an anodic dissolution which is of importance, since this will affect the value of the k-parameter.

Many authors have reported current efficiency dependencies. For example, Landlolt [36] when machining nickel in a 1Molar $NaClO_3$ electrolyte, has shown that the dissolution efficiency falls rapidly from 100 %, at current densities of 30 A/cm^2 and above, to below 20% as the current density drops below 10 A/cm^2.

Datta and Landlolt [37] report on dependencies between current efficiency and both flow velocity and current density during the dissolution of iron in sodium nitrate electrolyte. Current efficiencies of around 70% were reached for low flow velocities in the region of 1 m/sec. For higher flow velocities, of up to 10 m/sec, they reported an increase in efficiency towards 100% as the current density increased.

Clarke and McGeough [25], using a mild steel anode in a nitrate electrolyte, also measured increases in current efficiencies with increasing flow velocity (in this case based on the assumption of divalent iron dissolution). When using a sodium chloride electrolyte with the same mild steel anode they reported a constant efficiency of close to 100% over a wide range of machining conditions.

Bejar and Gutierrez [38] used a technique which involved measurement of the rate of change of gap size to determine current efficiency dependencies. Their method involved measuring the value of current density in the case when the cathode is held static and the anode dissolves thereby increasing the gap. They then measured the rate of change of gap, dz/dt, at predefined intervals (using a mechanical probe and presumably by the interrupting the process to make each measurement) and related this measurement to the current occurring at that time. They then computed the efficiency, E, according to:

$$E = \frac{F\rho}{\varepsilon J}\frac{dz}{dt}$$

Equation 3.1-12

This relationship is based on the application of Faraday's laws as formulated in Equation 2.2-1. The value of dz/dt is computed by fitting a simple exponential relationship to experimental data. Bejar and Gutierrez's measurements were made using a high speed steel anode in a sodium nitrate electrolyte at a wide range of concentrations (2.5% – 10%) and temperatures (20 °C – 50 °C). At low current densities (less than 20 A cm^{-2}), their results show current efficiency dependencies with gap size, current density, temperature and flow velocity. At higher current density of around 30 A/cm^2, Bejar and Gutierrez reported that the efficiency level off at around 80% (the valency in this case is assumed to be divalent).

Several authors have also reported valency sensitivity to process parameters. For example, Moir and Harvey [39], report a transition from $Fe^{3+}Cr^{6+}$ to $Fe^{2+}Cr^{3+}$ dissolution in the case when machining a stainless steel (En38J) anode in a sodium chloride (20% wt/wt) electrolyte. This transition is observed as a change on the anode surface from a smooth, bright area, which is associated with $Fe^{3+}Cr^{6+}$ dissolution, to a pitted grey surface, which is associated with $Fe^{2+}Cr^{3+}$ dissolution. In correlation with the proportion of each surface associated with each dissolution mode, proportional changes in current density, as would be expected in accordance with Equation 2.2-3 have been observed. Although Moir and Harvey do not give a detailed reasoning of why this valency change

occurs, they do correlate this transition with flow rate and / or current density. Specifically, they report that a boundary, corresponding to the transitions between $Fe^{3+}Cr^{6+}$ to $Fe^{2+}Cr^{3+}$, moves along the flow path in proportion to the increase in flow volume (over the range 0.6 to 1.9 gal/min). Moir and Harvey also report Fe^{3+} to Fe^{2+} transitions occurring in carbon steel as the flow rate is reduced. These observations have been supported by Mileham [40] in an investigation using a cylindrical electrode arrangement.

3.2 Process and tool design modelling

Throughout the literature there are many examples where workers have developed methodologies for determining transferred characteristics between the tool and workpiece in ECM. In essence, these methodologies determined shape characteristics by computing the distribution in gap size between the tool and workpiece surface, for a given set of parameter conditions. Commonly such methodologies make simplifying assumptions as to the existence of ideal conditions within the gap.

The most basic of these techniques, termed the cos θ method [24], models the gap size at a particular point as being inversely proportional to the cosine of the angle between the tool feed direction and a normal to the workpiece surface at the point being considered. This technique is illustrated in Figure 3.2-1 for the case of parabolically shaped tool, specified by co-ordinates (x_t, y_t) and workpiece surfaces specified by the co-ordinates (x_w, y_w).

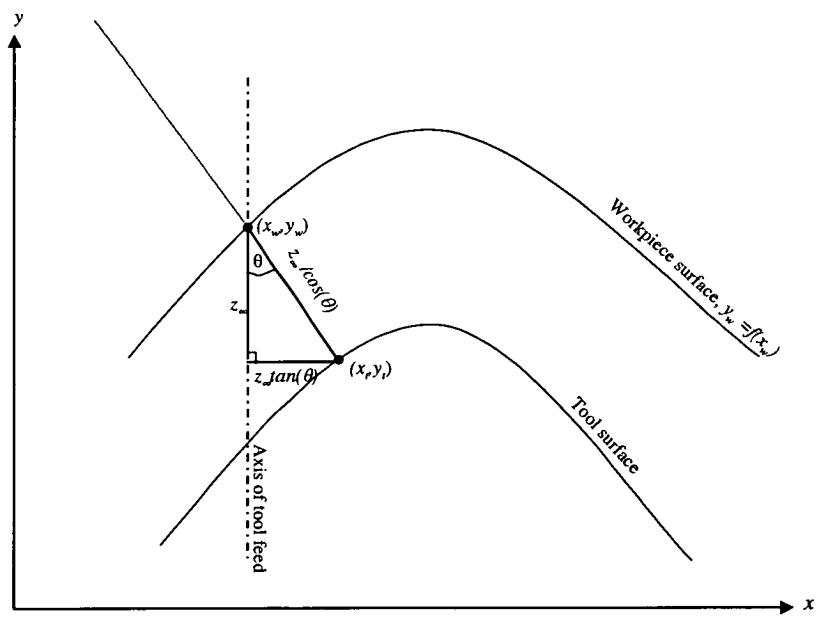

Figure 3.2-1:Application of 'cos(θ)' rule for non-planar gap determination (for details see [14)

This technique can be applied at equilibrium when all points on the workpiece surface will be moving along the feed axis at a rate equal to the feed rate such that the gap normal to the workpiece surface, z_{n_∞} will be equal to $z_\infty . cos(\theta)$. Substituting for k from Equation 2.2-11 , the normal gap at equilibrium for the non-planar case can be expressed in terms of the k-parameter as:

$$z_{n_\infty} = \frac{k}{f\,cos(\theta)}$$

Equation 3.2-1

The cos(θ) methodology is applicable only with the assumption that the lines of electric flux are straight between adjacent equipotential lines. For cases where the equilibrium gap profile is increasingly complex, this assumption becomes increasingly inaccurate and more sophisticated methods are required.

In broad terms, these more advanced techniques can be classified into two groupings, both of which aim at the achievement of appropriate tool designs through numerical and/or analytical analysis, as follows:

- **Tool design computations** (often referred to as the *inverse problem*); in which the workpiece shape is specified and the corresponding tool shape computed at a given set of conditions. Applying such techniques usually requires that the gap conditions be specified as being either equilibrium or transient (i.e. on the approach to equilibrium).

- **Process simulation computations**[‡] (often referred to as the *direct problem*); in which a pre-defined tool is considered and the resultant workpiece shape evolved. In this case, computation of the workpiece may not produce the desired shape on the first iteration. Thus achieving acceptable tolerances may require several runs in which the tool is modified between iterations. In contrast to the tool design computation, process simulation is generally achieved regardless of whether an equilibrium condition has been specified.

A detailed review of both ECM tool design methodologies and process simulation strategies is given in [19]. In the following sections, a brief comparative overview of the work of others is presented. As an alternative to full-form tool design strategies, the technique of using non-conformal tools is

[‡] It is noted that some workers use the term "tool design" when discussing algorithms that are actually process simulation. In this thesis using the term "process simulation" or the term "tool design" are used only in the context of the definitions as above.

briefly reviewed. The section concludes with a brief review of strategies used for modelling and representing parameters interdependence in ECM.

3.2.1 Process Simulation in ECM

A review of the literature reveals a larger body of work devoted to the application of process simulation as a means of achieving tool design rather than the use of direct tool design computations. It seems to be the case that this technique is easier to achieve and has greater flexibility than tool design computations. In general process simulation is achieved as follows:

> Based upon an initial tool design and initial relative tool position, these techniques compute the electric potential distribution within the IEG determined as a solution to the Laplace equation. This solution is then applied to a determination of the current density distributed over the workpiece surface. The erosion rate can then be determined by applying Faraday's law. An intermediate workpiece shape is then established using the erosion rate distribution and a pre-defined temporal interval. The tool position is then incremented according to a pre-selected feed rate and the computation repeated to calculate the next stage in the evolving workpiece shape. These iterations are repeated until the desired workpiece is achieved in the transient state or until the current density distribution, and therefore the workpiece shape, becomes invariant in time (the equilibrium condition).

In the majority of the work on process simulation several simplifying assumptions are made. These assumptions, which can be collectively termed as *ideal conditions*, ignore any variation in fundamental machining parameters that would otherwise produce, for example, a sensitivity in the erosion rate with a dependence on factors other than the magnitude of the local current density. Such *non-ideal* conditions, which can occur due to valency, overpotential, and /or electrolyte conductivity changes have been discussed in detail above.

Within the general grouping of ideal process simulation techniques, different methodologies have been developed for representation of the tool and workpiece surface and the way in which the field distribution is discretised and incremented. For example the finite element technique is applied using a rectangular mesh [41, 42] and alternatively a triangular mesh [43,44] for representing and incremented nodal descriptions of the electric field distribution. In these latter cases, the use of a triangular mesh is reported to improve the accuracy of the computed workpiece shape. In the work reported in [42] the finite element algorithm is employed in conjunction with an optimisation formulation. This optimisation process minimises the deviation between each computation of the workpiece shape, from that which is required, to produce a more accurate simulated shape.

Hardisty *et al.* have carried out work [45, 46] in which a rectangular mesh finite element computation is carried out for the special case of a stepped tool profile. As part of this system, Hardisty *et al.* also develop algorithms for the prediction of the minimum depth of material that must be provided on the initial blank for the machining of the required step size to a specified tolerance. In a later work [47] Hardisty *et al.* give details of a more advanced model in which the rectangular meshing algorithm is replaced by one in which the mesh co-ordinates are specified at key points. Hardisty *et al.* report that this modified method improves surface irregularities that had previously been associated with the rectangular meshing algorithms.

As a variation to applying the finite element technique to solve the simulation problem, several workers have applied other methodologies such as finite difference techniques [48, 49] and the boundary element method [50,51, 52]. Improved accuracy and reduced computation times have been reported in this latter case.

Several workers have also addressed the process simulation problem under conditions (or when using certain electrolyte/ material combinations) when non-ideal effects become significant [53, 54]. In work carried out by Reddy *et al.* [55] a correction factor method for tool design is described. This approach employs the process simulation algorithm of [18,56] with the addition of a successive update to the tool shape to produce a workpiece to the required tolerance. The system, after each iteration of the process simulation algorithm, augments the gap profile by an analytical model of temperature and void fraction distribution. Reddy *et al.* report successfully toleranced workpiece forms (using experimental profiles from the work of Bhatia[•] as a comparison) for the relatively simple example cases of plane parallel, sloped and exponential configurations. For the more complex case of hole sinking, however, they report significant errors with discontinuities appearing in their generated tool designs. In their conclusions they attribute such errors to the limited accuracy of their analytical description. They go on to suggest that their models could be improved if augmented by data from actual ECM trials. They do not provide details of how this could be achieved.

In a programme of work similar to that carried out by Reddy *et al.*, Filatov [57] carried out two-dimensional numerical simulation of the distribution of the electrolyte velocity, pressure and temperature. Unfortunately, no experimental validation of the data generated is given.

[•] **Bhatia, S. M.** Effects of electrolyte conductivity on the ECM process accuracy. *M. Tech. Thesis* IIT, Bombay, 1971.

Neid and Perry [58] have carried out a one-dimensional finite element simulation coupled with one dimensional analytical descriptions of heat transfer and current density distribution (these are essentially the equations outlined in section 3.1.1 above). For some simple cases their simulation shows reasonable correlation with machined profiles. Neid and Perry do, however, point out that their model only provides limited accuracy and therefore should only be used as a guide in establishment of an initial tool profile. Their method will therefore not completely negate the requirement for trial and error iterations.

3.2.2 Tool design for ECM

Tool design methodologies (the so-called inverse problem) attempt to compute the tool shape as lying along an equipotential boundary relative to the required workpiece form (also assumed to be an equipotential boundary). In the case of many workpiece examples there is found to exist a family of tool form solutions of which only some can actually be manufactured. For specified machining conditions, however, parameters can usually be defined that will ensure that only realisable tools are generated (see [86] as appended in Appendix A1).

For the case of ideal conditions workers have addressed the tool design problem using a number of different strategies. For example, using numerical boundary element methods [59, 60] and also as a Cauchy problem for the Laplace equation solved by analytical continuation [61].

Research on tool design methods in which a consideration of non-ideal effects are included are not widely reported. One of the few examples is that of the work of Chang *et al [62].* who has augmented a finite element solution to the tool design problem with a model describing the inter-electrode thermal-fluid properties. This model represents the case of one-dimensional two-phase flow in order to compute the variation in the velocity, temperature and void fraction as the tool shape iterates. In common with the example of [55], Chang *et al.* conclude that their model has greater success with simple shapes compared with more complex shapes where the occurrence of significant errors have been noted.

3.3 ECM with non-conformal tools

Before concluding this section, it is worth noting that all of the methodologies discussed so far involved computations aimed at producing conformal tools. That is: tools designed for specific full-form workpiece shapes when moving along a pre-defined, usually one-dimensional, feed axis. Such tools are most commonly an approximate inverse shape of the required workpiece shape. There is, however, an alternative approach to ECM full-form machining operations. These methods, described in a series of papers by Kozak *et al.* [63, 64, 65], by Ruszaj [66] and by Zawistowski [67], utilise a universal tool with a simple shape (e.g. planar or cylindrical), which is traversed along a complex

path, via computer numerical control (CNC) in two or three dimensions. Such an approach is often referred to as ECM-CNC. Kozak *et al.* suggest that this method can overcome many of the non-ideal effects that are often exacerbated by the long flow path lengths required in the cases of full-form tools. Kozak *et al.* discuss a range of appropriate tool shapes and the algorithms required to define the required tool traversing co-ordinates for a range of workpiece profiles. For some of these cases close correspondence is obtained between simulated and experimental workpiece profiles.

A significant disadvantage of the ECM-CNC approach is that since only relatively small areas are being eroded at any one time, the overall machining rate is considerably reduced compared to full-form ECM operation. It is therefore likely that ECM-CNC will be uneconomic in many applications. Kozak *et al* do however point out that non-conformal ECM-CNC techniques can be economical when applied for use in finishing surfaces which have previously been machined to an approximate shape by other methods.

The need for conformal tools can also be avoided by using sectional tooling. This idea, which is discussed in detail by *Shulepov et al.* [68, 69, 70], involves the use of a planar tool in the form of two or more individual sections which are electrically insulated from each other. *Shulepov et al* described a concept in which each of the individual sections can be powered separately, so as to control the local rate of machining within the region of each section. In this approach, different voltage levels cannot be applied to more than one section at any one time. If this was done then because one of the tooling sections would be anodic relative to the other, machining (and therefore damage) of the adjacent tooling sections would occur. *Shulepov et al* suggest that complex full form shapes can be machined by individual selective activation, and by controlling the magnitude and duration of the voltage, of each of the tooling sections. *Shulepov et al* concentrate on describing the control system for such an arrangement. They do not however provide details of the range of shape variation (particularly in terms of depth variation) that could be realistic achieved with such a system.

A significant limitation of this concept becomes apparent when the relationship between machining rate and gap size is examined. This relationship exhibits an exponential decay in machining rate as the gap size is increased (this is discussed in detail, in relation to the characterisation strategy, in Chapter 4). At gaps in the region of 2 mm the rate of machining can fall by an order of magnitude relative to those obtained at typical machining gaps in the region of 0.5 mm. Thus if realistic machining rates are to be achieved, then the sectional tooling concept will be limited to applications where only shallow depth profiles are required. It would also be the case that many tooling sections would be required for complex profiles. Implementing the system would therefore require very complex tooling assemblies with sophisticated sectional control. In the opinion of the author such an approach will find only very specific application and is therefore unlikely to have general economic viability.

3.4 Modelling and representation of parameters interdependence

Throughout the ECM literature few workers have attempted detailed studies in the area of parameter representation in ECM. It is suggested that the reason for this is in part due to the complexities of the problem, but also due to the lack of available analysis techniques. This latter reason will be addressed in detail in this thesis. It is however worth noting, as part of this review, two studies which have attempted, at least in part, to address these issues.

Khairy [71], for example, has developed a system in which a hierarchically structured knowledge-based system (KBS) can be applied for optimising process operation in ECM. In this approach, Khairy avoids the need for detailed analytical models by defining a structure that enables updating of limits over which specified parameter relationships are valid. For example, a particular feature, which forms a part of an overall profile (i.e. a step or pocket etc) is given certain attributes which define process relationships for that feature. The system can then provide an assessment as to whether, for example, the flow velocity regime, that can realistically be achieved over the complete component profile, will successfully provide the required dissolution characteristics for that particular feature. Khairy suggested that such an approach could be readily integrated with the tool design strategies of the type discussed above. He demonstrates the use of the KBS strategy applied to a single machining system (steel in a NaCl electrolyte) and reports success in the generation of appropriate processing parameter set-ups. In order to apply such an approach to a wide range of ECM systems, Khairy suggests that the database would need to be expanded based upon information from other workers and reference works such as the Machine Data Handbook [72]. The problem with this approach is that it would require extensive database input in order to describe the process complexities to the required degree. The work of others and available reference works do not, in general, provide the required level of detail. It is however suggested that the KBS approach could form a useful component in an overall system for ECM representation. In particular, the generation of characterisation data using the set-up as discussed later in this thesis would complement the use of a KBS system.

Bhattacharyya and Sorkhel [73], have addressed the parameter independence complexity problem by use of a response surface methodology (RSM) based approach. Hewidy and Fattouh [74] also apply an RSM approach with specific application to tubular electrodes. In this system parameter interdependence is specified using two empirically derived functions. These functions, based around second order polynomial surfaces, map the primary machining criterion of overcut and metal removal rate to the primary machining parameters of electrolyte conductivity, electrolyte flow rate, machining voltage and gap size. To achieve this representation a series of trials (31 in the example given) are carried out to determine the order and value of the coefficients for the surface functions. Bhattacharyya and Sorkhel demonstrate how these surface functions can be used to correctly predict parameter relationships at values that were outside the range of the coefficients determined during

trials. This predictive parametric approach appears to provide a good degree of modelling accuracy, at least for the specified system characterised.

The question arises, however, as to whether these methods could be effectively applied to give a general description independent of the system type. Nether Bhattacharyya and Sorkhel or Hewidy and Fattouhdo provide a clear answer to this question. It does seem probable to the author that different parametric relationships would need to be generated for each of the required ECM systems.

3.5 Chapter overview and conclusions

This chapter has detailed the work of others in their attempt to provide analytical and/or empirical based descriptions of IEG phenomena. Although these models have provided a degree of resolution of certain interrelationships, they have failed to provide the level of resolution necessary for a complete description of IEG characteristics. Achieving this may be unrealistic given the complexities and heterogeneous nature of ECM phenomena.

Most of the work on design and process modelling in ECM has not attempted to include modelling of non-ideal phenomena. Even so such work has provided a useful insight into the general form of tool to workpiece transfer characteristics. Specifically, such work has provided insight into the limitations of ECM (i.e. the range of shapes that can be machined) and also for estimating the removal envelope required for forming specified shapes. Those workers who have attempted to incorporate non-ideal effects into their tool design/ process simulation systems have reported a limited degree of success, but only when applying their systems to relativity simple shapes. Approaches that use non-conformal tools are aimed at niche ECM applications and will not therefore expand its general usage.

The work in this thesis is aimed at providing parameter representation for tool design and process modelling in ECM, but avoiding reliance on any analytical solution. This empirical approach is to be realised through the direct measurement of certain process parameters and their distribution within the IEG. The formulation of these ideas is the subject of the next chapter.

Chapter:

4 Theoretical Development

This chapter details the development of current-time and gap-time methodologies for k-parameter measurements. These developments build upon the basic dynamic equations, described in Chapter 2, applied to the cases of cylindrical and planar ECM configurations. The concept of the C-function is then introduced as a means for mapping k-parameter sensitivities against selected process variables. A representation is developed for defining the C-function in spatial co-ordinates of flow path length.

The theoretical developments and definitions outlined in this chapter are used for the general characterisation work described in Chapters 7 and the C-function work described in Chapter 9.

4.1 Current and gap-transient k-parameter characterisation

The basis of k-parameter characterisation is the dynamic description of planar dynamics in the form of Equation 2.2-10 as developed in section 2.2, as follows:

$$\frac{dz}{dt} = \frac{k}{z} - f$$

Equation 2.2-10

Analysis of the dynamic situation described by Equation 2.2-10 can made by solving this system for the parameter *k* in terms of time, *t*, as follows. From Equation 2.2-10 and Equation 2.2-11, dz/dt can be expressed in terms of the equilibrium gap as:

$$\frac{dz}{dt} = k\left[\frac{1}{z} - \frac{1}{z_\infty}\right]$$

Equation 4.1-1

And making the substitution:

$$\frac{1}{z} - \frac{1}{z_\infty} = \frac{z_\infty - z}{z.z_\infty}$$

So that Equation 4.1-1 can be written:

$$\left[\frac{z.z_\infty}{z_\infty - z}\right]dz = kdt$$

Equation 4.1-2

Integrating Equation 4.1-2 (details in Appendix A3) from t = 0 to t = t for $z = z_0$ (at time t=0) to z=z (at time t = t) gives:

$$\frac{z_0 - z}{z_\infty} + \ln\left[\frac{z_\infty - z_0}{z_\infty - z}\right] = \frac{kt}{z_\infty^2}$$

Equation 4.1-3

From Equation 2.2-11, the equilibrium gap is given by $Z_\infty = k/f$, so that the RHS of Equation 4.1-3 can be written in terms of the feed rate as $f^2 t/k$. It is also useful to express the LHS of Equation 4.1-3 in terms of a dimensionless gap by dividing through by Z_∞ so that:

$$\frac{z_0}{z_\infty} - \frac{z}{z_\infty} + \ln\frac{\frac{z_\infty}{z_\infty} - \frac{z_0}{z_\infty}}{\frac{z_\infty}{z_\infty} - \frac{z}{z_\infty}} = \frac{f^2 t}{k}$$

Equation 4.1-4

Which re-arranges to:

$$\frac{z_0}{z_\infty} - \frac{z}{z_\infty} + \ln\frac{1 - \frac{z_0}{z_\infty}}{1 - \frac{z}{z_\infty}} = \frac{f^2 t}{k}$$

Equation 4.1-5

Equation 4.1-5 defines the gap-time system function in implicit form (an explicit form of this relationship cannot be formulated [45]). This function can be plotting using an iterative computation (mathcad's *Minerr* function, see appendix 2 for details) using the example condition as used in section 2.3 (i.e. k = 1.064 x 10^{-8} m^2 s^{-1}) from which the equilibrium gap can be computed using Equation 2.2-5 as 0.64mm. This plot is shown Figure 4.1-1 for the case of three values of initial gap, z_0. These trends illustrate, as would be expected intuitively, that the equilibrium gap is approached in a time which reduces depending on how close the initial gap is to the equilibrium gap.

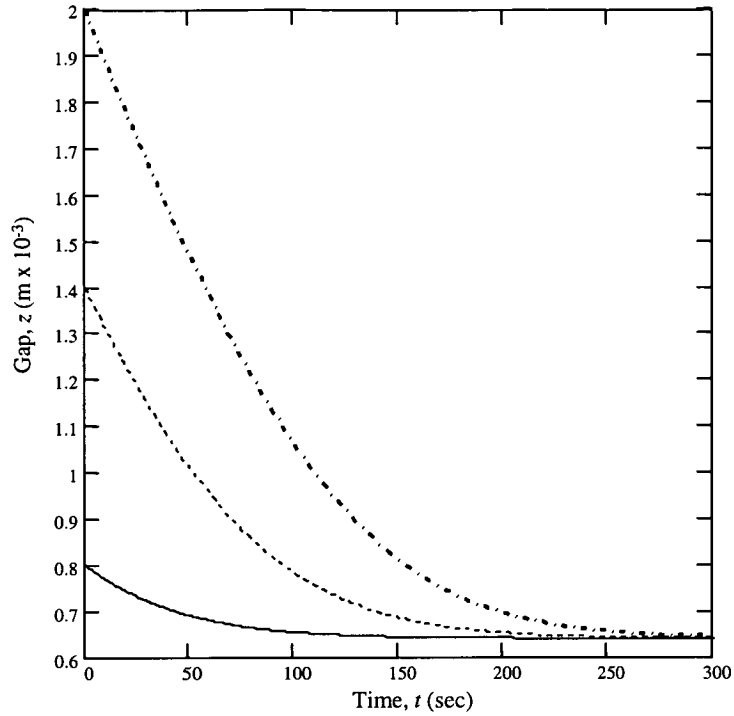

Figure 4.1-1: Gap-time solution for k=1.064 x10^{-8} m^2s^{-1} , f = 1.667 x10^{-5} ms^{-1} (1 mm min^{-1}) plotted for initial gaps of 0.8 (solid line), 1.4 (dotted line) and 2.0 (dot and dash line) m x10^{-3}

Now since the feed rate, *f*, can be set as a fixed parameter then the RHS of Equation 4.1-5 would become a linear function of *t* assuming constant *k*. For conditions when *k* is not constant, deviations in the fit of Equation 4.1-5 to experimental data (indicated by an increase in mean squared error values) would reveal such sensitivities. Thus Equation 4.1-5 could be used as the basis for the measurement of the k-parameter and its sensitivity to process conditions.

It is also noted as has been indicated by Tipton (see page 160 in [14]), that the case of circular symmetry, in common with the planar configuration, also provides conditions in which electric field lines are orthogonal to both the workpiece and tool. Equations equivalent to those developed above can therefore also be developed so that this system can also be examined as a method to obtain the *k*-parameter. A circular symmetric configuration would consist of a static cylindrical tool eroding a workpiece surface symmetrically from a common central axis. In this case the gap can be considered to be equal to the difference between the radius of the cut r_w (the width of cut being $2r_w$) and the tool radius r_t. Such a system can be solved (see Appendix A3 for details), by integration, using the boundary condition that $r_c = r_t$ at t=0, and $r_c = r_w$ at time t=t, to give:

$$\frac{1}{2}r_w^2 \ln\frac{r_w}{r_t} - \frac{r_w^2}{4} + \frac{r_t^2}{4} = kt$$

Equation 4.1-6

Where k is the machineability parameter as previously defined by Equation 2.2-9 above.

Measuring and fitting the radius of the workpiece, r_w, as a function of time according to Equation 4.1-6 for the case of circular symmetry could be used as a method for directly determining the value of k. An example of this method was applied in a spin-off project from this thesis in which cylindrical tooling electrodes were employed (details of which are given in the appended publication [13] in Appendix A1). For the primary work reported in this thesis, however, it was considered that a planar configuration was more representative of flow path arrangements used in actual ECM machining operations. Also the dynamics described by Equation 4.1-6 are based on a static tool (i.e. no feed) so that the current density is falling with time. In the most practical ECM operations the opposite is the case.

Returning then to the current-time solution for planar ECM with tool feed, further insight can be made by substituting the ohmic relationship:

$$J = \frac{(V - V_0)\kappa}{z}$$

Equation 2.2-4 (section 2.2)

into Equation 4.1-5 for the conditions that J_∞ is the equilibrium current density occurring at a gap of z_∞ and J_0 is the initial current density occurring at the initiation of machining when z equals z_0. Thus Equation 4.1-5 can be written in terms of the current density as:

$$\frac{J_\infty}{J_0} - \frac{J_\infty}{J} + ln\frac{1-\frac{J_\infty}{J_0}}{1-\frac{J_\infty}{J}} = \frac{f^2 t}{k}$$

Equation 4.1-7

The implicit equality of Equation 4.1-7 can be used in the same way as Equation 4.1-5 to monitor the parameter f^2/k but in this case using a measurement of the current density. The k-parameter can thus be deduced for any specified feed rate, f. The form of this relationship can be demonstrated by setting a sequence of values for J_0, setting J_∞, f and k to a constant value and iteratively determining the current transient form of J against t. This plot can be computed corresponding to the same machining conditions for the gap-time plot shown in Figure 4.1-1 by substituting appropriate values for initial current densities and equilibrium current densities as calculated using Equation 2.2-4 from

the initial and equilibrium gaps of Figure 4.1-1. That is, initial current densities of 22, 31.34 and 55 x 10^{-4} A m^{-2} corresponding to initial gaps 0.8, 1.4 and 2.0 x 10^{-2} m respectively as shown plotted in Figure 4.1-2.

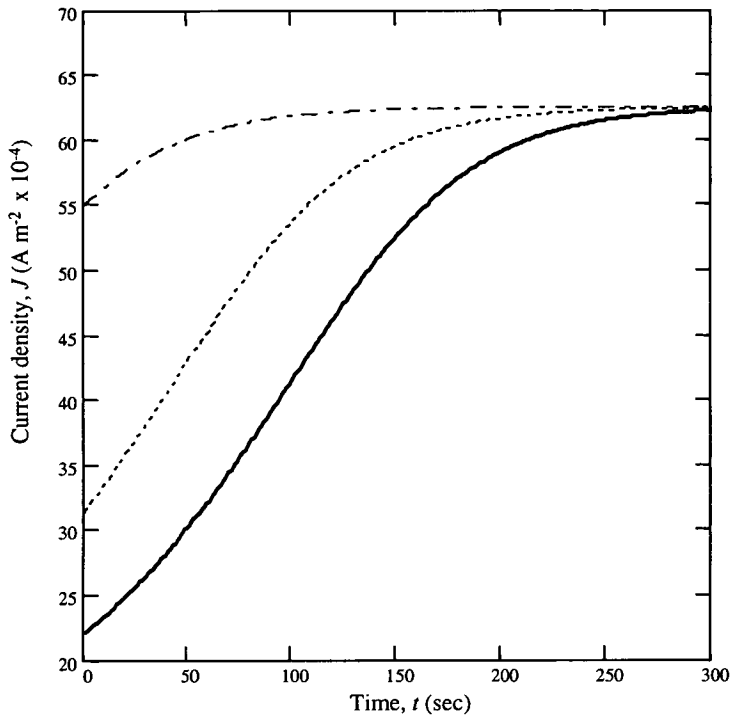

Figure 4.1-2:Current-time solution for k =1.064 x10-8 m^2s^{-1} , f = 1.667 x10^{-5} ms^{-1} plotted for initial currents of 22, 31.34 and 55 A m^{-2} x 10^{-4}

4.2 Determination of basic machineability parameter interdependencies

Although this thesis is ultimately directed towards measurement of the k-parameter, it is a useful to develop and identify methods by which the dependency of constituent variables within the k-parameter can be resolved. Such analysis will ultimately lead to a clearer understanding of the mechanisms driving such sensitivities. These techniques are applied to the measurement of these basic machineability parameters, for the systems to be studied using the C-function measurements, as detailed in Chapter 7.

Using static techniques (no tool feed), the parameters of overpotential, V_0 and conductivity, κ, can be readily determined, from the intercept and gradient respectively of the linear proportionality between J_0 and V-V_0, using the relationship:

$$J_0 = \frac{\kappa(V - V_0)}{z_0}$$

Equation 2.2-4, see section 2.2

In this case J_0 can be measured for a series of settings of the parameter, V, for the same initial gap value z_0.

A disadvantages of this method is that is does not readily enable parameterisation at realistic ECM conditions (i.e. tool feed conditions).

The current-time solutions however provide a means to parameterise ECM at realistic machining conditions, within a machining set up that could be similar if not identical to the requirements of the production set up. In this method parameterisation is achieved by plotting k/f^2 against V and determining the intercept, to obtain V_0, and gradient, to obtain κ, based on the linear dependency of solution time constant, k/f^2, as follows:

$$\frac{k}{f^2} = \frac{\kappa M (V - V_0)}{nF\rho f^2}$$

Equation 2.2-9 , see section 2.2

The valency is then determined by equating the mass of material dissolved to the electrode current passed in accordance with Faraday's laws (making the assumption of constant valency throughout the measurement).

$$n = \frac{J_\infty M}{fF\rho}$$

Equation 2.2-3 , see section 2.2

Determining the valency sensitivity, in the case where the valency is a variable can be made by rearranging Equation 2.2-1 to give the valency n, as follows:

$$n = \frac{1}{\frac{dt}{dy}} \frac{JM}{F\rho}$$

Equation 4.2-1

Thus insensitivity of n with J could be established by confirming the linearity of the gradient (and zero intercept) in a plot of n against dt/dy according to Equation 4.2-1.

Tracking of sensitivities in V_0 cannot be achieved with interdependence from values of κ since these two parameters are inherently related by the ratio:

$$\kappa = \frac{Jz}{V - V_0}$$

Values of κ can of course be determined in the bulk of electrolyte by the independent measurement. This however is not relevant to the approach of this work which is concerned only with the magnitude of these quantities during machining. Thus, although V_0 and κ cannot be independently monitored, general sensitivity of k with J can be examined by assuming constant V_0. This will be reasonable for systems when independent measurement, by for example current-time analysis (described in section 4.1), has already established stability in V_0.

4.3 C-function parameterisation

As already noted (in section 4.1) the *k*-parameter can be determined by fitting current-time data to the current time solution of ECM planar dynamics, Equation 4.1-7. The value of *k* obtained using this method will be averaged over the parameter range required to vary the value of J from J_0 to $J\infty$. Since such characterisation trials can only realistically be carried out by varying the gap size, then correlated variations in current density, electrolyte velocity and pressure will also occur. Thus the k-parameter computed by current or gap-time fitting would only be valid with the assumption that any of the constituent parts of *k* (specifically *n*, V_0 and κ) were not sensitive to variations in these parameters. However, as discussed in Chapter 3 there are a number of known dependencies in which such sensitivities exist. Therefore if unambiguous mapping of the *k*-parameter is to be realised, then a more direct determination of *k* that was independent of successive time dependent measurements would be required.

Such a method can be realised by noting, as was described in section 2.2, that *k* can be expressed as part of the description of the change in gap with time, dz/dt, for the case of a planar tool/workpiece configuration, by rearranging Equation 2.2-10, as follows:

$$k = z\left(\frac{dz}{dt} + f\right)$$

Equation 4.3-1

With reference to Equation 4.3-1 it can be seen that a mapping of the value of the k-parameter can be obtained directly from a knowledge of, the gap size, *z*, the rate of a change of gap size, *dz/dt*, and the feed rate, *f*. This computation can be made at each of the time intervals *dt* (in practice this would be at the sample rate of the data logging system) and would therefore not be prone to the averaging of parameter inter-relationships as would be the case when fitting the current-time or gap-time

relationship. The mapping of the k-parameter according to Equation 4.3-1 can be thought of as a characterisation function, or C-function, expressed as:

$$C(v_1, v_2..v_N) = z\left(\frac{dz}{dt} + f\right)$$

Equation 4.3-2

Where, v_1 v_2 $....v_N$, is a variable space representing a general sweep of all significant machining parameters, and N is the number of parameters that have significant interdependencies. In many cases the parameter space will only need to be defined in terms of certain critical parameters. For example, as has already been discussed in Chapter 3, the parameter k is, for some systems, particular sensitive to current density, J, and flow rate, U.

The C-function defined by Equation 4.3-2 will thus describe process dependencies at the specified point of measurement of the values of z and dz/dt. For example, in the specific case of mapping k against current density, J, then the 1-dimensional, 1-point C-function can be defined as:

$$C(J) = z\left(\frac{dz}{dt} + f\right)$$

Equation 4.3-3

Where the variation of J could be set so as to cover the range required for a particular tool design.

In order to incorporate k-parameter sensitivities along the axis of the flow field (to model the form on non-ideal effects as described in Chapter 3), the C-function definition must be further generalised by defining the function at pre-defined intervals along the axis of the flow path.

Thus a 1-dimensonal (i.e. mapped for J only), m-point C-function can be formulated according to:

$$C(J,m) = z_m\left(\frac{dz_m}{dt} + f\right)$$

Equation 4.3-4

Where m is a discrete index representing intervals of position along the axis of a single axis flow field. Thus $m = 0$ at the flow inlet position and, for flow path intervals of, l, the flow path length at the index position, m, is given by ml. This notation is illustrated in Figure 4.3-1 for the 1-dimensonal, n-point C-function of Equation 4.3-4, for the example case of a parabolic tool form.

Figure 4.3-2 shows how the C-function is represented for the case shown in Figure 4.3-1 but plotted against the discretisation index, m.

The discretisation intervals[§] can readily be calculated, for example, using an x,y co-ordinate representation of the workpiece surface, such that:

$$l_m = \int_{x_{m-1}}^{x_m} \sqrt{1+[s'_w(x)]^2}\,dx$$

Where $S_w(x)$ is a function representing the workpiece surface.

For full details on how this is achieved see Appendix A2.

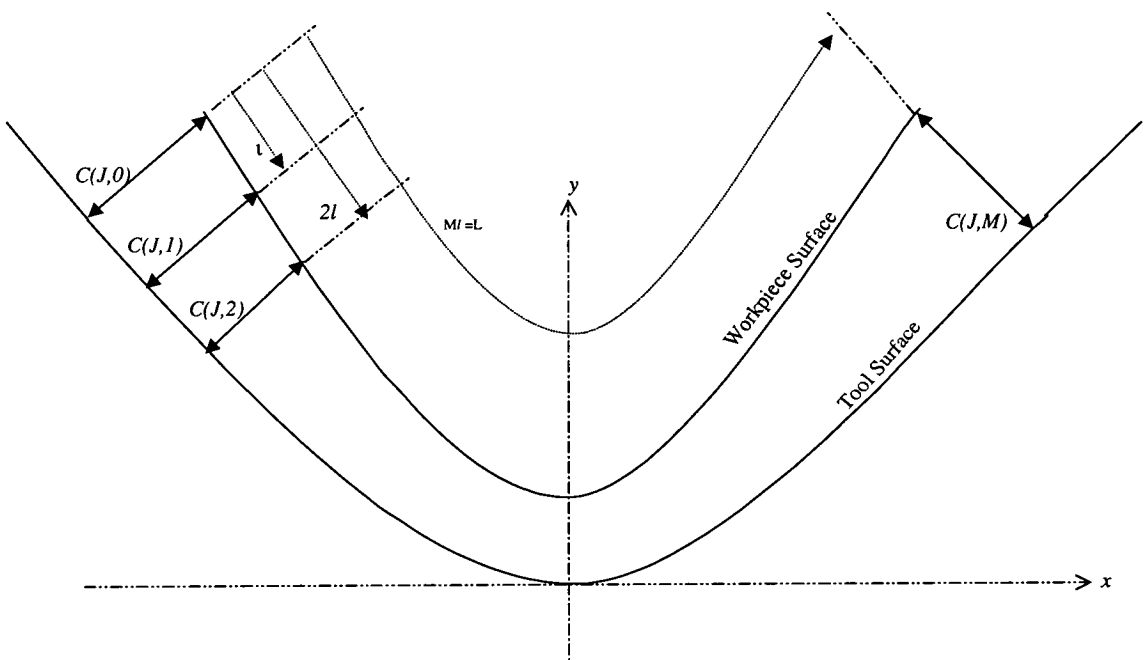

Figure 4.3-1: Discretisation of C-function along equal intervals of the flow path length along the workpiece surface

[§] The workpiece surface is chosen rather than the tool surface since, for example when calculating a process simulation algorithm, erosion rate computations (that will be augmented by the C-function) are computed at nodes on the workpiece surface.

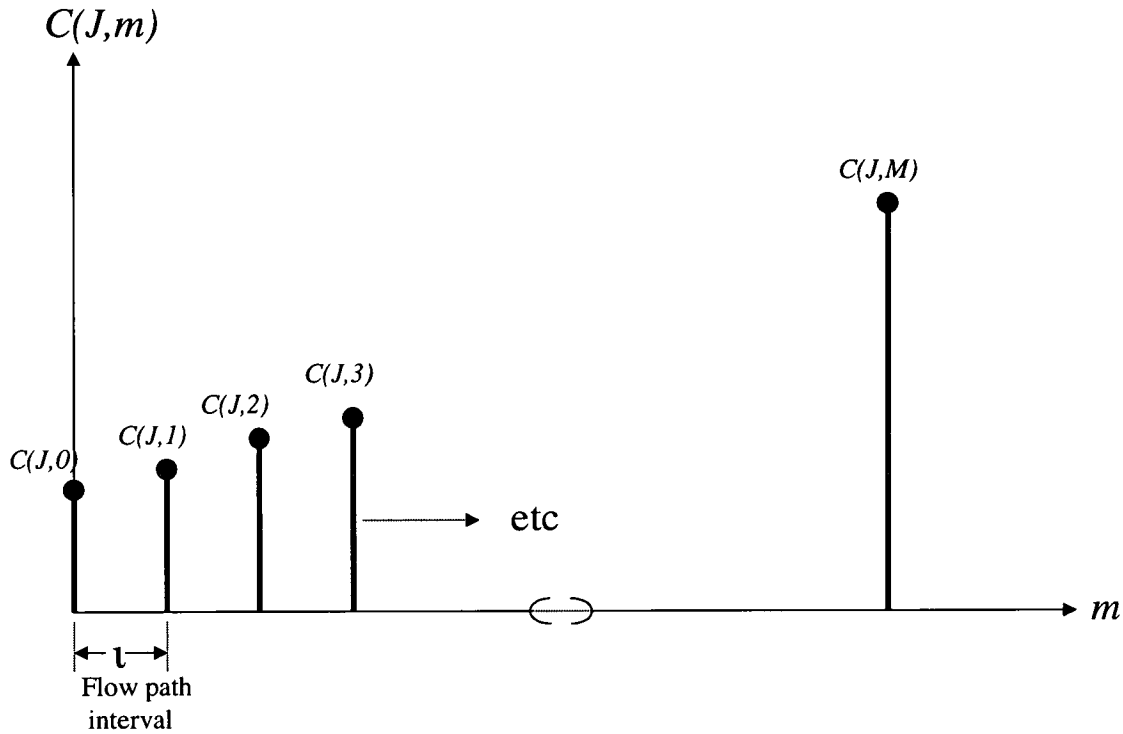

Figure 4.3-2: C-function plot against the discrete index, m

For basic tool design strategies, such as the cos θ technique (see section 3.2), for each component of $C(J,m)$, the normal gap component $z(m)$ is calculated for $m = 0$ to M as follows:

$$z(m) = \frac{C(J,m)}{f\cos(\theta_m)}$$

Equation 4.3-5

where θ_n is the angle between the normal on the workpiece surface at the index m, and the axis parallel to the direction of feed.

A more convenient and compact representation of the C- functions can be formulated by summing the components of $C(J,m)$, in terms of a spatial variable, p, as follows:

$$C = C(J,0)p^{-0} + C(J,1)p^{-1} + C(J,2)p^{-2} \ldots\ldots + g(M)p^{-M}$$

Equation 4.3-6

Which in compact notation becomes:

$$C = \sum_{p=0}^{M} C(J,m)p^{-m}$$

Equation 4.3-7

In this representation the spatial co-ordinate is defined by the index of a power series in the variable, p. This representation is an analogue to the method commonly used for representation of discrete functions (commonly known as the z-transform). One advantage of this representation is that, for certain C-function forms, it may readily lend itself to closed-form solutions. This may be of use if applying the C-function to error compensation when computing an analytical solution to the tool design problem. A further aspect of this representation becomes apparent when the spatial variable p is set equal to the value of $p = \exp^{j\Omega m}$ (where Ω is the angular frequency) in Equation 4.3-7. This provides a discrete harmonic representation of the C-function with coefficients providing the amplitude of individual harmonic components. Such representations are commonly used to represent workpiece and tool profiles in both process simulation and tool design systems, for example see [42, 60].

Measurement of the C-function will require gap measurements (to calculate both the z_m and dz_m/dt components of C) to be made at M spatial intervals. In some cases however, extrapolation may be applicable when the general form of the C-function is known or estimated in advance. In such cases gap measurements may only then be required at two or three points depending on the C-function form. In this thesis a 2-point measurement system is deployed and the full C-function generated through extrapolation. These measurements are reported in Chapter 8.

4.4 Chapter overview and conclusions

This chapter has provided an outline of the theoretical relationships by which basic machineability parameters can be measured. The use of current-time parameterisation has been proposed as a method by which these parameters can be measured at realistic ECM conditions. Relationships have also been defined by which certain parameter sensitivities can be resolved. The use of the C-function for representation of parameter interdependence has been proposed. Measurement of the C-function will require the use of real time gap measurement, at a minimum of 2-points along the flow axis.

The next chapter describes the experimental set-ups developed for carrying out measurements of the theoretical relationships outlined in this chapter.

CHAPTER:

5 ECM Equipment Tooling and Characterisation Cell Development

---

All ECM equipment, tooling and ECM flow cells were developed and manufactured specifically for the work of this thesis. Throughout these developments innovative design solutions have been applied in order to provide experimental measurements of a higher precision than would normally be obtained by using a standard industrial set-up. This Chapter details the design criteria for the systems developed and describes their set-up, calibration and operation.

5.1 ECM machining system development

At the onset of this project no available ECM equipment appropriate to the required work existed. Off-the-shelf ECM equipment is not readily available and in any case such equipment, if it could be obtained, would not readily provide access to control signals and would therefore be of limited flexibility. Commissioning an ECM company to customise a system for the project was considered prohibitively expensive. It was therefore decided to build a complete ECM machining system in-house. In addition, all ECM tooling systems and all machine cells were designed and purpose-built for the work.

The overall consideration was to design and manufacture a system in which monitoring, control of machining parameters and variables could readily be achieved. In addition, a primary design criterion was that reconfiguration of monitoring/control systems could be carried out with minimum system adjustment. The overall system set-up has included the design and implementation of a fully customised programmable logic controller (PLC) control system and a computerised data logging arrangement. The system can be divided in terms of the following distinct elements:

- Electrolyte supply system
- ECM gap power system
- Feed control system
- Parameter control and monitoring/ data acquisition system

An overall schematic representation, showing the relationship between these elements, is given in Figure 5.1-1.

The following sections detail how particular design criteria were achieved for these systems and describes their development, set-up, calibration and operation.

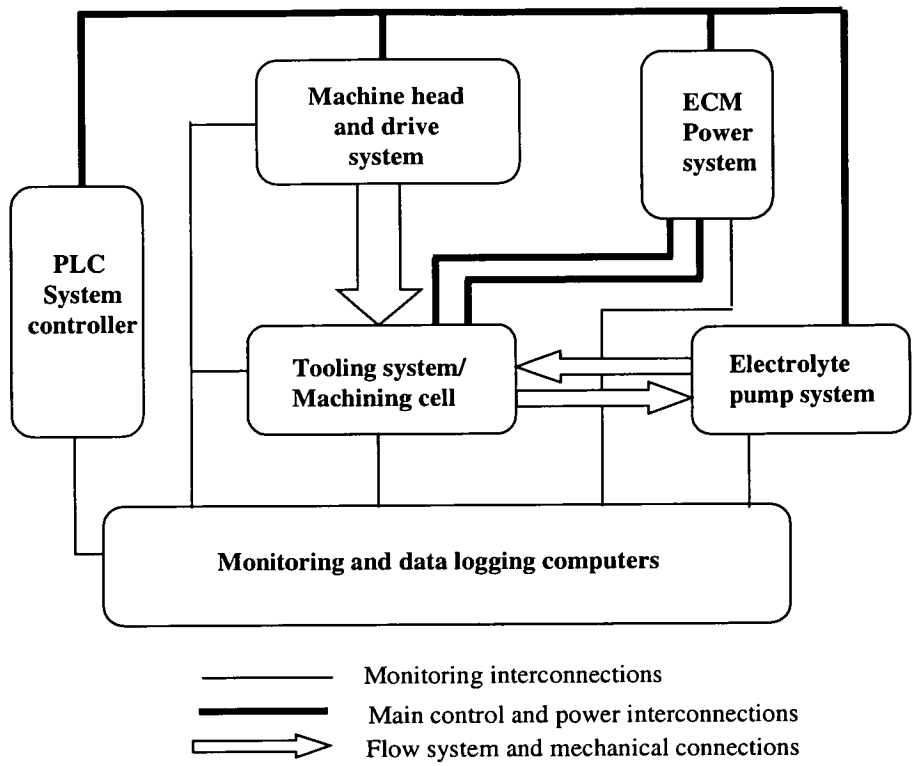

Figure 5.1-1: General configuration of experimental ECM system

5.1.1 Flow system requirements

Flow system requirements are based upon supplying a planar IEG with a width of 12 mm and a length of 40 mm.

A important requirement for the successful application of ECM is that stable dissolution is maintained across the full active area of the workpiece surface. Maintaining this state requires that the products of dissolution (precipitated and gaseous) are removed at a sufficient rate. Also, temperature build-up in the IEG, primarily due to Joule heating, will need to be controlled to avoid the possibility of local voids forming due to vaporisation and to avoid the possibility of general boiling. To achieve these conditions the electrolyte needs to be forced through the IEG at a sufficient rate. Reports on what are considered as sufficient rates vary, but in general, they are those that provide flow velocities in the range of 10-40m sec^{-1}[page 143 reference 14]. The upper value of flow velocity being required for high dissolution current densities and/or long flow path lengths in order to minimise non-ideal effects when required (see Chapter 3). For the requirements of the work of this thesis the flow velocity is required to be variable down to lower flow velocities to simulate non-ideal conditions. An additional requirement is that the flow passes through the gap at a

uniform rate, without pulsation. Any significant pulsation, due to some pressure variations, could cause physical movement of either or both the tool and workpiece and this could result in tooling damage.

The pressure range required in order to provide the specified velocities has been detailed by Bennett [page 149 reference 14] who has estimated that for flow passing through a 0.25 mm high, 40 mm long channel, in a plane parallel configuration (the basic arrangement being considered for this work), a mean flow velocity of 30 m sec^{-1} can be achieved by providing inlet pressures in the region of 40 bar. Several assumptions are made in this analysis that, as Bennett points out, mean that actual pressure requirements will be lower than this figure (by as much as 5 times) and that this pressure should be considered as an absolute upper maximum.

The volume of flow required to achieve flow velocities in the region of 30 m sec^{-1} can be calculated as the cross-sectional area of the flow channel divided by the velocity of flow. For the reference system being considered in the thesis (i.e. through a planar gap with a width of 12mm) flow velocities can be plotted over a range of gap values for a flow volume range of 1.5 x 10^{-4} m^3 s^{-1} to 5 x 10^{-4} m^3 s^{-1} (10 to 30 $l.min^{-1}$), as shown in Figure 5.1-2.

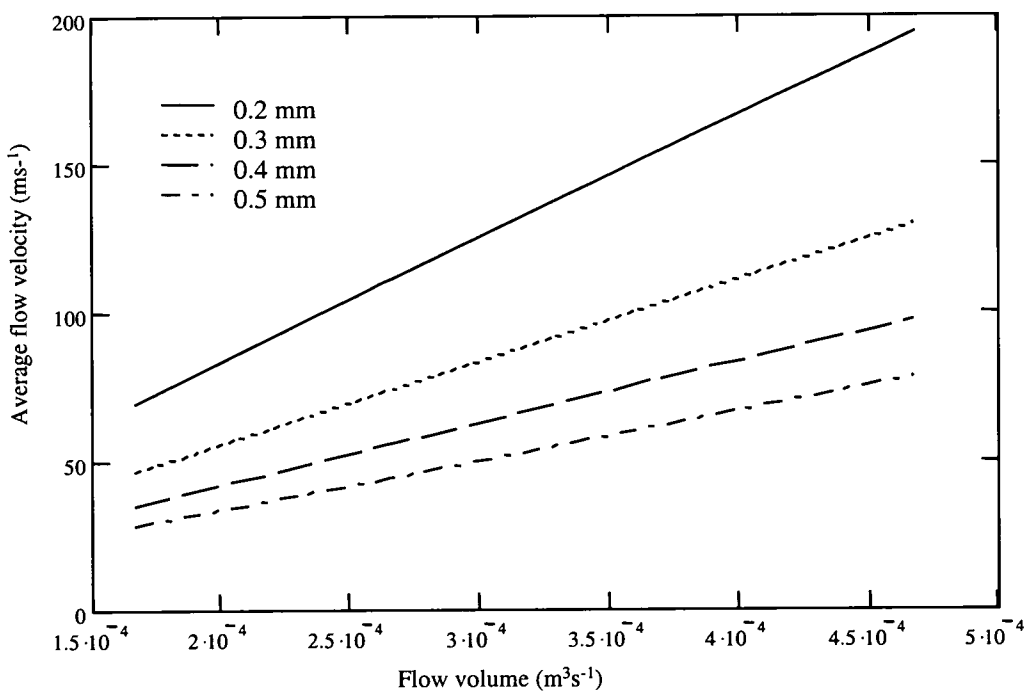

Figure 5.1-2: Calculated average flow velocity against flow volume (1.5 x 10^{-4} m^3 s^{-1} to 5 x 10^{-4} m^3 s^{-1} corresponding to 10 to 30 $l.min^{-1}$) through a planar gap with a width of 12mm for a typical range of operating gaps

With reference to Figure 5.1-2 it can be seen that the lower limit of required flow velocities (30 m sec^{-1}) will be achieved, over the range of typical operating gaps, for flow volumes of about 12 l min^{-1} and above.

The corrosive nature of the electrolyte used in electrochemical machining will also need to be a consideration in pump selection. This is especially the case for chloride and acidic based electrolytes which are known to attack a wide range of metallic parts.

The requirements for the electrolyte supply system, in the context of the reference tooling considered here, can be summarised as follows:

- Flow rates up to 30 l min^{-1}
- Pressures of up to 40 bar
- Ability to deal with corrosive liquids
- Ability to deal with re-crystallisation of salt crystals
- Ability to deal with liquids containing particulates (i.e. hydroxides)

5.1.1.1 Selection of electrolyte pump

The apparent lack of an optimum pumping system for ECM application was discussed by Bennett [Chapter 8 in reference 14]. After a review of the available pumping systems Bennett concluded that: "non of them were suitable for pumping corrosive electrolytes at the capacity required in an electrochemical machine".

For the current work, in order to assess developments in pumping technology since the work of Bennett, a wide range of pumping options were considered. The criterion for selection was not only those indicated in section 5.1.1, but also that maximum flexibility was provided in terms of achieving control over flow velocity.

The pumping systems available for the pumping of low viscosity liquids can be grouped into two broad categories: those operating through *rotodynamic* principles and those operating through *positive displacement* principles. A detailed consideration of the characteristics of a range of pumping systems, from both rotodynamic and positive displacement groups, is given by Massey [75]. For a more mathematical description see Douglas [76].

In the case of rotodynamic systems, a distinction must be made between axial and centrifugal in the ECM context. Although the output (characterised by flow volumes and pressures achieved) is a fundamental characteristic of rotational velocity for both systems, in the case of axial systems the operating efficiency tails off steeply, outside a specified optimum flow capacity. Axial systems are

therefore better suited to applications in which delivery capacities are fixed. For the trials intended in this work this inflexibility would be prohibitive since a wide range of flow velocity would be required. Axial systems were therefore not considered further as a viable option.

Centrifugal systems, in contrast, possess a more broadly defined flow volume/pressure characteristic in which efficiency falls of at a shallow rate [reference 76, page 667]. Stability can therefore be maintained over a wider range of flow capacities. The pressure variation resulting as the gap closes towards equilibrium, in an ECM operation, is therefore not likely to produce large efficiency changes. Centrifugal systems are the system types commonly employed in commercial ECM machining systems.

After an examination of the specification of available centrifugal pumps (multi-stage impeller units were the main types considered) it was concluded that, although flow capacities could be provided with a wide range, the flow pressures required, of above 25 bar, could not readily be achieved (this pressure constraint arises due to trade-offs between mechanical strength and rotational velocity). It was decided that this constraint would limit characterisation at the extreme limits of stable dissolution (i.e. at small gaps of 0.2 millimetres and below this pressure would not be sufficient to maintain appropriate flow velocities). An additional problem with centrifugal pumps, is that they generally operate at fixed rotation speeds (determined by the number of phases in the actuating motor) and flow volume control is usually achieved by use of a bypass valve (or pressure relief valve) on the pump outlet. Such valves provide only a coarse control and it was decided that control of the flow velocity could not be achieved with sufficient resolution using this method. A further disadvantage of centrifugal systems is that they do not readily lend themselves to pumping of corrosive liquids since the liquid being pumped usually comes into contact with the pumps impeller. In this author's experience, centrifugal pumps when used in commercial ECM systems have to be regularly serviced and sometimes replaced after only one or two years operation.

When considering the capabilities of positive displacement pumps, it was realised that only reciprocating piston pumps were capable of providing the required flow volumes (gear pumps and hydrostatic pumps were not suitable in this respect). Altering the reciprocating rate can vary the rate of delivery from this type of pump. A significant drawback with this type of system, however, is that the piston action produces pulses of pressure with a duration equal to the reciprocating frequency. One way to smooth out these pulsations is by use of a pulsation damper. These devices, which consist of a rubber enclosure pressurised within a metal cylinder, act as a low pass filter to remove the pulsations. However, this technique requires that the damper is pre-set to work optimally at a particular pulsation rate correlated to a particular flow volume. Although a damper could have been preloaded for the conditions of each experimental trial, this was considered as being too cumbersome a procedure. In addition, such an approach would not allow trials in which the flow rate was varied

throughout the run. A piston pump/ pulsation damper arrangement was therefore not considered further as a viable option.

After considering the relative merits of the available options in the context of the discussion above, one system seem to stand out as having the most balanced characteristics. This system, a Hydracell model D-25XL (*Wanner Engineering Inc. USA*) provided the high capacity characteristics of centrifugal type systems together with the high-pressure capabilities of a positive displacement system, but without any significant pulsation.

The Hydracell is a Diaphragm pump in which all metallic parts are isolated from contact with the fluid, which passes only through the rubber diaphragm enclosure. Thus the potential problem of salt precipitation within moving parts is negated. Pulsations are also minimised (to less than 3% of the flow volume) by driving the diaphragm at three concentric points around a central axis. The system provides high flow pressures (up to 70 bar) with flow capacities of up to 45 l/min (well within the specification stated above). The system allows the flow capacity, and hence the flow velocity for any specified ECM gap, to be varied (by varying the rotational speed of the pump) to a high resolution whilst still maintaining negligible pulsations. This pump was considered as having ideal characteristics for the required ECM investigations**

The Hydracell pump forms part of an integrated flow system as shown in Figure 5.1-3. This assembly incorporates a 3.3kVA motor driven by a S3 (*PIV electronics, the Netherlands*) frequency inverter to enable pump speed and hence flow volume control. To provide sufficient driving head to the pump inlet, the electrolyte is contained within a 60-litre capacity storage tank situated above the pump assembly. The electrolyte is maintained at a constant temperature ($\pm$ 1°C) by use of a TN2-1kVA (*Therm-o-level ltd, UK*) heater/temperature sensor arrangement which works in parallel with a water driven heat exchanger. A PDH13 (*Pall process filtration Ltd, UK*) high-pressure filter assembly is situated on the outlet (high pressure) side of the pump in order to remove precipitated solids greater in diameter than 10 μm (this was considered sufficient to remove hydroxide products and also to protect the ECM gap from possible ingress of other contaminant particulates).

** The year after this pump was incorporated into the system for this work an American ECM company, *Turbo Products* in Massachusetts, independently identified this pumping system as having ideal characteristics for ECM. The system is now incorporated into their commercial ECM machines.

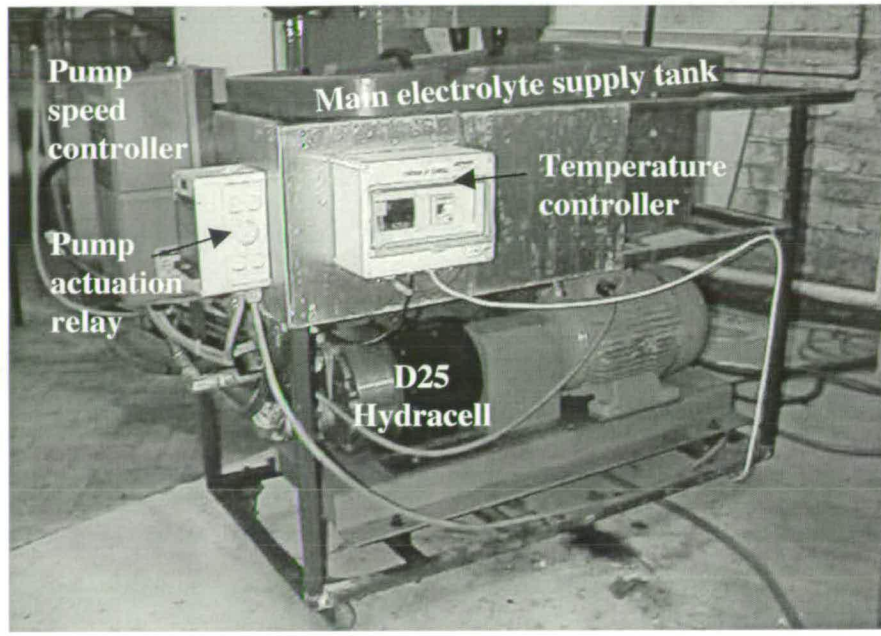

Figure 5.1-3: Flow system assembly incorporating pump speed controller and electrolyte tank with temperature controller

5.1.2 ECM gap power system

The ECM gap power was supplied using a RDOA 100/240/415 3-phase variac (*Bonar Brentford Electric ltd, UK*) and an isolating transformer/ rectifier assembly (*Goodyear Ltd UK*) with an output of up to 600A at 45V. A requirement of the system was that the voltage across the gap could be maintained at a steady value irrespective of the dissolution current (this is necessitated according to the characterisation equations developed in Chapter 4). Such voltage control can be readily achieved in the case of relatively low currents (less than 100 A) by use of regulating transistors and associated control electronics situated in the supply line. The use of regulating transistors for controlling much higher currents, as would be required in this case, was considered, but found to be impractical due to high inefficiencies resulting in heat build-up within these devices. It was decided therefore to regulate the voltage using more direct mechanical means. This was achieved by the development of a mechanical motor controlled positioning arrangement that could adjust the relative displacement between primary and secondary stages of the system's variac transformer (see Figure 5.1-4). Calibration tests showed that the system could achieve voltage regulation of ±0.15 V.

5.1.3 Feed and system control system

Control of the drive system, flow system and power systems are all achieved from the system controlled desk (see Figure 5.1-4 and Figure 5.1-5). Within the control desk an S5-100u (*Siemens plc*) Programmable logic controller (PLC) has been incorporated for controlling and monitoring of

actuation control signals. This system was programmed (using S5-ladder program assembly software) to provided sequencing and control of ECM operations, including:

- **Timed sequencing of flow, ECM power and tool feed systems.** This sequencing is designed to protect the tooling by ensuring that the flow rate through the system is sufficient to maintain stable ECM prior to the initiation of the ECM power and that the dissolution current is flowing before the feed rate is initiated. To ensure that the feed position can be correlated accurately to erosion current etc without significant time offsets recorder on the data logger, the delay between these operations is less than the one second sample interval used on the data logger.

- **Auto-selection and adjustment of voltage and flow rate parameters.** Control signals are generated by the PLC for the setting and adjustment of the machining voltage and the flow rate (by setting the pump speed). This automatic arrangement has been designed to facilitate trials in which predefined voltage and flow rate sweeps are required. Such trials have been carried out when mapping out the sensitivity of the C-function to these parameters (in Chapter 8).

- **Tool feed control and positioning.** Feed reference signals (at pre-selected values) are generated by the PLC to drive the main feed axis via a DC D110 (*Unimatic plc*) servo controller powering a 33D-series(*Unimatic plc*) servo/tacho motor. The PLC maintains control over start and stop positions using signals from the start and end-stop inductive limits switches (see insert in Figure 5.1-5).

- **Over current, change of current and spark-out protection.** A comparitor module is incorporated into the PLC system to enable detection of excessively high machining currents. Such currents will occur when either the feed rate has been set too high or an electric discharge occurs between the tool and workpiece (often caused when the filter fails and the contaminant level within the gap rises too high). When either of these conditions occur, the plc shuts down and energises an audible alarm. The PLC system in combination with the visual design software (see following section) will also produce an audible alarm, indicating possible problems, when conditions arise in which the feed rate is finite and the dissolution current is falling (this is flagged when the visual designer software detects a negative differential in the dissolution current value AND'ed with a TRUE feed rate value). Such a condition will not normally occur during stable dissolution conditions and therefore usually indicates a problem, such as the initiation of passivation on the workpiece surface or when insufficient electrolyte is entering the gap for some reason.

An important requirement for the tool feed system has been high stability combined with high accuracy. Stability has been achieved by use of a DC motor/tacho system driven by a speed compensated (integral controlled) pulsed width modulated MSM-series (*Infranor ltd*, Switzerland)

servo driver. Such systems enables highly toleranced motor velocities to be achieved. In order to provide high positional resolution a precision ground anti-backlash ballscrew system has been used to drive the main feed axis. The ball screw is connected to the motor via a 100:1 ratio anti-backlash gearbox. This relatively high ratio (in combination with a 6mm pitch ballscrew) ensures that the motor velocity is relatively high, so that a high torque can be provided, whilst the tool feed rates are relatively low (typically 1 mm/min) and can be controlled with high precision.

The machining base and machine head (shown in Figure 5.1-5 and as part of the complete system in Figure 5.1-6) were constructed from the basis of a reconditioned quill and machine base system donated to the project by AmTech Ltd (this machine had previously been used as part of an ECM production set-up). The system provides the required high rigidity by using an I-beam construction configuration. The machine head rigidity is provided using box-section construction and by use of four symmetrical positioned linear bearings situated along the full length of the travel.

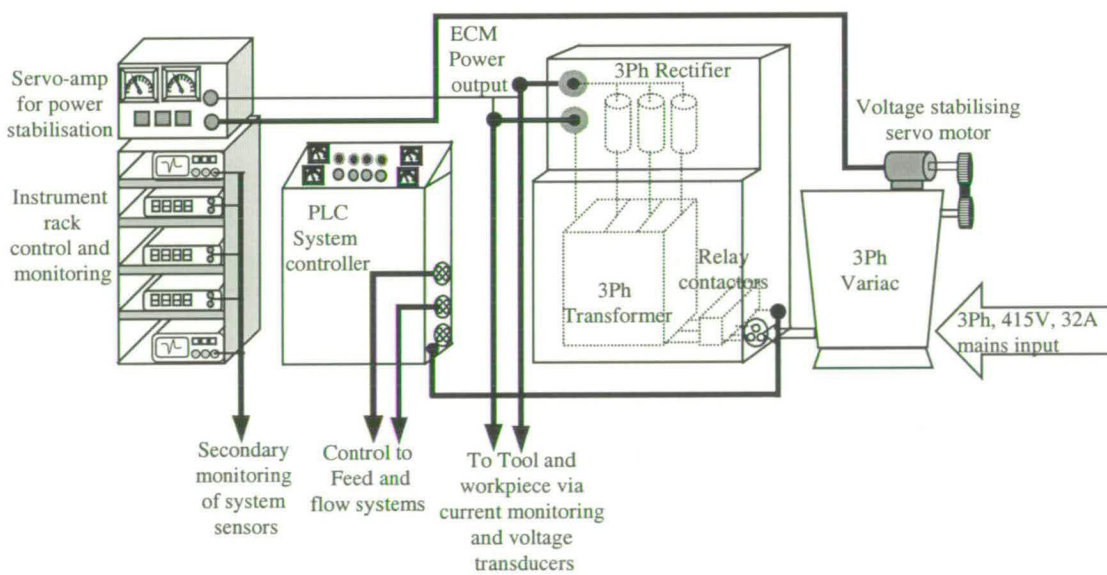

Figure 5.1-4: ECM power and control/monitoring system arrangement

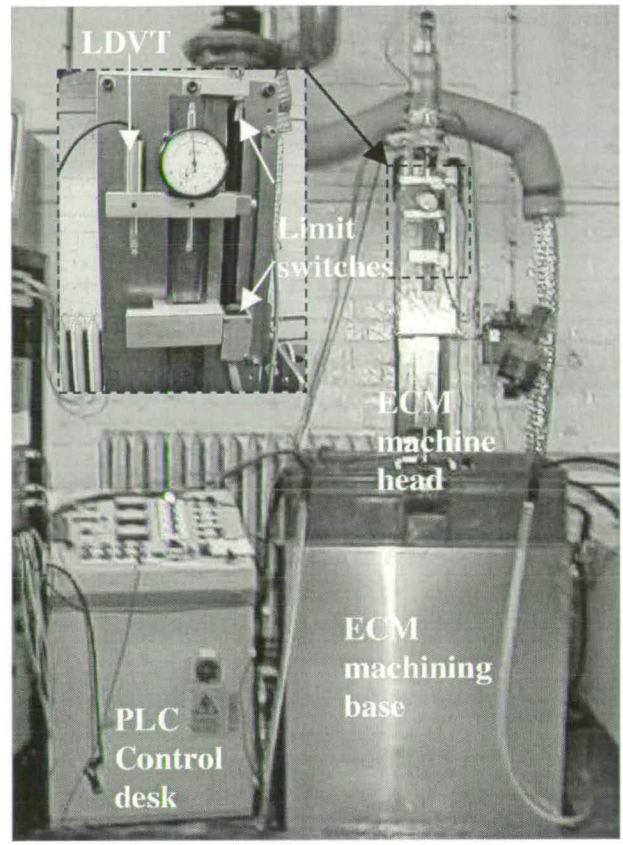

Figure 5.1-5: PLC control desk and machining base (insert shows LDVT tool position sensor and limit switches)

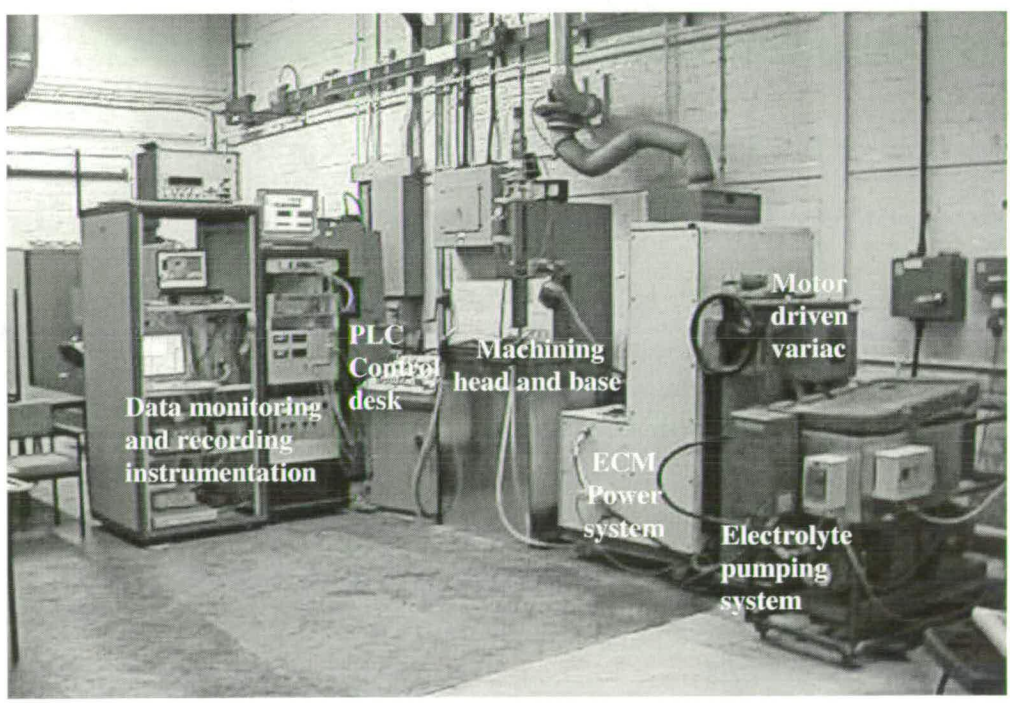

Figure 5.1-6: View of ECM machining system

5.1.4 Parameter control and monitoring/ data acquisition system

The scope of the work required the measurement and logging of all significant process variables and parameters. These measurements have been achieved using the following systems:

- **Segment and total dissolution currents** have been monitored using split-core, type-200SID (*LEM-HEME, Switzerland*) Hall effect transducers. These devices provide true rms data with an accuracy of ±1% of full scale deflection (fsd). (i.e. fsd = 200 A and 500 A for the segment current and total current transducers respectively). The transducer array used for monitoring the individual segment currents is shown in Figure 5.1-7.
- **Feed rate** is monitored using a digital-to-analogue converter (DAC) module which processes signals from an EC6-CW25C (*Omron Ltd, UK*) incremental optical encoder, situated on the main feed drive shaft (directly to the motor output before gearing down). This device produces 1000 pulses per revolution which translates to 16,000 pulses per mm travel (i.e. calculated using the six millimetre drive screw pitch and 100:1 gear ratio). It is estimated that the resolution of the feed rate data recorded by the data logger (i.e. after conversion through the DAC) is ±0.01 mm/min.
- **Flow rate** is measured using an NT13 (*CT-Platon Ltd, UK*) turbine type flow rate meter having a capacity range of 4 to 30 l/min with repeatability accuracy of ±1% of fsd.
- **Machining voltage** is measured using a Type-3192 (*LEM-HEME, Switzerland*) Hall effect voltage transducer having an accuracy of ±1% of its 50 V fsd.
- **Outlet/inlet pressures** were monitored using piezoelectric type-PTX1400 (GEMS Transinstruments Ltd, UK) with an accuracy of ±1% over an fsd of 0 to 40 bar. Note that in the trials reported in this thesis only the inlet pressure has been recorded. In all these trials the outlet pressure was at ambient (< 1bar).
- **Tool position** data is recorded using a linear differential voltage transducer (LDVT) Type-DG2.5 (*Solartron Metrology Ltd, UK*) having a travel of 5mm and a positional resolution of ±0.005mm. This level of accuracy was important since the tool position data is part of the computation of the machining gap values. Hence the positional resolution will determine the accuracy in the gap measurement (see Chapter 7).
- **Inlet and outlet gaps.** The methodology and equipment used for measuring inlet and outlet gaps are described in detail in Chapter 8

Calibration and range checking of all sensors and transducers was carried out using known reference sources with outputs signals being calibrated using a Microcal Type-1030 (*Time Electronics Ltd, UK*) voltage reference.

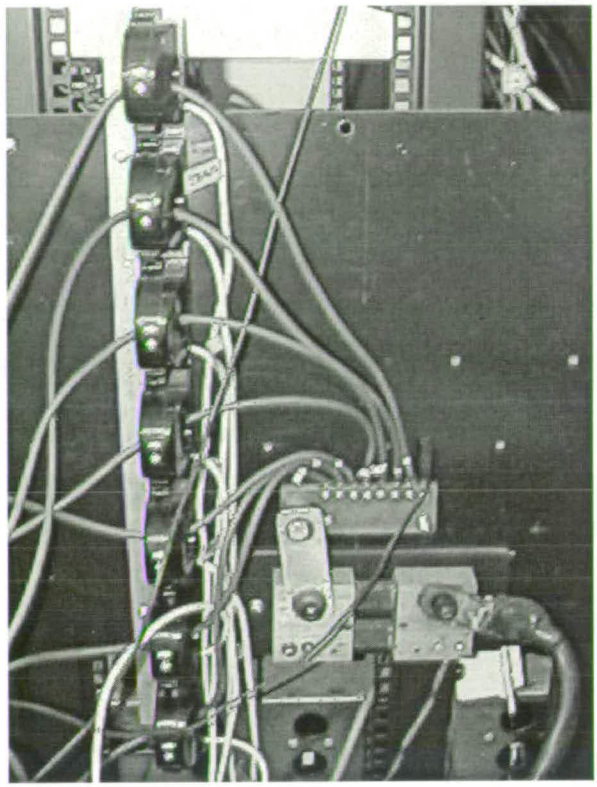

Figure 5.1-7: Hall-effect transducer array for monitoring of individual segment currents

The range of trials intended would also require flexibility when configuring the selection of parameter measurements for each of the trials. In order to facilitate these aims a fully re-configurable/programmable parameter monitoring and logging system was developed.

A detailed schematic of the overall data logging system is given in Figure 5.1-8 and shown in Figure 5.1-9. A patchboard arrangement (shown in Figure 5.1-10) was used to route all sensor and transducer signals within this system. The patchboard arrangement enables re-configuration of the system to be readily achieved. In addition, this arrangement also enables signals to be passed, without interruption of the main data monitoring circuit, to additional monitoring equipment (such as multi-metres and oscilloscopes) when required during system set-up and calibration. Data logging was facilitated using a PCI-20377W (*Burr-Brown inc., USA*) multifunction data acquisition board housed within an Optiplex GX100 (*Dell inc., USA*) 330 MHz personal computer.

Several different algorithms were written, using the Visual Designer software (*Burr-Brown inc., USA*) to compute, in real time, the system parameters that were relevant to any one particular set-up. This system is an icon based application generator that will produce programmes for logging, manipulation and analysing of data. An example of one of these programmes, in this case applied to the computation of C-functions (used throughout the trials described in Chapter 8) is shown in Figure 5.1-11.

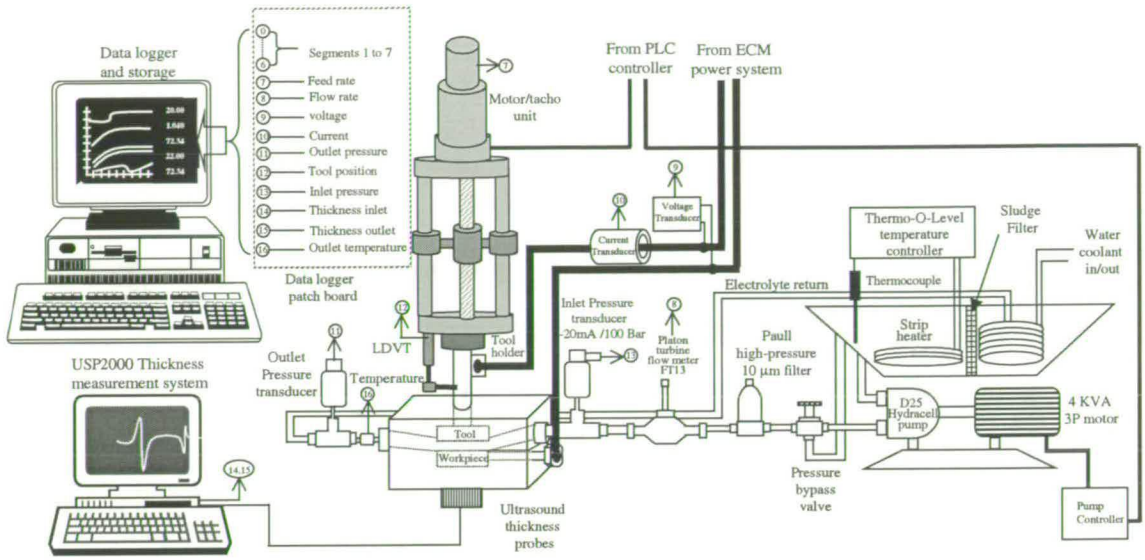

Figure 5.1-8: Detailed Schematic showing system monitoring and transducers arrangement

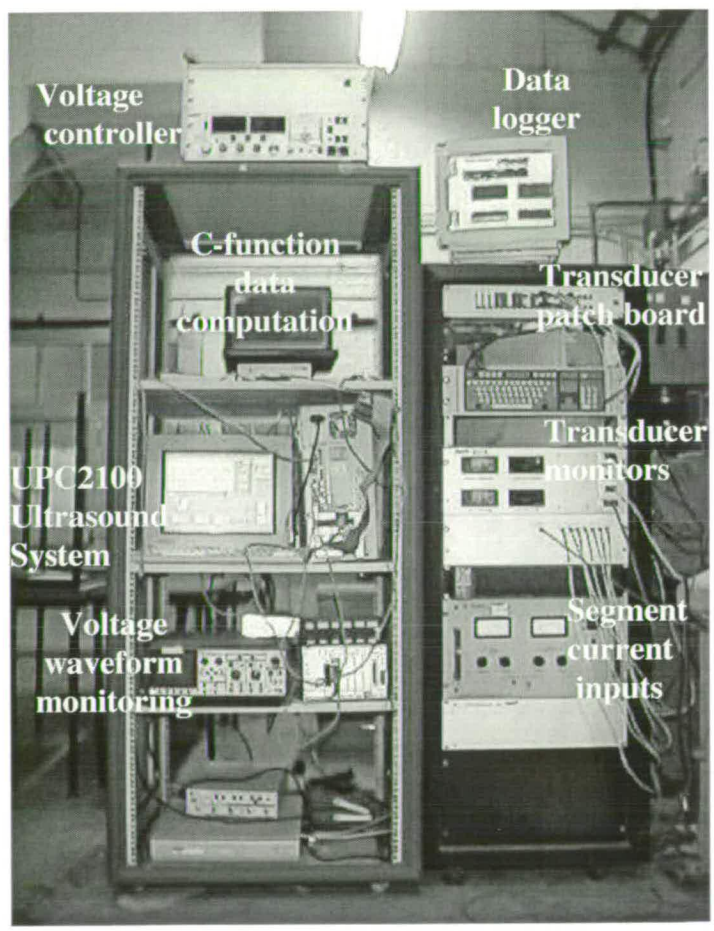

Figure 5.1-9: System monitor and data logging arrangement (USPC2100 detailed in Chapter 7)

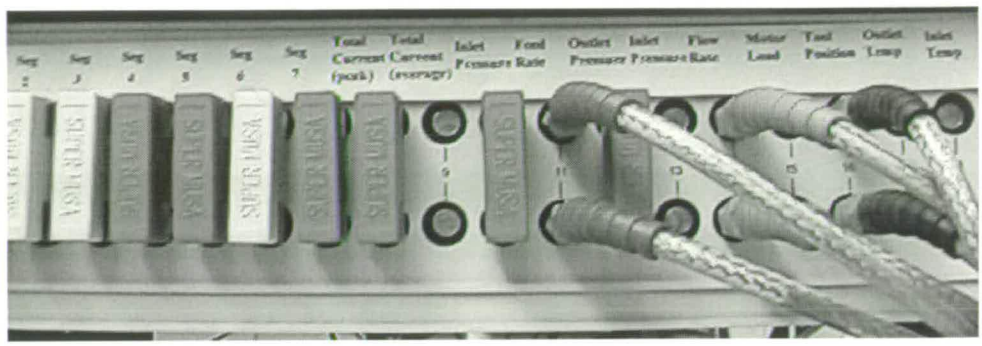

Figure 5.1-10: Patchboard for routing of parameter signals to data logger and/or diverting to monitors

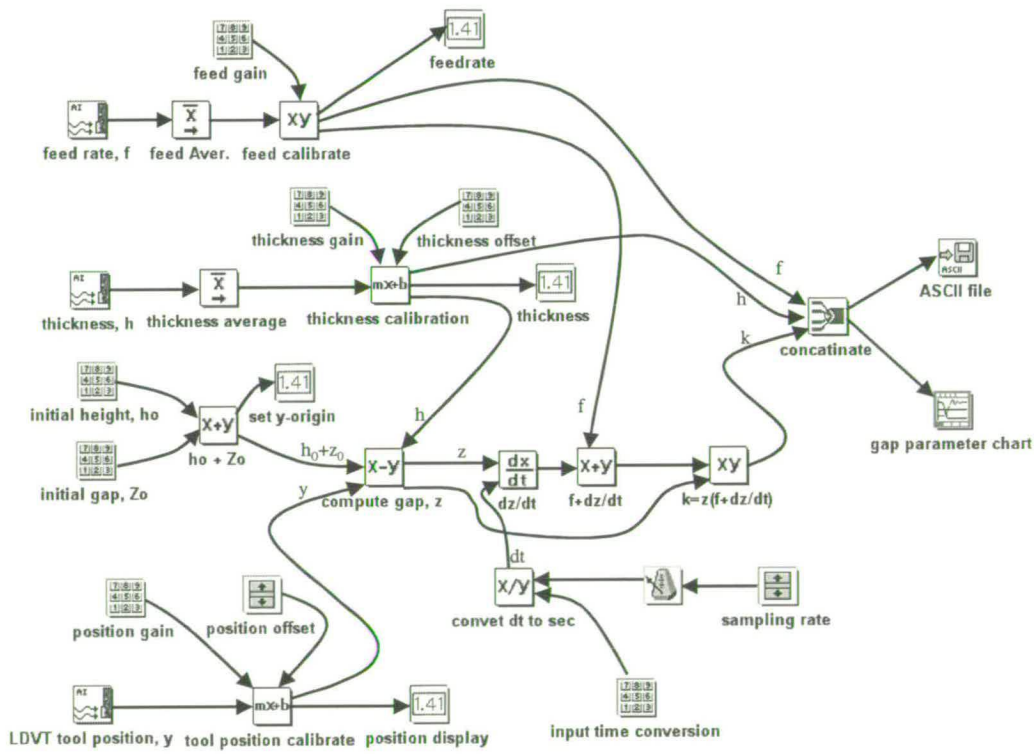

Figure 5.1-11: Visual Designer Data flow diagram for C-function measurement

5.2 Machining cells: flow cells and tooling configurations

In the majority of commercial ECM machining systems the tooling workpiece and associated semi-open flow directing systems are usually enclosed within a machining chamber. This chamber acts as an enclosure to confine the spray of stray electrolyte. Thus it is often assumed that the tooling and workpiece arrangement is such that only a certain proportion of the inlet flow will enter and exit the IEG without losses. Such an arrangement would be unacceptable in the case of the characterisation trials being considered here where the flow velocity (calculated from the overall flow volume through the IEG) is an important variable. Therefore, for all experimental trials a series of machining cell systems, in which the tooling and workpiece are fully enclosed within a flow confinement system, were developed. Each *machining cell* was designed as an assembly consisting of the *electrode configuration*[††] and *flow cell*[‡‡]. In these systems the electrode configurations have been designed to be interchangeable with the various flow cell designs.

Three main flow cell arrangements were developed together with a range of tooling configurations. The flow cell systems have been named, in order of their development, as cell-97, cell-99 and cell-2000. Cell 97 was designed to carry out general planar, 2-D and segmented ECM experiments (detailed in chapter 6). Cell-99 incorporates a single ultrasound gap sensor and was designed to develop the gap measurement system (detailed in chapter 7). Cell-2000 was an advancement on cell 99 incorporating two ultrasound gap sensors, one at the flow inlet and one at the flow outlet. Cell-2000 was designed to enable measurements of the sensitivity of gap-time and C-function data to a predetermined flow path interval (detailed in chapter 8).

In this section, the tooling configurations are described together with specifications and the evolution of designs for all the flow cell systems.

5.2.1 Tooling configurations

In designing the tooling configurations criterion common to all systems have been :

- Encapsulating the IEG flow channel so as to maintain a uniform flow path length within a minimum dependency upon tool feed position. Achieving this would mean that the local flow velocity could be readily determined from a knowledge of the flow volume through the cell irrespective of the tool position. The flow velocity being an important parameter during most of the characterisation trials.

[††] The *electrode configuration* is the term used to describe the tool and workpiece block arrangement and components directly attached to these such as the feed pin and side cheeks.

[‡‡] The *flow cell* is the enclosure arrangement and related auxiliary components that are used to guide and confine electrolyte flow in a predefined way.

- Removing electrolyte flow effects (low velocity boundary layers) away from the active machining zone. Such boundary layers are known to produce instability in most dissolution systems and in the case of few systems result in passivation along the edge of the flow field (titanium is particularly prone to this problem).

The general arrangement used for all tooling configurations is illustrated in Figure 5.2-1.

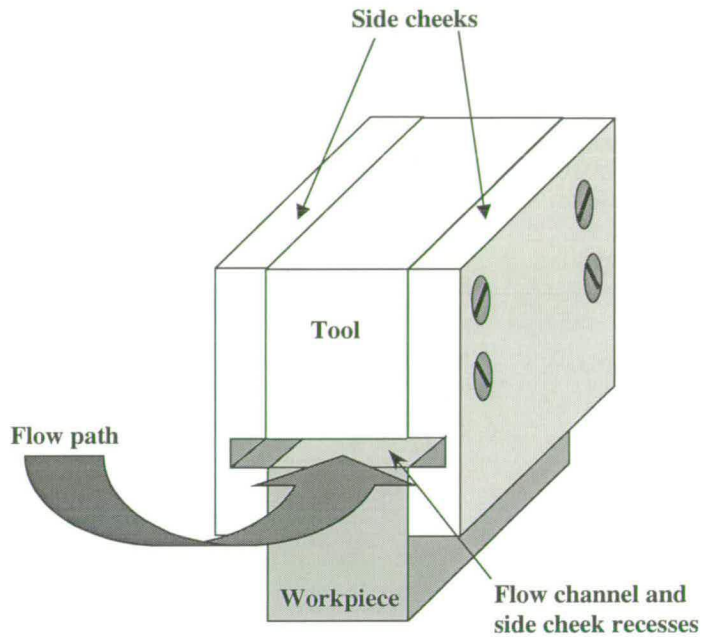

Figure 5.2-1: General tooling configuration

Encapsulating the flow channel has been achieved by incorporating insulating side cheeks attached to either side of the tooling block. The side cheeks extend beyond the tool face so as to enclose the workpiece block and act as a guide in positioning the electrodes relative to the flow cell workpiece cavity. As the tooling (or workpiece in the case of cell 2000) feeds, the side cheeks slide into recesses in the cell base and seal against a recess wall at the flow inlet end. This arrangement prevents electrolyte flow around the sides of the workpiece and forces the electrolyte exclusively through the IEG channel.

The use of this side cheeks arrangement also enables the removal of low velocity flow regions from the active machining zone. This is achieved by incorporating two small recesses into the side cheeks running along each side parallel to the flow channel and in-line with the workpiece surface. This feature means that flow boundary layers at the edges of the flow field move away from the active tooling face. Under these conditions the flow velocity, in a plane perpendicular to the direction of flow, should be relatively constant and therefore product removal will be efficient over the full dissolution zone.

The tooling assembly and feed pin arrangement shown in Figure 5.2-2 is one of the primary systems used throughout the characterisation trials. This arrangement is a flexible system that can be converted to machine either planar or 2-D shapes by replacement of the tooling bit. The system retains the same side cheek assemblies for use in both configurations. The tooling system shown in Figure 5.2-3, and illustrated schematically in Figure 5.2-4, is an extension of the planar tooling system incorporating seven independent tool segments. This novel arrangement has been designed to develop spatially distributed characterisation data with a correlation to position along the flow path length. Each of the system's segments is insulated from its neighbour by 0.05 mm mica spacer plates. Because the dimensions of the plates is small relative to typical ECM gaps, then it is assumed that the field lines from each of the segments can be considered as essentially parallel to each other, as is the case in the planar tooling configuration. Two recessed brass bolts, insulated by a nylon sheaf, pass through each of the spacer plates and each tooling section to hold the assembly together. Power is fed individually to each of the segments through an array of seven power connection pins. These pins are screwed into the individual sections at one end with the other end secured to the main feed block (see Figure 5.2-4). The power cables are secured to each of the pins via purpose made miniature spigot clamps. An array of seven Hall effect transducers (illustrated as part of Figure 5.2-4) was used for independent monitoring of the current flowing through each segment (this monitoring system was described in more detail as part of the overall experimental set-up in section 5.2).

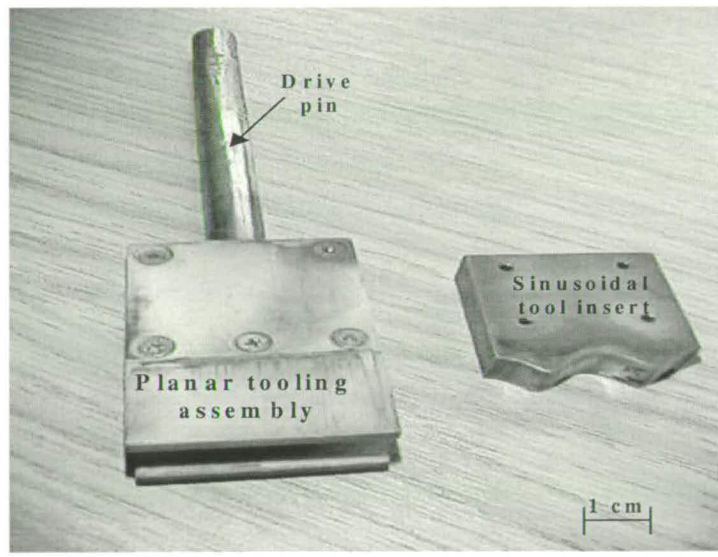

Figure 5.2-2: Planar tooling together with 2-D sinusoidal tool insert (see section 8.4)

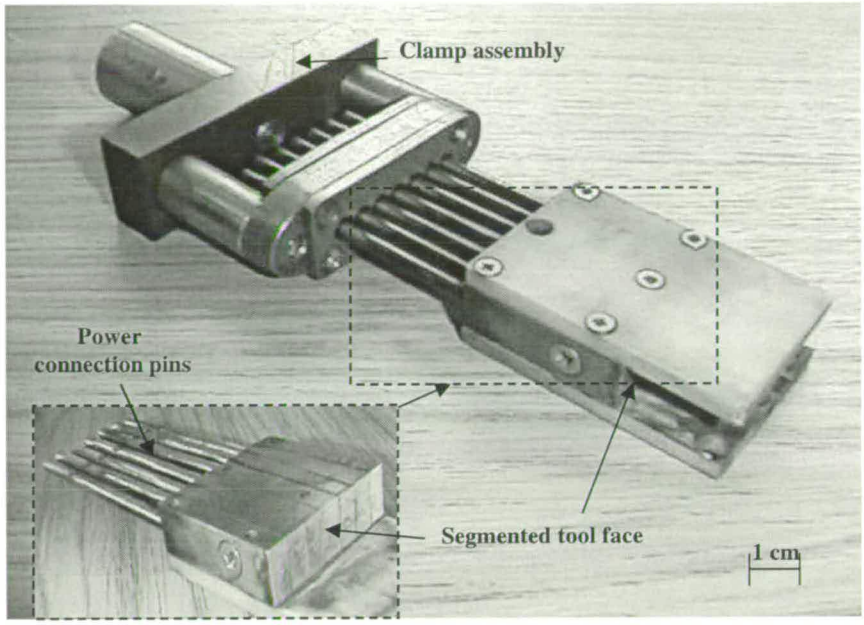

Figure 5.2-3: Segmented tooling system

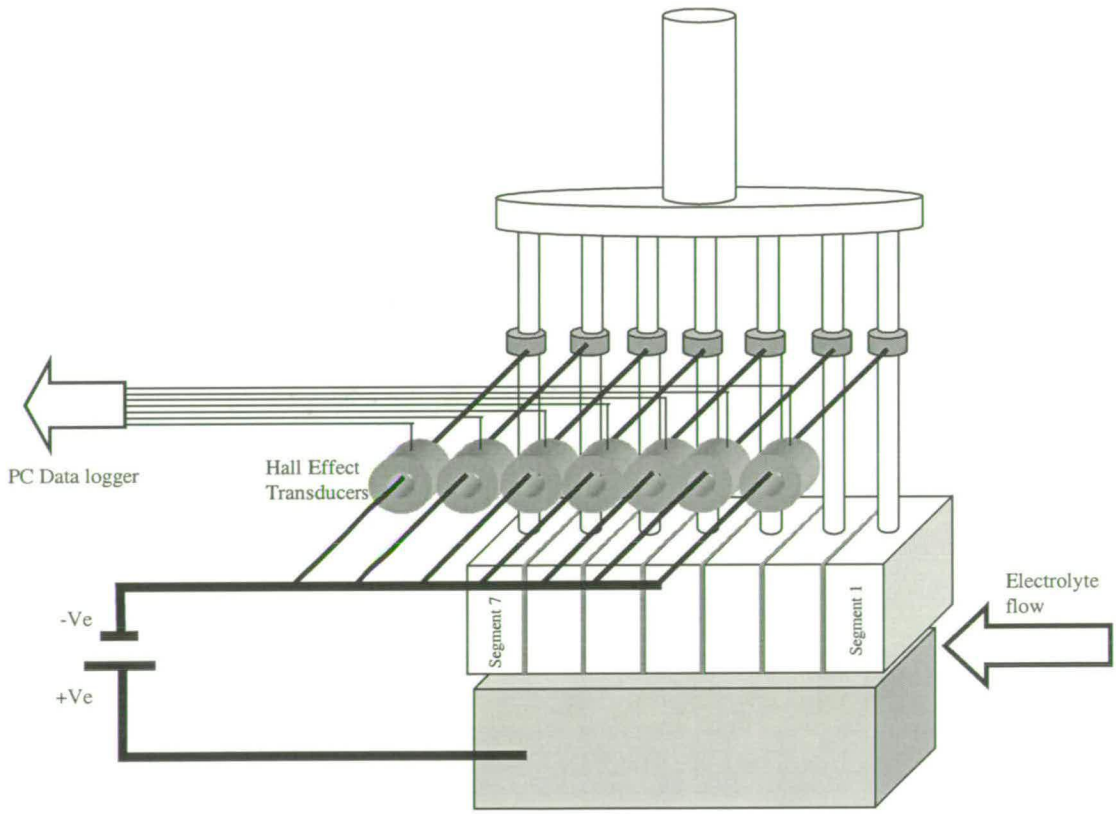

Figure 5.2-4: Segmented tooling arrangement showing power distribution and monitoring arrangement

5.2.2 Cell Configurations

Although each cell incorporated specific features designed to carry out certain experiments, as the project progressed these cells also incorporated improved general features. In this section, the general evolution of these features is described. When particular features have been incorporated into cell-2000 as a result of inefficiencies with previous designs then these improvements are described in context of these designs. Also because cell-2000 represented the most evolved stage of cell development, only this system is described in detail in regard to set up and system operation. In the case of other cells when set up detail differs, or is relevant to particular experiments, additional specific details are given in the appropriate experimental section.

5.2.2.1 Flow path variance

It is generally realised in ECM that flow path geometry and the related inlet and outlet conditions can affect dissolution characteristics. Ideally then, the criterion for stable characterisation data is that flow path conditions are invariant with time. In particular, this requires that flow path conditions are the same, or similar, irrespective of the relative tool and or workpiece position. The primary variables being the relative displacement between the flow inlet port and the IEG flow channel. Figure 5.2-5 illustrates flow path conditions for two different configurations; one in which the tool is fed relative to the inlet port and a fixed workpiece, and the other where the workpiece is fed relative to the inlet port and a fixed tool. In the case where the tool surface is displaced relative to the inlet port Figure 5.2-5 ((a) and (b)) then the IEG flow channel moves away from the flow inlet port, increasing and distorting the flow path, as the erosion of the workpiece occurs. This situation occurred in the case of cell 97 and cell 99. It was realised that this distortion could be significantly reduced by inversion of the tool and workpiece electrode arrangement. This novel arrangement, which was implemented in cell 2000, is illustrated in Figure 5.2-5 (c) and (d). The tool surface now remains in line with the flow inlet regardless of the position of the feed system. When the workpiece is been fed at a constant feed rate (this is the most common situation) then an initial transient period will occur when the IEG height (the gap) will vary and the workpiece edge will move slightly relative to the flow inlet port. This will however be a small displacement and during equilibrium machining, when the feed rate equals the erosion rate, this relative displacement will be zero, and the flow path geometry will be fixed.

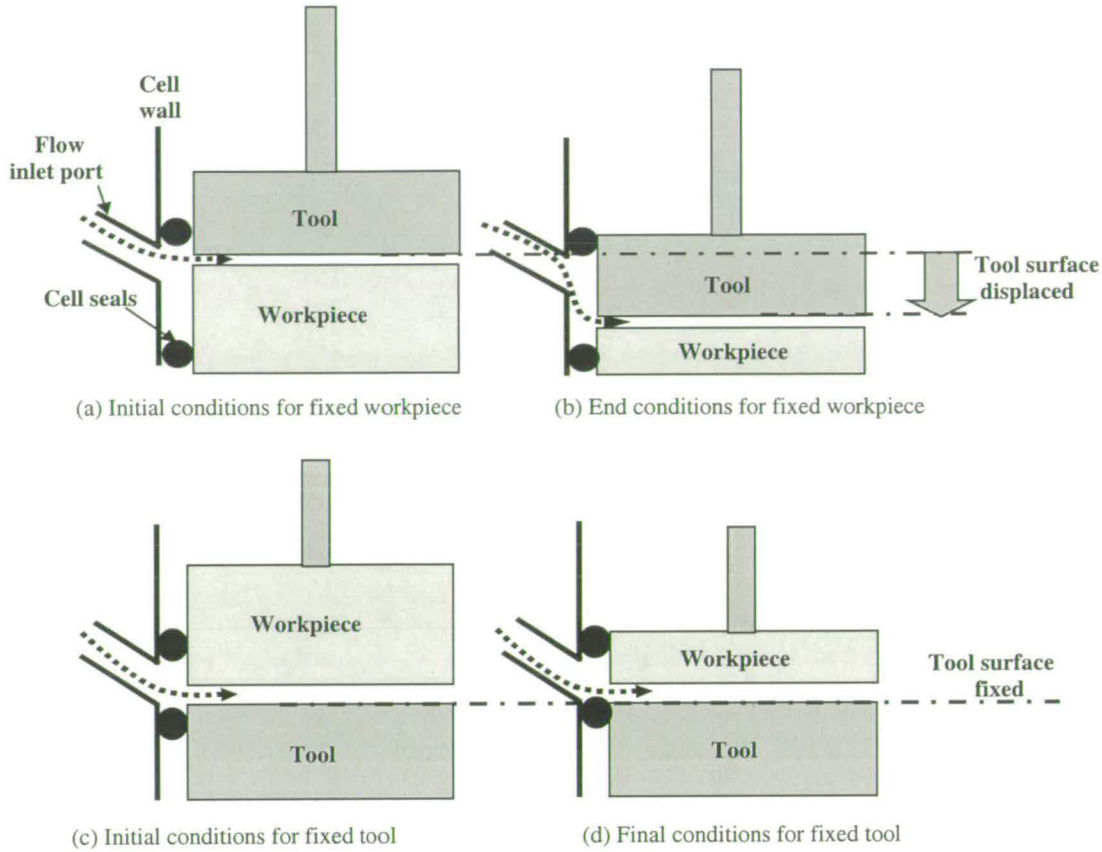

Figure 5.2-5: Showing flow variation for fixed workpiece or tool configurations

5.2.3 Cell-97: Planar, 2-D and segmented tooling

Cell-97 was used for the series of trials described in Chapter 5. In common with other cell designs, cell-97 is split into three sections consisting of the top plate, central section and bottom plate. The bottom plate encloses and clamps the workpiece electrode, the central section encloses and defines the flow path, and the top section guides and locates the tooling arrangement. All three sections are clamped together by symmetrically positioned toggle clamps. Bayonet type quick-release flow connectors are used to attach inlet and outlet flow ports. The use of quick release connectors aided improved set-up times since it was found that if the flow connectors were left attached during a tool retraction, then bending of the drive pin could result (this was particularly the case when using the segmented tooling assembly). Workpiece power is fed through the walls of the lower cell plate via a brass bolt that also acts to clamp the workpiece in position.

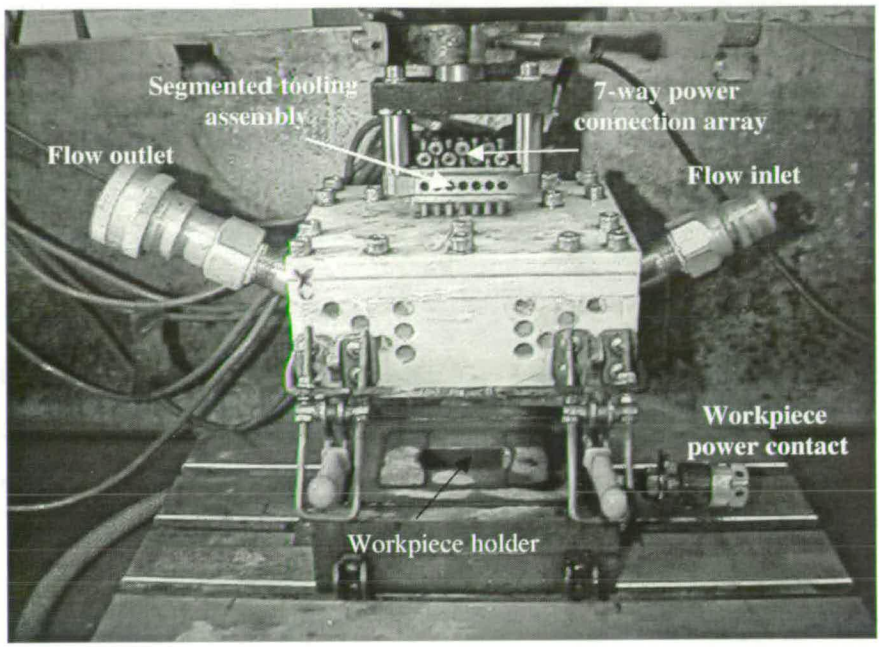

Figure 5.2-6: Cell-97 shown with segmented top plate and segmented tooling in place

Cell 97 was designed for use with the planar tooling, the 2-D tooling bits and the segmented tooling assembly. Flexibility was achieved by having an interchangeable top plate. One with a single orifice, for the planar and 2-D tooling configurations and the other with a line of seven individual orifices to guide the segmented feed pins when operating with the segmented tooling configuration. Figure 5.2-6 shows the cell with the segmented tooling and segmented top plate in position.

5.2.4 Cell-99: single channel ultrasound measurements

Cell-99 was used for the series of trials described in Chapter 6. This system, shown in Figure 5.2-7, incorporates an LDVT position sensor attached to the tooling feed pin and an ultrasound probe (see section 7.3.1 for details) attached centrally to the workpiece enclosed within the cell base. The main body of the LDVT, containing the sensing coil, is clamped directly to the machine head whilst the sliding pin, containing the transmitting core, is screwed into a rigid mounting plate which is securely attached to the cell top plate. Mounting the LDVT assembly direct to the cell, and not at a remote position on the machine feed axis, ensured that any compliance in the drive/ feed system was not misinterpreted as a change in tool position. During later trials this problem was overcome, in the case of cell 2000, by use of an anti-backlash ball screw.

Other features, such as flow channel design, flow and power connections, are in common with cell 97, as described in section 5.2.3 above.

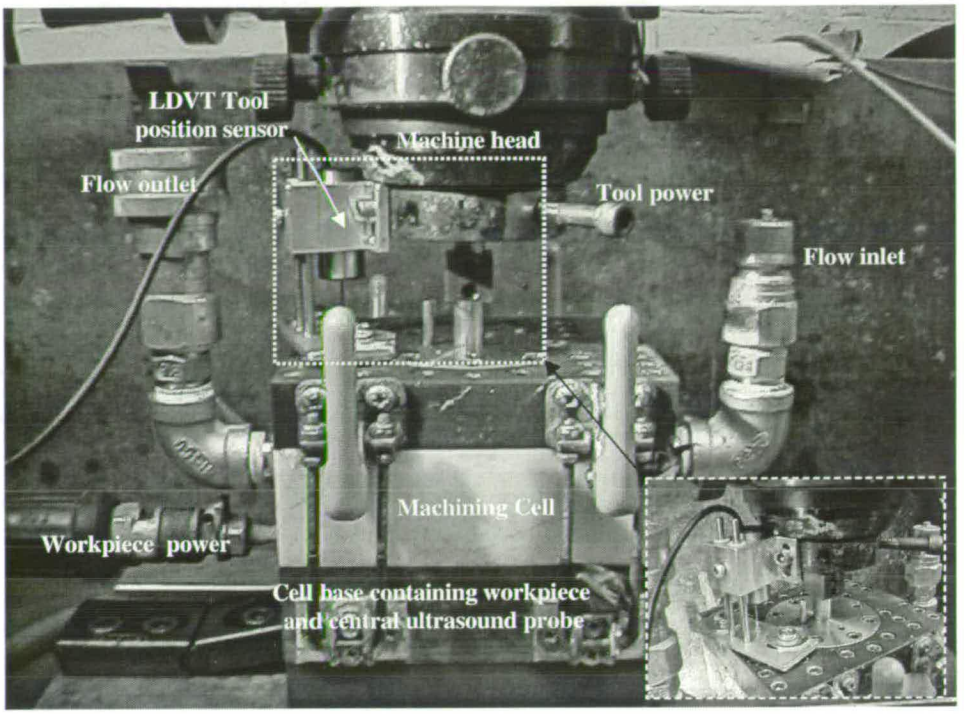

Figure 5.2-7: Cell-99 shown with LDVT sensor in position

5.2.5 Cell-2000

Cell-2000 was used for the series of trials described in Chapter 8. This system consists of three main elements: A tooling block, a workpiece holder/feed pin assembly and the main cell enclosure. The primary features of cell 2000 are the use of a three sectioned design and the incorporation of an inverted feed arrangement in which the workpiece is attached to the drive system (not the tool as used in all previous designs) with the tool held stationary relative to the machine base. This novel arrangement provided several advantages over other designs:

- Improved rigidity
- Providing a constant flow path length during dissolution (see section 5.2.2.1)
- Improvement of initial gap setting procedures during system set-up
- Improvement in the sealing system so that the electrolyte was unable to come into contact with the ultrasound probes
- Removing the need for sliding feed pins on the segmented tool which had previously been difficult to seal

Cell 2000 was used exclusively on the Doncaster's machining base fitted with an anti-backlash ball screw and since set up trials on this system showed no measurable compliance problems the need to situate the LDVT directly to the cell top plate, as was required with cell-98, was negated. The LDVT

position sensor was therefore now positioned on the main screw assembly, remote from the cell. This arrangement improved the set-up time when using this cell.

Figure 5.2-8 shows the main cell enclosure split into its three sections: a tooling plate, the central block and a top plate. The tooling plate is positioned at the bottom of the cell and is used to locate the tooling assembly. Two tool assemblies have been designed for this system: A planar tool and a segmented tool. A single release bolt enables the systems to be interchanged readily. A tool power connector passes through and locks to the tooling plate to provide the main ECM current to the tooling assembly. The central block locates, via the tool side cheeks, so as to line up the tooling relative to both the workpiece assembly and the flow feed ports. Eight toggle clamps are situated symmetrically around the sides of the central block; half of these act to pull and seal the central block onto the tooling plate and the other set clamp the top plate onto the central block. The workpiece feed ports act to locate and seal the workpiece assembly in alignment, via the central guide channel, with the tooling face.

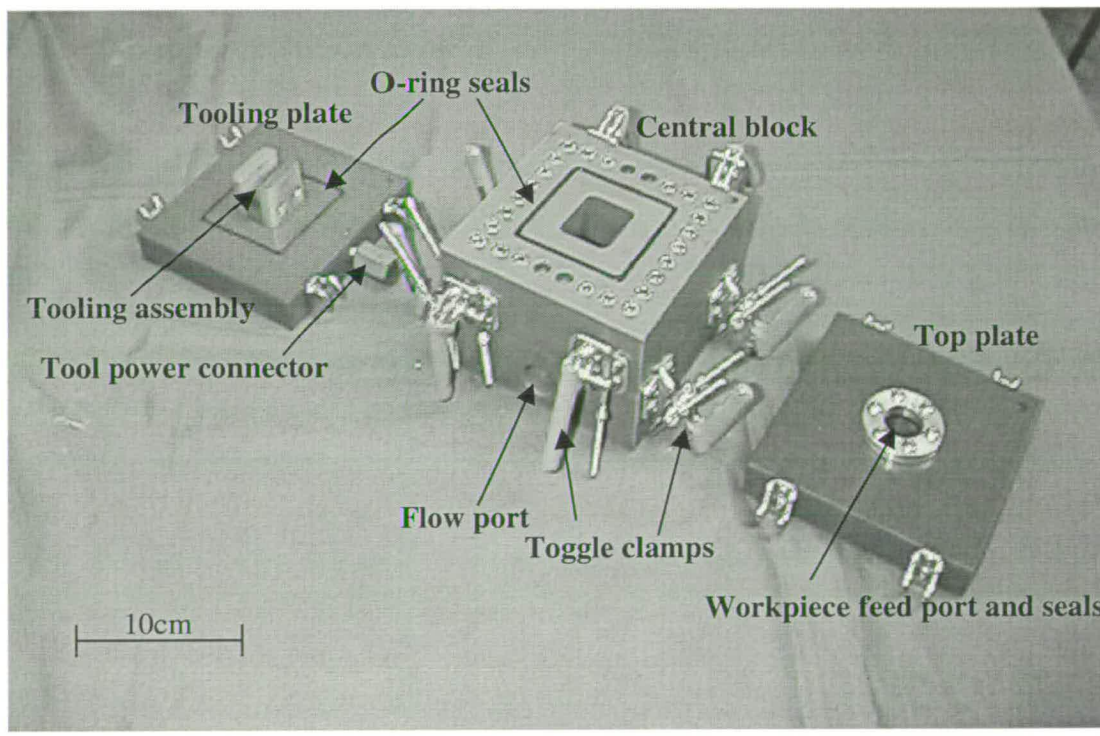

Figure 5.2-8: Component parts of cell-2000

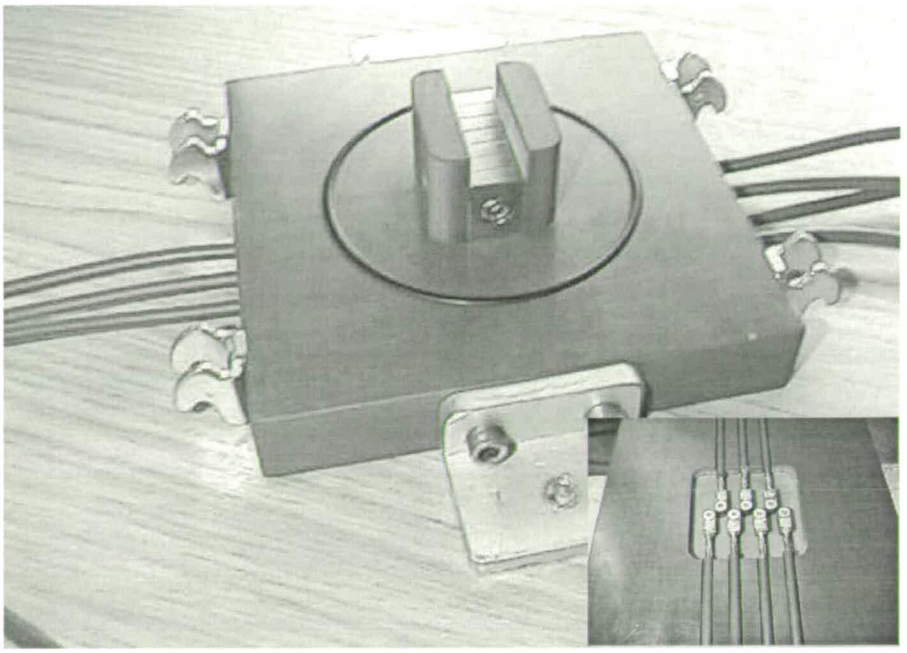

Figure 5.2-9: Segmented tooling plate for cell200 with underside view (insert) showing individual segment connections arrangement

When carrying out trials using the segmented cathode the tooling plate is reconfigured by replacing the planar tooling assembly with the segmented assembly shown in Figure 5.2-9. Power connections were made to each of the seven segments via pins that pass through the plate and locate with individual power cables (see insert in Figure 5.2-9). The bolts that connect the power cables to the segment pins also act to clamp the tooling block to the tooling plate. An advantage of the cell-2000 segmented tooling arrangement over previous designs is that the segmented power connection pins are now held stationary within the tooling plate. In previous systems these pins were fed with the tooling system through the cell enclosure (see Figure 5.2-6) and this required that individual sliding seals were used for each pin. This could be problematic since it was often the case that a trade-off would need to be made between sealing effectiveness (requiring a tight seal) and smoothness (requiring a loose seal) of tool feed velocity. In previous designs this had often led to either leaks from the segmented feed pins or a "sticking" of the feed motion (due to compliance of the drive system).

A series of detailed views of the cell-2000 workpiece/drive pin assembly are shown in Figure 5.2-10 (a) to (d). A feature of this system is the incorporation of the ultrasound probes into the body of the workpiece assembly. These probes are situated symmetrically about the centre of the flow channel and are aligned with cavities/guide slots which pass through the workpiece holder block. Two springs are secured to the drive pin end plate (Figure 5.2-10(a)) and act to align the probes flat against the underside of the workpiece. This is required to achieve the maximum power of transmitted and received phases in the ultrasound pulses (set up trials had indicated that the power of

the ultrasound could be significantly attenuated if the contacts interface between the probe and the workpiece surface were not parallel). The spring arrangement was also required to ensure that an appropriate amount of contact pressure was achieved (by adjustment of the spring length) at the probe tip/workpiece interface. The tool holder assembly is sealed by use of a silicon rubber compound and cap screws which attach the workpiece holder block to the drive pin end plate. The probe contact points are sealed from ingress of electrolyte, at the back-end of the workpiece, by the sealing configuration as shown in Figure 5.2-10 (b). Locating the workpiece firmly against the seal is achieved by tightening the clamping bolt that is part of the clamping tool arrangement as shown in Figure 5.2-10 (c). After locating the workpiece on this seal the workpiece clamps screws are tightened to secure the workpiece in position prior to removal of the clamping tool.

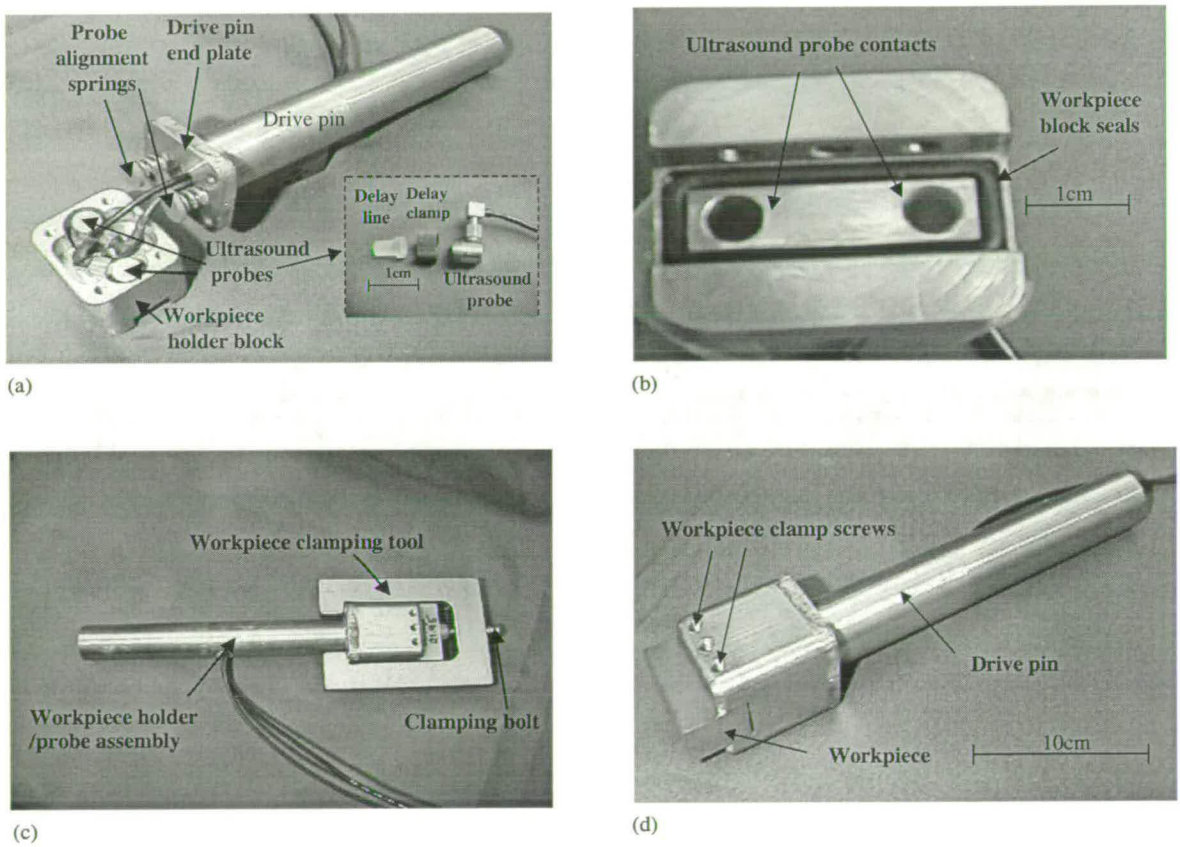

Figure 5.2-10: Views cell2000 workpiece/drive pin assembly illustrating; (a) internal view of workpiece block showing encapsulated probes, (b) probe contact points and block seals, (c) procedure for workpiece clamping, (d) completed assembly

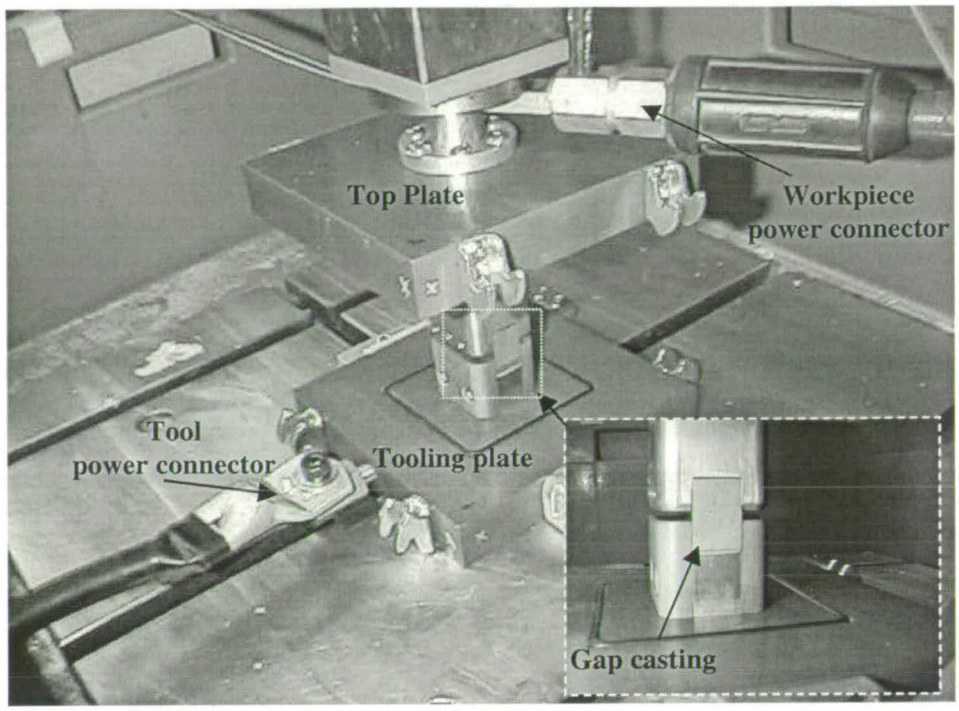

Figure 5.2-11: Cell 200 gap measurement procedure

The three block configuration of cell 2000 aided the accurate pre-setting of the IEG prior to a machining run. This procedure, illustrated in Figure 5.2-11, involved first removing the cell central block and then aligning the tool and workpiece electrodes within the side cheeks sections. The cell top and bottom plates were then located and clamped to the machined head and the work table respectively. A feeler gauge was then used to set the position of the tool face at the required pre-set initial gap relative to the workpiece face. A polyether casting solution (*Permerdyne*) was then injected into the tool/workpiece gap. The close-up insert in Figure 5.2-11 shows the casting compound as solidification is occurring[§§]. After solidification, which took about two minutes, the gap casting was removed and sectioned along its central axis. The casting thickness was then measured at intervals along the flow axis. This was achieved using a spring loaded *Mitutoyo* thickness gauge calibrated against a reference gap casting which had previously been dimensioned on a travelling microscope. The casting was used to provide accurate confirmation of the gap setting and also to ensure that the gap was parallel along the machining axis. In cases where the gap is not parallel (usually due to the initial workpiece specimen not being accurately machined) then an initial ECM machining was carried out, prior to the actual experimental trial, in order to set the workpiece flat relative to the tool surface. Once the initial gap size has been confirmed the LDVT position output was then zeroed on the computer monitoring system (further details on this process are given in Chapter 7).

[§§] The Permerdyne material does not shrink or require a release agent

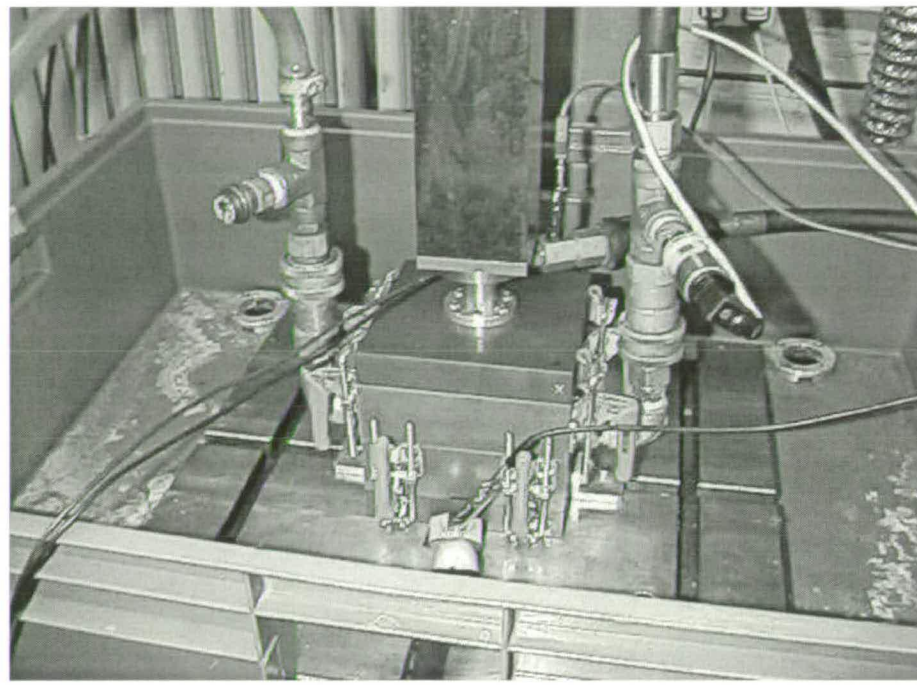

Figure 5.2-12:Cell 2000 assembled in machine enclosure

Once the initial set-up procedures have been carried out the central section of cell is then positioned on the tool plate and pulled onto the lower seals via the lower four toggle clamps. The workpiece plate is then fed back into the set-up position (by re-zeroing the LDVT output) and the remaining four toggle clamps fastened with sufficient force to ensure isolation of the flow channels within the cell and also sealing of the cell against electrolyte loss into the machining chamber. Finally, before initiating a machining trial, flow inlet/outlet, electrode power connections and gap voltage monitoring clips are attached to the cell in the arrangement as shown in Figure 5.2-12.

5.3 Chapter overview and conclusions

This chapter has detailed the development of the complete range of system set-ups designed for the measurement of ECM machineability. In particular, the development of the segmented tooling system will enable spatial resolution of parameter sensitivity and the use of the gap measurement system will enable C-function measurements to be made.

The following chapter details the usage of both the planar and segmented tooling systems applied to the general measurement of parameter sensitivity.

CHAPTER:

6 General planar and segmented characterisation trials

This chapter describes a detailed series of trials in which the machineability characteristics of various material/electrolyte systems are examined. These characteristics are defined in terms of parameters deduced from current-time data as outlined by the theory in sections 2.2, 4.1 and 4.2. Additional analysis has been achieved through use of a novel segmented tooling system which has enabled parameter sensitivities to be decomposed as a spatial distribution along the axis of the flow path.

6.1 Introduction and background

The following details a series of experiments in which the basic characteristics of a selection of electrolyte/material systems are studied using current-time and static analysis according to the planar relationship as outlined below and detailed in Chapters 2 and 4. The main aim being to identify certain process interrelationships and to determine sensitivity of these relationships between different machining systems. The emphasis directed to developing techniques through which this data can be readily obtained, the primary interrelationships determined along with the testing of these relationships. Certain characteristics are also determined which are later used for cross-checking when developing the C-function characterisation strategy as described later in Chapter 8. The work of this chapter together with some additional information on the chemical stoichiometry of the systems studied is given in the appended publications by Clifton et al.[77] and Mount [34]. Additional related work, with particular reference to the use of the segmented tooling, carried out by the author in collaboration with Mount is given in the appended publication [78].

In section 7.2, a theory was outlined in which current-time data generated from a planar electrode configuration could be used to define machineability data for any given material/electrolyte system. With certain assumptions (see section 2.2) this machineability data can be formulated as a grouping of the fundamental constants and parameters of machineability in the form of a single constant, k, defined by:

$$k = \frac{\kappa\varepsilon(V - V_0)}{\rho F}$$

Equation 2.2-9 (see section 2.2)

And computed from a current-time system response based upon an iterative fit to the non-explicit relationship:

$$\frac{J_0}{J_\infty} - \frac{J}{J_\infty} + ln\frac{1 - \frac{J_0}{J_\infty}}{1 - \frac{J}{J_\infty}} = \frac{f^2 t}{k}$$

Equation 4.1-7 (see section 4.1)

The fit of this relationship to experimental data will produce a value of the k-parameter as an average of parameter sensitivities over the range of current density J_0 to J_∞.

In section 7.2 the following relationships were noted as providing means of establishing values for the individual constituents of the parameter k. The valency, n, can be obtained using:

$$n = \frac{J_\infty M}{fF\rho}$$

Equation 2.2-3 (see section 2.2)

and V_0 and κ from the intercept and gradient respectively of the linear proportionality between J_0 and $V\text{-}V_0$ using the relationship:

$$J_0 = \frac{\kappa(V - V_0)}{z_0}$$

Equation 2.2-4 (see section 2.2)

Confirmation of V_0 and κ can be made at conditions more applicable to ECM in practice, using current-time data fits to obtain the intercept and gradient in the expression:

$$\frac{k}{f^2} = \frac{\kappa M(V - V_0)}{nF\rho f^2}$$

Equation 2.2-9 (see section 2.2)

6.2 Selected workpiece/electrolyte systems

Before beginning these trials it was realised that any one machining system would have different stoichiometric characteristics when compared to other systems. Indeed, the need for the work in this thesis is based on the realisation that a fundamental basic description applicable in general to ECM systems cannot readily be achieved. It was decided therefore that a wide range of representative characteristics would be best achieved by selecting workpiece materials from two different elemental alloy families commonly associated with the application of ECM; one a nickel based alloy and the other a titanium based alloy, by machining these alloys using each of the two commonly used electrolyte systems; one nitrate based and the other chloride based. This selection would allow an examination of the effect of interchanging either the material or electrolyte component for a given system. It might therefore be expected that these characterisation trials would produce a significantly wide range of characterisation variations. Also, because all of these systems are known to produce stable dissolution (i.e. non-passivating), it was decided to examine an additional grouping by including a titanium aluminide alloy that had previously been associated with passivation phenomena in ECM [79]. In this previous work it had been discovered that titanium aluminide will readily passivate in chloride and many other electrolyte systems. It was therefore decided to include in the present study an examination of the characteristics of titanium aluminide in which passivation was not observed. This alloy was therefore machined using many different electrolyte compositions

(for details see [79]). From these trials it was discovered that only a perchlorate electrolyte would produce stable dissolution with titanium aluminide. The system was therefore examined further in the current work by applying current-time analysis to compare the TiAl/chloride system (in which passivation occurs) with the TiAl/perchlorate system (in which passivation does not occur). Thus the systems studied have been as follows:

- Ti6-4/nitrate system
- Ti6-4/chloride system
- In718/nitrate system
- In718/chloride system
- TiAl/chloride system
- TiAl/perchlorate system

For details on material compositions see Appendix A4

Note that this work also forms part of a wider investigation in which these systems are examined as part of a detailed examination into the chemical stoichiometry occurring during ECM. This investigation is currently in its first year and will be reported in a separate thesis by Howarth [16]. In the context of the aims of this thesis the characteristics of interest will be those which will produce geometric sensitivities that can be represented in terms of C-function characterisation described later in Chapter 8.

6.3 Experimental procedures and equipment

Full development and operational details of the experimental ECM equipment has been given in Chapter 5. All the experimental results reported in this chapter were obtained using cell-98 configured for use as appropriate to each experiment with either the planar or segmented tooling assembly. Figure 6.3-1 illustrates the general experimental configuration in the case of trials undertaken with the segmented tooling set-up. This general configuration was also used during trials with the planar tooling. Note that in the case of the segmented arrangement there exists a small overlap (1 mm) of the tool edges relative to the workpiece (illustrated by the dotted line in Figure 6.3-1.). This feature was engineered into the system since it was realised that current passing through these end segments would flow along field lines which were slightly distorted due to extension around the edges and onto the sides of the workpiece. Such effects could be negated if a system was developed in which the sides of workpiece were not exposed to machining. A method of achieving this would be to use spring loaded sliding inserts positioned flush to the sides of the workpiece. Implementing such an arrangement would require that the insulating inserts were able to track downwards in parallel with the eroding surface of the workpiece. It was realised, however, that such a mechanism would be complicated and hence probably reduce the reliability of the system. It

was decided therefore to simply allow these edge effects to occur. This would result in a slight rounding of the edges of the workpiece and would mean that current-time data generated at these positions would be slightly distorted (especially at larger gaps where field line distortions are increased). It was also realised that the form of the distortion to the current-time data could be used to analyse these edge effects. This analysis is not considered to be important for the objectives of this thesis, but will be detailed separately in a future publication by the author and Mount. It is this related analysis that has required the accurately defined one millimetre edge overlap. Thus in general, for the purposes of the work in this thesis, the data from segments one and seven are not considered in respect of generating characterisation data. Calibration procedures for the segment current transducers are given in Appendix A4.

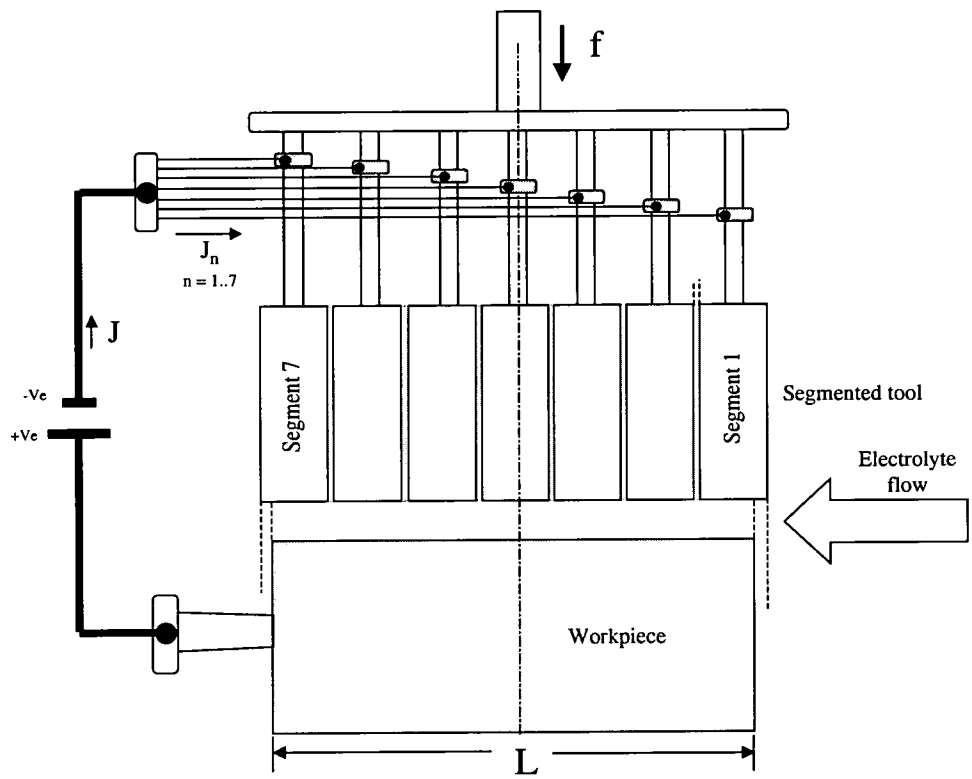

Figure 6.3-1: General experimental configuration for segmented tooling trials (cell 97 configuration)

Detailed elemental compositions and microstructural characteristics for the three workpiece materials are given in Appendix A4. Electrolytes where made up using AnalaR quality sodium based compounds (i.e. sodium chloride, sodium nitrate and sodium perchlorate). The three electrolyte solutions were made up as 60 litres w/v solutions of 15.0% NaCl, 21.7% $NaNO_3$ and 31.4% $NaClO_4$[***], for the chloride based, nitrate based and perchlorate based electrolyte respectively. These percentage concentrations were chosen to ensure that the ions in solution gave an equivalent

[***] All supplied by Anderson, Gibb and Wilson Ltd.

molarity of 2.56 mol dm^{-3} relative to a *standard* concentration of sodium chloride at 15%. This would ensure equivalent conductivity's in terms of the ion concentrations in the bulk of each solution. Also, to ensure that the bulk conductivity was not significantly affected by temperature all electrolyte solutions were maintained at a bulk temperature of 30 ±1 °C. To achieve this the electrolyte was initially heated up to the required temperature, and then during the experiments, when bulk heating of the electrolyte would otherwise takes place due to Joule heating, cooling of the electrolyte was achieved in the main storage tank using a water driven heat exchanger (see Figure 5.1-8 in section 5.1). Except for those trials in which the flow rate was a variable, the flow volume was set and maintained at a value of 16 or 20 l/min. The electrolyte solution was renewed between each trial. This was done to ensure that chemical change (accumulation of ions or changes in pH) and physical change (accumulation of precipitated products) would not occur to a degree that could otherwise affect measurements in subsequent experiments.

For each of the machining systems a series of trials have been carried out using the planar tooling configuration in which the initial gap value, z_0, was set to a value of 0.80 ±0.01mm. This tolerance was maintained using the gap casting procedure as outlined in section 5.2. The machining voltage was incremented between trials in 4 volt intervals. During each trial the machining voltage was held constant using a servo-controlled variac (see section 5.1) to a tolerance of ±0.05 V. Note that the servo controller was referenced to connections attached directly to the tool and workpiece. This was to ensure that voltage drops along the main power connections, which would otherwise vary with machining current, could be compensated for. Except where indicated the feed rate was held constant in all trials at a value of 1.00±0.01 mm/min.

Ensuring stability and accuracy in the value of the feed rate was of critical importance when measuring current-time constants (i.e. k/f^2 according to Equation 4.1-7) since this parameter is particularly sensitive to variations in f. It was found that the feed rate setting could sometimes go slightly out of tolerance when operating at a high pressures (small gaps). Because of this cross-checks with the value of the servo feed signal were made by timing 1mm of feed distance using a stop watch. The data was discarded on occasions when the feed rate was out of tolerance and systems adjustments made to compensate before repeating the run.

During all trials system parameters and variables were recorded at 1 sec intervals using the Visual Designer data logging system (see section 5.1). At the end of each run, once equilibrium conditions had been reached, the equilibrium machining gap, z_∞, was measured by terminating machining and making a second gap casting.

Trials using the segmented tooling system were carried out only on certain systems. These trials repeated the planar trials but with an additional adjustment made to the flow velocity towards the

end of the run. These trials were carried out in order to test the sensitivity (and distribution along the flow axis) of certain process relationships to flow velocity.

Fits to all current-time data were carried out using Mathcad's (2000 edition) non-linear iterative minimisation *Minerr* function. Full details of how this was achieved are given in Appendix A2.

6.4 Results

The results provided in the following sections are divided into planar trials and segmented trials. Further details of all the trials are given in the appended publication and [77 and 78].

6.4.1 Results and discussion (planar trials)

General machining relationships in the form of voltage/equilibrium gap trends and feed rate/current density trends, for all six of the machining systems considered are shown in Figure 6.4-1 and Figure 6.4-2 respectively. These data exhibit generally good fits to linear trends as would be predicted by Equation 2.2-4, in the case of voltage/gap trends, and, Equation 2.2-3 for the case of current density/feed rate trends. Such data, however, only represents the general trends at equilibrium conditions. A more detailed breakdown of specific trends will be clearer when examining current-time data. Note that in the case of the In718/nitrate system a transition state has been identified in which the equilibrium condition exhibits a slightly higher current density than would commonly be expected. This phenomenon is to be examined in more detail using current-time data, and additional experiments as detailed in the following.

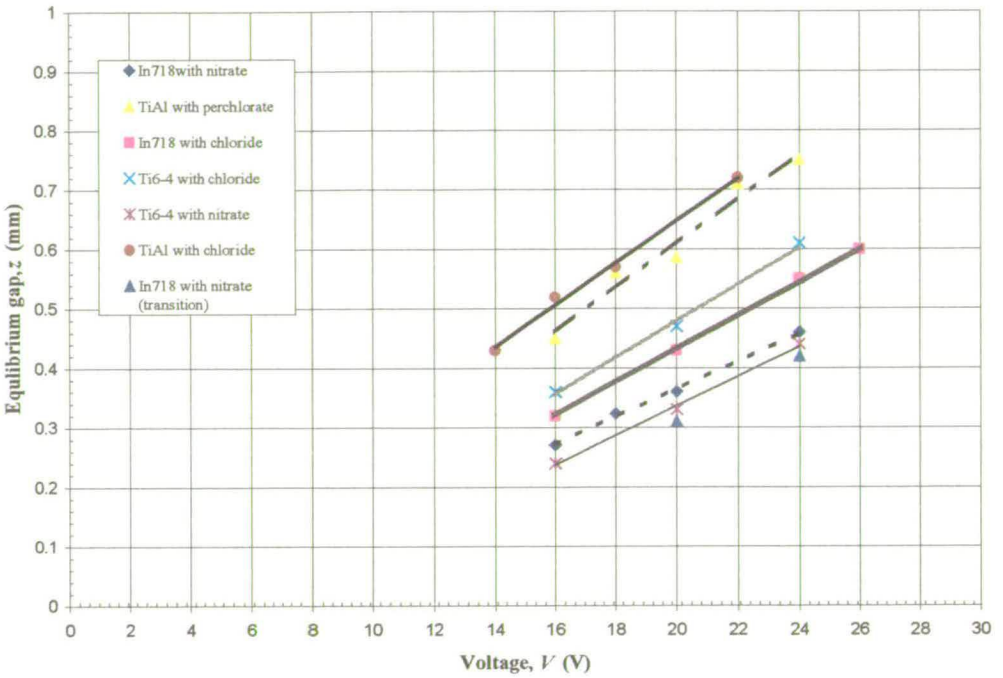

Figure 6.4-1: Voltage Vs gap relationship for all machining systems at 1.0 mm/min feed rate

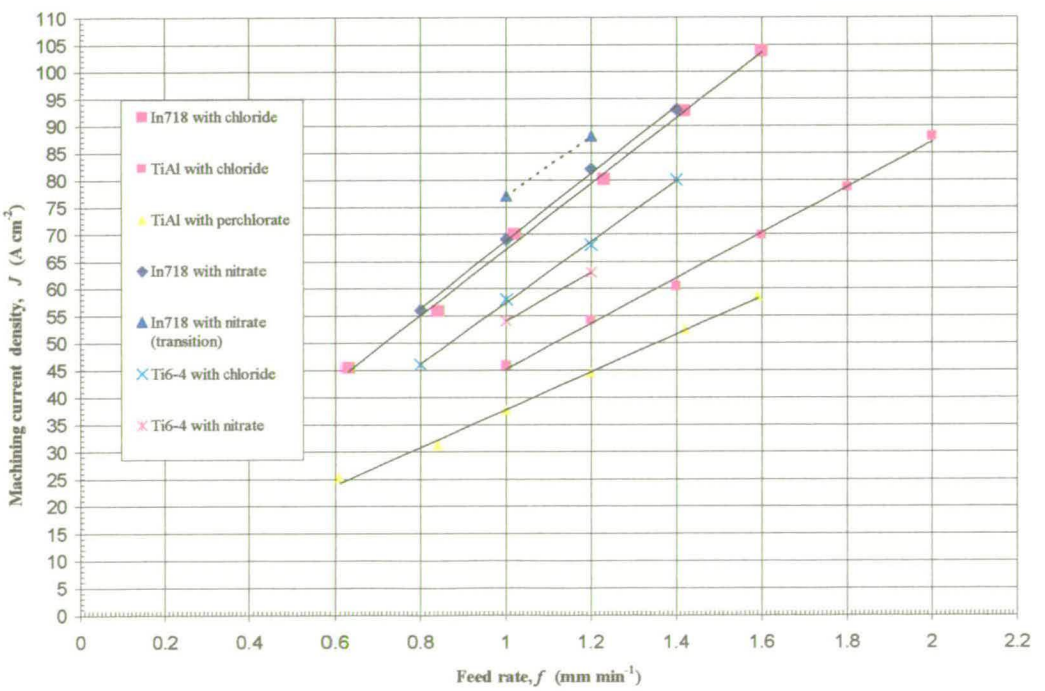

Figure 6.4-2: Feed rate against current density for all machining systems

Considering first the Ti6-4/chloride and Ti6-4/nitrate system. Figure 6.4-3 and Figure 6.4-4 show representative examples of current-time data for the Ti6-4/nitrate system and Ti6-4/chloride system respectively. These data are shown together with theoretical fits to Equation 4.1-7 as generated by Mathcad's Minerr function. Values of the machining parameter k, obtained from the fitting algorithm, and the time constant k/f^2 are given in the figures for each of the data sets. It is clear that good theoretical fits are obtained (mean squared error values are given in the respective figures) for all the data sets. From these and other data (see [34] in Appendix A1) for each of the systems the value of J_∞ remains approximately constant (independent of voltage) at 52±1 Acm^{-2} for the Ti6-4/nitrate system and slightly higher, at 56±1 Acm^{-2} for the Ti6-4/chloride system. From these values of J_∞ the average valency of dissolution[†††] can be calculated according to Equation 2.2-3, using measured values of ρ(Ti6-4) = 4.413 g cm^{-3} and M(Ti6-4) = 45.80 g mol^{-1} (calculated from the elemental breakdown given in Appendix A4), to give n = 3.4 ± 0.1 for the Ti6_4/nitrate system and n = 3.6 ± 0.1 for the Ti6-4/chloride system.

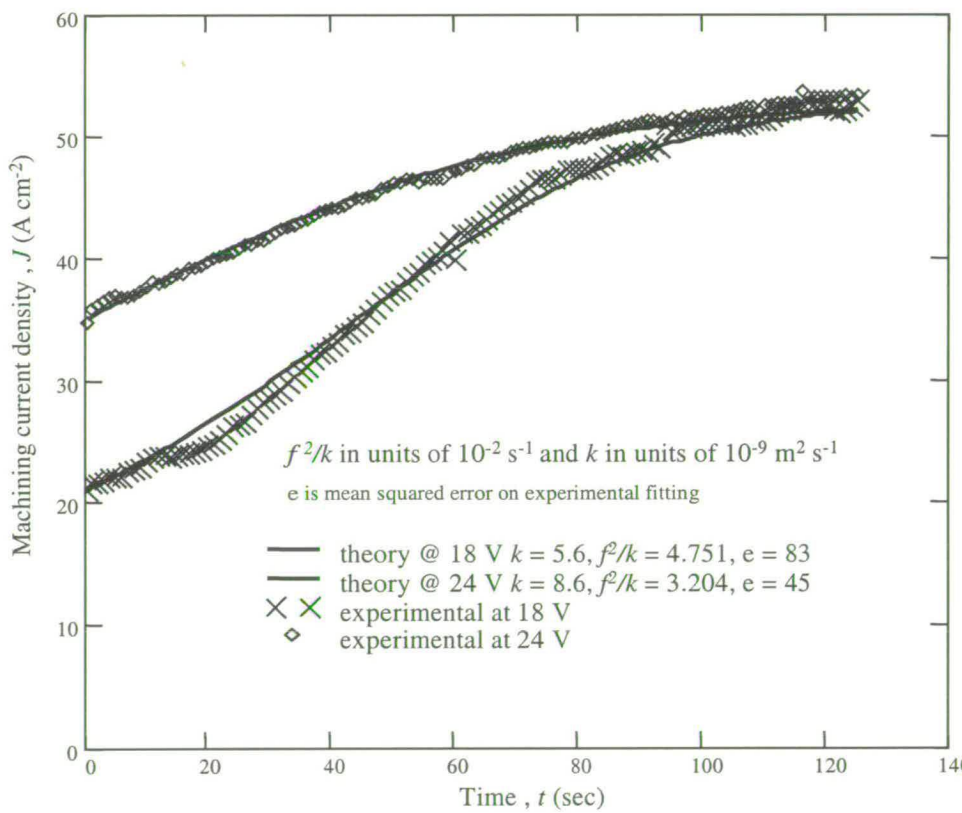

Figure 6.4-3: Current-time plot for titanium 6-4 with nitrate at 18 and 24 V

[†††] based on assumptions of 100% dissolution efficiency (see section 2.1)

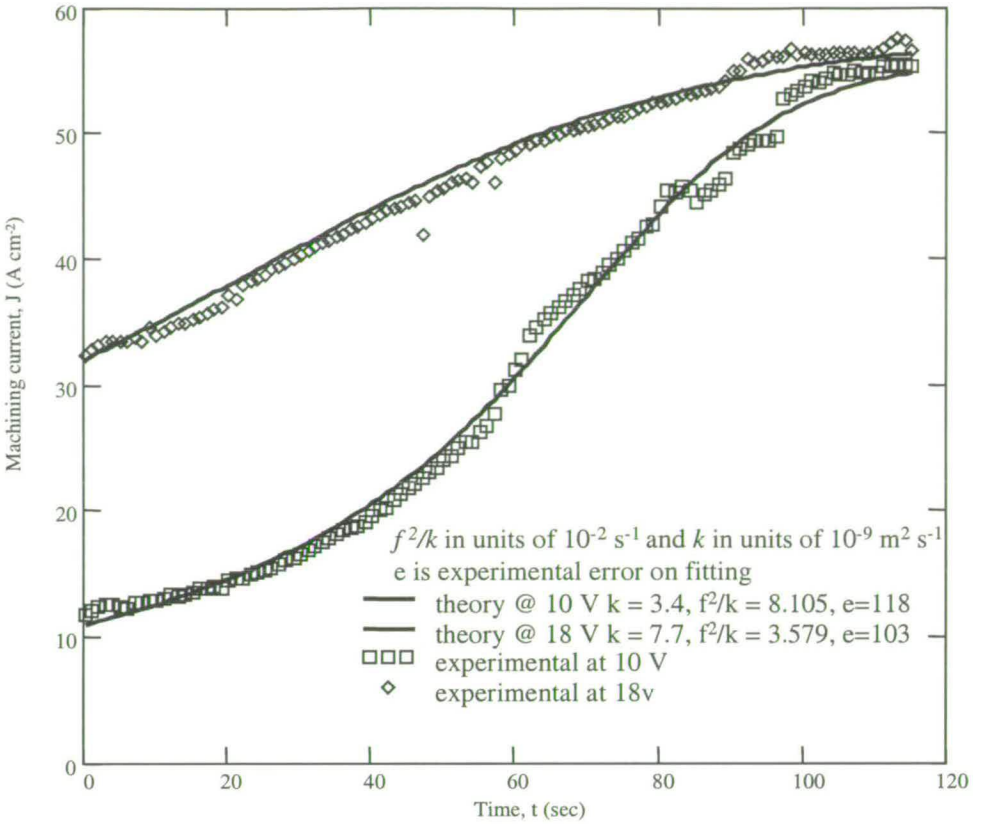

Figure 6.4-4: Current-time plot for titanium 6-4 with chloride at 10 and 18 V

Plotting of J_0 (at 0.8mm initial gap) against V, in accordance with Equation 4.1-7, and also plotting k/f^2 against V, in accordance with Equation 2.2-9 and using the iterative fits to current-time data provides two independent values V_0 (from the V-axis intercept) and κ (from the gradient) for the titanium chloride system. This plot, shown in Figure 6.4-5, gives value of $V_0 = 5.4 \pm 0.1$ V and $\kappa = 20 \pm 1$ S m^{-1} for both the k/f^2 and J_0 plots. The equivalent analysis in the case of the Ti6_4/nitrate system (for details see [34] in Appendix A1) gives values of $V_0 = 9.8 \pm 0.1$ V and $\kappa = 20 \pm 1$ S m^{-1} for both the k/f^2 and J_0 plots. The close correlation is seen as a validation as to the applicability of current-time analysis to ECM parameterisation.

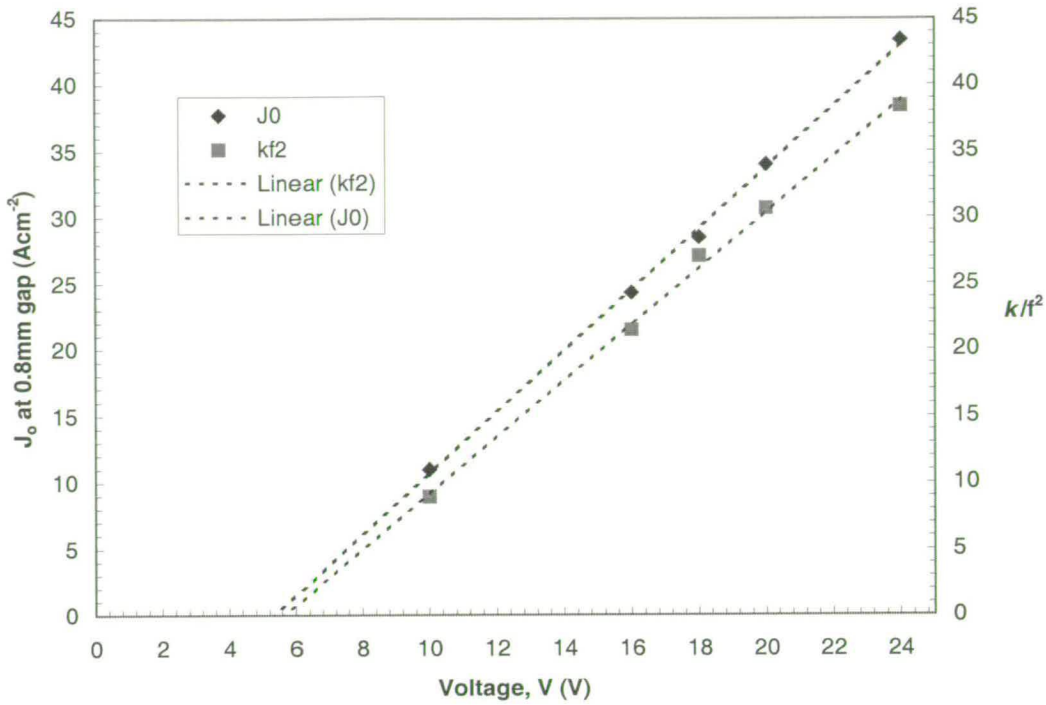

Figure 6.4-5: Plot of V against J_0 and k/f^2 for Ti6/4 chloride system at 1.0 mm/min feed rate

Considering now the case of In718/chloride and In718/nitrate systems. Figure 6.4-6 and Figure 6.4-7 show current-time data for the In718/chloride and In718/nitrate systems respectively. In the case of the In718/chloride system close correspondence between the theoretical and experimental data is noted with mean squared errors in the approximate region of those noted above for the titanium systems. However, in the case of In718/nitrate system the correlation between the theoretical fit and experimental data is not as close with mean squared error values of the order of several times of those found in previous fits (in the region 300 as compared to 100). It has also been observed that in the case of the In718/nitrate system two different groupings of current-time transient are seen to occur. That is, transient with fast rise times (low values of k/f^2) which reach an equilibrium current density of in the region of 78 Acm^2. This characteristic is exhibited by the 12V and 24 V current-time data as shown in Figure 6.4-7. Compared with transients exhibiting slow rise times (high values of k/f^2) which reach the lower equilibrium current density value of in the region of 70 Acm^2. This characteristic is exhibited by the 16 V current-time data as shown Figure 6.4-7. If data from the slow rise-time characteristic (for the In718 nitrate system) is considered separately together with the current-time data for the In718/chloride system then plotting k/f^2 and J_0 characteristics in the same form as for the Ti6/4 systems then values of $V_0 = 5.4 \pm 0.1$ V and 3.0 ± 0.1 V are obtained for the In718/nitrate and In718/chloride systems respectively. From the gradient of these plots the parameter κ is equal to 20 ± 1 S m^{-1} for both systems. The details of this analysis is given in a Figure 9 in publication [34] appended in Appendix A1. The valency of dissolution can be calculated

for the In718 systems from J_∞ using Equation 2.2-3, with ρ(In718) = 8.228 g cm^{-3} and M = 59.79 g mol^{-1} (from data in Appendix A5), to give values of n = 3.2 for both the In718/nitrate (slow-transient data only) and In718/chloride systems.

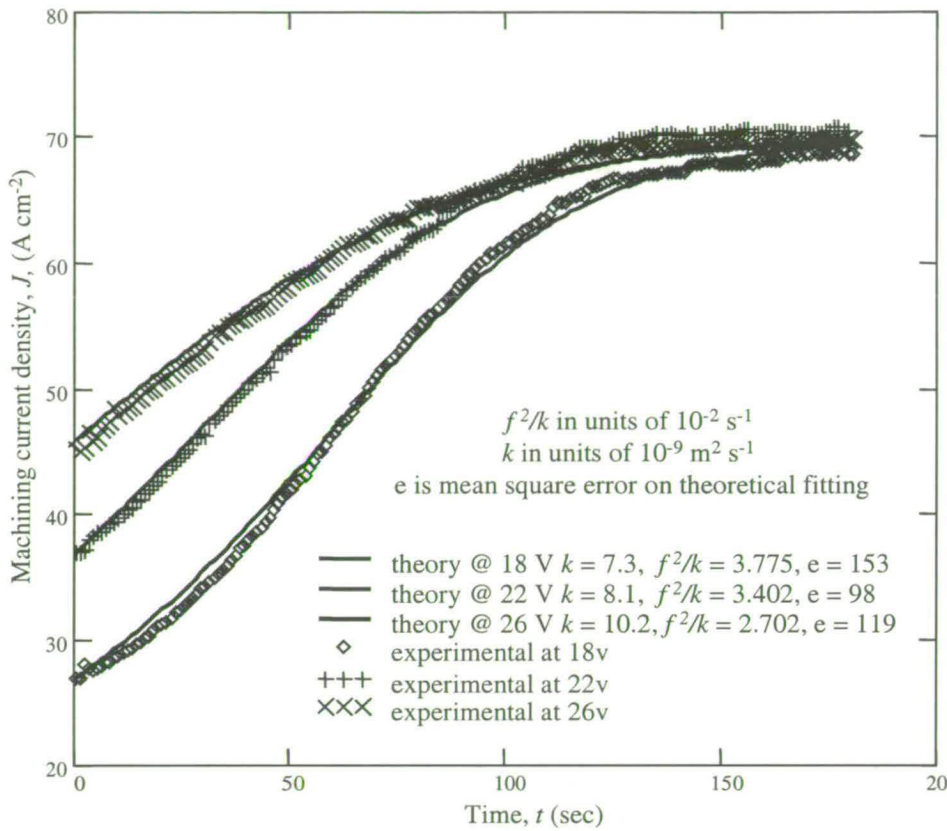

Figure 6.4-6: Current-time plot for In718 with chloride at 18, 22 and 26 V

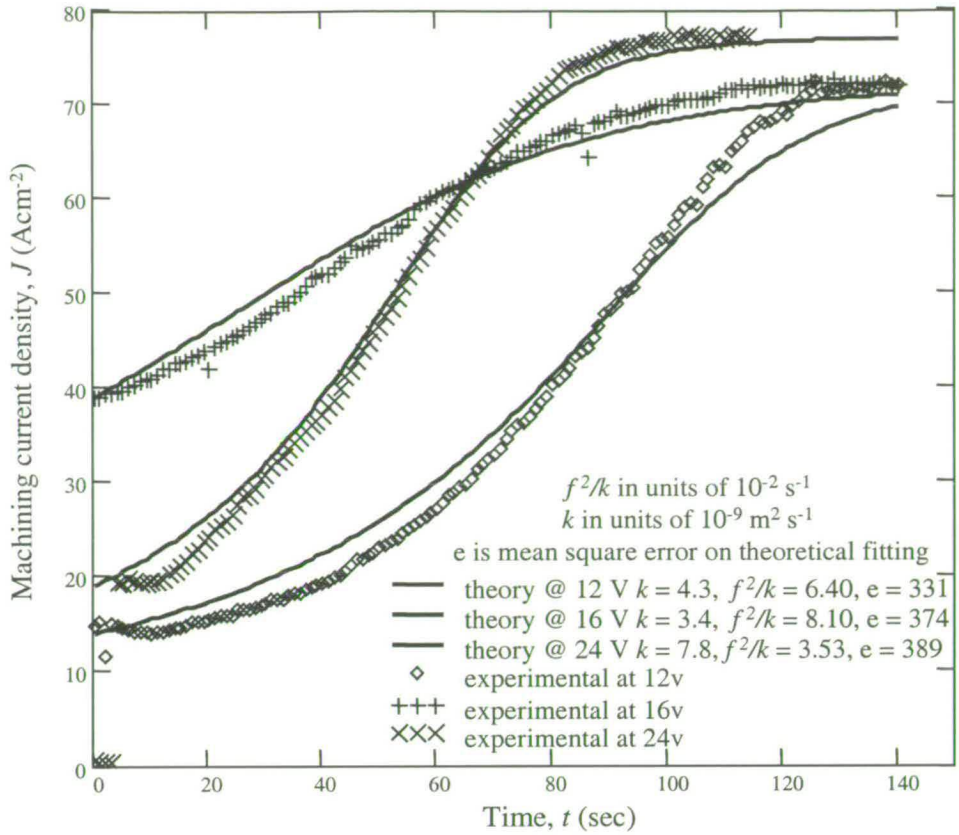

Figure 6.4-7: Current-time plot for In718 with nitrate at 12, 16, and 24 V

The fast rise-time (higher equilibrium current) characteristic observed in some cases when machining the In718/nitrate system was a phenomenon that was not noted when machining any other system. This characteristic could not initially be correlated with any set process parameters. However, it was realised that a correlation may have existed between the occurrence of this phenomenon and the machining conditions that had been present during the previous machining run. In particular it was noted that this phenomenon appeared to occur in the case when a trial had been carried out on a specimen which had previously been machined at a lower voltage. Although most of the trials were carried out starting at a higher voltage and incrementing the voltage downwards between trials, in a few cases, usually when checking data from a previous trial, the reverse was done. Thus occasionally the voltage increment between trials, when using the same specimen, would be from a low voltage to a high voltage. Although this was the case when machining all systems, it was only in the case of In718/nitrate system that this change in the ECM dynamic was noted.

In order to confirm and examine whether this characteristic could be correlated to the direction of voltage transition, a further trial was carried out on the In718/nitrate system. In this trial, machining was initiated with V set to 16 V and with an initial gap set to equilibrium conditions for the case of V = 16 V (i.e. $z_\infty = 0.27$). For this condition equilibrium conditions occurred from the initiation of the

trial. The voltage was incremented upwards to 24 V in intervals of 4 volts with equilibrium conditions being established between each increment of voltage. Once equilibrium was established at 24 V the direction of voltage increments was then reversed back down to 16 volts and then back up again to 24 V. The change in current density profiles were recorded together with the voltage data as shown in Figure 6.4-8. Note that in this figure the voltage increments are shown to change via a ramp profile. Such ramping occurs as a result of the 10 point average that is applied to remove the three phase ripple from the voltage signal. The actual voltage change was carried out in a discrete fashion so that voltage increments are made to within one sample interval.

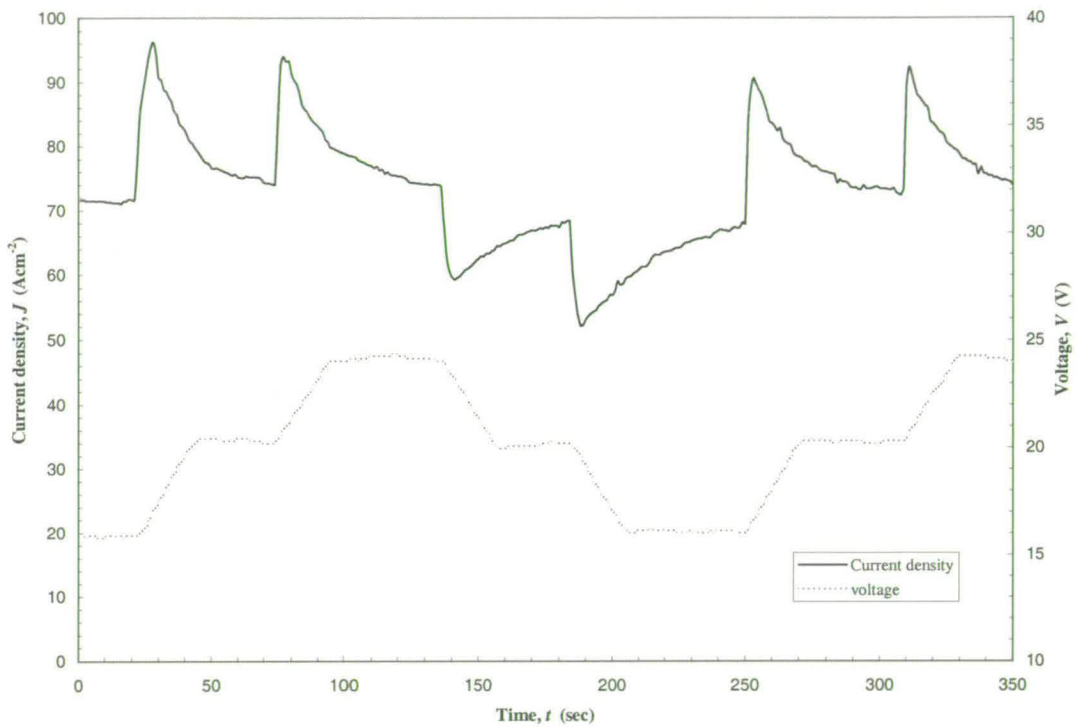

Figure 6.4-8: Hysteresis phenomenon occurring in In718/nitrate system for bi-directional voltage sweep giving k/f^2 in the range of 1.84 to 1.96 and 2.31 to 2.45 x $10^{-9}m^2sec^{-1}$ for the low to high transitions and high to low transitions respectively

With a reference to Figure 6.4-8 it can be seen that two distinct current transient forms occur; one that reaches a higher equilibrium current as low to high voltage transitions are made and one that achieves a lower equilibrium current as high to low transitions are made. According to Equation 4.1-7 with the assumption of constant V_0, κ and n, then it would be expected that equal current rise-time or decay-time constants would be obtained for equal intervals of voltage change, irrespective of the increment direction. However for the data shown in Figure 6.4-8 values of rise-time/decay-time constants (k/f^2 values) are in the range of 1.84 to 1.96 and 2.31 to 2.45 x $10^{-9}m^2sec^{-1}$ for the low to high transitions and high to low transitions respectively. By taking an average, k/f^2 values are seen to increase by about 26% when the direction of voltage transition reverses from a low to high to a high to low transition (see voltage data in Figure 6.4-8). As far as the author is aware the occurrence of

such a phenomenon has not been previously noted in the ECM literature. As an analogy to known directional phenomenon that occur within the field magnetism this phenomena is given the term *electrochemical hysteresis.*

A shift in k/f^2 values which occur during *hysteresis* will result in a change in n (indicated by a change in the value of J_∞ at constant f according to Equation 2.2-3) and also a possible change in either V_0 or κ (according to Equation 2.2-9). It seems likely, however, that changes in stoichiometry resulting in a variation in n would be associated with changes in chemical species at the surface of the anode and that this change would result in variations in V_0 and not κ. Further detailed analysis of the *hysteresis* phenomenon is considered beyond the scope of this thesis. This aspect of the work is now being pursued further using detailed chemical analysis, by Howarth [16].

Considering now the TiAl/chloride and TiAl/perchlorate systems. Figure 6.4-9 and Figure 6.4-10 show representative current-time data and the iterative fit to these data for the machining of TiAl in chloride and perchlorate electrolytes respectively.

In a case of the data for the TiAl/perchlorate system, shown in Figure 6.4-10, it is clear that good theoretical fits are obtained. From these data a constant a value of J_∞ of 37±0.5 A cm^{-2} is obtained. Using measured values for ρ(TiAl) of 3.90 g cm^{-3} and M = 37.45 g mol^{-1} gives n = 2.4±0.1. By plotting J_0 and k/f^2 against V as shown in Figure 10 in [77] as appended in Appendix A1 (the equivalent plot as that shown in Figure 6.4-5 for the case of the Ti6-4/chloride system) then independent values can be found for both V_0 (from the V-axis intercept) and κ (from the gradient). These are: $V_0 = 3.8\pm0.1$ V and $\kappa = 0.13\pm0.01$ S cm^{-1}.

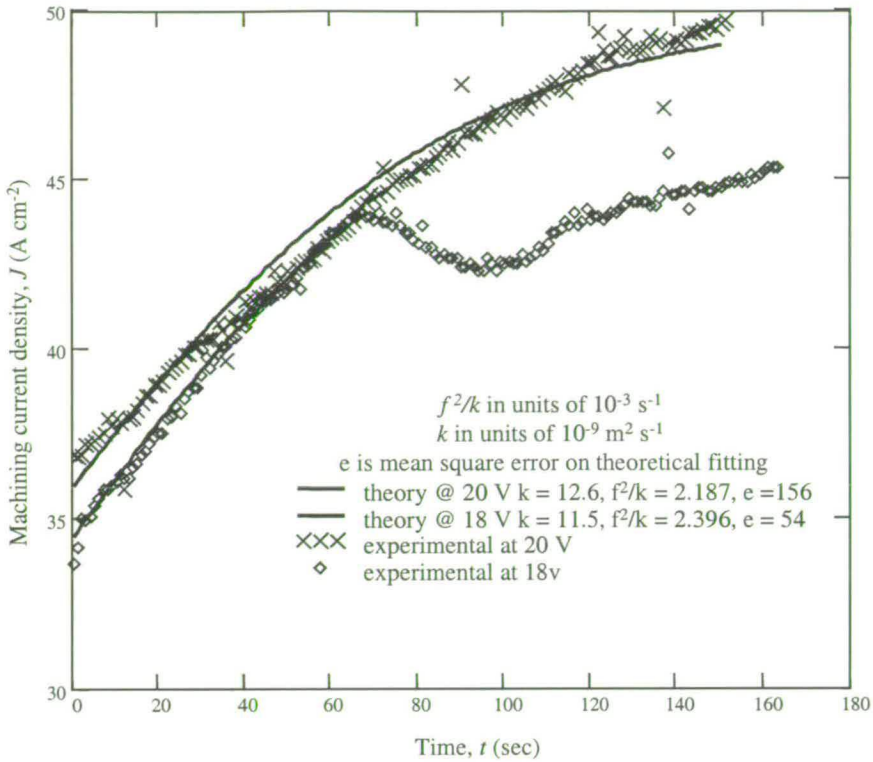

Figure 6.4-9: Current-time plot for titanium aluminide with chloride at 10 and 18 V

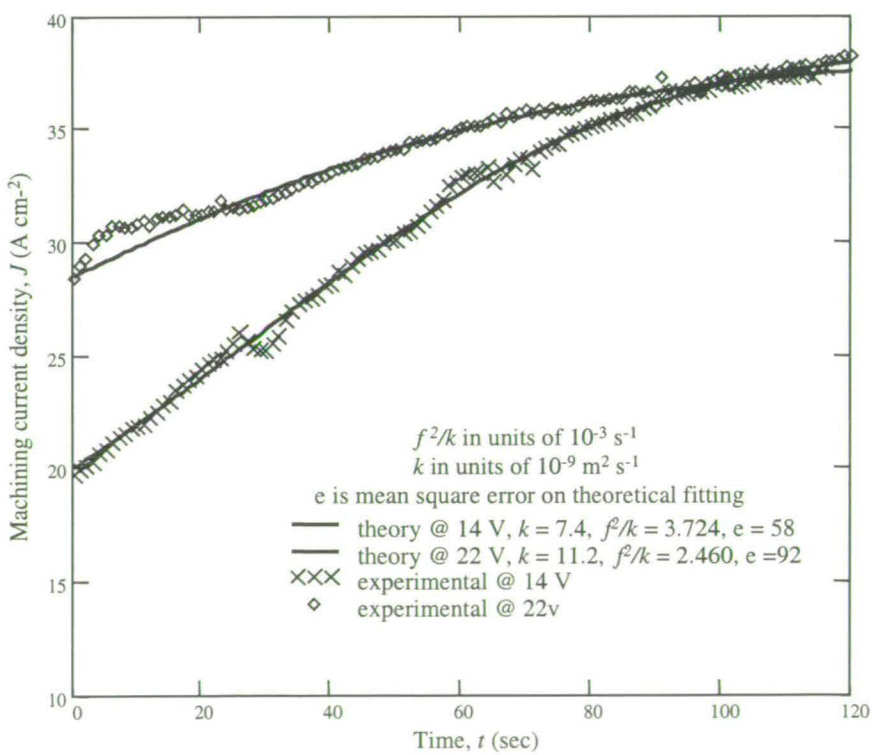

Figure 6.4-10: Current-time plot for titanium aluminide with perchlorate at 14 and 22 V

With regard to the data for the TiAl/chloride system, shown in Figure 6.4-9, two forms of current-time data are shown. One transient, at 20 V, showing the current density progressively increasing to equilibrium, and the other, at 18 V, exhibiting a rise and then a sharp decrease in the current-time gradient. It is clear that an iterative fit to this latter data using Equation 4.1-7 will produce a very poor fit. It was found that this pattern was repeated for machining voltage of 18 V and below. The change in slope of the low voltage current-time data can be seen as indicating some change in the machining process at this time for example, due to passivation (the formation of an anodic insulating oxide layer) on the surface of TiAl which impedes further dissolution from occurring. When machining is terminated after the fall off in the current value and the surface of the TiAl is examined, a grey white adherence can be seen on the machined surface (see Figure 12 in [77] as appended in Appendix A1). However, assuming that stable dissolution is occurring prior to the break point then fitting of this initial portion of current-time data should produce reasonable fits to Equation 4.1-7. This has been done for the 18 V data shown in Figure 6.4-9. For the data produced at 20 V the full data set has been iteratively fitted to produce the f^2/k time constant as shown. It is noted for this data that the current-time data appears initially to fall in gradient towards the profile of the 18 V data but then recovers and continues upwards. It can be concluded that the passivation phenomenon is quasi-stable at around the transition interval of 18 to 20V. Current-time data above 20 volts exhibited closer fits to the theoretical solution. Plotting I_0 and f^2/k values against V for all the high voltage data and using the early portion of the data at lower voltages (i.e. prior to the passivation occurrence) then values of $V_0 = 4.3 \pm 0.1$ V and $\kappa = 0.319 \pm 0.01$ S cm^{-1} are obtained (see figure 6 in [77] as appended in Appendix A1).

Comparing characteristics between the TiAl/chloride system and TiAl/perchlorate system it becomes apparent that the significant reduction in valency and associated changes in overpotential states can be associated with an extended regime of dissolution stability in the case of the TiAl/ perchlorate system. This variation in chemical stoichiometry can be further analysed by examining dissolution characteristics between the phases of TiAl, namely: γ-TiAl (about 90 vol. %) by volume and the Ti_3Al α-2 phase (about 10 vol. %). This analysis (for details see [77] appended in Appendix A1) shows that observed differences in dissolution characteristics between the phases could arise from the differences in proportion of Ti and Al in these phases. It is suggested that this difference gives rise to changes in the overpotential for dissolution at the surface of these phases. If this was the case, then resulting variations in the machining gap (according to Equation 2.2-5) could be correlated to height variations on the surface of the materials over each phase (this would be a form of cross colony attack). The existence of these variations has been confirmed using optical interferometry plots of these surfaces. In contrast, the equivalent analysis for the TiAl/perchlorate system has indicated that both Ti and Al species dissolve with a valency of three and with an increased mean overpotential. In this case, there is less difference between dissolution characteristics between the phases. The resultant smaller height differences from the interferometry plots confirms this (for

details see [77]). This form of electrolyte sensitive surface effect is not observed for any other system in this investigation. Although, other authors, for example [80], have reported surface finish dependencies with electrolyte concentration and current density, in the case of the TiAl system, significant changes in surface properties are indicated with dependency upon the electrolyte composition. Such reports are not common in the ECM literature. In particular, correlation as to the level of cross grain attack and the electrolyte composition, as far as its author is aware, have not been previously reported in the ECM literature.

For ease of reference, a summary of all the fundamental machining parameters as obtained from the current-time analysis for all six machining systems are given in Table 2.

Machining system	J_∞ @ f=**1.00 mm/min (A cm^{-2}) ±0.5**	**V_0 (V) ±0.2**	**κ (S cm^{-1}) ±0.01**	**n ±0.1**
In718/nitrate	71.0 , 78.0	5.4	0.20	3.2
In718/chloride	71.0	3.0	0.20	3.2
Ti6/4/nitrate	53.5	9.8	0.20	3.4
Ti6/4chloride	57.5	5.4	0.20	3.6
TiAl/chloride	45.0	4.3	0.22	3.0
TiAl/Perchlorate	37.5	3.8	0.13	2.4

Table 2 : Summary of machining system parameters obtained using current-time, and static data from planar characterisation trials

6.4.2 Segmented trials

The segmented tooling configuration (shown in Figure 6.3-1) was employed to test the sensitivity of characterisation data to variations in certain flow characteristics. Most of the phenomena that have usually been associated as flow velocity effects in ECM, such as the increase in resistivity resulting from void fraction build up, have been reported (see section 3.1) to occur as flow velocities are decreased relative to nominal values (i.e. below 30 m s^{-1}). Before examining these lower flow velocity effects however an initial trial was carried out in order to check if there were any measurable effect with increasing flow velocities. These tests have been carried out using a constant volumetric flow rate with a sloping gap as the initial conditions. The gap therefore has a taper such that the gap decreases and therefore the flow velocity increases from the inlet to the outlet position. This configuration enables the sensitivity of the parameter, k, to be mapped in relation to varying flow velocity (at constant flow volume) at a range of current densities, which will vary in different

portions as equilibrium is established. If the parameter k is insensitive to both increasing flow velocity and current density then k/f^2 time constants for each segment will be constant. This technique has also enabled the values of one of parameters of either k or V_0 to be obtained in a way which does not involve repeated trials as has previously been the case using the methods as described above.

In a second series of tests, the gap is initially parallel at equilibrium conditions and the flow volume and therefore flow velocity is ramped downwards. In this case, flow effects can be examined for conditions of equal current density with sensitivities in k producing changes in equilibrium gap width as would be expected in cases where the gap resistivity rises towards the end of the flow field (as discussed in section 3.1).

6.4.2.1 Results and discussion (segmented trials)

In the trials for the case of an initial slopping gap, the gap at the inlet was set at 0.80mm (at the centre of segment 2), with a slope of 0.16 between each segment such that gap at segments 6 is 0.54mm. The flow volume was set at 20 l/min; the upper limit of volumetric flow rate used throughout all trials. Thus the velocity of the electrolyte at the position of segment 2 can be calculated from the cross-sectional area as 35 m s^{-1}. This velocity will ramp up to 52 m s^{-1} at segment 6. These conditions have been chosen so as to represent the typical upper range of flow velocities encountered in ECM. Figure 6.3-1 shows current-time data recorded for the case of an In718/chloride system. This system was chosen since previous data had exhibited a close fit to the theoretical solution indicating stability in parameters. Any instability, which for example is known to occur when machining the In718/nitrate system would produce possible ambiguity in the result of this trial. The data is shown only for segments 2 to 6. This is because data from the edge segment (segment 1 and 7) would not be consistent with the data from the central segments for reasons as explained above in section 6.3. Iterative fits have been computed for current-time data from each of the segments. These fits give time constants values, f^2/k, in the range of 4.15 $\pm$0.01 x10^{-2} s^{-1} for all of the segment data. This indicates that dissolution characteristic for the In718/chloride system are constant and not sensitive to the range of upper flow velocities used in this trial.

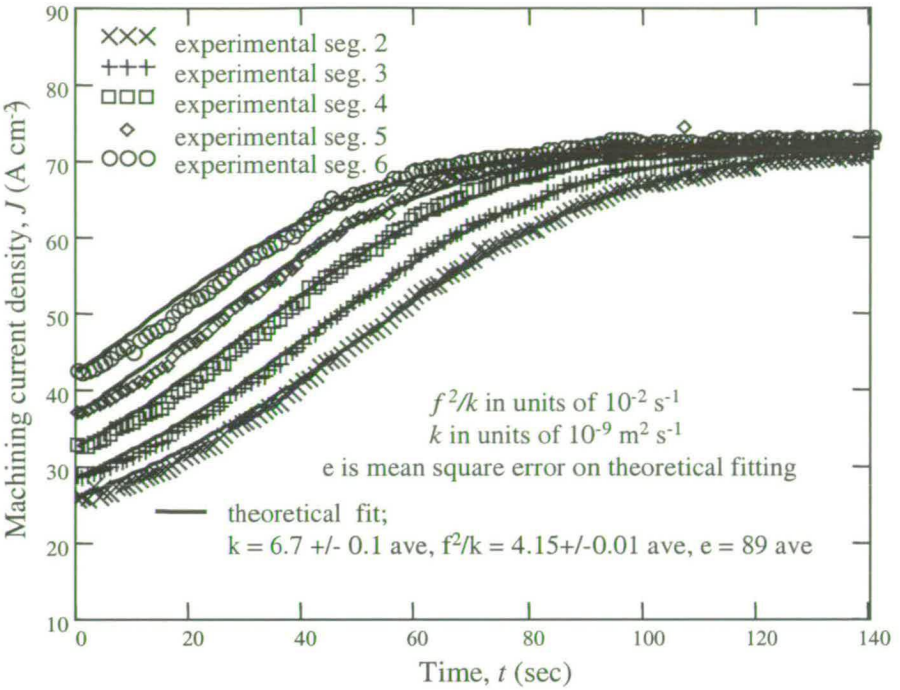

Figure 6.4-11:In 718 with chloride at 16 V gaps from seg 2 to seg 6 off 0.8, 0.73, 0.67, 0.60, 0.54 mm respectively

The data from this trial can also be used to determine the electrolyte conductivity, κ, with the assumption that V_0 is constant over these conditions. This seems reasonable since the closeness of fit of Equation 4.1-7 has already indicated that the parameter k (and hence V_0) is stable for this system. κ can be obtained by plotting J_0, against the reciprocal of z_0 for each of the segments. This gives a gradient of $\kappa(V-V_0)$ according to Equation 2.2-4, as follows;

$$J_0 = \frac{\kappa(V - V_0)}{z_0}$$

This relationship is shown plotted in Figure 6.4-12 corresponding to the data shown in Figure 6.4-11. From the gradient of this plot (273 A m^{-1}) and using a value of V_0 for the In718/chloride system (from Table 2) of 3.0 V and for V = 16 V, gives a value of κ of 21 ±1 S m^{-1}. This is in good agreement (within experimental error) of both the static and the current-time technique (see data in Table 2) values as previously obtained. Thus this arrangement has been shown to be effective for obtaining conductivity values using instantaneous measurement (i.e. only one sample interval at the initial conditions of the trial), thus avoiding the need for repeated trials as was previously the case.

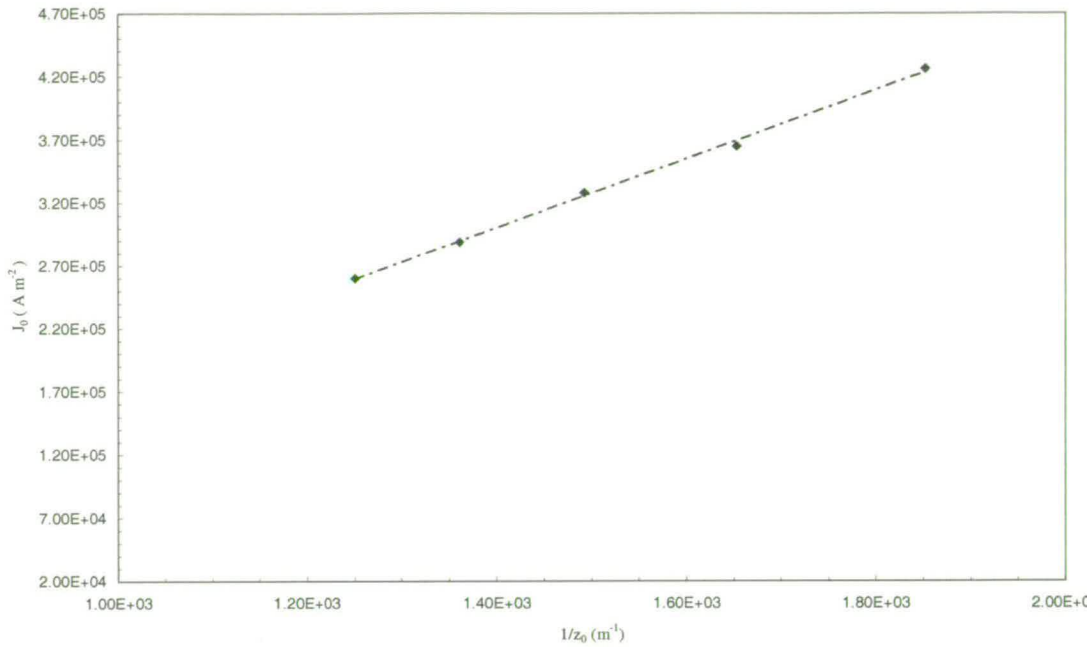

Figure 6.4-12: Plot of J_0 against $1/z_0$ for data shown in Figure 6.4-11 gives gradient of 273 A m^{-1} which at 16 V and V_0 = 3.0 V give a value of κ of 21 S m^{-1}

Considering now the trials carried out over a decreasing range of flow velocities. These trials were carried out using the four systems; Ti6-4/chloride, Ti6-4/nitrate, In718/nitrate and the In718/nitrate system. These trials have been carried out with the machining voltage fixed and set at 20 V and with the flow volume decremented downwards in fixed intervals from a maximum of 20 l/min, until conditions occur in which changes in segment currents indicate significant changes in process dynamics.

Comparing first the data for the Ti6-4/chloride and Ti6-4/nitrate systems as shown in Figure 6.4-13 and Figure 6.4-14. In the case of the Ti6_4/chloride system each decrement in flow volume produces an overall reduction in segment currents followed by a recovery back to the previous value of equilibrium current. The amount of change increases as the flow volume decreases until, once the flow volume reaches a value of 8 l/min, the fall off in the current value is seen to separate significantly between each of the segments. The fall off in current density at this condition is seen to be greatest at the far end of the flow field (segment seven) and decreasing, so that the effect is less pronounced towards the inlet end of the flow field (segment one). This general trend indicates that the parameter k is sensitive to changes in the flow volume causing a change in either or both κ and V_0 (it seems reasonable to assume that n is constant since equilibrium conditions are restored). The system returns to the same equilibrium current because the gap size adjusts so that the volumetric removal rate will match the feed rate, irrespective of the value of k according to Equation 2.2-10. The separation of segments current, occurring at 8 l/min, indicates the spatial sensitivity in k along

the flow axis. In this case the recovery to equilibrium conditions will produce a gap taper in which the gap is smaller at the outlet (indicated by the largest current change, and therefore largest change in k, occurring at segment seven). These geometric considerations are to be considered in detail in Chapter 8.

Now referring to the equivalent experiment carried out for the Ti6-4/nitrate system. Reductions on the flow rate from 20l/min down to 8 l/min produced no measurable change in current density. Thus in comparison with the Ti6-4/chloride system, the parameter k, was not observed to be sensitive to flow volume. As the flow rate is reduced further to 6 l/min a fall off in current on all the segments is noted. The magnitude of fall-off been greater at the outlet than the inlet. Unlike in the case of the Ti6_4/chloride systems, the segment currents do not recover to equilibrium. This characteristic, given the term *choking*, can be considered as indicating the limit of stable dissolution and not as a discrete change in the parameter k (in this case the recovery to equilibrium conditions would occur). *Choking* indicates a breakdown in the dissolution process. Such a breakdown probably occurs because at very low flow rates the build-up of dissolution products within the gap reaches sufficient levels so as to significantly impede the electrolysis current. As this current falls-off, and the gap decreases as a consequence, the relative proportion of the products within the gap increases further thereby further increasing the impedance. This model is indicated in the data by the rapid fall off in current that results and also by the fact that this current fall-off is at its steepest at the far end of the flow field where the accumulation of products would be greatest.

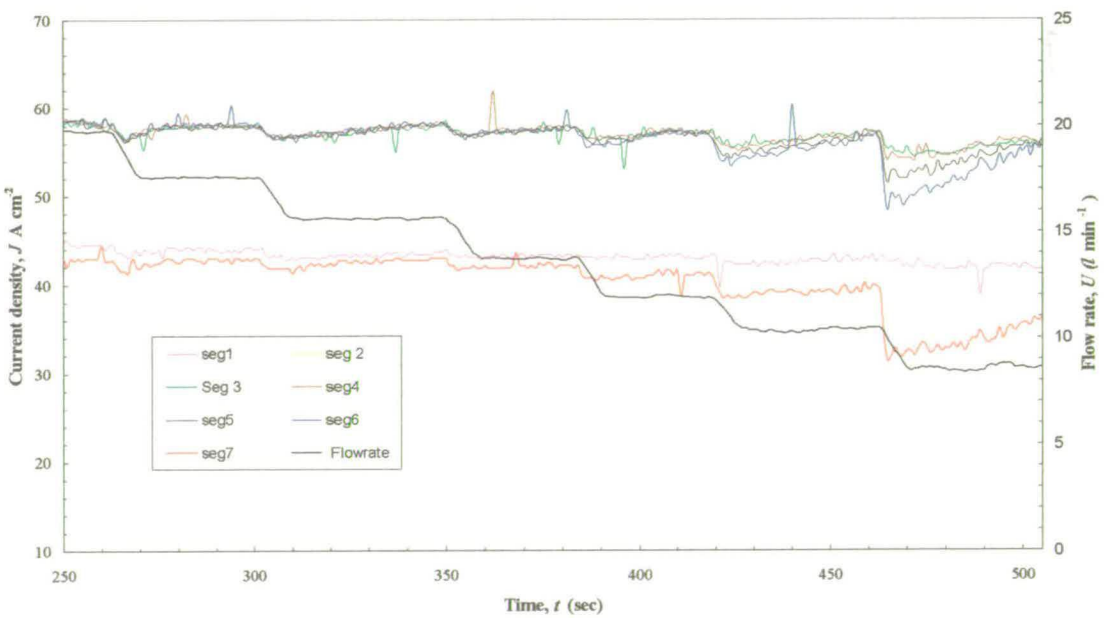

Figure 6.4-13: Segment currents for varying flow rate for Ti6-4 with chloride at 20V

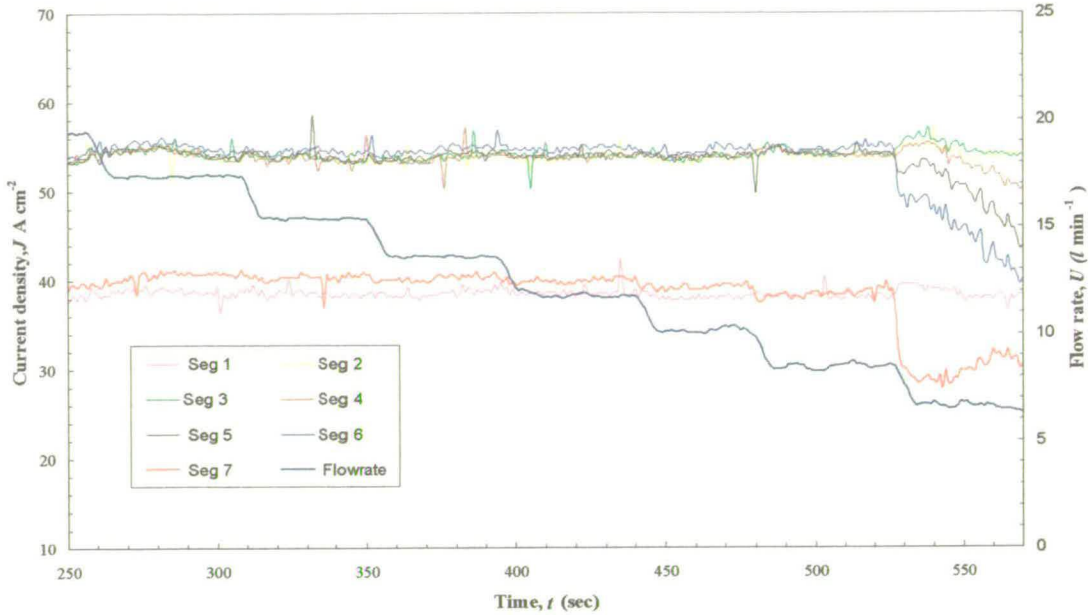

Figure 6.4-14: Segment currents for varying flow rate for Ti6/4 in nitrate at 20 V

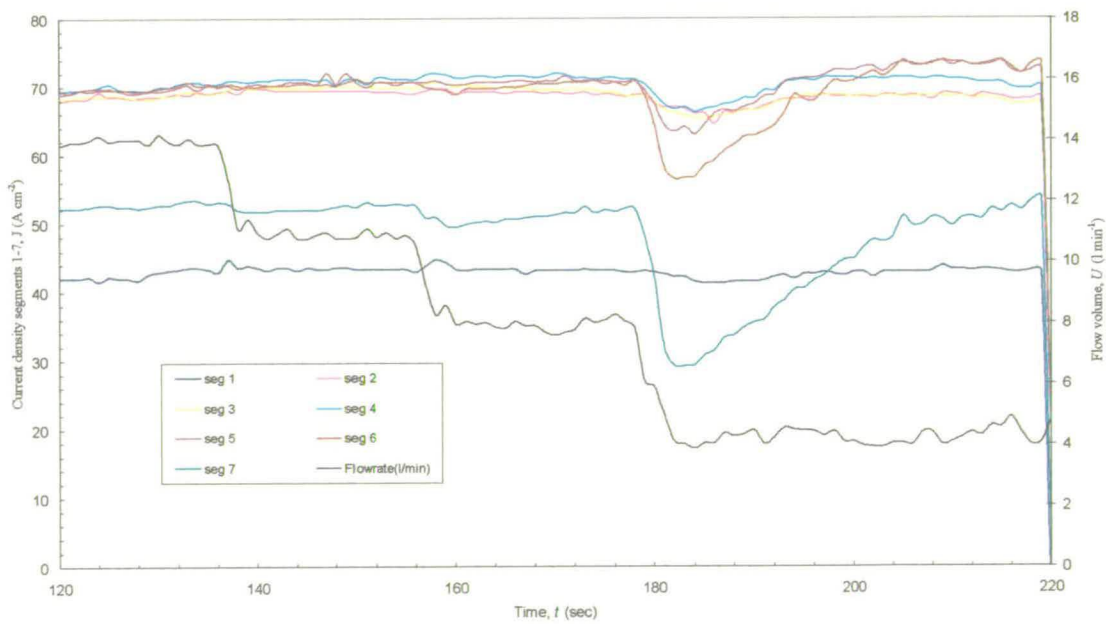

Figure 6.4-15:Segment currents for varying flow rate with In718 with chloride at 20 V

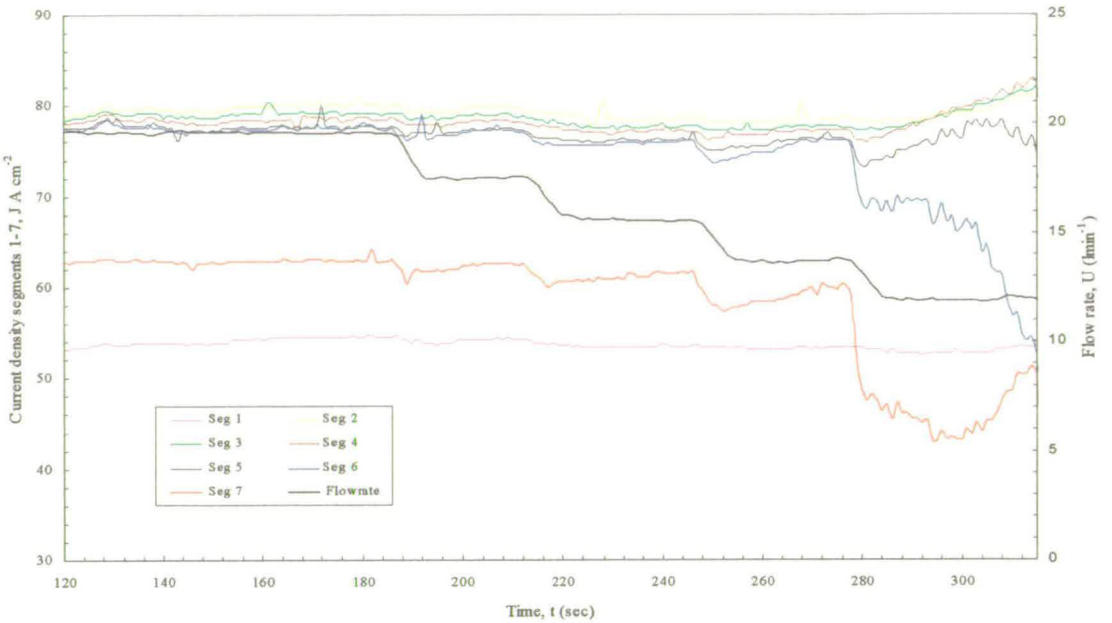

Figure 6.4-16:Segment currents for varying flow rate with In718 in nitrate at 20 V

The segmented data for In718/chloride system and In718/nitrate system are shown in Figure 6.4-15 and Figure 6.4-16 respectively. As the flow rate is reduced from 12 to 8 l/min in the case of the In718/chloride system, a small change in the value of k is noted in cases of the end segments (seven and six). As the flow is reduced further down to 4 l/min a more significant transition occurs as with that obtained for the Ti6-4/chloride system (Figure 6.4-3), although in this case the recovery is to a slightly higher equilibrium current for the end three segments. As the flow rate is reduced from 14 to 12 l/min in the case of In718/nitrate system, a combination of choking (segments six and seven) and changes in the parameter k, as indicated by a recovery to equilibrium (segments two to five), is observed. The transition in this case is occurring at a higher flow velocity than the other systems investigated and also the recovery reaches a significantly higher equilibrium current. Thus a higher valency state is reached after the perturbation in k *occurs*. It is interesting to note that this characteristic may be associated with the *hysteresis* phenomenon which had previously been noted when machining the same system (Figure 6.4-8). Although in this previous case, the phenomena was associated with directional changes in voltage state relative to previous voltage states, it may be the case that since a reduction in flow rate produces an increase in resistivity and therefore a transient deviation to the potential gradient. It could therefore be the case that the transitional state observed in Figure 6.4-16 has a similar stoichiometric mechanism to that observed in Figure 6.4-8.

Further detailed trials will be required to investigate this. This is however considered as beyond the scope of this present investigation but will be included as part of the work of Howarth [16].

6.5 Chapter conclusions and overview

These trials are have confirmed the usefulness of both current-time analysis and the segmented tooling array applied to the resolution of ECM system dependencies. For the selected machining systems studied a complex series of process interdependence has been revealed. A general summary of these interdependencies follows:

- **General sensitivity of *k* *(i.e. for any one machining system without flow variation):*** throughout the parameter range of each trial the general sensitivity of *k* has been established by the closeness of fit of current-time data to the theoretical model. Mean squared errors were small for most systems, particularly In718 in chloride, indicating stability in the parameter *k*. In the case of the In718 in nitrate system the theoretical fit exhibited in a poor fit resulting in a relatively high mean squared error indicating a drift in the parameter *k*.

- **Sensitivity of *k* (due to changes in *n* and V_0) with electrolyte:** This has occurred for both, Ti6/4 with chloride and nitrate electrolytes, and also TiAl with chloride and perchlorate electrolytes. In the TiAl system these sensitivities could also be associated with different dissolution characteristics between the two phases in the material. In addition, the analysis has indicated that low valency/low overpotential states in the case of the TiAl/perchlorate system can be associated with an extension to the range of dissolution stability (i.e. the parameter range over which passivation will not occur).

- **Sensitivity of k (due to changes in *n* and V_0) with a dependency upon initial conditions (*hysteresis*):** This has been noted only in the case when machining the In718/nitrate system. The sensitivity was correlated to initial voltage conditions and also associated with changes in flow velocities.

- **Sensitivity of *k* (due to changes in flow velocity):** Increasing the flow velocity above the nominal value of 16 l/min has revealed no dissolution sensitivities. Decrease in the flow velocity below this range has shown, as would be expected from the work of others (as described in section 3.1), that an apparent increase in electrolyte resistivity occurs which is increasingly pronounced towards the far end of the flow field. The characteristic of this sensitivity has been shown to have different forms between different machining systems. Some exhibiting a continuous relationship between the flow volume and the transition in gap resistivity (Ti6-4/chloride), and others exhibiting no significant decay in resistivity up until the onset of choking (Ti6-4/nitrate). This varying characteristic is not readily accounted for by

previous work (section 3.1) where simple exponent decays in resistivity have been suggested (see Equation 3.1-10 for example).

Through the application of current-time analysis and the development of the segmented characterisation system, the work here has extended the methodology by which parameter mapping can be obtained in situations applicable to ECM systems. The range of parameter independence identified provides general confirmation, as indicated by other workers, as to the importance of requiring a detailed parameters mapping for any one ECM system. The characterisation methodology applied in this chapter is limited to providing only averaged values of the parameter k over a pre-defined range of process variables (particularly current density). As pointed out in section 4.3, a more detailed examination of these dependencies, and the resolution of such dependencies in terms of a single variable, the C-function, can only be realised if gap-time data can be recorded at the same time as current-time data. To achieve this in line active measurement of the ECM gap will be required. This is the subject of the next chapter.

CHAPTER:

7 The development of a system for in-line measurement of the ECM gap

---

This chapter describes the development of a novel technique in which ultrasound is employed to provide a direct in line measurement of the ECM gap. As discussed in section 4.3, the realisation of such a measurement would enable the direct resolution and correlation of fundamental ECM parameters. Furthermore by providing gap-time data, such a technique would enable the direct generation of the system C-functions (see section 4.3). The work of this chapter together with some additional information on the usage of the ultrasonic gap measurement technique is given in the appended publications by Clifton et al. [81].

7.1 Introduction and background

Throughout the literature there many examples where workers have undertaken measurement of the ECM gap. In most of these cases, however, these measurements were made only after interruption or termination of the dissolution process. For example, Hopenfeld and Cole [28] carried out measurements on the ECM gap using a travelling microscope directed into the gap through a glass plate. Such a technique would not be able to make measurements during dissolution where the high inhomogeneity of the two phase flow field would obscure the view prohibiting accurate determination of the tool and workpiece edges. Although it maybe the case that careful positioning of lighting sources could overcome this problem, it was realised that for the case of continuous measurement of gap time data then tracking of the movement of the workpiece surface as it erodes would be required. One way to achieve this automatically would be to connect the microscope to a high resolution traversing table controlled by an image which had been processed for edge detection. After some consideration the development of such a technique was considered as being too ambitious and unlikely to be successful.

There are many options of "physical contact" techniques that can be considered for gap measurement. The simplest of these would involve introducing some sort of physical media into the IEG, such as some sort of mechanical contact probe. Such a mechanism could be introduced into the gap, by passing through the tool surface to make contact with the workpiece surface, at predetermined time intervals. This sort of technique was used to generate gap-time data by [38]. Although in this case the technique was only developed as a manual technique for gap measurements after interruption of the process. Adapting such a technique for automated use would involve the use of a displacement transducers/force sensor arrangement so that gap readings could be automatically generated. After some consideration, however, it was decided that such techniques would be unacceptable since it was considered that the introduction of a probe when dissolution was active would cause possible instability in the ECM process. This instability arises since any initial flow disturbance, causing a local retarding or termination of dissolution, will result in the initiation of a small raised area on the workpiece surface. Once formed this raised area will continue to disturb the flow pattern and thus dissolution stability will not be restored after removal of the probe (this was considered a potential problem in particular is machining titanium alloys where surface oxide formation is known to be highly sensitive to flow disturbances). It was therefore considered that physical contact methods of gap sensors could not be readily applied with sufficient flexibility. Developments of intrusive methods of gap sensors were therefore not considered further.

One technique by which it was envisaged of achieving non-intrusive gap sensing was by monitoring of the pressure drop along the length of the flow channel (the IEG). Under ideal conditions, this measurement together with the measurement of the flow volume would be an indication of the gap

cross-section from which the gap could be computed. However such measurements would be subject to certain ambiguities. For example, both temperature and void fraction distribution could affect the pressure drop measured for the same gap and flow velocity. For example, trials have shown that the pressure drop along a 40 mm flow path increases by 1 Bar when the dissolution power is turned on. This pressure increase is attributed to the formation of hydrogen at the cathode that produces an overall increase in the ambient pressure along the gap. Thus pressure drop data is not exclusively dependent only upon the dimension of the gap. Although these effects could be calculated their existence could produce uncertainties in certain cases (if for example the volume of hydrogen being produced was not known) and therefore this method of gap measurement was not pursued further. A more direct, less ambiguous, method of gap measurement was sought.

A method that has been suggested by Ing *et al* [82] as a means of in-line measurement of the ECM gap, is through application of eddy currents. Ing *et al.* suggest, and to some extent have demonstrated, that induced eddy currents, circulating in the workpiece, resulting from an emitting coil embedded in the tool, provide accurate gap measurements. Although Ing *et al.* report that their method can be accurate to ±0.02 mm, they do point out that the technique is sensitive to certain process characteristics and parameters. For example, the material of the workpiece and the conductivity of the electrolyte can affect the measurement. This latter factor would be a particular problem in the application being considered here, since gap variations due to changes in electrolyte conductivity need to be measured. This technique would therefore produce ambiguities in the application being considered here. Also, there was concern as to possible interference problems (or high levels of electrical noise) when attempting to apply such a technique in ECM. The primary concern was, since both workpiece and tool are subject to field variations resulting from ripple in the applied machining voltage, then how would such factors affect the eddy current measurement. This point was not addressed in detail by Ing *et al.*

As an alternative to the use of eddy currents, it was envisaged that ultrasound could be applied to gap measurement. It was felt that ultrasound could be applied with minimal process interaction, and was hence considered to be more *passive*, in the ECM context, than the use of eddy currents. The use of the reflection of ultrasound applied to non-intrusive detection of interfaces within or between two different materials is well-established [83]. It was considered that the application of ultrasound to provide in-line gap measurement in ECM was worth pursuing further. The investigation/developments, as detailed in the following sections were therefore carried out.

7.2 Background; ultrasonic non-destructive measurement technology

A brief overview of directly relevant aspects of the application of ultrasonic measurement is now given. For further general information on the basic principles of the technology see Berk [83].

Ultrasound non-destructive measurement technology is based on the principle that sound energy will be partially reflected and partially transmitted when intercepting a discontinuity within the elastic properties of a material (commonly correlated to density discontinuities) or across the boundary of two joined materials. The most common implementation of this technology is in the detection and sizing of defects such as inclusions in welded sections. The technology is also applied to making thickness measurements. In this case measurement is made by the timing of the transmission delay of an ultrasound pulse between the two interfaces. Commonly these interfaces are the contact point of the ultrasound probe and a second surface where there exists an abrupt change in materials density. For example, the thickness of a surface coating can be readily measured by this technique. The technique can also be used to measure a thickness where the reflective surface is the interface between an inner wall and some other material (or just an air boundary on an internal surface).

An important factor with regard to the application being considered here will be how the sound energy is attenuated and reflected with dependence upon conditions at the reflecting and absorbing interfaces. Considering first attenuation characteristics for a sound beam travelling in a homogeneous material. As the sound energy passes through the material it will be attenuated in proportion to the length of the sound beam path resulting in both beam divergence and absorption. The degree by which the beam diverges, and therefore its attenuation at any one point along its path, will depend on the shape of the transmitting pizeo-electric crystal within the probe. Disc shaped crystals are often used to minimise this divergence. Energy absorption, which occurs due to internal friction within the material, will be dependent upon the transmission medium.

A second important factor concerns the parameters that determined the overall power of the reflected energy. This will depend not only upon the initial incident sound power at the interface (which is dependent on the attenuation factors as explained above), but also the ratio of the acoustic impedance across the discontinuity. Sound energy travelling from a medium with a high acoustic impedance, say steel with an acoustic impedance of 45.0 $x10^6$ kg m^{-2} s^{-1}, to water with a low acoustic impedance of 1.5 $x10^6$ kg m^{-2} s^{-1}, will be reflected with a low attenuation of 0.6 dB (for details of this calculation see [84]). Conversely, if sound energy is travelling from a medium with a low acoustic impedance to a medium with a high acoustic impedance, then reflections will be highly attenuated (in the case of transfer between water to steel this attenuation will be around 24 dB [84]). If applying ultrasound to measuring the ECM gap then reflections will be required from the interface between the electrolyte solution (with a low acoustic impedance) and at least one of the electrode surfaces (with a high acoustic impedance). Thus it would be expected that such a reflection would undergo significant attenuation.

The available ultrasonic distance/sizing technologies can be grouped into two distinct systems. The most basic of these options are generally grouped under the term; *thickness measurement systems* [84]. Such systems measure reflection timings using short sharply defined ultrasonic pulses and are

usually employed for simple measurements such as tolerancing, for example, the thickness of thin plate components. More sophisticated facilities are provided by the second group of ultrasonic measurement systems; *flaw detection systems.* Such technology, as well enabling the same facilities as thickness measurement, provide additional display and manipulation of the transmitted waveform and control over how the thickness is computer in relation to the shape of the received waveform. Such systems are usually employed for positioning and sizing of defects within welds and metal structures. Because of uncertainties about how the dissolution processes would affect the ultrasound, the more sophisticated flaw detection technology was employed so as to allow a detailed analysis of the reflected sound energy for this investigation.

After an extensive survey of the available technology a USPC2100[‡‡‡] flaw detection system was obtained. This system, with a claimed measurement resolution of 0.005mm, appeared to be the most advanced of all the options. In addition to providing a very high measurement resolution, the system also provides a multi-channel upgrade that enables measurements to be made at several points in parallel. It was envisaged that this facility would be deployed in later stages of the work when applied to the measurement of distributed C-functions (Chapter 8).

The probe selected was a CLF4 (Buehler Krautkramer Ltd) piezoelectric / perspex delayline system operating at a frequency of 15 MHz. This probe has a disc shaped transmitting crystal to minimise beam divergence. The probe is configured to operate in *pulse-echo mode*[§§§] with a pulse repetition frequency of 500 Hz. The perspex delay line acts as an interface between the probe face and the surface through which detection is required.

7.3 The application of ultrasound to ECM gap measurement

A search through the literature provided no examples of the use of ultrasound applied to gap measurement in ECM. When considering the possibility of developing such a technique several factors have required consideration, as follows:

- **Would any of the characteristics of dissolution affect the transmission or reflection of the ultrasound**? That is, would the workpiece surface whilst undergoing high current dissolution

---

‡‡‡ Krautkramer Ultrasonics UK Ltd.

§§§ In pulse echo mode the piezoelectric device producing the ultrasound pulse is configured during the pulse-off period into receive mode whereby it is used as a detector of sound energy. The pulse repetition frequency needs to be set so that an appropriate amount of time lapses in order that all relevant returning sound pulses are detected. A range of transmission velocities will exist depending on the transmission medium. In metals the velocity does not usually exceed 8 $x10^3$ m sec^{-1}. Therefore using a pulse interval of 500 Hz (2 x 10^{-3} sec) is sufficient enable deflections over at least 4 m to be detected (2 m time-of-flight). This is typically an order of magnitude greater than wall thicknesses that are likely to be measured in an ECM gap measurement applications.

provide a clear reflection of the ultrasound. Also, how would reflection across the gap be affected by the high velocity fluid flow and/or the dissolution products (particularly gaseous products). An additional concern was whether the inter-electrode electric potentials would affect the piezoelectric device (or other associated electronics) within the ultrasound probe.

- **What would be the maximum workpiece or tooling thickness through which ultrasound could be effectively transmitted**? Absorption of the sound energy would occur throughout both the electrode material and the electrolyte medium (see section 7.1). These losses would eventually be such that resolution of reflections would no longer be possible.
- **Could the ultrasound be effectively coupled to the workpiece or tooling surface**? Effective transmission of ultrasound into a medium requires a good surface contact at the probe tip. How this transmission varies through different surface types, such as milled and ground, and how such effects would affect the accuracy of the measurement would need to be assessed.
- **How accurately could the gap be measured?** The accuracy of the gap measurement will ultimately determine the resolution of the C-function data. This will in turn determine the tolerance to which tool designs, based on such C-function can be specified.

In order to address these questions and with a view to applying the technique to generate gap-time and C-function data a series of trials were carried out, as described in the following sub-sections.

7.3.1 General characteristics of ultrasonic thickness measurements

Before going on to describe the developments of ultrasound applied directly to ECM gap measurements, some results from initial set up trials together with general definitions and operational characteristics of the USPC2100, are first detailed.

Figure 7.3-1 shows the configuration used throughout this work in which the ultrasound sensor is attached to the bottom of the workpiece surface (an initial reflection termed the *primary interface reflection*, IR_p will occur at this surface). The ultrasound being directed up through the workpiece with reflections occurring at the workpiece surface/electrolyte interface (termed the *primary backwall reflection,* BR_p) and also a second reflection (termed the *primary gap reflection*, GR_p) occurring, through the electrolyte, at the tool surface/ electrolyte interface.

The ultrasound probe assembly is an arrangement consisting of the ultrasound transmit/receiver transducer connected in series with a perspex delay line tip. This delay line acts to "clean" the sound signal by dampening the sound energy as it is transmitted from the transducer face (the IP signal) to the surface of the object undergoing measurement (the IRp signal). The differences in IP and IR_p signals are illustrated in Figure 7.3-2 which shows the improved signal definition for the IR_p signal

relative to the IP signal. The time-of-flight**** measurements are therefore made with improved accuracy relative to the "clean" sound signal occurring at the tip of the probe and not, as would be required if the delay line were not used, the distorted IP signal occurring at the face of the transducer.

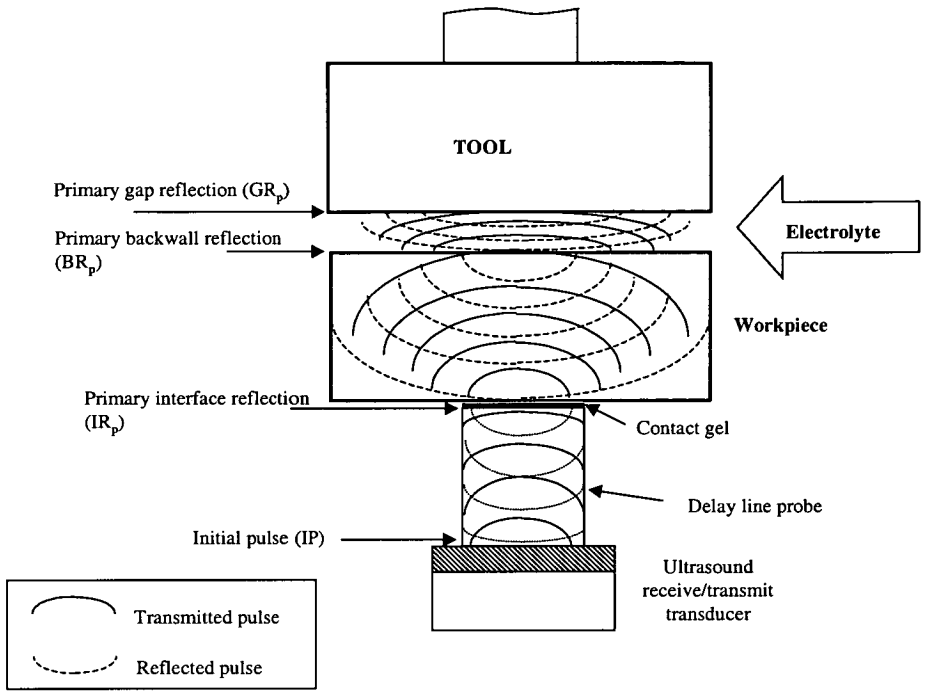

Figure 7.3-1: Ultrasound terminology and configuration

Figure 7.3-2(b) illustrates the *gating* method used to define the trigger point for the time-of-flight measurement. The start gate is a pre-selected time interval over which the initiation of a time-of-flight measurements is made. Three trigger mode options are pre-selectable on the USPC2100. These are: *flank mode*, which will initiate timing as soon as the received signal amplitude passes through a pre-set threshold (the height of the gate); *peak mode* in which timing is initiated at the peak value of the signal enclosed within the gate; and *zero-crossing mode* which causes initiation of timing as the signal returns through the zero point threshold after the peak value has been reached.

**** The *time-of-flight* data is an amplitude vs. time signal representing the energy of the received ultrasonic pulse. This data can be displayed on the USPC2100 chart output (see Figure 7.3-5) in units of microseconds or as a distance in millimetres. In this latter case the distance is computed from the predetermined velocity of sound for the material being examined. The term *time-of-flight* is used regardless of whether the measurement is made in units of micro seconds or in millimetres. Also, note that the system will always divide the *time-of-flight* data by two before displaying it since it assumes that reflections are produced by a return path and has therefore covered twice the distance of the thickness being measured.

Which of these modes is most appropriate to the application considered here, is investigated in section 7.4.

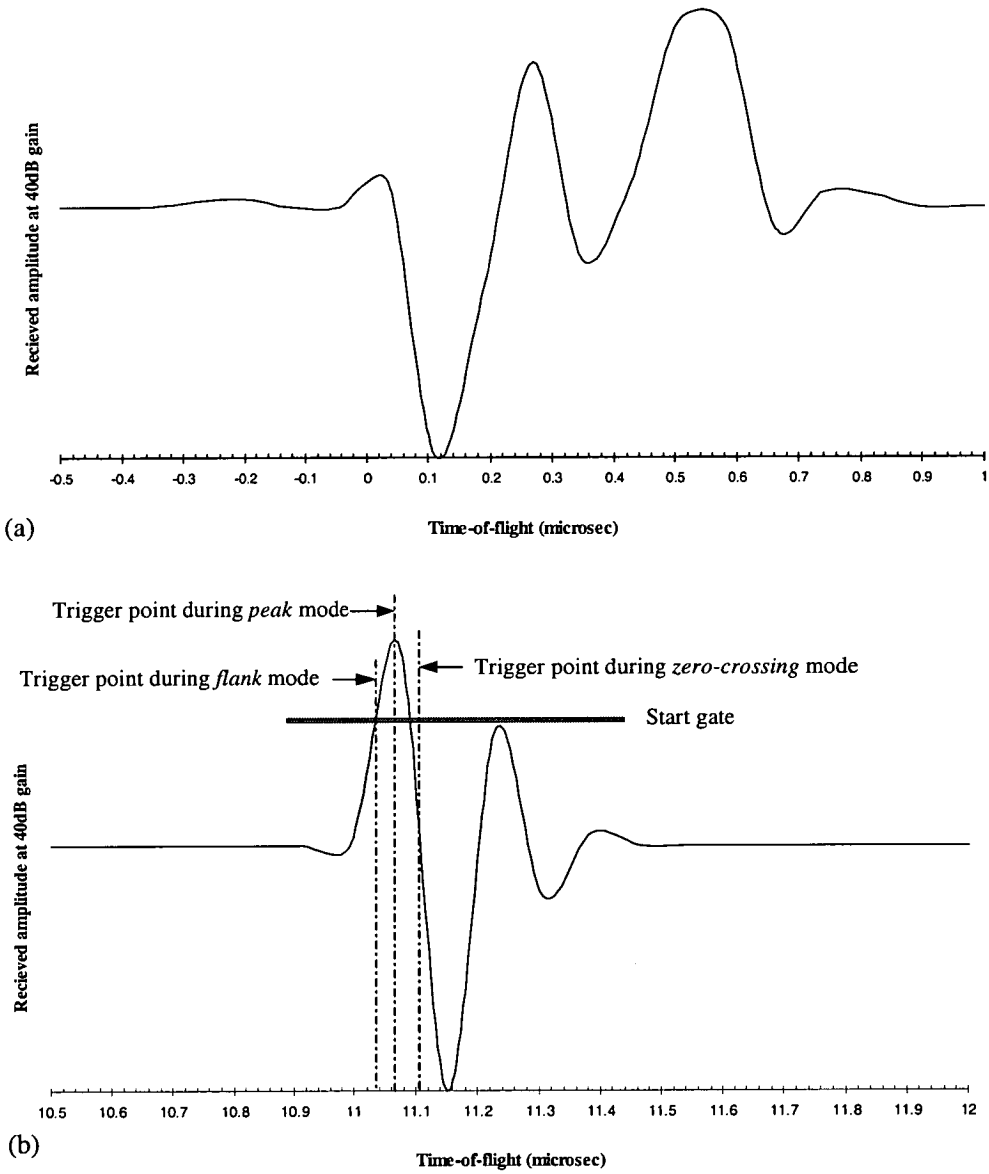

Figure 7.3-2: Showing distorted form of IP waveform (a) and cleaner interface reflection (b) with illustration of peak, flank and zero-crossing modes trigger position

The general attenuation characteristics of the ultrasound beam can be examined by measuring the decay in amplitude of multiple reflections of the IR_p signal within the perspex delay line tip. This characteristic (see Figure 7.3-3) shows the IP signal (occurring at the trigger point of 0 μs) followed

by the primary interface reflection, IR_p, and second and third interface reflections, each occurring at equally spaced time intervals. The second interface reflection is attenuated by 9.5 dB relative to the primary interface reflection and third interface reflection attenuated by 9.5 dB relative to the second interface reflection. Such factors will be important when determining the maximum workpiece thickness through which the ultrasound can be effectively transmitted.

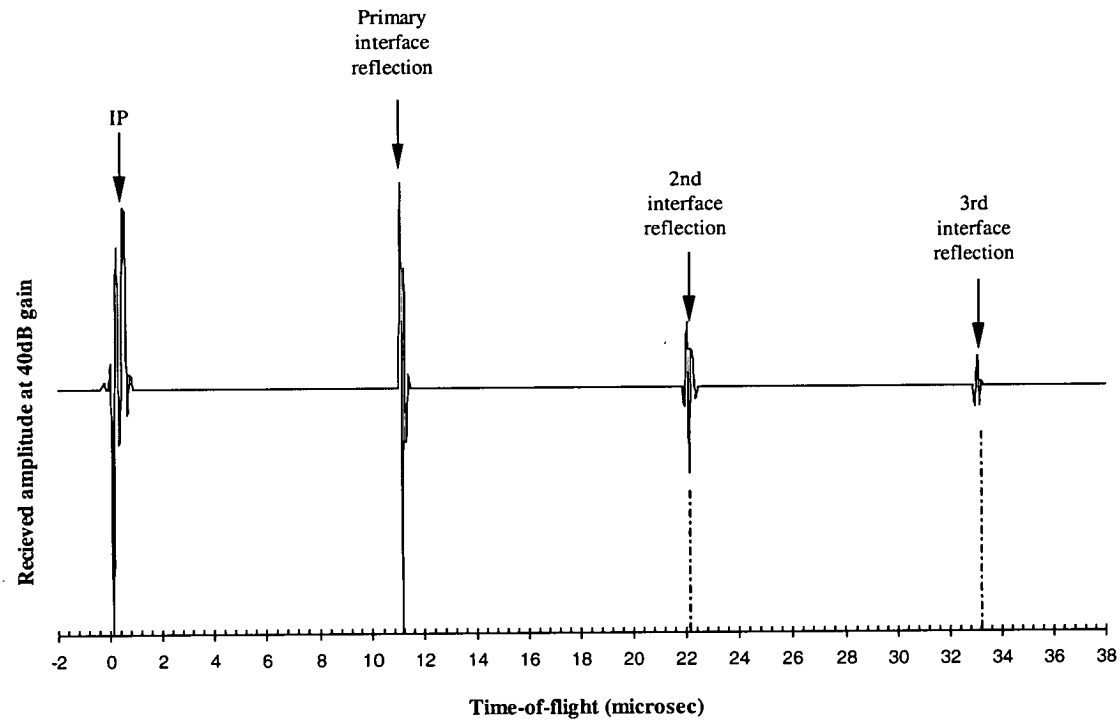

Figure 7.3-3: Ultrasound reflection from delay line tip

When the ultrasound probe is attached to the workpiece surface the transmission power will have a dependence upon surface characteristics at the point of contact. This effect is illustrated in Figure 7.3-4 which shows the differences in IR_p signals received for cases when connecting the probe to a milled surface, with a 40 micron R_a surface, and a 2 micron R_a ground surface. In the case of the rougher milled surface, multiple reflections can be seen to occur just after the main IR_p signals. Such near-surface-reflections will absorb power and therefore result in attenuation of the remaining signal used for the gap measurement. Although this attenuation is small it will nevertheless reduce the sensitivity of gap measurements. In the case where the contact point is with the smooth ground surface (see Figure 7.3-4(a)), such reflections are not observed. Therefore, prior to undertaking gap-time trials the contact surface of the workpiece has been ground to 2 micron R_a to maximise the range and accuracy of the gap measurement.

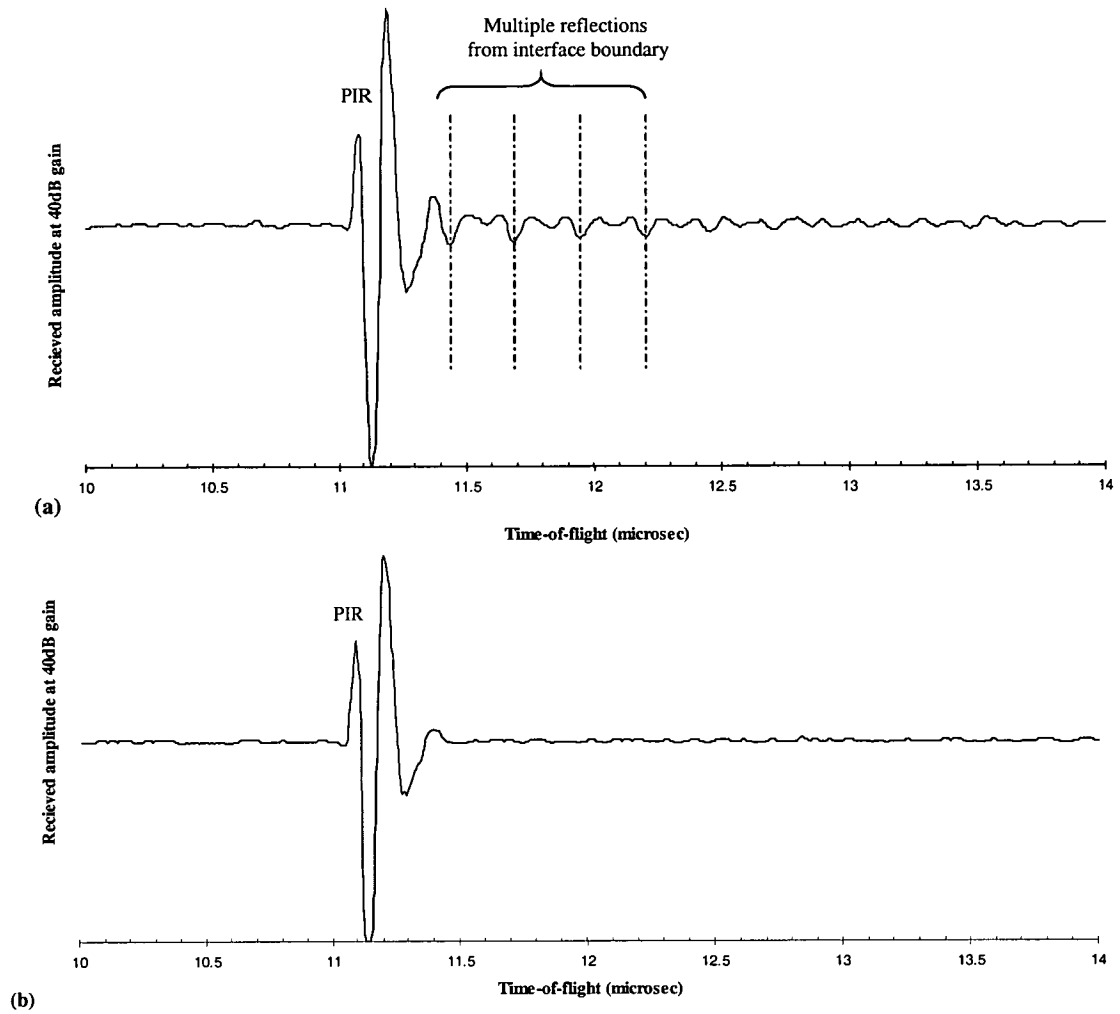

Figure 7.3-4: (a) Multiple reflections and slightly distorted PIR in case of 40 micron milled surface at interface and (b) Improvement for 2 micron ground interface

Before carrying out the set up trials the transmission velocities of the ultrasound through the materials to be used in this investigation needed to be measured. This was done by timing an ultrasound pulse through a accurately machined/ground 10.00 mm specimen of both In718 and Ti6-4 materials. (The TiAl material was not used in the ultrasound trials because after the general characterisation trials additional material could not be obtained). The transmission velocities were measured as:

Ti6-4	6.265 km s^{-1}
In718	5.720 km s^{-1}

The time-of-flight data shown in Figure 7.3-5 (in the form of an A-scan window) was obtained from an initial trial in which the ultrasonic probe was attached to the bottom of the workpiece surface (this is an arrangement similar to that shown in Figure 7.3-1., but without the electrolyte within the gap). The first signal, occurring at around 32mm into the trace (tracking from left to right), and enclosed by the start gate, is the primary interface reflection, IR_p. This represents the sound pressure occurring as a result of reflections from the contact point of delay line probe with the bottom of the workpiece surface. The second signal occurred at around 47 mm into the trace, enclosed by the measurement gate, is the primary backwall reflection BR_p. The thickness of the workpiece computed using the time-of-flight between these reflections, equal to 2.6 μsec, and the transmission velocity of the sound pulse within the workpiece, 5.720 km/s for In718. By multiplying the velocity by the time-of flight the workpiece thickness is computed as 15.28×10^{-3} m. The workpiece thickness was confirmed using a micrometer as 15.28 ± 0.005 mm.

When undertaking measurement of the gap, at least one interface (such as the workpiece surface) will be moving relative to the probe. In this situation a constraint will be placed on the maximum distance through which this interface can move whilst providing a continuous output of data. This problem is illustrated by the time-of-flight data shown in Figure 7.3-6. In this case, the backwall reflection from the surface of a titanium specimen is shown for workpiece thicknesses of 40mm (Figure 7.3-6(b)) and 30mm (Figure 7.3-6(a)). If the signals were gated throughout this range, in order to provide continuous gap-time data, then the gate range would also include the time-frame of the secondary IR reflection. Therefore, as the backwall reflection time-of-flight varies from 40 millimetres to towards 30 millimetres the trigger signals will cross through the secondary IR reflection. This will result in a loss of the gap-time data during the crossover period. Because this loss is unacceptable, workpiece heights have been used that are below a certain threshold (i.e. less that 30 mm for Ti6/4) so that this cross-over problem does not occur.

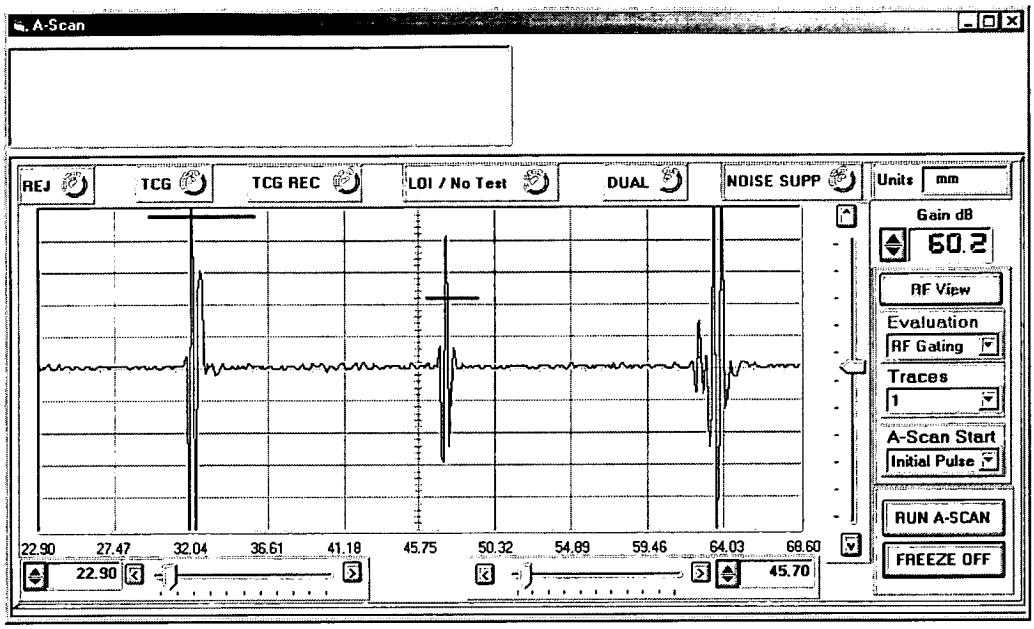

Figure 7.3-5: Showing A-Scan measurement window; trace shows backwall reflection from 15.28 mm In718 sample

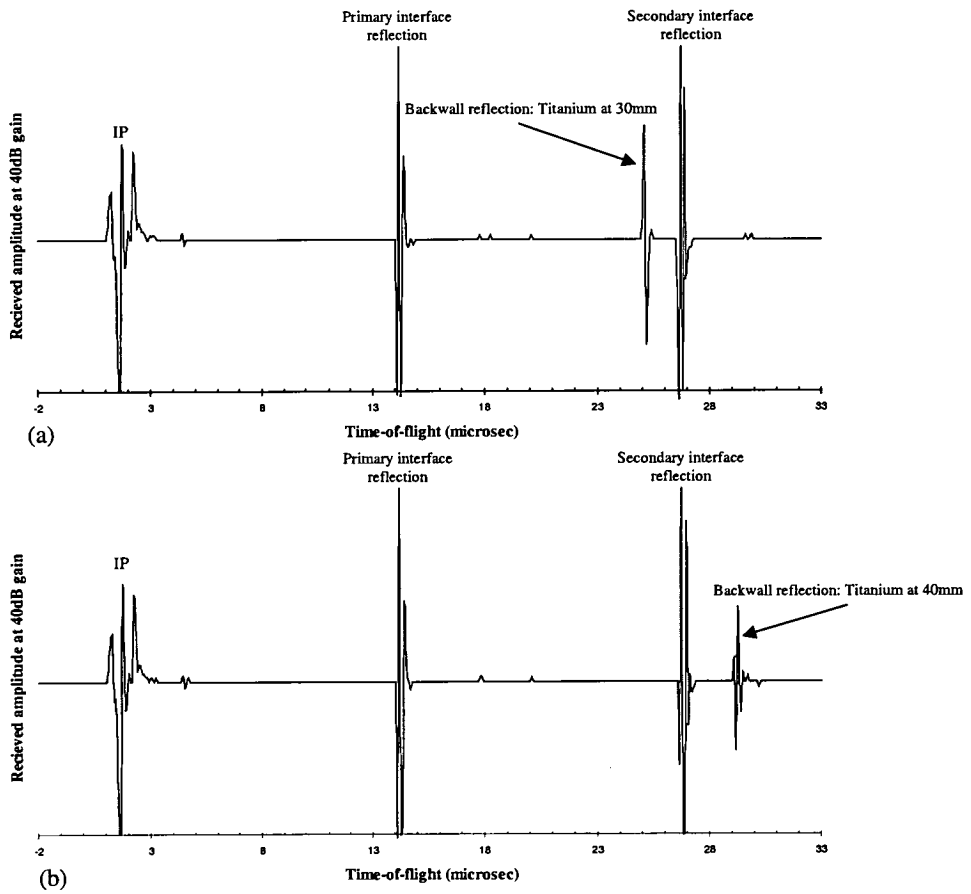

Figure 7.3-6: Illustrating problem of interference with secondary interface reflection for workpiece thickness greater than 35mm

Attenuation of the ultrasound as it passes through the workpiece material will ultimately determine the maximum workpiece thickness through which gap measurements can be resolved. This problem is illustrated by the series of time-of-flight measurements, shown in Figure 7.3-7, made using In718 specimens with 15mm, 20mm and 30mm heights. An increase in signal attenuation can be seen as the thickness of the specimen increases. This relationship is further illustrated in Figure 7.3-8 which shows the attenuation of backwall reflection, BR_p relative to the primary interface reflection, IR_p, for a series of workpiece thicknesses for both IN718 and Ti6/4 specimens. The limit of achievable signal resolution has been determined by positioning the detection gate just above the threshold at which the noises in the time-of-flight signal start to register within the gate. This limit, which occurs at 49 dB attenuation relative to the main IR_p reflection, is shown as a horizontal dotted line in Figure 7.3-8. Extrapolation of the thickness measurements, shown in Figure 7.3-8, onto this threshold reveals that the maximum thickness through which the ultrasound signal can be effectively resolved are 52mm and 75mm for the In718 and Ti6/4 specimens respectively. The decreased level of attenuation noted for the Ti6/4 specimens relative to the In718 specimens can be explained due to the decreased Young's Modulus in the case of the Ti6/4 material. In the case of the trials that have been considered here these limits on maximum thickness should not be problematic since the maximum sample heights will not exceed 30mm. In the case of the general application of ultrasound to ECM gap measurement then these limitations could cause resolution problems in some cases.

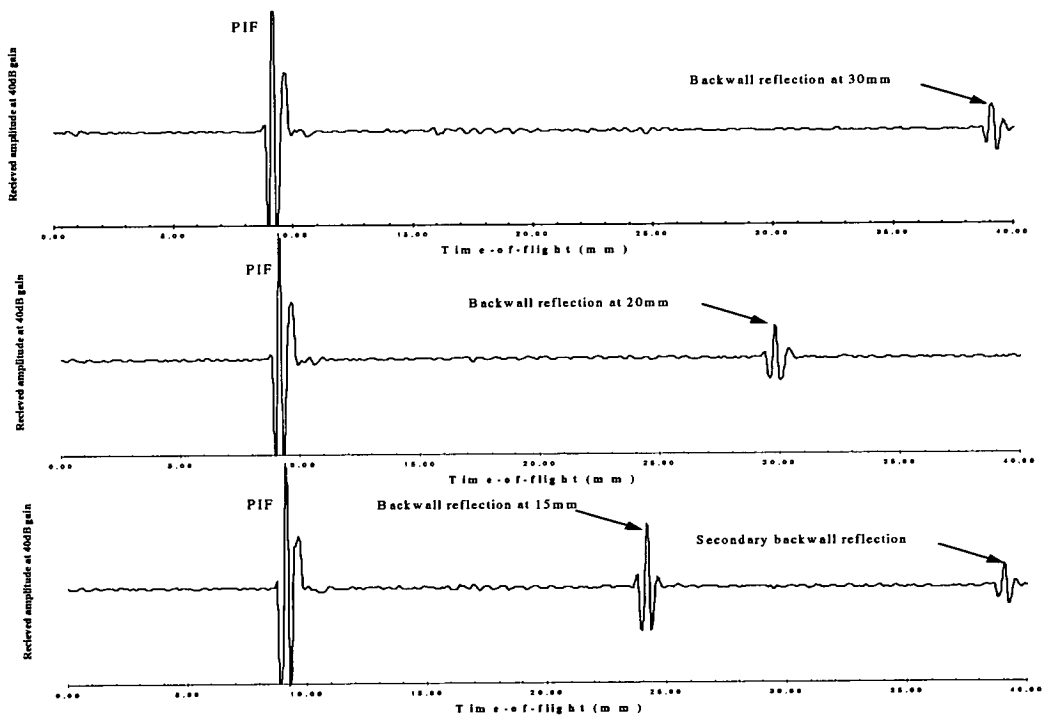

Figure 7.3-7: Backwall reflection as workpiece height is varied from 30 to 15 mm; note appearance of secondary backwall reflection at 15mm height

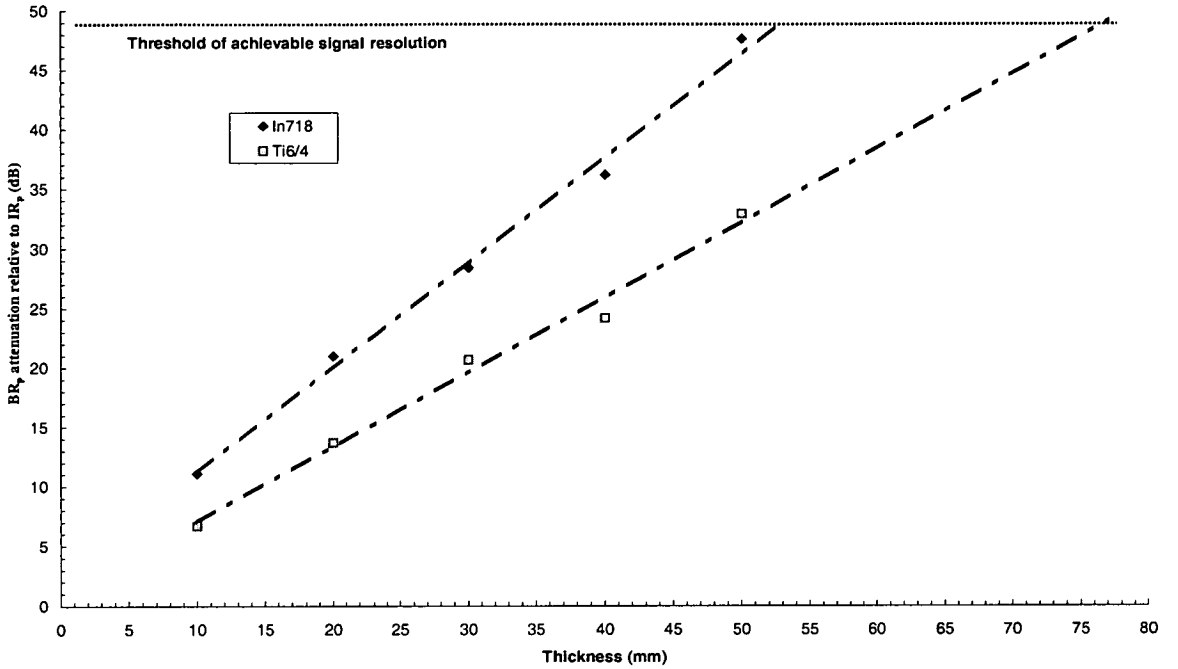

Figure 7.3-8: Attenuation of ultrasound backwall reflection for In718 and Ti6/4 material

A final consideration, before examining the usage of ultrasound for gap measurement, was whether the ultrasonic time-of-flight data was significantly variable over the range of temperatures that would be encountered in an ECM system. Resistive heating in the gap would produce heating of the electrolyte and also some heating, via conductance, to the workpiece and the ultrasound probe. In any one characterisation trial it was estimated that this temperature range would not be outside an interval of 10 to 50 ^{0}C. The question arises as to whether a change in temperature in the gap or in the workpiece/probe, over this temperature range would produce any drift in the time-of-flight data through the respective medium. Previous work on temperature dependency in ultrasonic transmission [85] has indicated that the speed of sound in liquid mediums varies by typically less that 0.1% over a range of 10 ^{0}C. Such a variation would be insignificant in the application being considered here. However, in order to check this and also to determine whether significant velocity/temperature dependencies would occur within the workpiece material, a basic trial was carried out. In this trial the ultrasound probe was clamped on the bottom surface of the workpiece (the opposite end to the gap) and the electrolyte was heated between each measurement in intervals of 10 ^{0}C. At each temperature interval the electrolyte was maintained in the gap for a period of five minutes, prior to the measurement, to enable heat conduction into the workpiece and the ultrasound probe assembly. Time-of-flight data was then recorded for transmission through the workpiece material and through electrolyte in the gap. Throughout the five trials over a temperature range of 10 to 50 ^{0}C no measurable change in the time-of-flight data, either through the workpiece or through the electrolyte, was detected. It is concluded that temperature effects, in the context of the trials being considered here, can be neglected.

7.3.2 Application of ultrasound to ECM gap measurement

The primary consideration was whether the ultrasound could be most effectively applied by configuring the system for *direct* or *indirect* gap measurement. These two options can be explained with reference to Figure 7.3-1. A *direct* gap measurement refers to the use of ultrasound to measure *time-of-flight* directly across the gap. That is, the timing of reflections through the electrolyte between the tool surface/electrolyte interface and the workpiece surface/electrolyte interface. Alternatively, the gap can be computed by *indirect* means as a difference between the tool face position and the workpiece height reference to the same origin. Carrying out indirect measurement would require that the initial tool position needs to be accurately pre-set and its position monitored throughout the measurement. The direct measurement has the advantage that a prior knowledge of the initial set-up position and continuous tool position monitoring would not be required. A series of tests were carried out in order to assess which of these options would be most effective.

7.3.3 Direct measurement of the ECM gap

An assessment of the feasibility of applying ultrasound to the direct measurement of the ECM gap was carried out using the cell-99 tooling and cell system. This arrangement incorporates an ultrasound probe spring loaded against the workpiece surface and positioned at the centre of the flow field. A detailed description of this system has been given in section 5.2.4. The aim of these initial trials was to assess whether the ultrasound could be transmitted, through the workpiece material and then through the electrolyte medium within the gap, with sufficient power so that assessment of the gap size could be achieved using BRp and GRp reflections. The trial consisted of recording time-of-flight data using the gap dimensions which were manually incremented through a series of values with the electrolyte flow and gap power initially inactive. A series of time-of-flight plots, obtained from these trials, for ultrasound pulses received from equilibrium gaps set at 0.4, 0.6, 0.8 and 1.0 mm intervals, are shown in Figure 7.3-9.

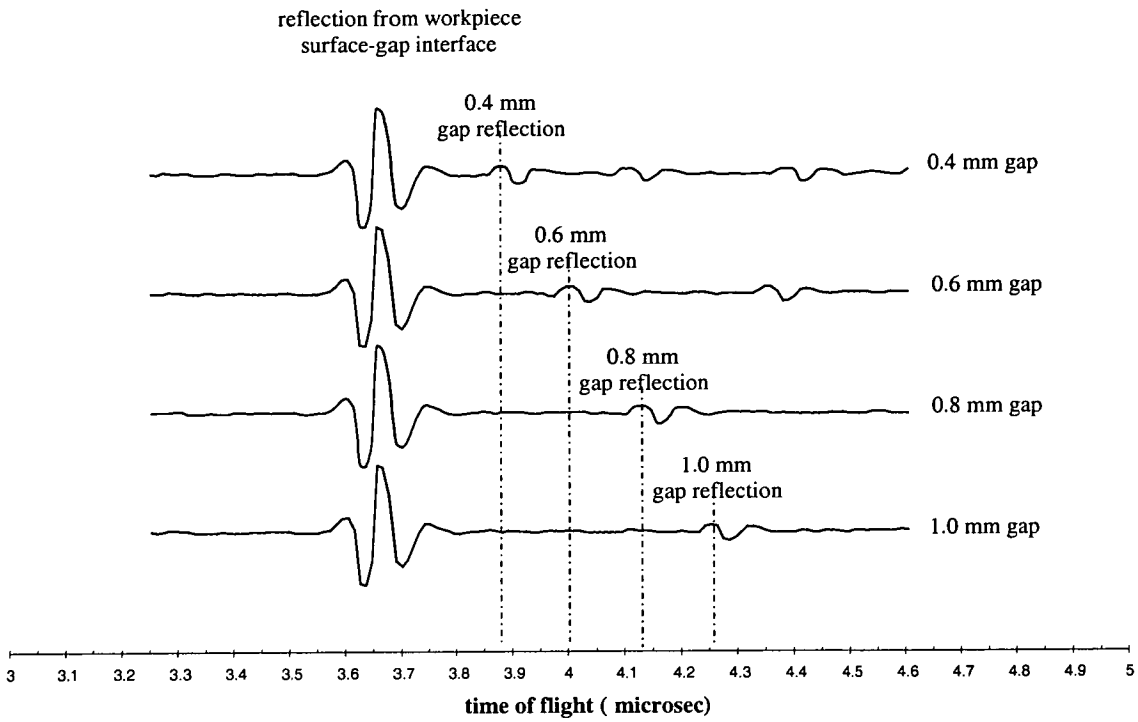

Figure 7.3-9:Time-of-flight traces for ultrasound pulses received from equilibrium gaps set at 0.4, 0.6, 0.8 and 1.0mm

From this plot it can be seen that the dominant ultrasound reflection is that received from the upper workpiece surface to gap interface. In this case the ultrasound has passed through only the workpiece material at a velocity of 5720 m/sec. The time of flight for this reflection is measured at 3.66 μs corresponding to a workpiece thickness of 20.93 $x10^{-3}$ m. A second reflection, resulting from the ultrasound passing through the electrolyte and reflecting from the lower tool surface, can also be seen in Figure 7.3-9. This reflection is attenuated by about 26dB relative to the main deflection from the workpiece surface. Such high attenuations would be expected for, as is the case for the GR_p gap reflection, when sound energy is travelling from a medium of low acoustic impedance (the electrolyte) to a medium with a high acoustic impedance (the tool). However, even with this high attenuation the form of this reflection can be resolved.

From Figure 7.3-9 it can be seen that each increment of gap reduction by 0.2 mm reduces the time-of-flight across the gap in 0.125 μs intervals. From these data the velocity of the ultrasound through the electrolyte has been calculated as 1605 m/sec. This compares to the velocity of sound in pure water of 1480 m/sec. The slightly higher velocity obtained through the electrolyte would be expected given its increased density with respect to water. Note that in the upper two traces, in Figure 7.3-9, representing the time-of-flight data for the cases of the smaller gaps at 0.4 and 0.6mm, multiple gap reflections can be seen. These are secondary (and a third order in the case of the 0.4mm gap) signals corresponding to multiple rebounds within the electrolyte across the gap. When gating these signals

care must be undertaken to ensure that only the primary gap reflection is gated relative to the main BR_p, otherwise gap data corresponding to integer multiples of the actual gap will be output by the USPC2100 system.

Whilst continuing to monitor the time-of-flight data the electrolyte flow was activated and ramped up slowly from a flow volume of 4l/min to 20 l/min. No change in the form of the time-of-flight data was noted. The flow volume was then held at 20 l/min and the dissolution power activated. When this was occurred the GR_p gap reflection became attenuated to such an extent that it could no longer be resolved. Such an observation can be explained if it is accepted, as concluded in work by for example Hopenfeld and Cole [26], that gaseous dissolution products (probably mostly hydrogen) accumulate within the gap during dissolution. Therefore assuming that gaseous products occupy a significant proportion of the gap it could be expected that the ultrasound would undergo almost full reflection at the workpiece surface electrolyte/gaseous layer (due to the very sharp change in acoustic impedance that would exist between the upper workpiece surface and gaseous products within the gap). Any ultrasound that was transmitted into the gap would undergo dispersion due to the inhomogeneity in the gap that would exist during the dissolution. There would therefore not be sufficient power reaching the tool surface to provide a significant GP_p reflection. The loss of the GR_p reflection upon activation of the dissolution power appears to indicate that gaseous products occupy a significant proportion of the gap.

If measurement of the ECM gap was carried out by direct means, using the GR_p reflections, then a strategy would have to be developed in which gap data is collected during the intervals with the dissolution power turned-off (and also presumably the tool feed in order to maintain the gap at a constant value). Such a strategy although ultimately feasible was considered as being too cumbersome. Because the BR_p deflection remains unchanged during dissolution, it was decided to direct effort at achieving gap measurement using indirect means.

7.3.4 Indirect measurement of the ECM gap

Indirect measurement of the ECM gap can be achieved by subtracting tool position data from a measurement of the workpiece height as erosion occurs. Thus the BR_p reflection can be used together with a continuous signal representing tool position. This arrangement, illustrated in Figure 7.3-10, incorporates the combined use of the(LDVT, to measure the tool face position, y, and an ultrasound thickness probe to measure the workpiece height, h.

Visual Designer data analysis/logging software has been used to compute the gap values using the LDVT and USPC2100 ultrasound output signals. For detailed description of how this is achieved see Figure 5.1-11 which provides a description and illustration of data flow for the case of a C-function

computation (the gap measurement being a subset of this computation). With reference to Figure 7.3-10 gap values were measured and logged using the following procedure:

- **Set the initial starting gap, z_0, at a pre-set value and input as offset parameter for Visual Designer**. Unless otherwise stated the initial gap was set at 0.800 ±0.005mm. This was achieved using a feeler gage to set an approximate value followed fine adjustment based upon optical measurement of a casting of the gap (see section 5.2-5 for further details of this procedure). An accurate setting of this initial condition was required otherwise computation of subsequent gap-time data would incur the same offset errors.
- **Adjust the LDVT to zero its output**. This was done both mechanically, by physical movement of the LDVT to position its feed pin at the start of the stroke, and also with the visual design software by adjustment of an offset parameter so that the tool position parameter, y was zeroed at the starting condition.
- **Offset the workpiece height signal to set gap co-ordinate at origin.** The initial workpiece height signal, h_0 from the ultrasound sensor is offset so that the computed gap z_0 is set to 0.80mm. Note that this will sometimes mean that the thickness measurement on the USPC2100 a-scan window will sometimes be slightly different from the data logged value. Such differences arise due to slight inaccuracies in the range outputs between the USPC2100 analogue outputs and the input analogue to digital converters of the data-logging card. This relative value of workpiece height will not change absolute gap values since it is only the difference in height, between initial conditions and at any other defined time, that is important in realising accurate gap-time data.

- **The gap, z, is then computed as $z = y - h$ for the initial condition that $z_0 = y - h_0$.** Visual Designer has been programmed to compute values of z at a range of pre-defined intervals. This interval has been set at one second in all trials unless otherwise stated.

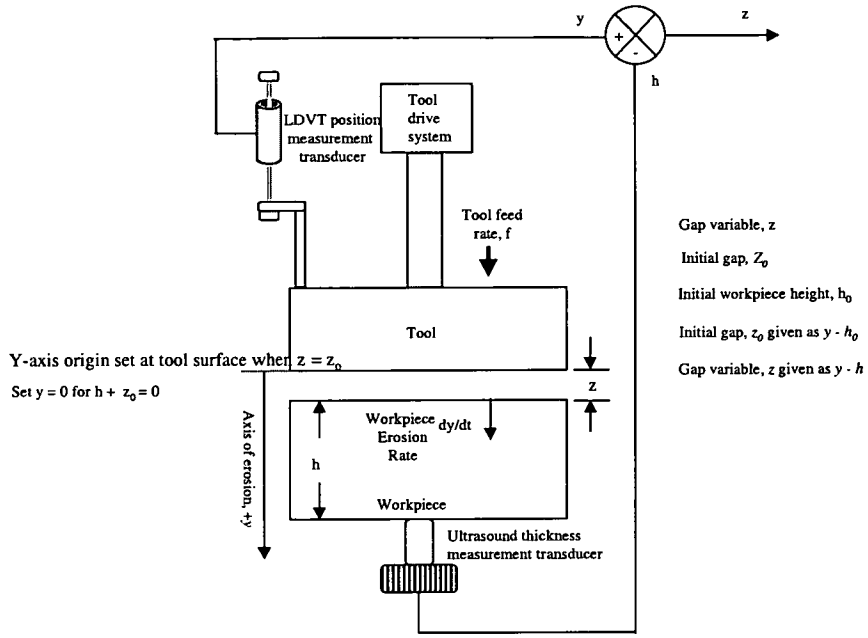

Figure 7.3-10:Tool and workpiece configuration and arrangement used for indirect gap measurement

7.4 Ultrasonic gap measurement trials

A series of trials were undertaken with the general aim of developing the application of ultrasonic time-of-flight data to ECM gap measurements. In all these trials the gap data has been computed by indirect means using the arrangement shown in Figure 7.3-10. The trials can be considered in two main groups, as follows:

- **Assessment of effectiveness of using different time-of-flight gating modes.** It might be the case that during dissolution some distortion in the ultrasound signal received from the dissolving surface might occur. If this is the case then the stability of the time-of-flight data will likely be sensitive to which of the trigger mode options (see section 7.3.1 and Figure 7.3-2) is operating.

- **Assessment of the overall accuracy of the gap measurement.** The accuracy to which the ultrasound can be used to determine both equilibrium gaps and general gap-time data will ultimately determine the accuracy for the generation of parameter independence and C-function data. For equilibrium conditions these measurements have involved comparing gap casting dimension data with ultrasonically computed gaps. During initial transient intervals the validity of gap-time data has been tested using a correlation of rise-time constants (the values of k in Equation 4.1-3 and Equation 4.1-7) for both current and gap data.

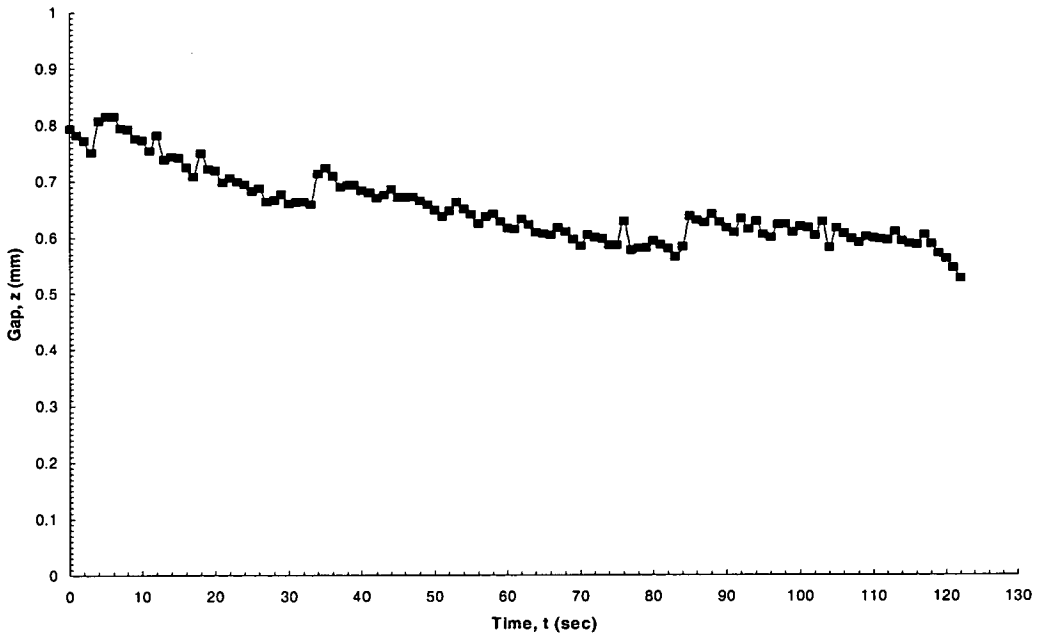

Figure 7.4-1: Gap-time data from Ti6/4 in chloride at 24 volts exhibiting signal "shifting" associated with peak detection mode

Figure 7.4-1 shows gap-time data computed using peak-detection mode for Ti6-4/chloride at 24 volts. Significant levels of "random" variation in the measurement are observed together with some overall drift. Because of the level of noise in the peak-mode measurements the accuracy of the gap-time data for any one sample interval has been estimated as being no better than ±0.03mm. This noise can be related to observed small fluctuations in the relative position (along the time axis) of the peak value within the BR_p reflection. These fluctuations only occur when the dissolution power is activated. It was thought that the peak value fluctuations could be caused by electrical interference within signal lines or more directly from the ECM power affecting the probe. To test this, all signal wires were re-configured, using a multi-way earthing (star configuration) arrangement and also by configuring the probe so that it was electrically isolated from the ECM power. This did not reduce the level of noise in the peak value signal. Although a detailed explanation for these fluctuations was not determined, it was thought that they were likely to be associated with the kinematics of the dissolution process.

When operating in zero-crossing mode the gap-time data was seen to switch between two different values (seen as a distinct transition superimposed upon the noise level). This phenomenon can be seen in the data plotted in Figure 7.4-2 for the case of a Ti6-4/chloride machining system at 16 V. From observations of the form of the BR_p signal this phenomenon can be correlated to discrete fluctuation between two distinct signals occurring along the time axis. The gating system appears to

be latching on to one signal and then the other in a random way. This differs from the noise observed during peak mode which was seen as random variations in the position of the signal peak. An interpretation of the "switching" phenomenon could be that it represents the transition between two distinct boundaries at the BR_p interface. It is possible that this transition represents reflections between the lower surface of the anodic oxide film, in contact with the workpiece surface, and the upper surface of the anodic oxide that is in contact with the electrolyte solution. If this was the case then the difference between these "thicknesses" will be an indication of the thickness of the oxide layer. Although it is not possible to quantify this thickness in any detail since the velocity through the oxide is unknown, it may be assumed that the velocity through the oxide will be of the order of three times faster than velocity through the workpiece material (for example the sound velocity through SiO_2 is 3 times that of the velocity through In718 [84]). In which case the thickness of the oxide layer can be approximated by dividing the transition distance (i.e. the y-axis shift between the two trends shown in Figure 7.4-2) by three. Thus with these assumptions the thickness of the oxide layer can be approximate to in the region of 0.08 mm.

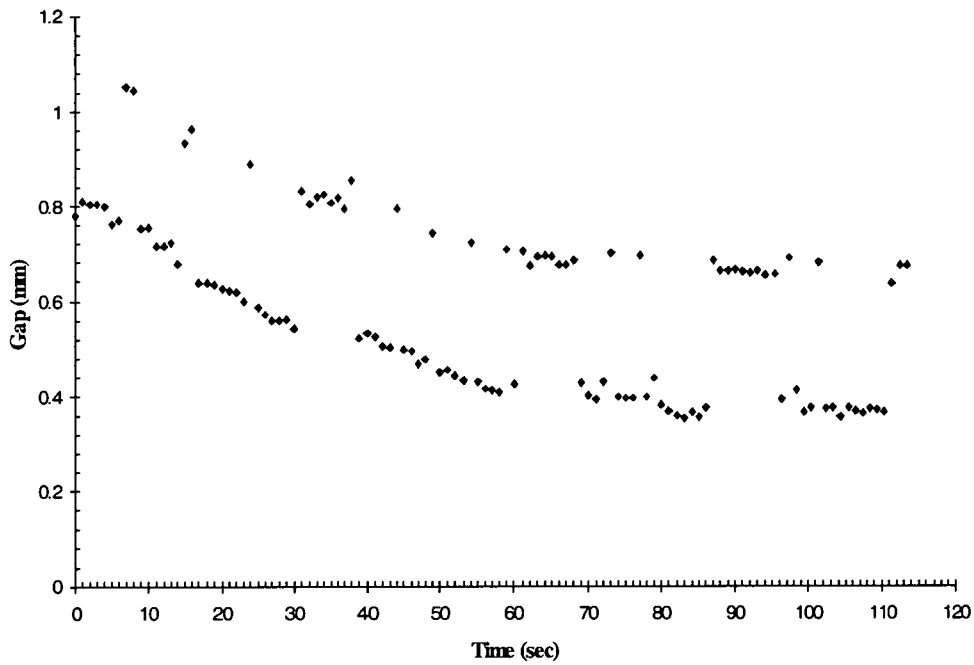

Figure 7.4-2: Gap-time data showing "switching" phenomenon associated with zero-crossing mode for Ti6/4 at 16V

Because the initial machining gap was set at 0.8mm, the lower of the two trends represents reflections corresponding to the actual machining gap. This is reasonable since once the dissolution power is turned off then the oxide layer will disappear, or be reduced significantly in terms of thickness, so that any mechanically measured gap value will be expected to correlate with the lower trend. However, if such data were to be used for general gap measurements then the data would need to be post-processed in order to remove ambiguities resulting from the switching phenomenon.

Although this would-be relatively easy to achieve in the case of the data show in Figure 7.4-2, where the distinction between the two trends is clear, there may be cases where this distinction is less obvious. This would occur, for example, when conditions are such that parameter interdependency (or variation) was producing both the erosion rate changes and also oxide thickness changes. In this case conditions may arise where it would be difficult to distinguish between gap values within the two trends. Thus it can be concluded that use of a time-of-flight data gated in zero-crossing mode cannot be readily deployed for general gap measurement.

An example of gap-time data computed from flank mode gating data is shown in Figure 7.4-3. This graph show data from a trial using the In718/Nitrate/16V system. By comparing this data with Figure 7.4-1 and Figure 7.4-2 it can be seen that gap values computed from flank mode time-of-flight data exhibit the most stability in respect of noise minimisation and the absence of switching phenomena. Although the reason for this is not clear, it has been noted that the instability in BR_p reflections occurred as either a variation in the peak height or a stretching out of the signal after the peak has occurred (this latter phenomena results in an increase in noise levels during the zero-crossing mode). These forms of instability do not affect the trigger level when operating in flank mode since the gated data occurs before the peak in signal amplitude and are therefore not influenced by data occurring after the trigger point. The signal form occurring before the peak in signal was stable and is not affected when the dissolution power is activated.

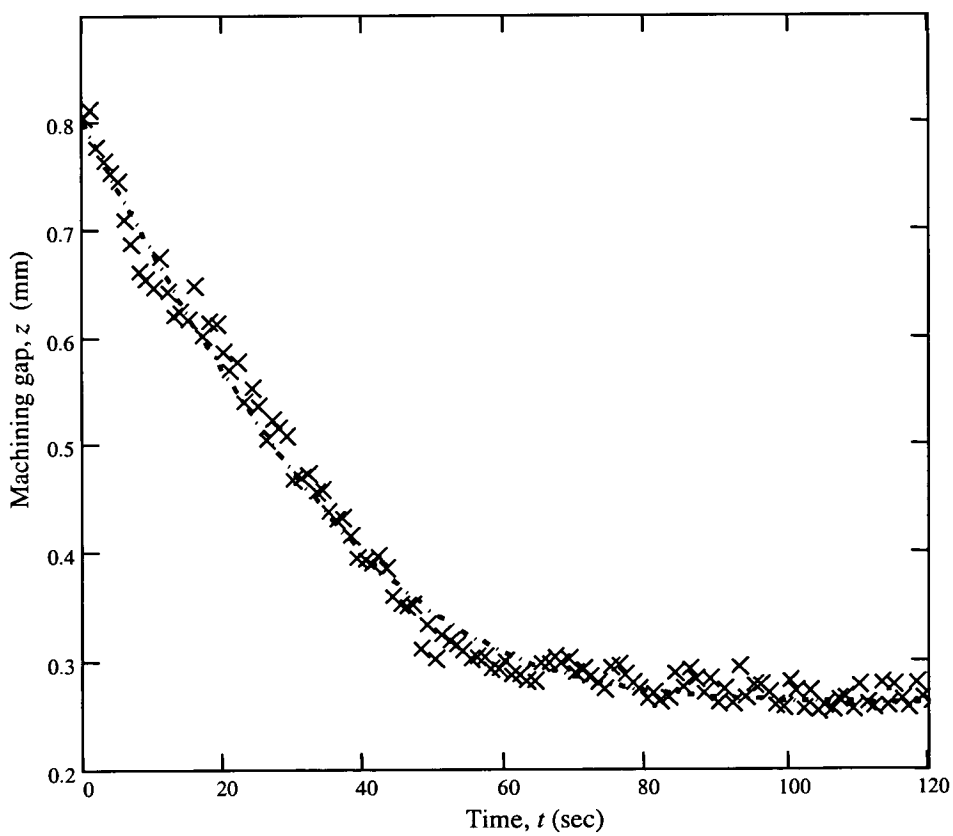

Figure 7.4-3: Gap-time data In718 in nitrate at 16 volts flank mode

Comparison of the gap value at the equilibrium shown in Figure 7.4-3, with the gap value obtained from gap castings, are accurate to within ±0.015mm. This improved accuracy (compared to the data generated using flank and zero crossing mode) is further confirmed by fitting the current-time data obtained during these runs. These data are shown in Figure 7.4-4 together with the iterative fits to Equation 4.1-5. This give values of k = 0.0039 mm^2 sec^{-1} for the gap-time data which compares to k = 0.0038 mm^2 sec^{-1} for the current-time data. This close correlation is seen as validation of the accuracy of the gap measurement technique. However, as already mentioned it should be noted that comparison of values of the k-parameter only indicates that on average the current variation can be correlated to the gap variation. Any small change in the value of k- parameter would be averaged out within this computation (this point is investigated further in Chapter 8).

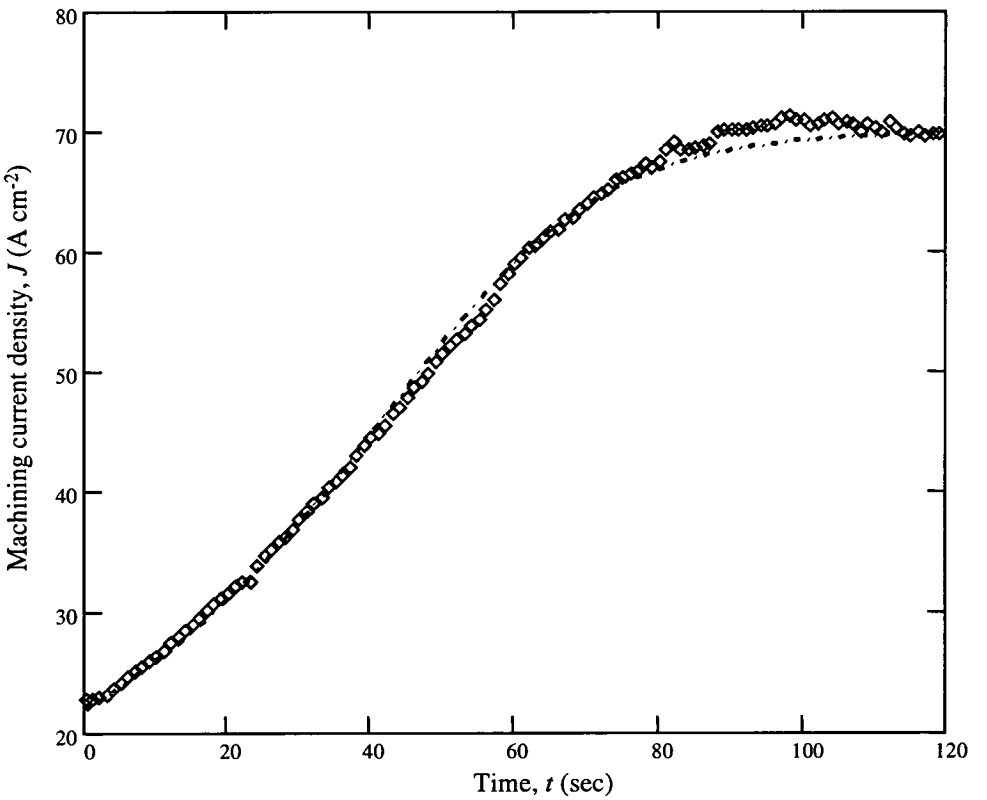

Figure 7.4-4: Current-time data corresponding to gap-time data in Figure 7.4-3

7.5 Chapter overview and conclusions

In this chapter:

- After consideration of the possible methodologies for in-line measurement of the IEG, the application of ultrasonic measurement technologies was considered as worthy of detailed investigation.

- The limitations and window-of-application of the ultrasonic measurement techniques have been studied. It can be concluded that measurement of the IEG through either the tool or workpiece electrodes will become difficult due to signal attenuation for electrode thickness above 52mm and 72mm for In718 and Ti6/4 materials respectively. Furthermore, the signal resolution will be further attenuated with dependence upon the roughness value of the contact surfaces between the probe tip and the electrode. In order to maintain good signal resolution all reference trials were carried out using interface surfaces ground to an R_a of less than 1μm and through thickness of less than 30mm.

- Measurement problems have been identified when using the peak gating mode, due to higher levels of signal noise, and during the zero crossing mode, due to switching phenomena. The flank gating mode has been identified as producing the most accurate data.

- The possibility of using ultrasound applied directly to measurement of the ECM gap, has been examined. Such a method cannot be readily applied since products within the gap (probably gaseous) impede the transmission of the ultrasound.

- By comparison of gap values to cast measurements and also by correlation to current-time data, ultrasound gap measurements have been determined to be accurate to within ±0.015mm.

CHAPTER:

8 C-Function characterisation and representation

In this chapter, 2-point C-function characterisation trials carried out using a number of selected machining systems are described. A simple 2-D shape is machined using both ideal conditions (high flow rates) and conditions where the *k*-parameter is sensitive to flow path length. Representation of this latter case using C-functions is discussed.

8.1 Introduction and background

Because of the complex nature of parameter interdependence in ECM (see discussion in Chapter 3) it is suggested that geometric variations caused by *k*-parameter sensitivities can be represented in the form of a distributed C-function. C-functions would provide descriptions to enable representation of *non-ideal* effects for purposes of process simulation and tool design

In section 4.3, the C-function was defined for a predefined range of conditions by equating ECM planar dynamics in the following form:

$$C(J,m) = z_m\left(\frac{dz_m}{dt} + f\right)$$

Equation 4.3-4 (see section 4.3)

m is a discretisation index representing position along the flow axis.

Mapping of the function of Equation 4.3-4 will involve a continuous measurement of the machining gap, z, and the feed rate, f. In the simplest case, of a 2-point C-function, this would involve gap measurement at 2 points, for example, close to the flow inlet and exit positions. In the case of the work in this thesis a two point measurement was considered sufficient in order to demonstrate the use of such an arrangement. In practice, full representation would probably require at least three and possibly more points.

In section 4.3 is was suggested that representation on the C-function could be conveniently made in the following the form:

$$C = C(J,0)p^{-0} + C(J,1)p^{-1} + C(J,2)p^{-2} \ldots\ldots + g(M)p^{-M}$$

Equation 4.3-6

In this chapter, the methodology for achieving a C-function measurement is explored using selected machining systems previously characterised by current-time techniques in Chapter 6. Comparisons can therefore be made in order to validate the accuracy of the measurement and also to demonstrate how the technique can be used to represent a wide range of parameter interdependence.

Demonstration of the applicability of C-function representation for the correction of non-ideal effects in the case of 2-D profiles, is achieved through the generation of appropriate profiles using an analytical solution to the tool design problem. This methodology, which has been developed in a collaboration with Alder (for more details see [86] appended in Appendix A1), considers a workpiece profile, $y_W(x_W)$, and decomposes it into N harmonic components defined by the Fourier series:

$$\frac{y_W}{L} = \sum_{r=0}^{r=N} a_r \cos\frac{r\pi x_W}{L}$$

Equation 8.1-1

where x_W and y_W are the workpiece co-ordinates; L is the profile length; and a_r (r = 1,N) is the amplitude of the component r. The model then produces a tool profile, $y_T(x_T)$, according to:

$$\frac{y_T}{L} = \frac{z_\infty}{L} + \sum_{r=0}^{r=N} a_r \cosh\frac{r\pi z_\infty}{L}\cos\frac{r\pi x_W}{L}$$
$$\frac{x_T}{L} = \frac{x_W}{L} + \sum_{r=1}^{r=N} a_r \sinh\frac{r\pi z_\infty}{L}\sin\frac{r\pi x_W}{L}$$

Equation 8.1-2

where x_T and y_T are the tool co-ordinates; and z_∞ is the nominal (i.e. planar) equilibrium machining gap.

8.2 Experimental procedures and equipment

All auxiliary experimental systems and the ECM machining equipment has been described in detail in section 5.1.

The cell 2000 system has been used throughout these trials. Details of the development of the system are given in section 5.2.5. A schematic overview of the system set-up is shown in Figure 8.2-1. This system combines the use of segmented tooling system with the gap measurement technology (as described in Chapter 7). The gap measurement being made at a position close to the flow inlet, at the centre of segment two, and towards the exit at the centre of segments six. For the

reasons described in section 6.3 the data from segments 1 and 7 was not used for this part of the work.

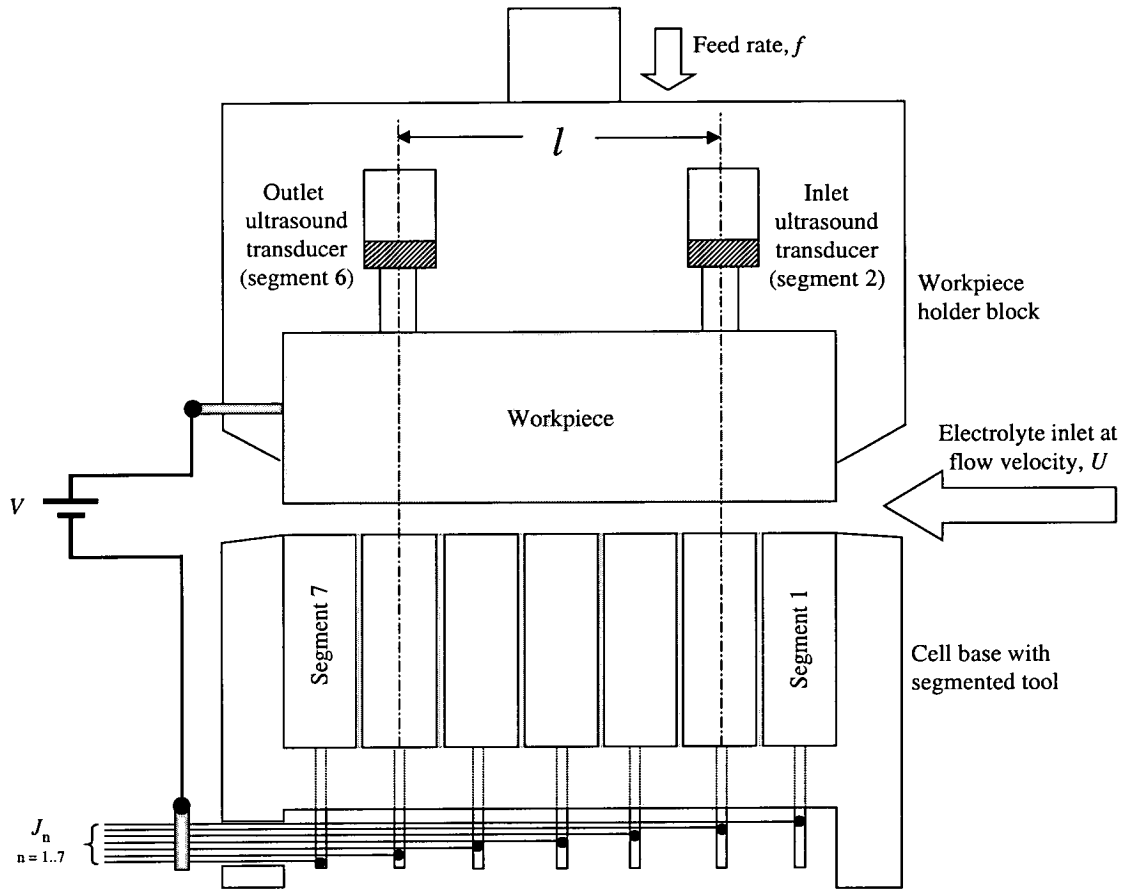

Figure 8.2-1: Schematic overview of C-function measurement system (cell 2000 configuration)

The C-function trials have been undertaken using the In718/nitrate, In178/cloride, Ti6-4/nitrate and Ti6_4/chloride Systems. The initial gap, z_0, was held constant at 0.8mm and the feed rate, *f*, held constant at 1.0 mm min^{-1} unless otherwise stated. The voltage was held constant at a pre-set value during each trial. Current density on each of the segments, the gaps at the two measurement points, and all other machining parameters (see section 5.1.4) were recorded at one second intervals. The gap casting technique (as previously described in section 5.2) was used throughout trials in order to check initial gaps and equilibrium gaps against the gap data from the ultrasound transducers. C-function computations were made in real-time as a 10-point moving average using the visual designer software running the algorithm as illustrated in Figure 5.1-11 (see section 5.1). Differential gap values, *dz/dt*, were computed between each one second interval, equal to the sample rate of the data logger.

8.3 Result: C-function and related measurements

The data presented here includes C-function measurements and other correlations that have been made possible using the gap measurement technique. Two groupings of experiments have been carried out. The first, carried out using flow volumes above an upper threshold at 16 l/min such that the gap width would be expected (from previous results in section 6.4.2.1) to be parallel along its length. In the second group of experiments the flow volumes are reduced so that changes in gap width would be expected. The full data set from all these trials are presented in graphical form in appendix 6. The following two subsections outline the primary features of this data.

C-function data has been presented as the plot of C-function against current density. This is considered as the most useful representation since current density will be the most significant variable when mapped out over the surface of any complex 2-D or 3-D shape. In cases where it is more appropriate, the C-function is represented by plotting against time. This has been the case, for example, when certain thresholds are reached when flow velocity is varied.

Each of the machining systems, with the exception of the In718/chloride system, was machined in separate trials using 20 and 24 V. In the case of the In718/chloride system machining was carried out at 20 V and 26 V. This change in voltage to 26 V meant that the equilibrium gap for this condition would be equal to 0.6mm (see Figure 6.4-1, section 6.4). This was done so that comparisons could be made between the planar characteristics for this system and 2-D characteristics using a shape which had previously been designed for a tool operating at a nominal equilibrium gap of 0.6mm.

8.3.1 High flow volume trial

A representative example of gap-time data recorded using inlet and outlet ultrasound transducers is shown in Figure 8.3-1 for the case of machining a Ti6_4/chloride system at 20 V using high flow volumes of 16 l/min.

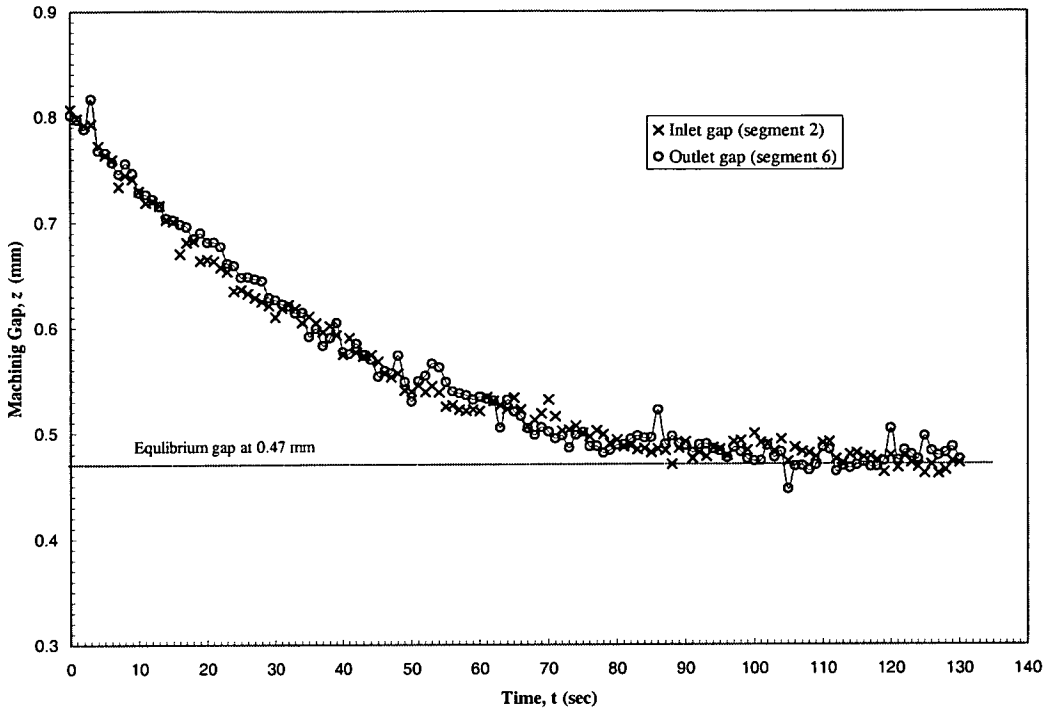

Figure 8.3-1: Inlet (segment 2) and outlet (segment 6) gaps for Ti6_4/chloride system at 20 V and 16 l/min flow

Within the observed noise envelope this data illustrates close correlation for gaps sizes at inlet and outlet positions. The accuracy of this data was confirmed by gap castings, at initial and equilibrium condition, to be accurate within ±0.015mm (see also equilibrium gap data presented in Figure 6.4-1, section 6.4). Correlation can also be established throughout the time interval of the data by comparing time constants with current-time data. This is demonstrated in Figure 8.3-2 using the same data shown in Figure 8.3-1 together with additional data recorded at 24 volts. These data are shown with fits to the theoretical solution of Equation 4.1-7 and the Equation 4.1-5 for current-time and gap-time data respectively (note that mse values are of the same order as those given previously, see Figure 6.4-4 for example). These fits produce k-parameter values of 7.9 and 8.0 10^{-9} m^2 s^{-1} for current-time and gap-time data respectively at 20 V , and k-parameter values of 10.1 and 10.2 10^{-9} m^2 s^{-1} for current-time and gap-time data respectively at 24 V. It is clear that close correlation (within experimental error) is observed for these cases.

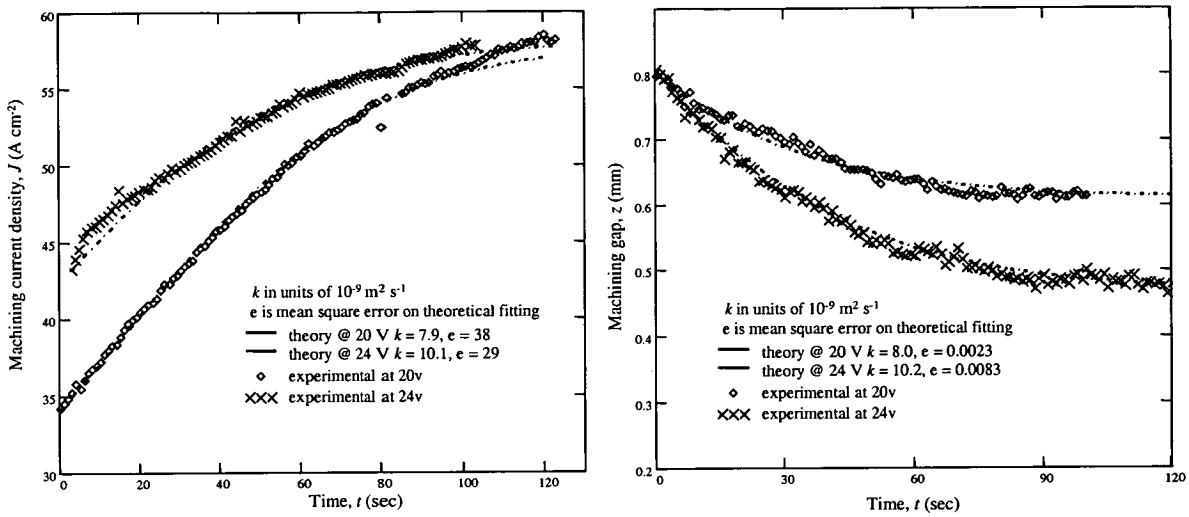

Figure 8.3-2:Current-time and gap-time data for titanium/chloride system at 20 and 24 volts at 16 l/min

The C-function data shown in Figure 8.3-3 has been computed from the data shown in Figure 8.3-2. The equivalent C-function data for the In718/chloride, Ti6-4/Nitrate and In718/nitrate systems are shown in Figure 8.3-4, Figure 8.3-5 and Figure 8.3-6 respectively. These data illustrates C-function against current density, for both inlet and outlet positions for both 20 and 24 (26 volts in the case of the In718/chloride system) trials. Linear line fits are shown fitted to each grouping of inlet and outlet data at the two voltage conditions. A high level of noise is observed in these measurements. This would be expected when it is noted that the differential component, *dz/dt*, is significant in the computation of the C-function in accordance with Equation 4.3-4. Thus the noise levels seen in the gap-time data (Figure 8.3-2) would be amplified in the computation of the C-function. Nevertheless, within this level of noise, the C-function exhibits a general overall trend of an increasing value with current density. If the C-function trends represent a sensitivity in one or more of the constituents that were previously masked (averaged out) in the current-time data, then it would be expected that C-function values as an average throughout this variation would correspond to the previously measured values of the *k*-parameter. For example, with reference to Figure 8.3-3, if lines are drawn from a point about half way along these data series to intercept with the C-function axis, then the value at this point should correspond with the average values of the *k*-parameter as previously found. In this case, mean C-function values exhibit close correlation with the fitted k-parameter values shown in Figure 8.3-2. Close correlation can also be seen by comparing averaged values of the C-function trends in Figure 8.3-4, Figure 8.3-5 and Figure 8.3-6 with the fitted *k*-parameter values obtained for those same systems as shown in the data sets of Figure 6.4-7, Figure 6.4-3 and Figure 6.4-6, respectively. This close correlation is seen as validation as to the general accuracy of the C-function computation.

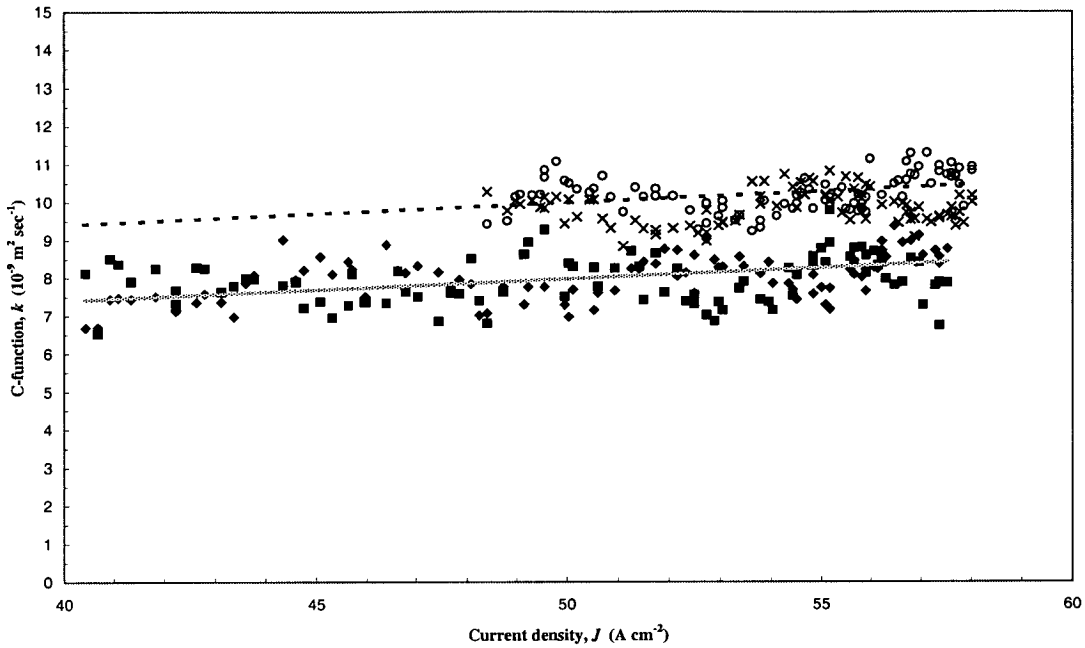

Figure 8.3-3: C-function data for Ti6_4/chloride for inlet 20 V (♦) 24 V (x) and at outlet at 20 V(■) and 24 V (o), shown with linear fits for 20 V and 24 V data sets, gradient = 4.0 10^{-14} m^4 sec^{-1} A^{-1} for both 20 V and 24 V data

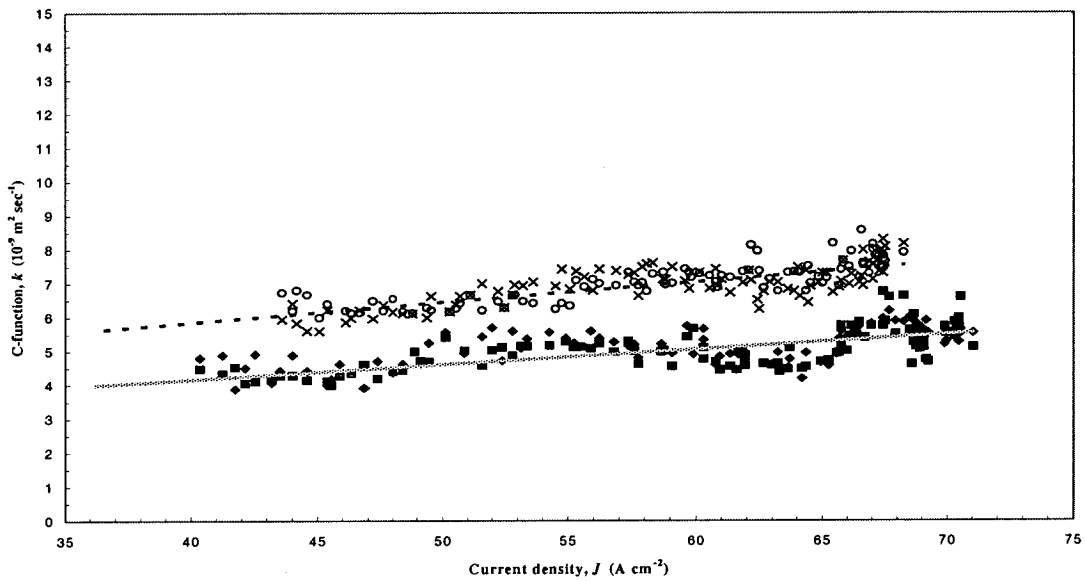

Figure 8.3-4:C-function data for In718/nitrate for inlet 20 V (◆) 24 V (x) and at outlet at 20 V(■) and 24 V (o), shown with linear fits for 20 V and 24 V data sets. Gradient = 5.4 and 6.0 10^{-14} m^4 sec^{-1} A^{-1} for 20 V and 24 V data respectively

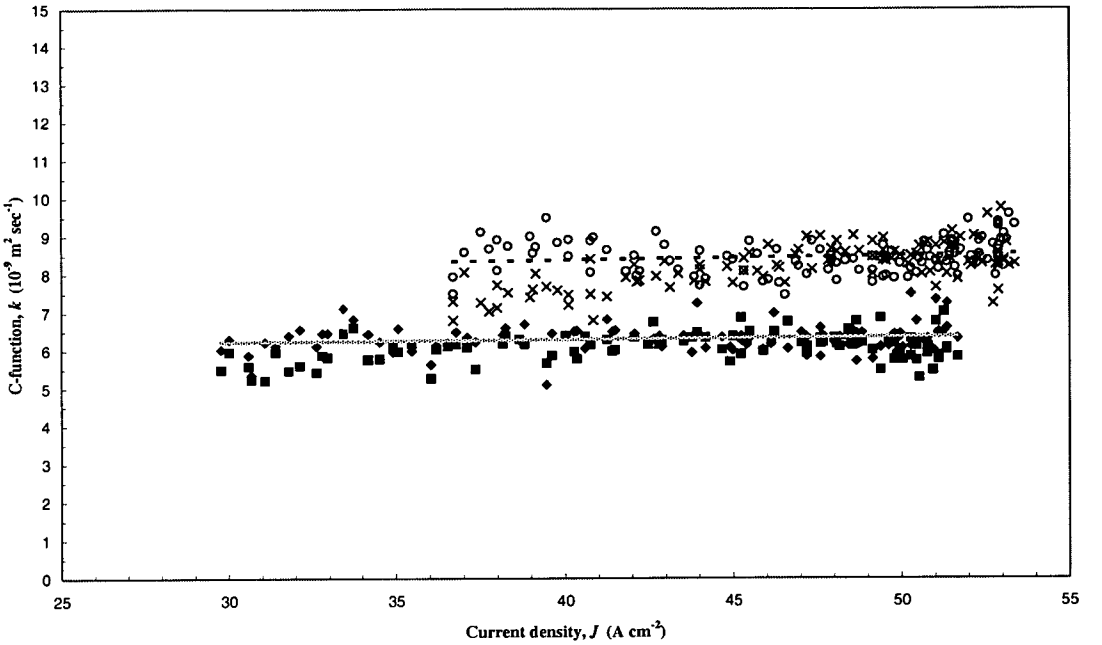

Figure 8.3-5: Ti6/4 with nitrate for inlet 20 V (◆) 24 V (x) and at outlet at 20 V(■) and 24 V (o), shown with linear fits for 20 V and 24 V data sets. Gradient = 1.1 and 1.2 10^{-14} m^4 sec^{-1} A^{-1} for 20 V and 24 V data respectively

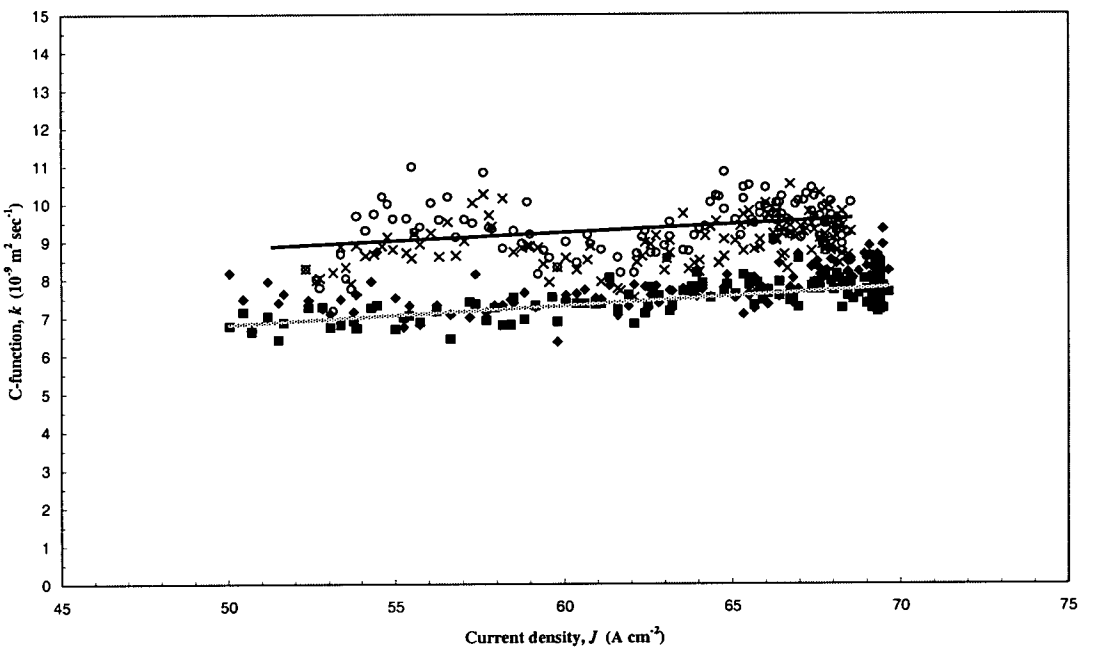

Figure 8.3-6:C-function data for In718/chloride for inlet 20 V (♦) 26 V (x) and at outlet at 20 V(■) and 26 V (o), shown with linear fits for 20 V and 24 V data sets. Gradient = 4.8 and 4.4 10-14 m4 sec-1 A-1 for 20 V and 24 V data respectively

Examination of the gradients of the C-function trends (see captions in Figure 8.3-3 to Figure 8.3-6) reveals that in the case of the Ti6-4/nitrate system this sensitivity is at its minimum and in the case of the In718/nitrate system this sensitivity is at a maximum. This indicates that although all the systems exhibit some form of sensitivity to current density this trend is more pronounced in the case of the In718/nitrate system. This is consistent with previous results where it was found that the In718/nitrate system produced the highest mean square error values when compared with the current-time fit (see Figure 6.4-7 for example).

Further examination of this sensitivity, for the In718/nitrate system, can be made by equating the current density to the rate of material removal (i.e. change in workpiece height *dy/dt*) throughout each time interval of the data (the value of *dy/dt* is already recorded as an intermediate stage in the computation of z). Thus in accordance with a rearrangement of Equation 4.2-1, as follows:

$$\frac{dy}{dt} = \frac{MJ}{n\rho F}$$

Equation 8.3-1

Assuming constant valency, a plot of dy/dt against J will be a straight line with a gradient of M/nρF. The plot of this relationship for the IN718/nitrate system, corresponding to the C-function data as shown in Figure 8.3-4, is plotted in Figure 8.3-7.

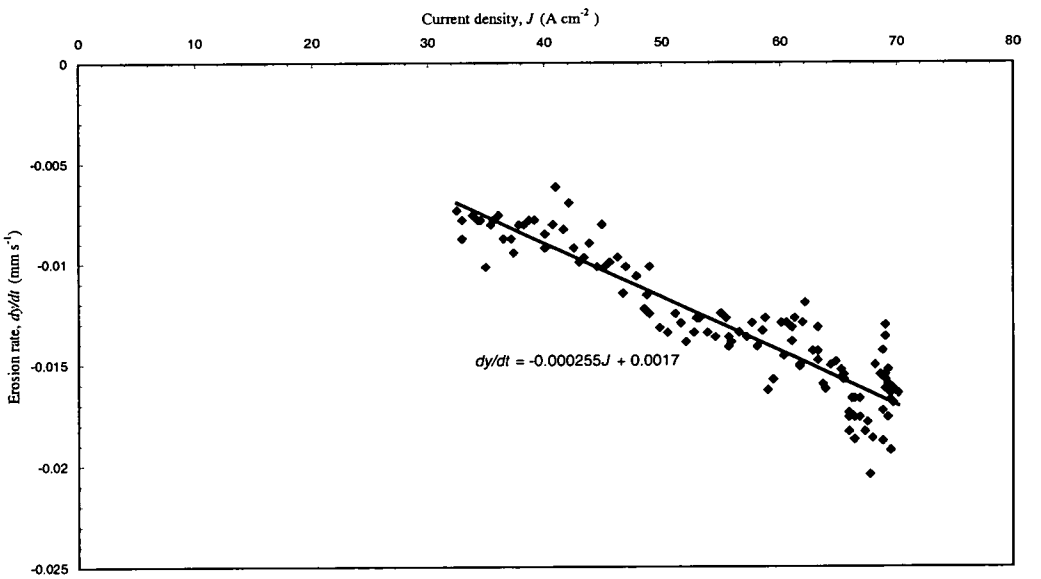

Figure 8.3-7: Erosion rate (inlet), dy/dt, against current density (segment 2), J_2, for In718 in nitrate system. Gradient, M/nFρ, equals 2.55 x10^{-11} m^3 sec^{-1} A^{-1}.

region of 4.1 x 10^{-9} m^{-1} sec^{-1}. The accuracy of the C-function values can be confirmed by applying the equilibrium condition that $z_\infty = k/f$ (Equation 2.2-11, in section 2.2) using a value of f = 0.0166 mm sec^{-1}. This gives a value of $z_\infty = 0.59 \pm 0.1$ mm and $z_\infty = 0.38 \pm 0.1$ mm at the inlet and outlet segments respectively. Correspondence within experimental error to the gap data recorded in Figure 8.3-8 is observed.

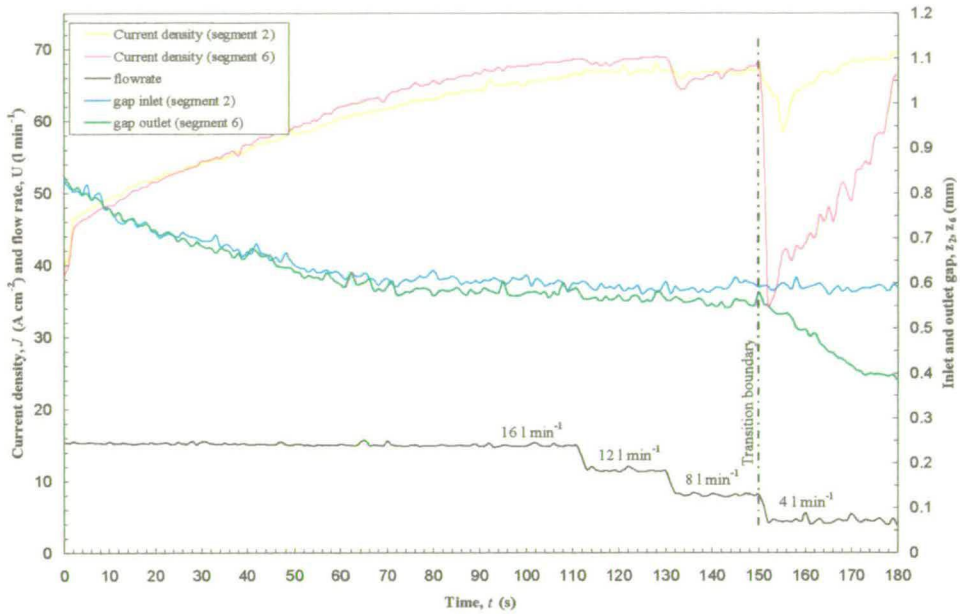

Figure 8.3-8:In718 chloride system at 26 V with flow rate varied from 16 to 4 l/min exhibiting transition in segments current density and the gaps as flow rate is reduced to 4l/min

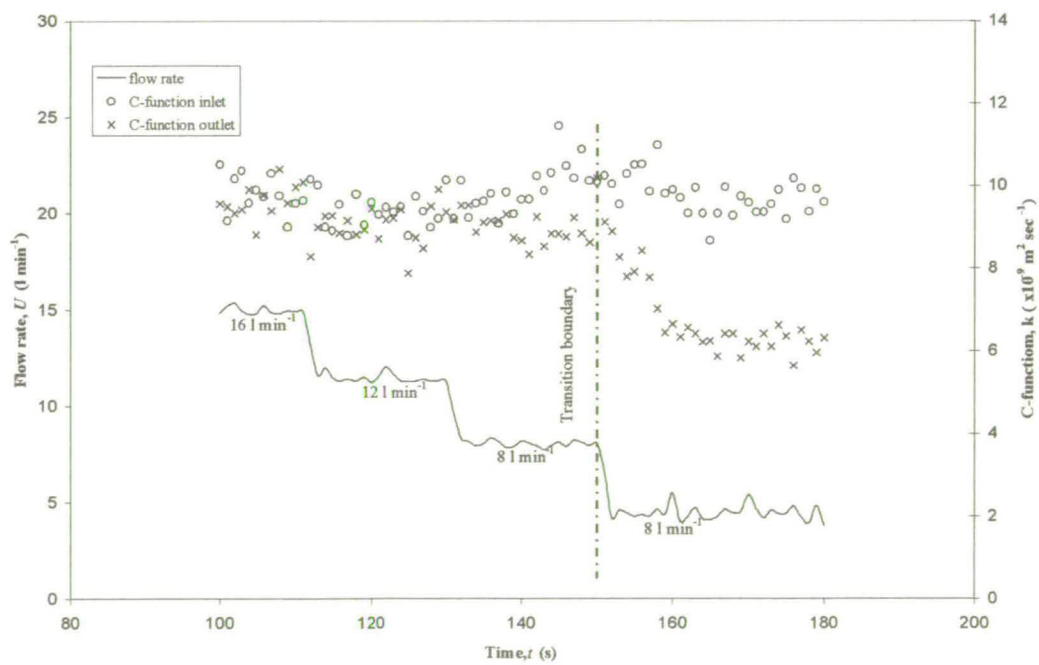

Figure 8.3-9: C-function data as flow rate varied from 16 to 4 l/min for In718 chloride system at 26 V

In the next section the 2-point C-function description of the In718/chloride system will be used for representing the "distortion" in gap taper for 2-D profiles. Before discussing this representation an assessment needs to be made as to whether gap tapers are equivalent to the planar (for the same machining parameters) in the case of 2-D geometries. That is; are *distortions* in the equilibrium gap only a function of flow path length and not geometry?

8.4 Application of C-function characterisations to 2-D machining

In order to examine the application of C-function data, obtained from a planar configuration, to the machining of 2-D shapes, a series of trials were carried out using the In718/chloride system using the same machining conditions as used for the trial data in Figure 8.3-8 and Figure 8.3-9. That is; 26 volts at 16 l/min and 4 l/min.

2-D shape profiles were machined using a tool designed according to a direct analytical solution operating under equilibrium conditions. The methodology was outlined in section 8.1 and is described in detail by Alder [86] as appended in Appendix A1. The chosen 2-D profile was the double cosine (DC) case with $a_1 = 0.5$ and $a_2 = -0.125$ in Equation 8.1-2. These coefficients become $a_1 = 5$ mm and $a_2 = -1.25$ mm when expressed in physical dimensions for a tool of 40 mm overall width. Equation 8.1-2 was then applied to give the required tool profile for a nominal machining gap of 0.6×10^{-3} m. This tool profile was then manufactured in the form as shown in Figure 8.4-1 (upper electrode). This shape was chosen because the steepness of the two "troughs" in the profile would produce significant variation in flow curvature along the axis of machining. Thus such a shape could be considered as being representative of moderate or worse case flow path sections that would occur in relatively complex workpiece geometries. Thus any effects that would cause gap variations different from those that would occur in the planar case would likely be apparent.

Geometric data in the form of gap measurements along the flow axis and co-ordinate data representing the workpiece surface were obtained as follows. After terminating machining a casting compound *(Permadydne)* was introduced into the IEG and the assembly reset to its machining position. After solidification the casting, the tooling electrode and the workpiece were removed from the machining cell and reassembled to be scanned to form an image of the flow path geometry, as shown in Figure 8.4-1. The high accuracy and rigidity of the casting enable the original relative positions between the tool and the workpiece to be re-established prior to scanning. A check of positioning accuracy was made by ensuring that the opposing flat sides of the workpiece and tool were parallel to each other, as was the case during machining. Also, in the case of the DC 2-D profile at 16 l/min, a check was made to ensure that the gap at the point half way along the profile was equal to 0.6 mm (this will be the case since at this point in the profile the workpiece and the

tooling surfaces were parallel, as shown in Figure 8.4-1. Note that the dark areas within the casting in this image (seen as apparent non-contact sections between the casting and the workpiece) were caused by the sharp cut-off in depth resolution of the scanner causing blank areas at positions where the casting was not in full contact with the scanner plate. Positioning was then made to ensure that both the tooling and the workpiece are in direct contact over the full surface (without compression) of the casting thus ensuring that accurate geometric co-ordinates were produced.

The image Scanning was carried out using a HP ScanJet 6300c having a dpi resolution of 1600 x 1200. The image was obtained in a bitmap format to provide a point to point pixel resolution of in the region of 0.015mm. *Imagetool* image analysis software was then used to produce geometric data consisting of gap sizes, measured orthogonal at the workpiece surface, at intervals (corresponding to the segment spacing of the segmented tool equal to 5.71mm) along the flow channel and co-ordinates representing the workpiece surface. In the case of the planar surface the spatial interval was obtained by simply incrementing the x co-ordinate by 5.71mm. In the case of the DC 2-D profile*, flow path intervals of 5.71 mm were mapped onto the x co-ordinate at equal intervals along the tooling profile. This involved mapping intervals of x co-ordinate differences (x_b–x_a) representing intervals of 5.71 mm along the profile of the workpiece function, $y_w(x_w)$, according to:

$$5.71mm = \int_{x_a}^{x_b} \sqrt{1 + y'_w(x_w)^2}\, dx$$

Full details of this methodology are given in the mathcad spreadsheet in Appendix A2.

In order to produce accurate spatial data a reference dimension is first obtained using the known 40 mm workpiece length. The software then used this reference to compute the inter-pixel distance for all subsequent measurements. An illustration of this measurement process, which involved zooming down to individual pixels and then manually positioning a measurement cursor, is given in Figure 8.4-1.

---

* *It was realised that small differences would exist between gap measurements made orthogonal to points on the workpiece surface (the method used here) and gap measurements made orthogonal at points on the tool surface. However since the gap data required is the difference in gaps between the two flow rate conditions, at 4 and 16 l /min, then the selection of a reference surface for the gap measurement will not be of significant relevance (in the case used here that the same reference is used for the two conditions).*

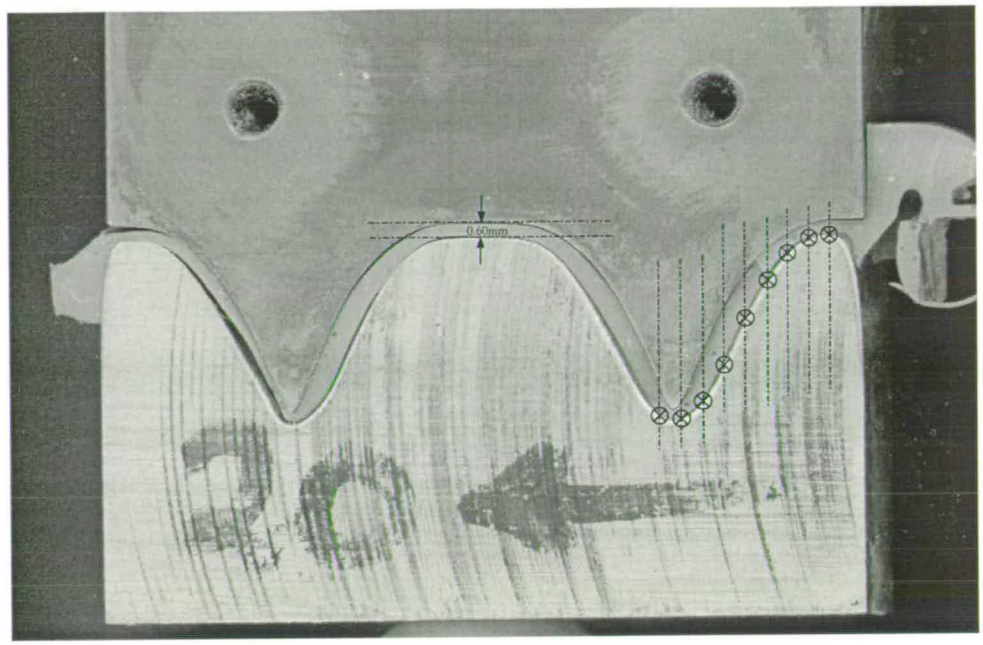

Figure 8.4-1: Tool (upper electrode) and workpiece from DC 2-D trials, illustrating gap and geometric measurement procedure

In order to confirm that the tool solution converged at the specified gap, additional machining operations were carried out at gaps slightly below and above the nominal value of 0.60 mm. These were 0.40 mm, using a voltage of 18.8±0.1V, and 0.80 mm using a gap voltage of 32.4±0.1V (obtained using the data in Figure 6.4-1).

Machined profiles produced at 16 l/min are plotted, with the theoretical profile (Equation 8.1-1), for the computed nominal gap at 0.6 mm and the additional profiles at gaps of 0.4 mm and 0.8 mm in Figure 8.4-2. A close spatial correspondence to the model workpiece shape can be seen at the set gap of 0.6 mm whilst, as would be predicted, at the gap of 0.8mm the machined profile is wider than the model shape and narrower for the 0.4mm gap. However, because the convergence to conformity between the theory and machined profile is difficult to quantify in the spatial domain a series of Fourier transforms were applied to produce the coefficients a_1 and a_2 for the experimental profiles. Convergence was then quantified as the minimisation of the difference $a_{1(diff.)} = a_{1(theroy)} - a_{1(exper.)}$ and $a_{2(diff.)} = a_{2(theroy)} - a_{2(exper.)}$. This gives $a_{1(diff.)}$ and $a_{2(diff.)}$ for the 0.4 mm gap profile of 0.14 and 0.31 respectively and for the 0.8× mm gap profile of –0.13, 0.27 respectively. Which compares with the case of 0.6 mm gap, on which the actual tool design was based, of 0.01 and 0.00 respectively. From these data, close convergence to correspondence at the tool design gap of 0.6 mm can be clearly seen.

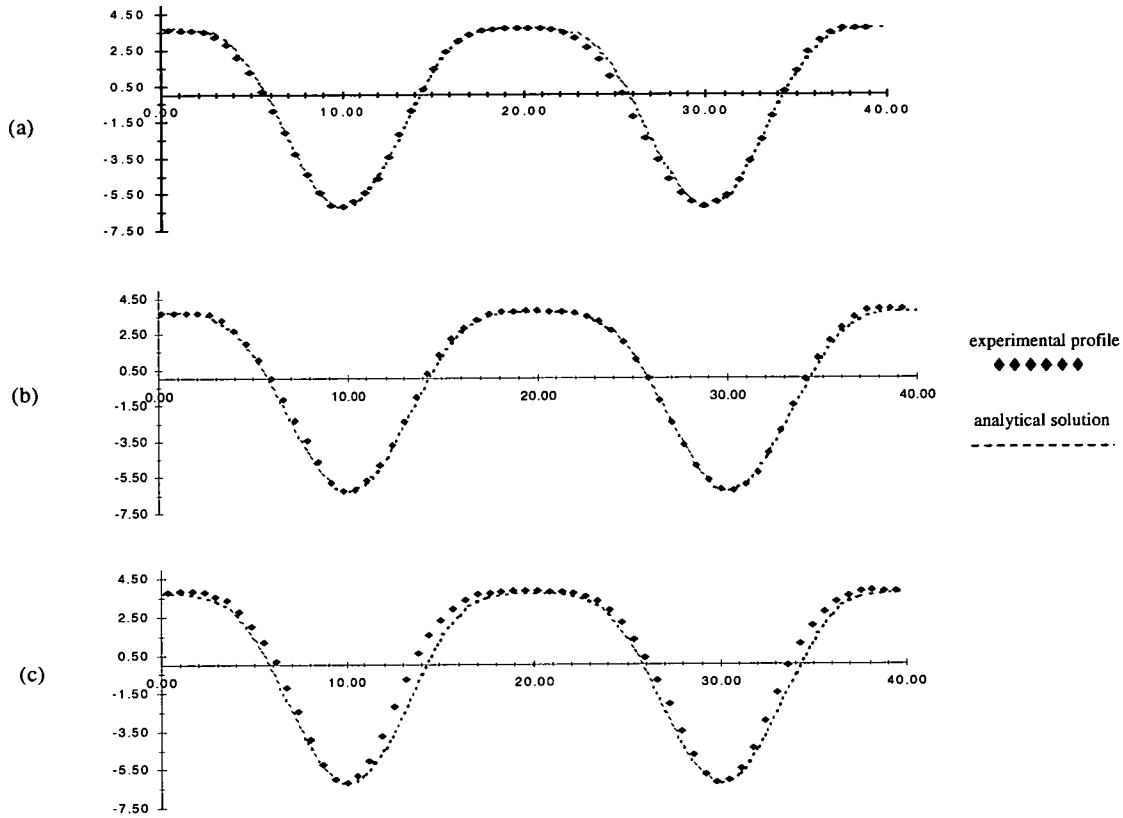

Figure 8.4-2: Theoretical solution (dotted line) plotted against machined form all at 16 l/min for nominal gaps of (a) 0.8mm, (b) 0.6mm and (c) 0.4mm (y-axis is in units of mm on all plots)

Gap data for the case of the trial carried at the lower flow rate of 4 l/min for both the planar and 2-D trials, are shown plotted in Figure 8.4-3. This data has been plotted at each point as a ratio of the gap measured at 16l/min to the gap measured at 4 l/min at each of the flow path intervals. This representation best illustrates the deviation in gap dimensions for the case of low flow rates (due to C-function dependencies) relative to gaps at constant k-values. The data is shown plotted with ±0.015 mm error bars corresponding to the estimated error when measuring pixel distances.

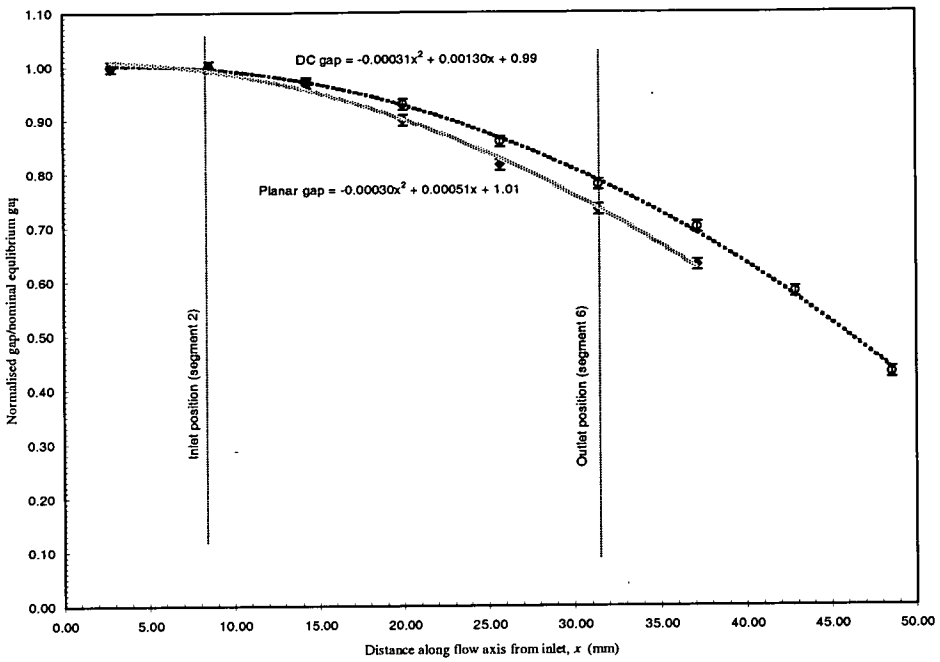

Figure 8.4-3: Gap deviation ratio normalised to inlet gap for both planar and DC profiles when machining In718/chloride system comparing flow rates of 16 and 4 l/min^{-1}

With reference to Figure 8.4-3 it can be seen that for the case of the planar configuration the gap decreases as the distance along the flow axis, x, increases. This relationship exhibits close correspondence to a second order polynomial fit of the form $C_1x^2+C_2x+C_3$ with C1 = -3.0 x 10^{-4}, C_2 = 5.1 x 10^{-4}, and $C_3 \approx 1.00$. In the case of the DC 2-D configuration the gap ratio against x relationship exhibits a close fit, within experimental error, to a polynomial with C_1 and C_3 equal to the case of the planar relationship, and the C_2 coefficient increased in value from 5.1 x 10^{-}3 to1.3 x 10^{-3}. Thus the difference between the two cases corresponds to a proportional shift of the gap against x relationship along the x-axis. Thus these results shows that gap against flow path length trends are not equivalent when comparing the planar case to 2-D shapes for this system. The shift in this relationship can however be modelled by the addition of a simple gain factor (to compensate for the differences in C_2 coefficients). It is hypothesised that this shift may be associated with the differences in pressure gradients which will exist in the two cases. Different pressure gradients will occur because of the differences in gap between the two cases and also the fact that in the 2-D profile the flow path length is approximately 20.9mm longer (see mathcad file "flow path length solver" in Appendix A2) than the 40mm of planar case. It seems likely that the differences in pressure profile would affect the degree by which gaseous products evolve out of solution. It is the existence of such products that seem to be the most likely cause of changes in the value of k, and hence the detected variations in C-function. In the case of the equal pressure gradients, then the C-function profile obtained using planar characterisation may be valid for the case of 2-D profiles without any need for adjustment. Investigation of this phenomenon further would require the use of back pressure

arrangements to control the distribution of pressure drop and assess if this would affect the IEG profile. It is likely that this profile will be sensitive to shape and that the apparent simple relationship noted in this case may be of limited use as complexity increases. Due to time constraints this was not carried out in the context of this thesis. Never-the-less, this work has shown that the small differences in gap profile between the Planer and 2-D cases can be modelled by use of a simple adjustment coefficient.

For the case of the In718/chloride system the C-function can now be formulated using the data in Figure 8.3-9 for positions at segment 2 and 6, and extrapolating for intermediate values using the polynomial function in Figure 8.4-3, as follows:

$$C(p) = 9.18 + 8.90p^{-1} + 8.52p^{-1} + 7.92p^{-1} + 7.14p^{-1} + 6.18p^{-1} + 5.04p^{-1}$$

Equation 8.4-1

The harmonic representation (see section 4.3) can be computed by setting on the loci of $p = e^{j\omega l}$ Equation 8.4-1 for $l=5.71mm$ with coefficients in units of $m^2\ sec^{-1}$.

Although a 7-point C-function formulation can be achieved readily by fitting of 2-point C-function data to the polynomial of Figure 8.4-3 in the case of the In718/chloride system, it was realised that this data could not be generated using only two point data for other systems. This can be demonstrated with reference to Figure 8.4-4 which shows the equivalent gap against flow path length relationship for the Ti6-4/chloride, In718/nitrate and Ti6-4/nitrate systems. These data are shown fitted with equivalent 2nd-order polynomials in the case of the equilibrium systems Ti6-4/chloride and In718/nitrate in Figure 8.4-4. Poor correspondence between the data for these cases and the polynomial fit is noted with deviations occurring well outside the ±0.1mm tolerance at some of the data points. In contrast to the In718/chloride system, these systems exhibit a relatively gradual fall-off in gap with a much steeper fall-off occurring towards the exit end of the flow path. In the case of the Ti6-4/nitrate system a linear fall-off in gap against flow path length is noted. In this case equilibrium conditions have not been established as indicated by the non-recovery of segments currents as the flow rate is reduced, as illustrated previously in Figure 6.4-14. This is the choking phenomenon and is not directly comparable to the equilibrium conditions that occur for the other systems where recovery of segment currents is noted (Figure 6.4-13,Figure 6.4-15 and Figure 6.4-16).

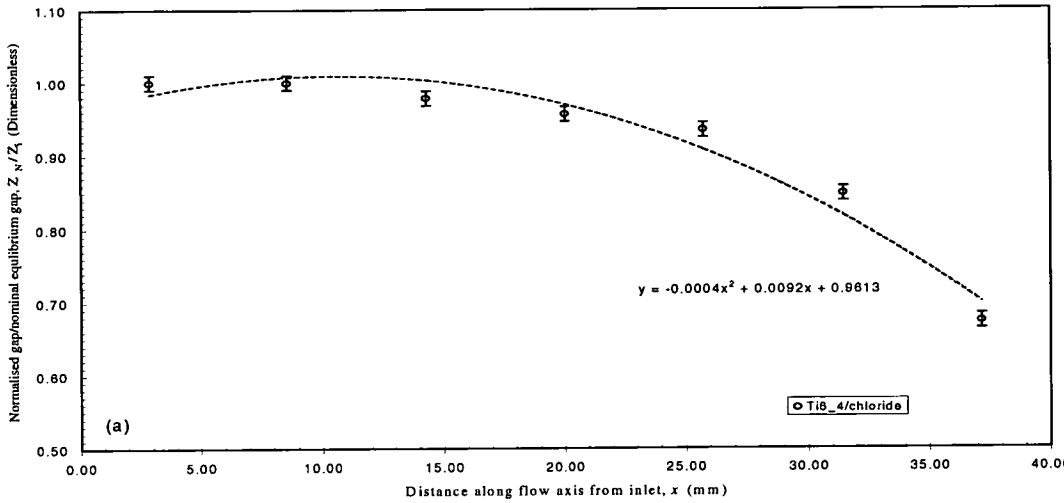

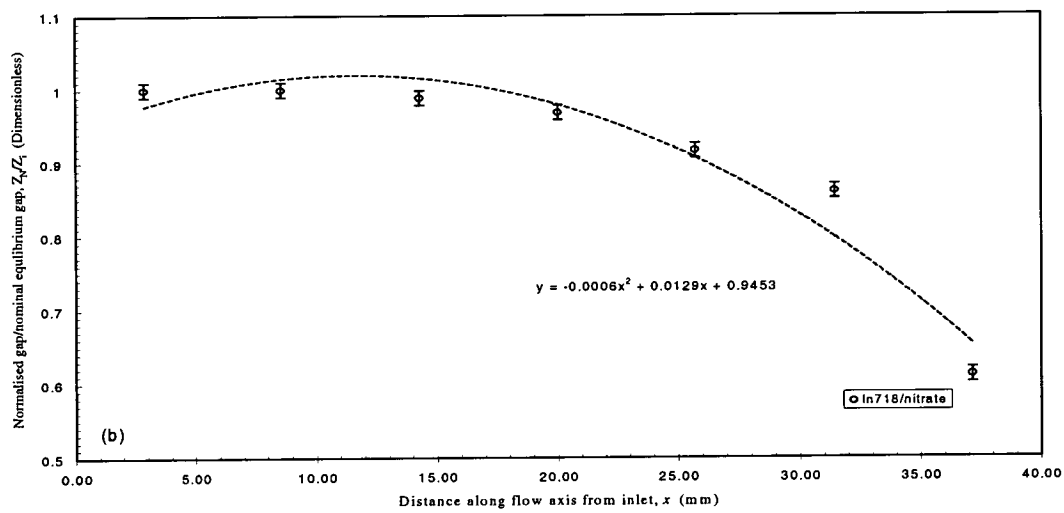

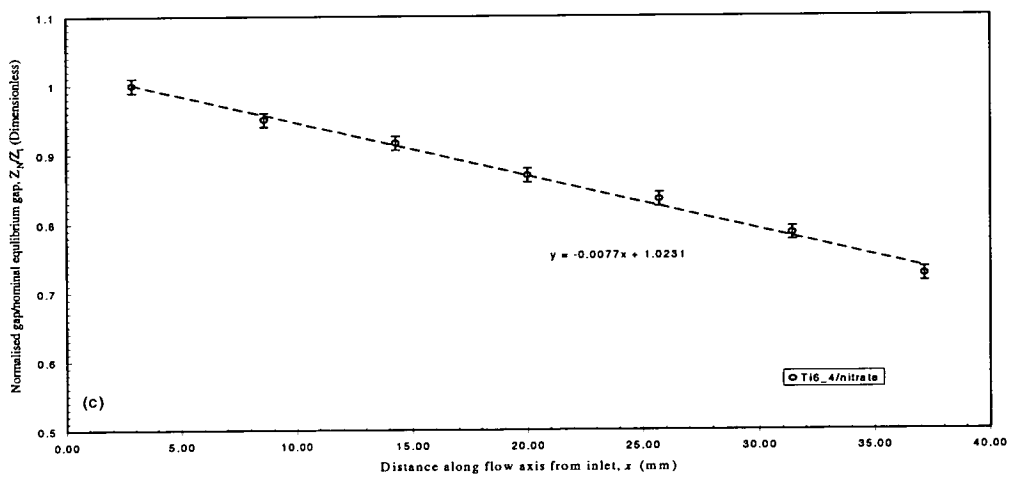

Figure 8.4-4: Normalised gap against flow path length at constant flow rate of 4l/min for: (a) Ti6-4/chloride system at equilibrium shown with 2nd order polynomial fit, (b) In718/nitrate system at equilibrium shown with 2nd order polynomial fit, and (c) Ti6-4/nitrate system shown with linear fit.

8.5 Chapter overview and conclusions

In this chapter, 2-point C-function characterisation data has been recorded for Ti6-4 and In718 materials machined in both chloride and nitrate electrolytes. Although the noise level in this data was of a significant level so as to prevent detailed analysis of relationship forms, some general trends have been identified, as follows:

- A general increases in k-parameter values with increasing current density occurring at high flow velocity conditions was noted for all machining systems. This effect was particularly pronounced in the case when machining the In718 /nitrate system. This is indicative of a drift in machining parameters that had previously been masked (although indicated by particularly large error values in the case of the In718/nitrate system) when using current-time and static measurement techniques.

- The change in workpiece height data, i.e. the erosion rate (generated in an intermediate stage in the gap measurement technique) has also been applied to compute the form of any valency drift with current density for the In718/system. No clear drift in this parameter was noted indicating that k-parameter drift was probably a result of V_0 sensitivities to J.

- At lower flow velocities non-ideal effects with differing forms occur in all systems. Representation of these effects in terms of 2-point C-functions has been demonstrated. It is confirmed (as indicated by other workers) that a gap taper forms at low flow velocities. This taper, which is characterised by a divergence in C-function between the flow inlet and exit sensing positions, probably result from the changes in gap resistivity. The causation of this change (i.e. whether caused by accumulation of products for example or not) is however difficult to qualify since the characteristics of these change is dependent on the system being machined. Thus simply attributing the void fraction parameter (as often done in the theoretical model by other workers) to parameterise these changes is not consistent with the results recorded here.

- Machining of a 2-D DC form has demonstrated that gap gradients are sensitive to the shape of workpiece to tool transfer characteristics. However, this difference in shape, which is likely due to differences in pressure distribution, can, in the case of the In718/chloride system, be characterised by a simple gain term applied to the C-function description. For other systems higher order C-functions would be required to provide sufficient resolution when extrapolation is used. In these cases gap measurement would be required at three or possibly more points.

CHAPTER

9 Conclusions and Future Directions

This section briefly reviews the work and conclusions of this thesis. Detailed expansions on these conclusions are given in the relevant chapters. An overview of intended future directions are given.

9.1 Thesis review and conclusions

The work of this thesis has been directed to the development of a measurement methodology for process characterisation of ECM. In Chapter one the justification for this work was provided through a discussion on the need to solve the process characterisation/tool design problem to avoid the iterative methodologies that are currently employed. From this discussion it was concluded that:

1. **The development of an effective characterisation strategy would lead to improved economic utilisation of the ECM process.**

The basis of the approach was established in Chapter two where it was concluded that:

2. **The k-parameter, which defines an assembly of machining parameters, represents an effective basis for the development of a process characterisation strategy.**

The work of others, described in Chapter four, has been directed primarily to the development of analytical descriptions of the ECM process. The review of this work concluded:

3. **That analytical descriptions of IEG phenomena provide useful insight, but do not provide the necessary accuracy for effective tool design purposes.**

4. **Achieving complete analytical descriptions may be unrealistic given the complexities and heterogeneous nature of ECM phenomena.**

As an alternative to these approaches the theoretical developments of this thesis, leading to a semi-empirical characterisation strategy, were outlined in Chapter four. From these developments it was concluded that:

5. **Current-time and gap-time solutions to planar dynamics are effective methods of obtaining averaged values for the k-parameter for conditions representative of practical ECM situations.**

6. **The C-function representation is an effective way of resolving averaging effects and mapping k-parameter interrelationships.**

The development of all experimental set-ups were described in Chapter five. In Chapter six, general current-time characterisation trials were detailed from which it was concluded that a wide range of *k*-parameter interrelationships existed, as follows:

7. **Relatively poor fit values in the *k*-parameter for the In718/nitrate system indicated drift in one or a combination of the constituents of *k***

8. **Current-time analysis applied to the TiAl/perchlorate and TiAl/chloride systems indicated the occurrence of different dissolution characteristics between the γ and α_2 phases of TiAl material.**

9. **The *k*-parameter values are sensitive to initial conditions (i.e. previous dissolution states) in the case of the In718/nitrate system.**

10. **From k-parameter fits to segmented current data, differing forms of dependency have been noted with reduced levels of flow volume for each of the systems studied. This is not readily accounted for by the analytical solutions reported by previous workers (Chapter three).**

The conclusions of Chapter six provide general reaffirmation that the *geometric response* of an ECM system to non-ideal conditions, of the kind often imposed in a practical set up, will be dependent upon a complex interaction of process variables. These complexities are probably indicative of different physiochemical and physical phenomenon occurring in the ECM system where there is a change in a system component (electrolyte or workpiece material) and/or machining parameters. This serves to illustrate that approaches, aimed at the development of fully analytical process descriptions, are probably unrealistically ambitious and unlikely to provide sufficient descriptive resolution. This leads to a justification of the semi-empirical description developed in this thesis as a means to characterise these dependencies. Achieving this by C-function measurement would require in-line determination of the ECM gap. The development of a method to achieve this by use of ultrasonic time-of-flight data, was described in Chapter seven where it was concluded that:

11. **The applications of ultrasound to gap measurement by *direct* means was found to be ineffective due to dissolution processes within the gap preventing effective reflection of the ultrasound.**

12. ***Indirect* means of gap measurement was found to be effective with gap measurements determined to be accurate to within $\pm$0.015mm.**

From the work described in Chapter eight, which reported on planar C-function trials and the application of C-function data to a 2-D double cosine profile, it can be concluded that:

13. **C-functions provide an effective representation of the effects, at low flow volumes (i.e. non-ideal effects), of the distribution of dissolution in ECM (i.e. local and spatial k-parameter variations).**

14. **The use of 2-point C-functions for representing non-ideal effects for the case of 2-D profiles is effective with the addition of a simple gain term added to the general equations in the case of the In718/chloride system.**

15. **Higher-order C-functions (probably 3rd order) would be required for representing other systems, especially when multiple interdependencies exist.**

9.2 Future directions

The work of this thesis has demonstrated the basis of applying C-function descriptions to ECM characterisation for planar and simple 2-D profiles. The wider application of C-functions to 2-D and 3-D profiles needs to be established. In particular, the ways in which C-functions are augmented for application to different profiles need to be further investigated. It has been suggested in this thesis that such an augmentation can be related to pressure distributions (which control the degree of void fraction influence) for the particular profile in question. This suggestion needs to be investigated in more detail.

The work of the thesis has considered C-function descriptions applied along single axis flow fields. In the wider application of ECM, however, particularly in the case of complex die production, then multi-axis flow fields (i.e. entering and exiting the IEG via more than one inlet/outlet port arrangement) may be required. In cases where each of these flow fields can be considered as independent then multi-axis C-function (a simple extrapolation of the work of this thesis) would be applicable. In case where these flow fields are not independent, which may be the case for particularly complex tooling, then the ideas presented in this thesis may need augmentation by high level flow modelling techniques (finite element methodologies, for example). These ideas are currently being considered in more detail.

Ultimately it is believed that application and subsequent further development of the C-function characterisation methodology will lead to the implementation of fully automated tool design/process specification system for ECM. Achieving this would lead to improved utilisation leading to greater competitiveness and hence wider application of the ECM process.

REFERENCES

[1] **Atkey, M.** Transforming Blades The Rolls-Royce Way. *The Industrial Robot*, December 1985, 231-235.

[2] Doc ref: **DW/EDM/5/10**, Marketing Information produced by Edinburgh Research and Innovation Services, using Web reference: http://www.eds.fr/charmilles/

[3] **Goyer, A.** ECM: Little known, but very useful. *Modern Machine Shop*, April, 1988, 62-69.

[4] **Larsen, J. M., Worth, B. D., Balsone, S. J. and Jones, J. W.** An overview of the structural capability of available gamma titanium aluminide alloys, *Proc. TiAl applications; The Minerals, Metals and Materials Society*, 1995, 821-834.

[5] **Yamaguchi, M., Inui, H. and Kishida, K.** Gamma Titanium Aluminide Alloys. *Materials Research Society Symp. Proc.*, 1995, **364**, 3-16.

[6] **Yoa, Z. and Marek, M** NaCl-induced hot corrosion of titanium aluminide alloy. *Materials Science and Engineering*, 1995, A192/193, 994-1000.

[7] **Golvin, G., Cianci, M., Kleyn, B. and Vanderleest, L.** Manufacture of XD gamma titanium aluminide airfoils. *Micro-structure property relationships in titanium aluminide alloys (The Minerals, Metals and Materials Society),* 1991 pp. 361-369.

[8] **Mantel, A. L. and Aspinwall, D. K.** Surface integrity and fatigue life of turned gamma titanium aluminide, *J. Mater Process Tech,* 1997, 72(3), 413-420.

[9] **Bently, S.A., Goh, N.P. and Aspinwall, D.K.,** Reciprocating surface grinding of a gamma titanium aluminide intermetallic alloy. *International Conference on Advances in Materials and Processing technologies*, AMPT-99. Dublin, 3-6/8/99, 331-340

[10] **Bentley, S.A. Mantel, A.L. Aspinwall, D.K.** The effect of machining on the fatigue strength of a gamma titanium aluminide intertmetallic alloy. *Intermetallics 7*, 1999, 967-969.

[11] **Mantel, A. L., Aspinwall, D. K. and Wise, M. L. H.** 3rd International Conference on the Behaviour of Materials in Machining, Institute of materials, UK, 1994, pp244-255.

[12] Offshore technology report: Fatigue performance of repaired tubular joints. *(OTH 89 307) HMSO*, ISBN 0014130965.

[13] **Clifton, D., Mill, F., Esanola, J., Kare, R. and Dover, W. D.** Diverless weld inspection and repair using it ECM ACFM techniques *J. of the Soc. for underwater Technology* 2000, 24(4) 131-141. (appended in appendix 1)

[14] **Debarr, A. E. and Oliver, D.** *Electrochemical Machining*, 1968 (Macdonald, London). Page 21-22.

[15] **Kellock, B.** Have a ball with a Cinderella process, Machinery and Production Engineering, May 1982, 41-46.

[16] **Howarth, P.** The chemistry of ECM, *PhD Thesis,* scheduled submission Oct 2002, Edinburgh University.

[17] **Wilson, J. F.** Practice and Theory of Electrochemical Machining, 1971 (John Wiley, London). Page 141, ISBN: 0-89874-229-3

[18] **Jain, V. K. and Pandey, P. C.** Tooling design for ECM *Precision Engineering*, 1980, **2**, 195-206

[19] **Jain V.K. and Rajurkar K. P.** An integrated approach for tool design in ECM. *Precision Engineering*, 1991, **13**(2), 111-124

[20] **Nilson, R. H. and Tsuei, Y. G.** Free boundary problem for the Laplace equation with application to ECM tool design *Transactions of ASME J. Applied Mechanics,* 1976, **8**(4) 54-58.

[21] **Datta, M**. Anodic Dissolution of Metals at high rates. *IBM J. of Res. and Develop.* 1993, **37**(2) 207-266

[22] **Mileham A. R., Harvey S. J. and Stout K. J.** The characterisation of electrochemically machined surfaces. *Wear.* 1986, **109**, 207-214

[23] **Tipton, H**. The dynamics of electrochemical machining. *Proc. 5th Int. Conf. Machine Tool Design and Research* . 1964, 509-522

[24] **Tipton, H.** The determination of tools shape for electrochemical machining *Machinery and Production Engineering*, 1968 (Feb), 325-328

[25] **Clark, W. G. and McGeough, J. A.** Temperature distribution along the gap in electrochemical machining. *J. of Applied Electrochemistry,* 1977, **7**(4), 277-286

[26] **Hopenfield, J., Cole, R. R.** Electrochemical machining - prediction and correlation of process variables *J. Engineering for Industry*, 1966, **88**(4), 455-461

[27] **De La Rue, R. E. and Tobias, C. W.** On the conductivity of dispersions, *J. Electrochemistry Society*, **106**(9) 1965, 827-833.

[28] **Hopenfeld, J., Cole, R.R.** Prediction of the one-dimensional equilibrium cutting gap in electrochemical machining. Trans. of *ASME J. Engineering for Industry*, 1969, **B**(8) 755-765

[29] **Thorpe J. F., Zerkle, R.D.** Analytic determination of the equilibrium gap in electrochemical machining *Int. J. Mach. Tool Des and Res.*, 1969, **9**, 131-144

[30] **Pramanik D. K., Agarwal R. A., De A. K.** Studies on the Electrolyte pressure distribution in the working gap in ECM using plane parallel electrodes *J. of the Inst. of Engineers,* 1977, **57**(5), 250-253

[31] **Jain V. K., Murgan S**. Investigations into the effect of cathode material on temperature distribution during electrochemical machining. *Int. J of production Research*, 1986, **24**(2), 439-450

[32] **Landolt D., Muller R.H. and Tobias C.W.** Anode potentials in high rate dissolution of copper *J. Electrochem. Soc.*, 1971, 118(1) 40-46

[33] **Davydov A. D. and Mirzoev R.A.** Effect of electrodes processes on the accuracy of electrochemical dimensional machining *Electrokhimiya*, 1972, **8**(10), 1463-1465

[34] **Mount, A.R., Eley K., Clifton, D.** Theoretical analysis of chronoamperometric transients in electrochemical machining and characterisation of titanium 6/4 and inconel 718 alloys. *J. Applied Electrochem,* 2000, **30**(4) 447-455

[35] **Bannard, J.** Electrochemical machining. *J. of Applied Electrochemistry*,1976 **7**(1), 1-29

[36] **Landolt, D.** Throwing power measurements during high rate nickel dissolution under active and transpassive conditions, *J. Electrochem. Soc,*1972, **119**(6), 708-712

[37] **Datta, M. and Landolt D.** On the role of mass transport and high rate dissolution of iron and nickel in ECM electrolytes - II Chlorate and nitrate solutions. *Electrochim. Acta*, 1980, **25**, 1263-1271

[38] **Bejar, M. A. and Gutierrez, F.** On the determination of current efficiency in electrochemical machining with a variable gap *J. Mater. Processing Tech.* 1993, **37**, 691-699

[39] **Moir, P. G., Harvey, J.** Some effects of electrolyte flow rates on the electrochemical machining process. 16th *MATADOR Conf.*, 1976, 257-281

[40] **Mileham, A. R., Jones, R. M., Harvey S. J.** Changes of valency state during electrochemical machining. *production points,* 1982, **4**(3), 168-170

[41] **Konig, W., Aachem, T. H., Humbs J.** A mathematical model for the calculation of the contour of the anode in electrochemical machining, *Annals of the CIRP*, 1977, **25** (1), 83-87

[42] **Zhou, Y., Derby, J. J.** The cathode design problem in electrochemical machining. *Chemical Engineering Science*, 1995, **50**(17), 2679-2689

[43] **Butt, R.** Optimum design with finite elements: design of electrochemical machining. *Journal of computational and applied mathematics*, 1993, 47(2), 151-165

[44] **Jain, V. K. and Pandey, P. C.** Finite element approach to the two dimensional analysis of electrochemical machining. *Precision Engineering*, 1980, **2**, 23-28

[45] **Hardisty,** H., **Mileham,** and **A. R. and Shivani H.** Theoretical and computational investigation of the electrochemical machining process for characteristic cases of a stepped moving tool eroding a plane surface. *Proc. Inst. Mech. Engrs. Part B: J. Engineering Manufacture.* 1997, **211(3)**,197 –210.

[46] **Hardisty,** H., **Mileham A. R. and Suirvani, H.** Analysis and computer simulation of the electrochemical machining process: a stepped moving tool eroding a plane surface. *Proc. Inst. Mech. Engrs. Part B: J. Engineering Manufacture*, 1996, **210(2)**, 109-118.

[47] **Hardisty, H and Mileham A. R.** Finite element computer investigation of the electrochemical machining process for a parabolically shaped moving tool eroding an arbitrarily shaped workpiece. *Proc. Inst. Mech. Engrs. Part B- J. Engineering Manufacture*, 1999, **213** (8) 787-798

[48] **Tsuei, Y. G., Yen, C. H. and Nilson R.H.** Theoretical and experimental study of workpiece geometry in electrochemical machining. *American Soc. of Mech. Engineers*, 1977, **3**(1), 1-5.

[49] **Deconinck J., Maggetto G.** Calculation of current distribution and electrode shaped change by the boundary element method. *J. Electrochem Soc.*,1985, **132**(12), 2960-2965

[50] **Tsuei, Y. G. and Nilson, R.H.** Effects of variable electrolyte conductivity on side gap geometry in ECM. Int. J. Mach. Tool Des and Res., 1977,**17**(1), 169-178.

[51] **Narayanan, O. H., Hinduja, S. and Nobel C. F.** The prediction of workpiece shape during electrochemical machining by the boundary element method. *Int. J. Mach. Tool Des. Res.*, 1986, **26**(3), 323-338.

[52] **Konig, W., Aachen, T. H. and Humbs, J.** Mathematical model for the calculation of the contour of the anode in electrochemical machining. *Annals of the CIRP*, 1977, **25**(1), 83-87.

[53] **Jain, V. K., Yogindra, P. G. and Murugan S.** Prediction of anode profile in ecbd and ecd operations. *Int. J. Mach. Tools Manufact*, 1987, **27**(1), 271-286

[54] **Kozak, J., Dabrowski, L., Lubkowski, K. and Rozenek, M.** The effect of electrochemical dissolution characteristics on shape accuracy in ECM. *Proc. 13th Int. CAPE Conference*, 1977, 511-519

[55] **Reddy, M. S., Jain, V. K. and Lal, G. K.** Tool design for ecm: correction factor method *J. Engineering for Industry*, 1988, **110**(1), 111-118

[56] **Jain, V. K. and Pandey, P. C.** Design and analysis of ECM toolings. *Precision Engineering*, 1979,1 (4), 1199-206

[57] **Filtatov, I. E.** The numerical simulation of the unsteady ECM process *Journal of materials processing technology* **109** (1) 2001, 327-332

[58] **Nied, H. A. and Perry, E. M.** Finite element simulation of the electrochemical machining process. *American Society of mechanical engineering materials division (publication).* 1990, 20(1), 37-57

[59] **Narayanan, O. H., Hinduja, B. E., and Nobel, C. F.** Design of tools for electrochemical machining by the boundary element method. *Proc. Instn. Mech. Engrs,* 1986, **200**(C3), 195-205

[60] **Shuvra, D.A.S. and Ambar, K. M.** Use of boundary element method for the determination of tools shape in electrochemical machining *Int. J. for numerical methods in engineering*, 1992, **35**(3), 1045-1054.

[61] **Nilson, R. H. and Tsuei, Y. G.** Inverted Gauchy problem for the Laplace Equation in Engineering Design *J. of Engineering Mathematics*, 1974, **8**(4), 329-337.

[62] **Chang, C. S., Hourng, L. W., and Chung, C. T.** Tool design in electrochemical machining considering the effects of thermal fluid properties. *J. Applied Electrochemistry*, 1999, **29**(1), 321-330

[63] **Kozak, J., Budzynski A. F. and** Domanowski, P. Computer simulation electrochemical shaping (ECM-CNC) using a universal tool electrode. *J. Materials Processing Technology*, 1998, 76(2), 161-164.

[64] **Kozak, J., Chuchro, M., Ruszaj, A. and Karbowski, K.** The computer aided simulation of electrical process with universal spherical electrodes when machining sculptured surfaces *J. of Materials Processing Technology* 107 (1), 2000, 283-287.

[65] **Kozak J., Dabrowski L., Lubkowski K., Rozenek M. and Slawinski R.** CAE-ECM system for electrochemical technology of parts and tools *J. of Materials Processing Technology* 107(1) 2000, 293-299.

[66] **Ruszaj, A.** Investigations aiming to increase electrochemical machining accuracy, *Precision Engineering,* 1990, **12**(1), 43-48.

[67] **Zawistowski, F.** New system of electrochemical form machining using universal rotating tools. *Int. J. Mach. Tool Manufacture,* 1990, 30(3), 475-483

[68] **Shulepov A. P., Kapstov, A.V., Shmanev, V.A. and Filimoshin, V. G.** Characteristics of electrochemical machining of titanium alloy by a sectional cathode under conditions of interruption of the process *Soviet Surface Engineering,* 1987, **5**(2),78-81.

[69] Shulepov, A.P., Kapstov, A.V., Shamev, V. A., and Filimoshin, V. G. A system to control the process of electrochemical machining by a sectional cathode. *Soviet Surface Engineering*, 1985, **2**(2), 85-87

[70] Shulepov, A.P. A study of the accuracy of electrochemical forming of a surface by a sectional tool with current commutation during the machining time. *Soviet Surface engineering*,1983, 6(1), 13-15

[71] Khairy, A. A knowledge-based system for electrochemical machining procedure. *J. Materials Processing Technology*, 1995, **58**(2), 121-130.

[72] Machineability data centre, *Machining data Handbook*, third edition vol. 2 (1980), ISBN: 09-3697-4001

[73] Bhattacharyya, B and Sorkhel, S. K. Investigation for controlled electrochemical machining through response surface methodology based approach. *J. Materials Processing Technology*, 1999, **86**(2) , 200-207.

[74] Hewidy, M.S. and Fattouh M. Electrochemical cutting using tubular cathodes: response surface approach *Int. J of production Research.* 1989, 27 (6), 953-963.

[75] **Massey, B. S.** *Mechanics of Fluids*, 6th edition Chapman and Hall, London, 1995. ISBN: 0-582-23408-5

[76] **Douglas, J. F. Gasiorek, J. M. Swaffield, J.A..** *Fluid Mechanics*, third edition, Logman, London 1995. ISBN: 0-442-30552-4

[77] Clifton D., Mount A. R., Jardine D. J. and Roth R. Electrochemical machining of gamma titanium aluminide intermetallics, *J. of Mater. Processing tech.*, 2001, 108 (3), 338-348 (appended in Appendix A1)

[78] Mount A. R., Clifton D., Howarth, P,. and Sherlock, A. An integrated strategy for materials characterisation and process simulation in electrochemical machining. *Proceedings of 9th Int. Manuf. Conf. In China,IMCC2000. Hong Kong, 2000* (appended in Appendix A1)

[79] **Clifton, D. and Mill, F.** The development of manufacturing processes in gamma titanium aluminide. EPSRC Final Report. 1995. IMI ref IMI/A/01/035, EPSRC grant Ref: GR/K67007

[80] Sorkhel, S. K. and Bhattacharyya, B. Parametric control for optimal quality of the workpiece surface in ECM *J. Materials Processing Technology,* 1994, ***40 (1),*** 113-134.

[81]Clifton, D., Alder, G. M., Mount, A. R., Jardine D. J. The use of ultrasound for in-line measurement of the inter-electrode gap in electrochemical machining. *Proceedings of 9th Int. Manuf. Conf. In China,IMCC2000. Hong Kong, 2000* (appended in appendix 1)

[82] Ing, C., Bignon, E.S. and Bedrin C. Application of eddy currents to in-process measurement of the gap in ECM. *Annals of the CIRP*, 1982, **31**(1), 115-119

[83] Berke, M. Basic principles of non-destructive material testing with ultrasonic, *Krautkramer publishing* (GMBH), SD218, 1996. (NB available only from Krautkramer publishing)

[84] Schlengermann, U,. The Krautkramer Booklet, *Krautkramer publishing (GMBH)*, 1982 (NB available only from Krautkramer publishing)

[85] Griffin, S. J., Hull, J.B. and Lia, E. Development of the novel ultrasound monitoring system for container filling operations. *Journal of Materials Processing Technology*, 2001, **109**(1) 72-77.

[86] Alder, G. M., Clifton, D. and Mill, F. A direct analytical solution to the tool design problem in electrochemical machining under steady state conditions. *Proc Instn Mech Engrs.*, 2000 **214** (B), 754-749

Process Characterisation for Electrochemical Machining

PhD Thesis

David Clifton

Appendices

A1. Publications

A2. Mathcad worksheets

A3. Mathematical derivations

A4. Alloy compositions

A5. Calibration of segment current transducers

A6. Raw data (in graphical form) from C-function trials

A1 Publications

The following appended publications have been published throughout the course of the work in this thesis. They include work which has been detailed in the thesis, and also some details which extend the work contained in the thesis.

Clifton, D., Mill, F., Esanola, J., Kare, R. and Dover, W. D. Diverless weld inspection and repair using it ECM ACFM techniques *J. of the Soc. for underwater Technology* 2000, 24(4) 131-141. [Reference 13 in thesis]

Mount, A.R., Eley K., Clifton, D. Theoretical analysis of chronoamperometric transients in electrochemical machining and characterisation of titanium 6/4 and inconel 718 alloys. *J. Applied Electrochem*, 2000, **30**(4) 447-455 [Reference **34** in thesis]

Clifton D., Mount A. R., Jardine D. J. and Roth R. Electrochemical machining of gamma titanium aluminide intermetallics, *J. of Mater. Processing tech.*, 2001, 108 (3), 338-348 [Reference **76** in thesis]

Mount A. R., Clifton D., Howarth, P,. and Sherlock, A. An integrated strategy for materials characterisation and process simulation in electrochemical machining. *Proceedings of 9th Int. Manuf. Conf. In China,IMCC2000. Hong Kong, 2000* [Reference **77** in thesis]

Clifton, D., Alder, G. M., Mount, A. R., Jardine D. J. The use of ultrasound for in-line measurement of the inter-electrode gap in electrochemical machining. *Proceedings of 9th Int. Manuf. Conf. In China,IMCC2000. Hong Kong, 2000* [Reference **79** in thesis]

Alder, G. M., Clifton, D. and Mill, F. A direct analytical solution to the tool design problem in electrochemical machining under steady state conditions. *Proc Instn Mech Engrs.*, 2000 **214** (B), 754-749 [Reference **83** in thesis]

ISSN 0141 0814. Journal of the Society for Underwater Technology, Vol. 24, No. 4, pp. 131–141, 2001

Diverless Weld Inspection and Repair Using ECM/ACFM Techniques

D. CLIFTON[1], F. MILL[1], J. ESNAOLA[1], R. KARE[2] and W. D. DOVER[3]

[1] School of Mechanical Engineering, University of Edinburgh, King's Buildings, Edinburgh EH9 3JL, [2] TSC Ltd, 6 Mill Square, Wolverton Mill, Milton Keynes MK12 5RB, [3] Department of Mechanical Engineering, University College London, Torrington Place, London WC1E 7JE, UK

Abstract

This paper describes the development and application of an integrated tooling/NDT system which provides the potential to undertake a weld inspection, carry out removal of the defective zone, and achieve validation of the repair, all within a single ROV deployment operation. Removal of the defect zone is achieved using a novel application of the electrochemical machining process (ECM). This system is integrated with the alternating current field measurement (ACFM) system, for crack detection, location and sizing. The paper describes the development of electrochemical machining process models to cover situations encountered in automated weld sampling operations. From these models, and data collected from experimental trials, it has been determined that the sampling/removal operation can be carried out at tool feed rates of up to 3 mm/min. The model has been extended for determining the change in gap dimensions for the case of zero tool feed. This relationship can be used as a control parameter when determining the degree of overcut required when inclusions are encountered and the tool is required to remain stationary for a certain duration. Tank trials of the system have been carried out, successfully demonstrating effective operation of the integrated strategy in a submersed environment.

1. Introduction

In many offshore oil and gas production platforms extension of use beyond the original design life is being sought. To achieve this, NDT inspections, and the application of defect repair techniques, will have to be undertaken. At shallow sea depths, the use of diver deployment can often be considered for such operations, although in many cases this is considered hazardous, cumbersome and costly. In some of these situations the use of ROV based inspection, repair and maintenance (IRM) systems would be considered advantageous. At depths greater than 200 m, ROV based IRM would be a common if not essential requirement.

IRM is commonly directed to structural welds. The first part of this operation involves the accurate detection of defects through the use of NDT technologies. In some cases a methodology is then deployed to remove the crack and repair the defective zone. NDT re-examination may then take place to assess the effectiveness of the repair operation. This paper describes the development and application of an integrated tooling and NDT system which provides the potential to undertake a weld inspection, carry out removal of the defective zone, and achieve validation of the repair, all within a single ROV deployment operation.

One way to remove a weld defect is by the application of conventional grinding systems. However, it has been reported [1] that the use of grinding can impart additional stress at the machined site and this can result in a residual surface which is prone to further crack growth. The system described in this paper achieves crack removal by a novel application of the electrochemical machining (ECM) process. This technique does not impart additional stress into the machined zone and is known to leave behind a surface of high structural integrity [2]. Also, because the process is essentially forceless it can readily be applied without the use of bulky mechanisms. Thus the system readily lends itself to ROV deployed operations. Furthermore, unlike grinding, the ECM system will enable a sample of the defective zone to be retained for subsequent metallurgical analysis. Such analysis can often provide an estimate of the residual life of a structure or be used to provide information about whether the defect was introduced at the time of manufacture or has arisen during service.

The basis of the ECM defect sampling system has previously been described [3]. This paper describes the development of process models to cover situations encountered in automated weld sampling operations. The model is used to provide parameterisation of the sampling process which is then validated through experimental trials. The paper describes the systems re-engineering for submersed operations and integration of the ECM tool with the alternating

current field measurement (ACFM) system, for crack detection, location and sizing. The tank trials of the integrated assembly are described.

2. ECM Sampling Process Model Developments and Validation

ECM is carried out by applying an electric potential across an electrolyte flowing in the gap between an electrode tool (biased as the cathode) and the welded structure (biased as the anode). This arrangement forms an electrochemical cell through which electric charge flowing as a result of the applied potential causes electrochemical dissolution of the weld zone in the immediate region of the cathode tool. The tool electrode is then traversed in an appropriate way so as to remove and/or sample the defect. For general background and overview on the ECM process see references [3] and [4].

The ECM sampling tool bit consists of a section of tubing shaped so that the outer cutting face forms an approximate inverse of the required sample site profile. This has commonly been a 'U'-shaped section of the form shown in Figure 1. The tube is slotted around the forward facing cutting surface to enable the supply of electrolyte into the active cutting zone in the direction of feed. During the sampling operation the tool is fed into the workpiece along a 'boat-shaped' profile. When set to machine a deep cut, the operation can be configured to remove a sample of material containing the defect. In the case of shallow depths of machining the process is used to dissolve the surface of the workpiece to remove the defect.

The important design constraints have been the degree by which the tool tip is deflected during the sampling operation and the accuracy of the cut. These constraints have been examined through the development of both a tool deflection and a cutting dynamics model, as described in the following sections.

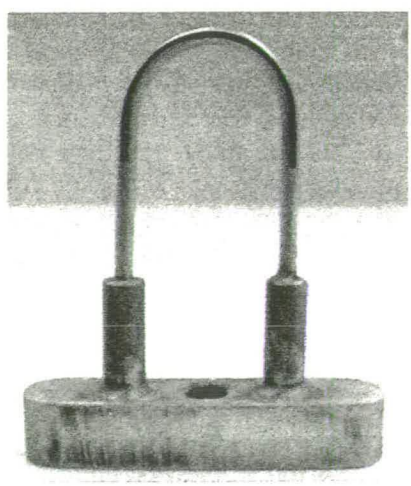

Figure 1 The ECM tool tip.

2.1 Tool deflection model

An important dependency with supply pressure will be the tool tip deflection; defined as the distance that the bottom tip of the tool is deflected in the opposite direction of tool feed, caused as a reaction to the momentum of the electrolyte flow rate in the direction of tool feed. This is considered as an important variable since if for any reason the supply was interrupted during machining then the tool tip would relax back to its non-pressurised position. If the deflection distance was greater than the tool to workpiece gap (in the direction of feed) then it would be possible for physical contact to occur between the tool tip and the workpiece. This is considered undesirable since tool damage may result if the situation is not recognised and the tool power remains on. To incorporate a fail-safe feature in this respect, a design criterion has been set to ensure that the tool deflection is less than the equilibrium gap. This criterion would enable re-entry of the tool path in cases where, for some reason, the original profile was not complete.

The tool tip deflection model, described in detail in reference [5], calculates the forces acting to deflect the tool due to the outflow of electrolyte, by calculating the change in fluid momentum at the supply slot. From this force, the strain energy as the function of the modulus of elasticity of the tool material is determined. Castigliano's theorem [6] is then applied to determine the maximum deflection occurring at the tool tip calculated as the sum of the individual deflections occurring at the curved section of the slot, the straight slotted section and the straight unslotted section of the tool.

The model has been used to calculate the degree of tool deflection in terms of the physical tooling parameters of outside diameter, o.d. (or $2r_t$, where r_t is the tool radius), the internal diameter, i.d., and electrolyte supply pressure. An important interdependence has been the relationship between the electrolyte supply pressure and level of electrolyte flow rate. The flow of electrolyte is required to remove solid and gaseous products of the dissolution process (i.e. mainly oxides of the metal being machined). There will exist a certain level of electrolyte flow rate, for a given level of forward feed rate, at which dissolution becomes unstable. Initial trials have shown a linear dependency between the limit of stable dissolution and the required flow rate of approximately 2.0 l/min for every 1 mm/min velocity of the tool feed.

2.2 ECM sampling process cutting models

The primary cutting parameters are the frontal gap, y, maximum overcut, g, and the maximum cut width, w, where it can be seen from Figure 2 that $w = 2r_t + (2g)$. Note that the overcut will be in all directions around the tool, and along the

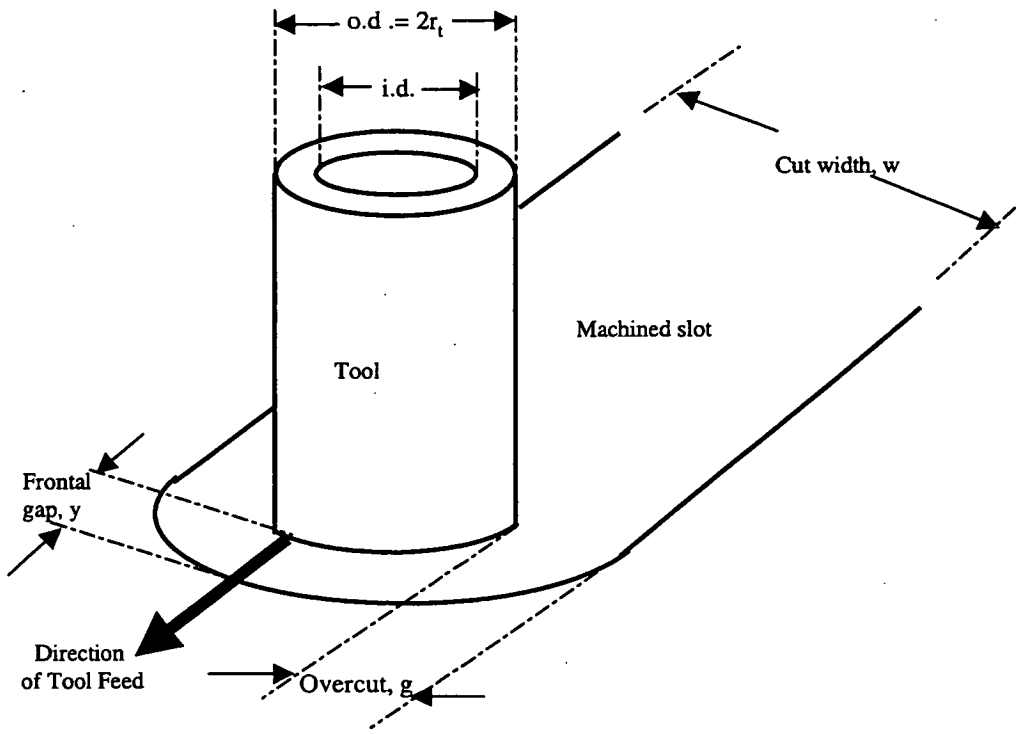

Figure 2 ECM tooling and cutting parameters.

length of the tool traverse, except at the tool face in the direction of feed. In this case the gap between the tool and workpiece is the frontal gap, y, which after a short period of machining, once equilibrium conditions have been established, becomes equal to the equilibrium gap, y_{eq}. The equilibrium gap will be the closest approach between the tool and the workpiece in the direction of the feed, and is therefore the parameter that must be quantified in relation to the tool deflection model. The process overcut (which corresponds to the accuracy of the cut) can be of critical importance when the wall thickness at the weld site is marginal within operation requirements.

A theoretical analysis of overcut and frontal gap can be made by considering the dynamic equations that relate the rate of material removal to the tool velocity and other set process parameters. This relationship can also be used to estimate the degree of overcut that will occur when the tool velocity is zero. Such a situation would occur when the tool encounters a non-conducting inclusion within the weld. In this case the tool is held stationary in order to increase the degree of overcut so as to machine around and free the inclusion from the surrounding material. The following theoretical analysis considers and develops relationships to address these situations.

Although seawater could be used as the machining electrolyte, the concentration is usually too low (at around 3%) to enable significant dissolution currents. The achievable removal rates would therefore be limited using seawater for the machining electrolyte. To enable relatively high removal rates, machining was carried out using a 15% NaCl solution made up in a separate tank and pumped to the tool tip. Because enriched electrolyte is directed only in the direction of tool feed, the gap model has been developed with the assumption that only the forward facing gap contains electrolyte at the enriched conductivity. The trailing face of the tool will only be in contact with a solution at the surrounding ambient concentrations and therefore components of erosion due to the trailing half circumference of the tool will be small, and have been neglected.

Figure 3 shows the two erosion situations that occur during the sampling operation; Figure 3(a) represents the situation for a finite constant tool feed and Figure 3(b) is a representation of the situation when the ECM tool bit is held static. The erosion model is first developed to determine the frontal equilibrium gap, y_{eq}, as shown in Figure 3(a), by considering the basic equations of ECM dynamics developed for the case where the tool surface is perpendicular to the direction of feed and where the lines of electric flux are parallel to the direction of feed. This situation occurs along the y-axis (representing the relative position of the workpiece surface referenced to the tool surface) as illustrated in Figure 3(a). In this area, the gap between the tool surface and the workpiece surface can be calculated using a general dynamic process description developed as follows.

Considering Figure 3(a), the rate of dissolution, as determined by Faraday's laws of electrolysis, is proportional to the current density, J, flowing in the electrolyte solution between the tool and workpiece surfaces. The current density, given

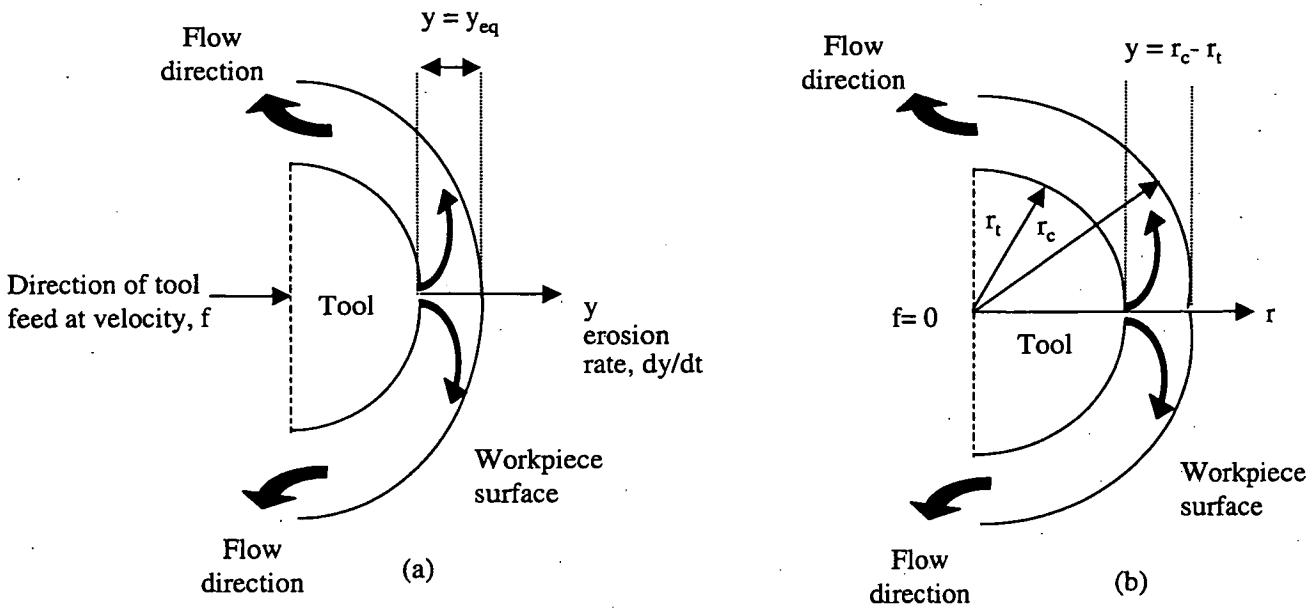

Figure 3 Gap model for two feed conditions: (a) constant, finite, feed rate and (b) static tool.

by $J = \kappa(V - V_0)/y$, can also be expressed in terms of the erosion rate, dy/dt, of the workpiece. Subtracting the change in position of the tool surfaces (i.e. the feed rate, f), moving along the y-axis, gives:

$$\frac{dy}{dt} = \frac{J\varepsilon}{\rho F} - f = \frac{\kappa(V - V_0)\varepsilon}{\rho F y} - f$$

or

$$\frac{dy}{dt} = \frac{k}{y} - f \qquad (1)$$

where k is a machinability constant given by:

$$k = \frac{\kappa(V - V_0)\varepsilon}{\rho F}$$

y is the gap measured along the y-axis as shown in Figure 3(a), $V - \Delta V$ is the voltage available to drive the current through the electrolyte (V is the applied machining voltage and ΔV is the total voltage loss at the tool and workpiece surfaces), κ is the conductivity of the electrolyte, ρ is the density of the workpiece material, ε is an electrochemical parameter calculated as the ratio of the average molecular weight of the workpiece material to the average valency of the ions precipitating into solution. It is assumed that the κ, ε and V_0 are constant and independent of other process parameters; F is the Faraday ($96{,}487\,\mathrm{Cmol}^{-1}$) and is a constant by definition.

In the limit $t \to \infty$, $dy/dt = 0$, equilibrium conditions are reached and $y \to y_{eq}$, the steady state gap value from which any steady state gap function can be formulated as:

$$y_{eq}(V, f) = \frac{\kappa(V - V_0)\varepsilon}{\rho F f} \qquad (2)$$

Equation 2 can be used to determine the equilibrium gap conditions as a function of set gap voltage and feed rate.

Examining the static tool condition illustrated in Figure 3(b) it can be seen that in this case the lines of electric flux, at equilibrium after a short period of machining, will be normal to the tool surface at all points on the tool. The gap can thus be considered to be equal to the difference between the radius of the cut r_c (the width of cut being $2r_c$) and the tool radius r_t, as illustrated in Figure 3(b). The volume of electrolyte between the tool/workpiece surfaces will increase with time, as the gap opens out, and hence the resistance of the electrolyte, R, in the gap, can be obtained by integration, thus:

$$R = \frac{1}{\kappa}\int_{r_t}^{r_c} \frac{1}{2\pi r} dr = \frac{1}{2\pi\kappa}\left[\ln \frac{r_c}{r_t}\right]$$

The current density at the workpiece surface, J_{r_c} is given by:

$$J_{r_c} = \frac{V}{R2\pi r^2} = \frac{\kappa V}{r_c \ln(r_c/r_t)}$$

And the rate of metal removal at the workpiece surface is given by:

$$\frac{dr_{r_c}}{dt} = \frac{\varepsilon J_{r_c}}{F\rho} = \frac{k}{r_c \ln(r_c/r_t)} \qquad (3)$$

Where k is the machinability constant as defined above.

Equation 3 can be solved, by integration, using the boundary conditions that $r_c = r_t$ at $t = 0$ and $r_c = r$ at $t = t$. Experimentally, the former boundary condition would correspond to touching electrodes, but in practice the experimental condition $r_c = r_t + \delta r$ is used, with δr made sufficiently small that $r_c \approx r_t$. This can be achieved by allowing the electrodes to touch, then separating them a small distance δr to prevent shorting. This gives the non-explicit relationship between the radius of the cut, r_c, and time, t, as follows:

$$kt = \tfrac{1}{2} r_c^2 \ln \frac{r_c}{r_t} - \frac{r_c^2}{4} + \frac{r_t^2}{4} \qquad (4)$$

Solving the equality of equation 4 for r_c in terms of t for a fixed value of r_t, will enable the interval of time for a required gap radius to be determined, for the case of zero tool feed.

In Section 5, the relationships developed above are applied to parameterise the defect removal/sampling process.

3. The ACFM Array Probe

Prior to defect sampling/removal, sizing and locating the defect is achieved using the ACFM system. The technique uses a uniform input current, arranged to flow in a direction normal to the expected crack direction, and requires measurement of two components of magnetic field, one parallel to the crack (Bx) and one normal to the surface under inspection (Bz). The presence of a surface breaking crack perturbs the uniform current flow, which in turn produces perturbations in both components of the magnetic field measured by the sensors. The Bx field responds to the surface current density, which decreases locally by an amount determined by the crack depth. The Bz field responds to circulation in the current flow, which is in a clockwise direction around one crack end and anticlockwise around the other end. In this way, the Bz signal exhibits a peak and trough, the separation of which determines the length of the crack.

In order to inspect the machined zone produced by the ECM tool, a purpose-built probe was produced. This has an interchangeable nose sized to fit the particular radius groove being cut. The nose produced contained eight sensor coils (four Bx and four Bz) arranged around a semicircular tip with an 8 mm radius. The array probe body included 'O' ring seals around the nose and on the removable side plate to prevent water access down to depths of around 10 m (this was the maximum depth required for the tank trials of this system).

4. ECM and ACFM Probe Carriage Assembly

A detailed view of the ECM/ACFM carriage/scanner assembly is shown in Figure 4. Both the ACFM probe and the ECM sampling tool are positioned within a single scanner assembly. The scanner assembly is driven by a single screw and nut arrangement, and guided via two guide rods positioned symmetrically about the drive screw. The drive screw, seen in Figure 4, is driven via a DC servo motor situated in the end enclosure. The end closure is sealed to operate at pressure in a submersed environment. The sampling tool and the ACFM probe are attached on opposite sides of a single sliding carriage to enable movement along a vertical axis. The sliding carriage is positioned via the position of a roller riding on a cam. The cam has two positions which are enabled by the hydraulic cam actuators. When positioned in a vertical orientation, during the ECM cutting phase, the cam acts to hold the ECM tool in position so that actuation of the feed motor moves the ECM tool along the required weld profile. When the cam is in the horizontal position the ECM tool retracts to its home position, and movement of the main screw then enables the ACFM probe to move along the surface of either the weld, when searching for a defect, or the sampled site, when the system is being used to validate the repair. The roller is of sufficient width and the cam has rounded edges to ensure smooth relocation of the roller and cam between the ACFM and ECM modes.

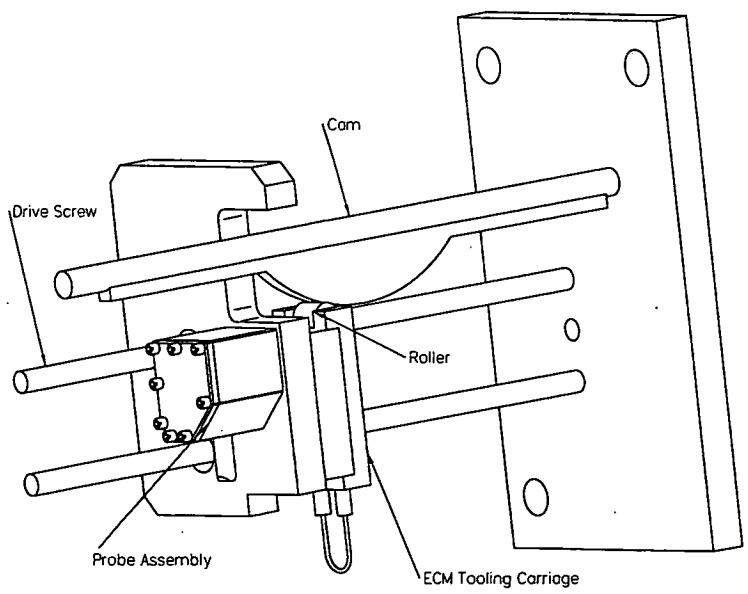

Figure 4 Schematic overview of ECM tooling and ACFM probe mounted on carriage/scanning assembly.

5. System Testing and ECM Tool Parameterisation

System testing and ECM tool parameterisation has been carried out for a range of process variables and two different tool configurations, made from copper tubing, as follows: tool A, 1.47 mm o.d./1.1 mm i.d. and tool B, 1.24 mm o.d./0.85 mm i.d. These sizes have been chosen as representing what is considered to be the lower and upper limit of outside tool diameter likely to be used in most practical situations. The tubing has been bent into a 'U' shape with a diameter across the machining face of 15 mm. The electrolyte supply slot runs across the face to cover a maximum machining depth of 10 mm from the surface of the weld.

Gap geometries and tool deflections have been measured by interrupting the process at the required conditions and then casting (using *Permadyne* dental casting paste) the region between the tool tip and the machined surface. The geometry is then measured by first sectioning the casting and then using a travelling microscope to read off the required dimensions. The angle that the cutting face makes with the horizontal reference position that the tool retracts to when the flow is turned off, is used to deduce the tool deflection during cutting when the flow is turned on.

Electrolyte solution has been made up as 15% wt/wt sodium chloride in water. The 15% concentration has been selected since it is easy to achieve such concentrations by agitation of the mixture for only a few seconds. In fact, some preliminary trials have suggested that this concentration could be achieved using an in-line salination system. If lower concentrations are used in subsea trials then the overcut and achievable feed rate will decrease, all other conditions remaining constant.

Trials have been undertaken using a workpiece in the form of a flat plate and also using flat T-butt welded sections. Figure 5 shows a typical example of the removed sample and sample site in the case of the T-butt welded section. These trials have been used to examine the following parameter trade-offs:

- Tool internal diameter against external diameter in relation to tool tip deflection for a range of pressure/flow characteristics. Any trade-offs considered for this relationship will be constrained by the requirement that the tool tip deflection should not exceed the forward cutting gap. The upper limit of tool deflection can then be used to confine other trade-offs.
- Inlet pressure against electrolyte flow rate. It is a requirement of ECM that the electrolyte is passed at high flow velocities into the machining gap. Such flow velocities should usually be in the region 2–4 l/min to achieve feed rates of between 1.0 and 3 mm/min.
- Machining current against feed rate. As the tool feed rate is increased the frontal cutting gap will decrease leading to a decrease in the gap resistance and hence an increase in the machining current. Limiting the machining current is of particular importance in a subsea environment where providing significant amounts of power could be cumbersome and expensive.
- Overcut against feed rate. The degree of accuracy of the sampling operation can be parameterised by the value of overcut. The accuracy of the operation will need to be specified if wall thickness tolerances at the sample are to be determined and held within specification.

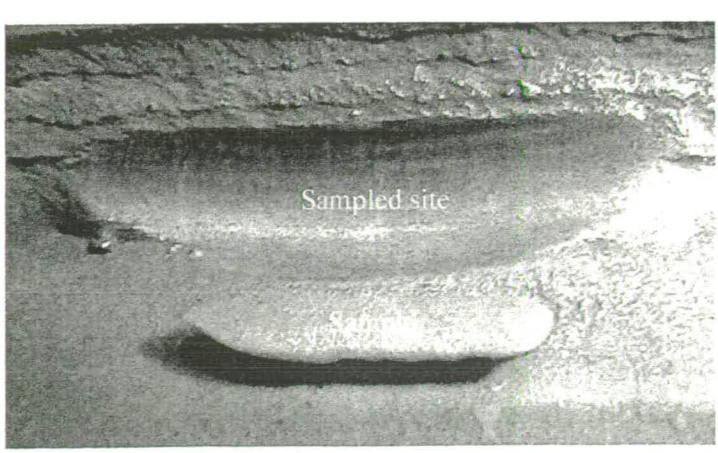

Figure 5 Removed sample and sampled site on T-section weld.

6. Tool Parameterisation Results and Conclusions

Tool parameterisation trials have been carried out over feed rates of 1–3 mm/min, 3 mm/min being considered to be the maximum feed rate that can reasonably be sustained given the required trade-offs on other parameters. From these trials it was noted that stable dissolution can be achieved at up to 3 mm/min when using a flow velocity of 4 l/min, for tool A (this flow velocity limit is slightly lower for B, because of the reduced area at the machining face). If the flow velocity is decreased then the feed rate needs to be reduced by a corresponding amount. From the experimental plot shown in Figure 6, inlet pressures of about 20 bar are required, in the case of tool A, to produce the flow rate of 4 l/min (slightly lower for tool B). Although increasing the pressure beyond this would provide greater flow rates, this would be at the added expense of requiring higher integrity enclosure seals and increased pump capacity. Therefore, if 20 bar is considered as a reasonable upper limit of tool supply pressure, then as an initial parameter constraint, tool tip deflections can be considered for supply pressure of up to 20 bar. Measured and

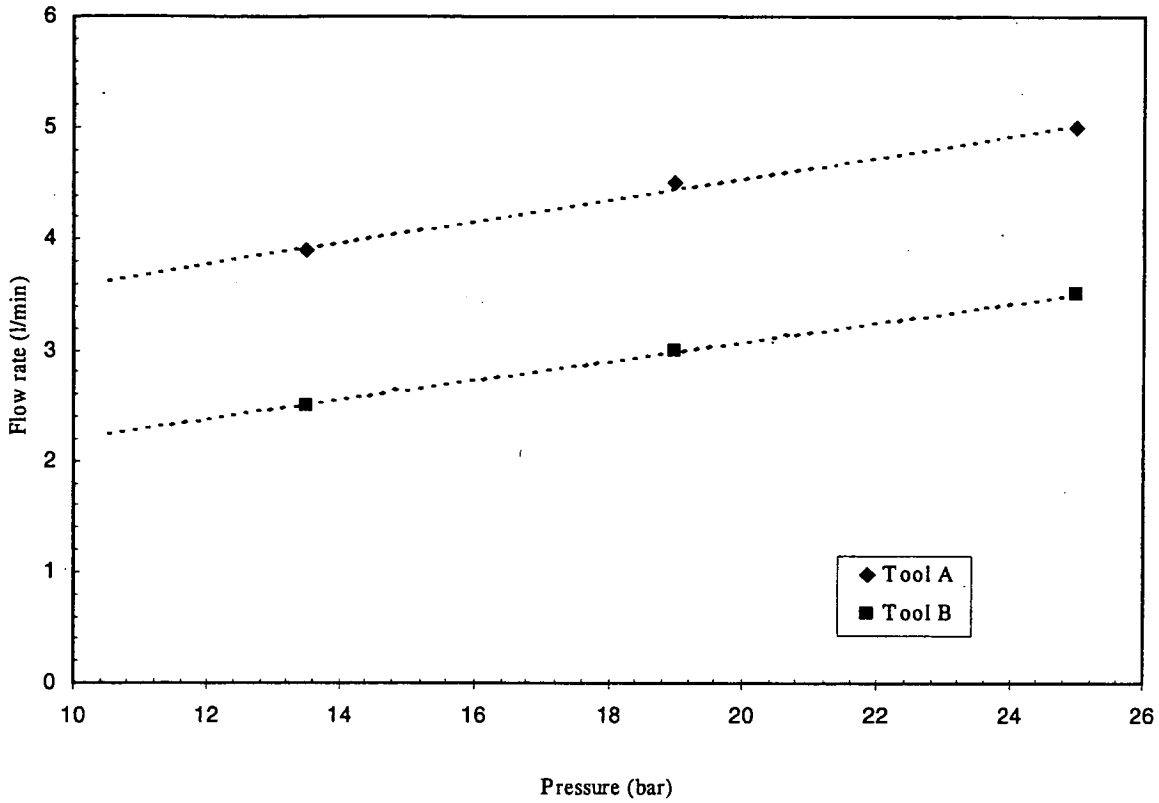

Figure 6 Flow rate against pressure for tool A and tool B shown with linear fit.

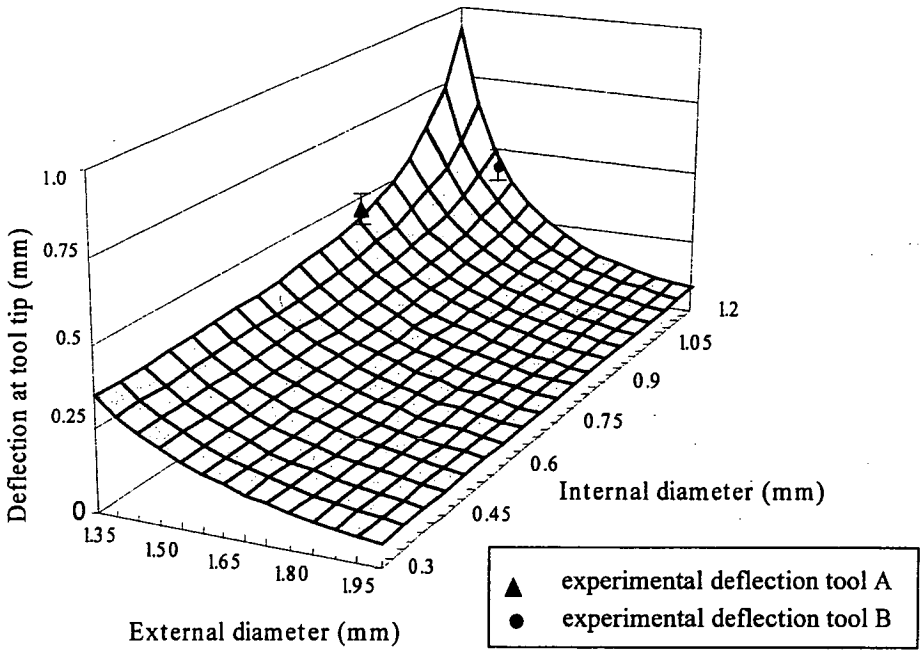

Figure 7 Surface plot of theoretical model and experimental tool tip deflection for copper tubing with a range of internal and external diameters, at maximum operating pressure of 20 bar.

theoretical defections are shown in Figure 7 plotted against variables of tool inside and outside diameters. The experimental points have been plotted with error bars of ±0.05 mm which is an estimated measurement tolerance. A close correspondence is noted between the experimental data and the theoretical surface in Figure 7, giving confidence in application of the model to other tooling configurations and process parameters.

To provide parameter ranges for tool deflection constraints, equation 2 has been used to examine the sensitivity of the frontal gap to the primary process parameters of V and f. Plotting this function, using the parameters of $\varepsilon = 28$ and $\rho = 7.8\,\mathrm{gcm}^{-3}$ for steel (as used in test trials, but these values should also be representative of the types of steels most commonly used subsea) and using a value of $\kappa = 0.2\,\mathrm{Scm}^{-1}$ (corresponding to the electrolyte concentration of 15% sodium

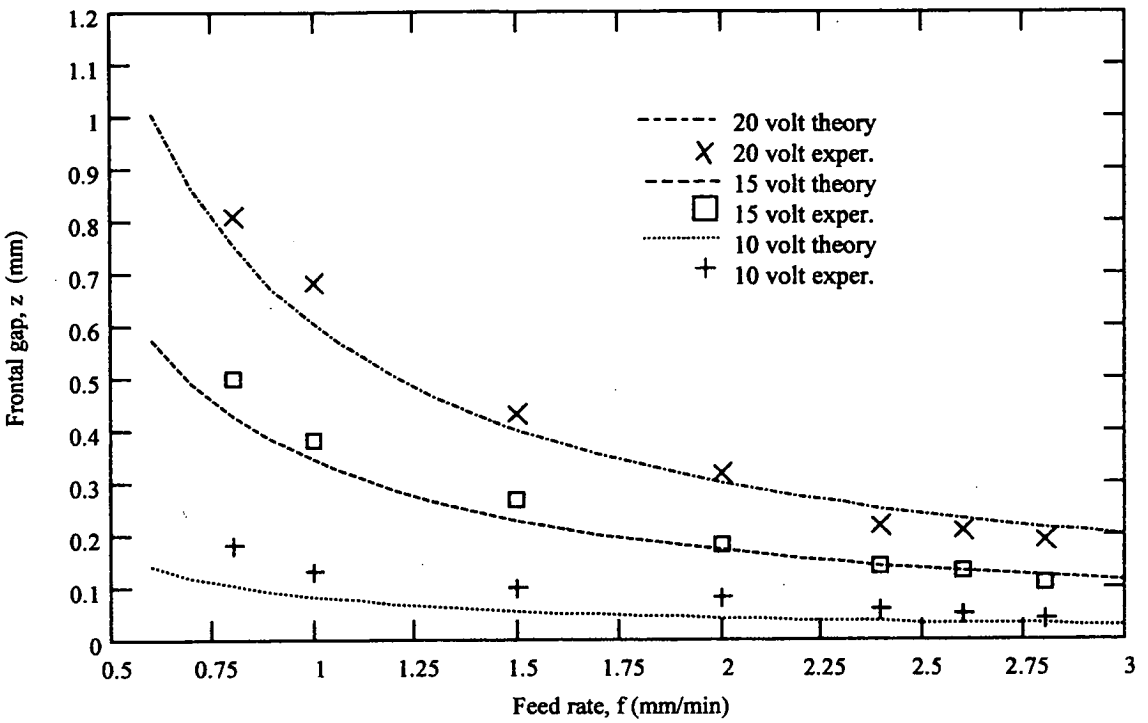

Figure 8 Frontal gap at equilibrium, z, against feed rate, f, at 10, 15 and 20 V for $k = 4.91 \times 10^{-9} m^2 s^{-1}$ using tool A.

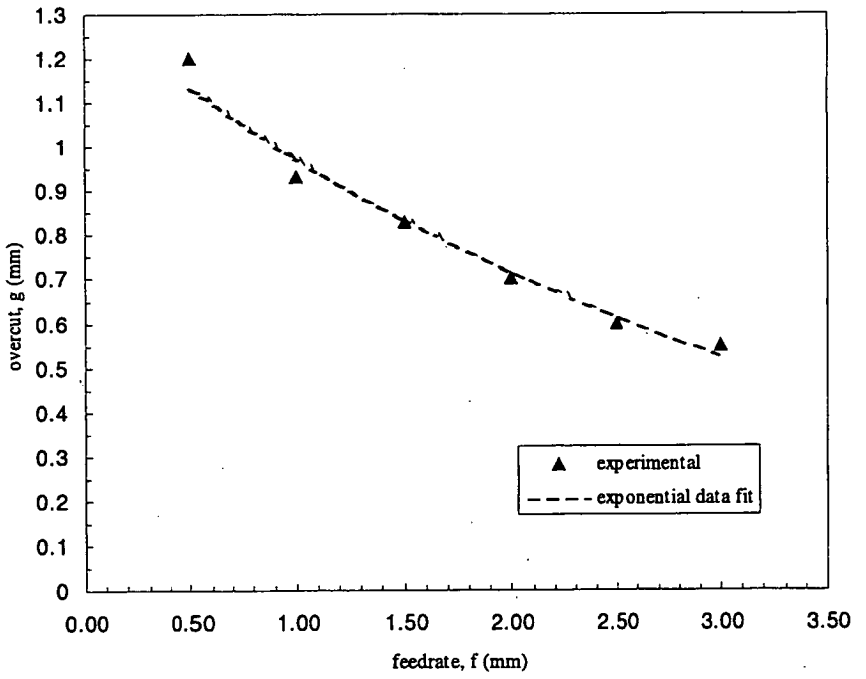

Figure 9 Overcut against feed rate for tool A shown with exponential fit.

chloride as used in the trials), gives the gap plot illustrated in Figure 8. Measured values of the frontal gap from experimental trials, plotted for the case of 10, 15 and 20 volts, show good correspondence to the theoretical line, thus providing confidence as to the validity of the plot for other sets of parameters. From this plot it can be seen that at the upper limit of feed rate of 3 mm/min when machining at 20 volts, the frontal gap at equilibrium is 0.2 mm. The tool deflection for this condition is in the region of 0.4 mm (Figure 9). Thus the tool deflection exceeds the frontal gap for this condition. A decrease in the supply pressure would decrease the tool deflection, but only at the expense of reducing the flow volume and hence the upper limit of attainable tool feed. Thus if feed rates of 3 mm/min are required, then the machining voltage would have to be raised (to in the region of 35 volts) according to equation 2, to increase the machining gap to 0.4 mm.

Now considering the parameter of overcut, g, in the case of a finite tool feed; it is noted that as the feed rate, f, is increased then the frontal gap will decrease (equation 2) and the overcut, which is also a function of the feed rate, will decrease. A

sampling head was fully submerged within a tank of electrolyte at a concentration of 15%. Some current would then flow between the workpiece and body of the sampling head. In the case of a subsea environment where the surrounding electrolyte will be at a concentration of only a few percent, then the base current will probably be in the region of a few amperes. The important information in Figure 11 is the gradient of the relationship between feed rate and machining current, which will be the same regardless of the base current value. From this relationship, it can be seen that the machining current, for a 15 mm width tool machining at a depth of 10 mm, will rise in approximate accordance to: $I(\mathrm{A}) = 22f(\mathrm{mm/min}) + \text{base current}$.

7. System Validation and Tank Trials

The system has been tested at a depth of 10 m using a tank testing facility at Oceaneering Ltd in Aberdeen. The test, shown in Figure 12, was carried out on a tubular node, submerged to a depth of about 10 m, in a tank of fresh water. The tubular welded T joint was made from BS4360 50D steel welded to typical offshore specifications. The T joint contained a fatigue crack at the hot spot stress site that had been produced using out of plane bend loading in a test rig at UCL. Figure 13 shows a close-up of the ACFM probe and the ECM sampling tool positioned over the weld toe. A 15% sodium chloride electrolyte was made up in a separate tank and supplied to the tool tip at a rate of 2 l/min. The sampling operation was carried out at a feed rate of 0.8 mm/min using a machining voltage of 12 V.

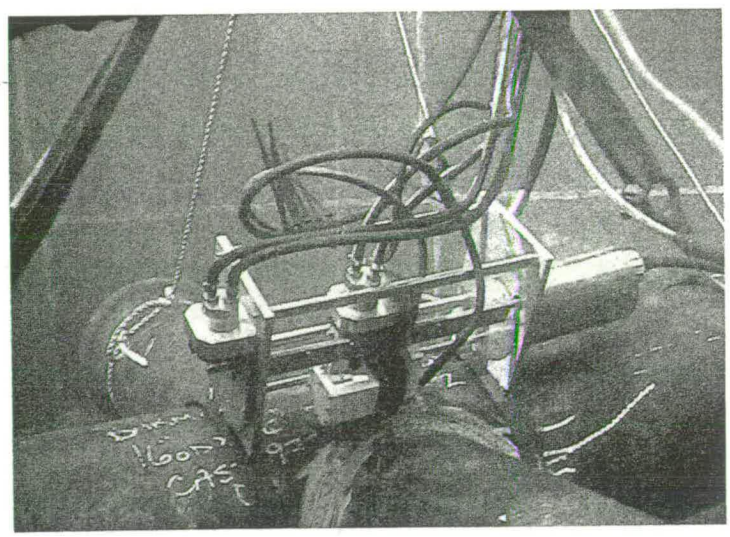

Figure 12 ECM/ACFM system during submersed operation in test tank.

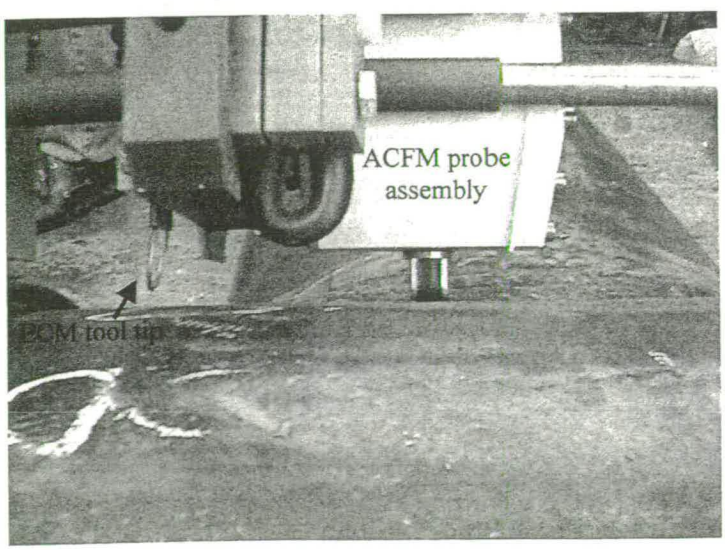

Figure 13 Close-up of ECM tool (in retracted position) and ACFM probe (in deployed positon) aligned at the weld toe.

The ACFM array probe and ECM drive actuator were connected through a 25 m underwater umbilical to the monitoring and control system, situated at the side of the tank. The weld toe at the cord side was scanned to determine the location and size of the defect. With the ACFM probe deployed and the ECM tool retracted the probe was driven along the brace/cord intersection. At the end of the scan the ACFM software displayed the crack signal as shown in Figure 14(a). The troughs in the Bx and Bz plots are typical of a defect present at the toe. The crack was sized as 20.9 mm long and 2.7 mm depth.

Once the presence of the defect was confirmed the ACFM array probe was retracted. The hydraulics were then activated to deploy the cam so that the ECM tool moved into position. The ECM tool was set to cut out the defect which it successfully completed in 55 min. The ECM tool was then retracted and the cam actuated to bring the ACFM probe back inline for scanning along the repaired surface. ACFM re-inspection was then carried out to confirm if the ECM had successfully removed the crack. Figure 14(b) shows an ACFM scan of the repaired surface. The absence of peaks and troughs in the ACFM traces confirm the complete removal of the crack.

8. Conclusions

The development of ECM parameter models, together with data from machining trials, has enabled the sampling operation to be accurately parameterised. From these models, and the data given in Figures 6 to 11, the following overview of tool parameterisation can be made. The defect sampling/removal operation can be carried out at tool feed rates of up to 3 mm/min. However, at these upper feed rates the quantity of electrolyte needed to obtain stable dissolution is in the region of 4 l/min supplied at a pressure of 20 bar. At this condition the tool deflection will exceed the frontal gap limit unless the machining voltage is raised to a value in the region of 35 V.

As an example of overcut parameterisation, consider using a 1.24 mm outside diameter tool,

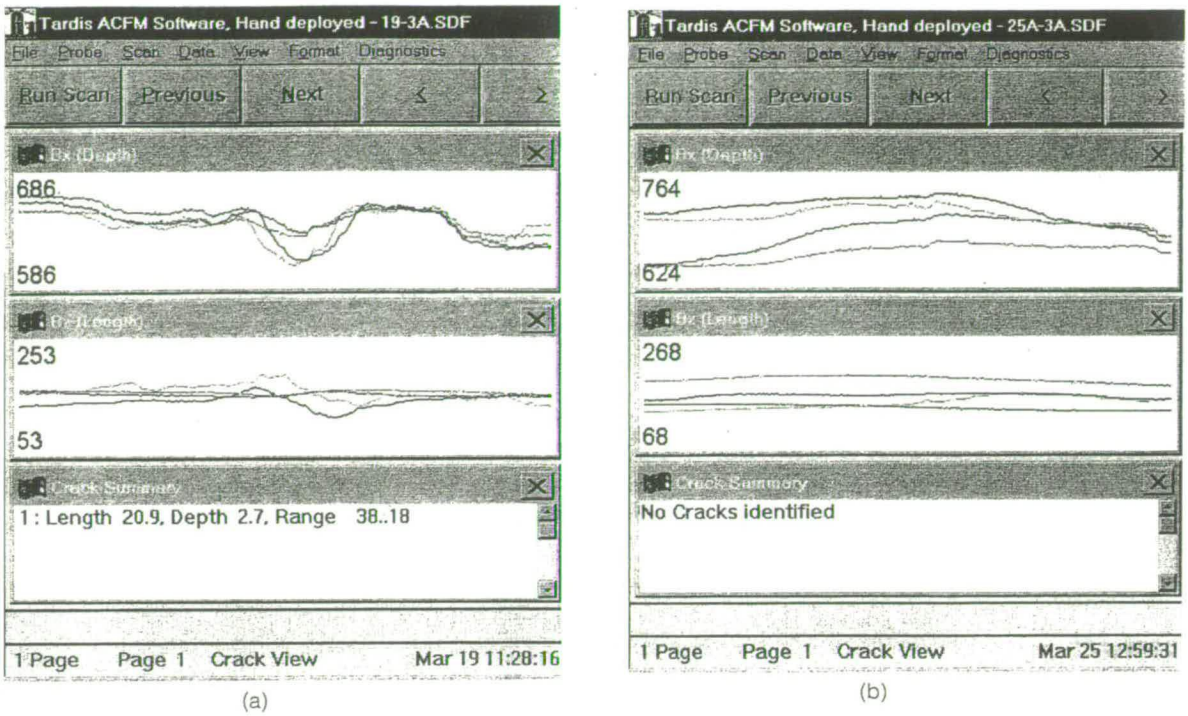

Figure 14 (a) ACFM traces showing signal trough corresponding to presence crack and (b) after ECM operation showing flat trace indicating the removal of the crack.

at a feed rate of 1 mm/min and a machining voltage of 15 V, using a 15% sodium chloride electrolyte, then the overcut will be 0.58 mm giving a total cut width of the order of 3.10 mm. Decreasing the overall cut width can be achieved by either decreasing the machining voltage or increasing the feed rate. However, increasing the feed rate must be accompanied by an increase in the flow velocity, by increasing the electrolyte pressure.

With regard to tooling parameters; larger internal diameters will provide greater flow output for the same supply pressure, but will consequently exhibit larger deflections. This problem can be offset by increasing the outside diameter of the tool, and hence the wall thickness, but this will be at the expense of increasing the cut width and the overall ECM power requirement.

The model developed for determining the change in gap dimensions, for the case of zero tool feed, has been successfully validated. This relationship can be used as a control parameter when determining the degree of cut required when inclusions are encountered and the tool is required to remain stationary for a certain duration.

The ECM defect removal/sampling system has been shown to be effective under remote control in a submersed environment. Integration of the ECM tooling with the ACFM system has enabled complete IRM operation to be achieved within a single deployment set-up.

Acknowledgements

The authors would like to thank the following: Andrew Holman at TSC Ltd, Milton Keynes, for carrying out the design and fitting of the ACFM probe array to the carriage assembly; Bob Gusthart and Derek Jardine for carrying out the design and manufacture of the equipment and for setting up and providing assistance at the validation trials; UCL for supplying some of the welded sections for validation trials; Oceaneering Ltd, Aberdeen, for providing facilities and backup personnel in support of the tank trials; and OSO and IMP for financial support.

References

1. *Fatigue Performance of Repaired Tubular Joints*, 1989, Offshore technology report (OTH 89 307). HMSO, London.
2. DeBarr, A. E., and Oliver, D., 1968, *Electrochemical Machinining*. Macdonald, London.
3. Clifton, D., Barker, M. B., Gusthart, R. W., and McGeough, J. A., 1991, An automated system for weld sampling and defect removal. *Journal of the Society of Underwater Technology*, **17**(4), pp. 9–17.
4. Wilson, J. F., 1971, *Practice and Theory of Electrochemical Machining*. Wiley, Chichester.
5. Esanola, J., 1997, *An Investigation Into Electrochemical Milling*. MSc thesis, Edinburgh University.
6. Shigley, J. E., 1986, *Mechanical Engineering Design*. McGraw-Hill, New York.

Journal of Applied Electrochemistry **30**: 447–455, 2000.

Theoretical analysis of chronoamperometric transients in electrochemical machining and characterization of titanium 6/4 and inconel 718 alloys

A.R. MOUNT[1]*, K.L. ELEY[1] and D. CLIFTON[2]
[1]*Department of Chemistry, and* [2]*Department of Mechanical Engineering, University of Edinburgh, King's Buildings, West Mains Road, Edinburgh EH9 3JJ, Great Britain*
*(*author for correspondence, e-mail: a.mount@ed.ac.uk)*

Received 12 July 1999; accepted in revised form 17 September 1999

Key words: characterization, current analysis, electrochemical machining, inconel 718, titanium 6/4

Abstract

An analytical expression is derived for the current–time transient for electrochemical machining (ECM) using a planar tool and workpiece configuration. This is obtained as a function of such parameters as the initial interelectrode gap, applied voltage, electrolytic conductivity, valency, density and feed rate. Good theoretical fits to experimental data are found for the alloys titanium 6/4 (Ti6/4) and Inconel 718 (In718) using both sodium chloride and sodium nitrate electrolytes, demonstrating the applicability of this theory. The values of the electrolytic molar conductivity obtained for chloride and nitrate are consistent with the expected conductivity obtained from molar conductivity measurements. The mean valency values obtained for Ti6/4 and In718 are 3.5 ± 0.2 and 3.0 ± 0.2, respectively. The fraction of the applied voltage used to drive the electrochemical surface reactions, V_0, has also been obtained. The variation in V_0 between alloys when using the same electrolyte and also for each alloy when using different electrolytes is attributed to differences in the thermodynamics of the removal of the metal from the surface metal oxide. For In718 using chloride electrolyte, an increase in V_0 is observed at higher applied voltages, consistent with a change in the electrochemical dissolution reaction. Analysis of the variation of V_0 at low applied voltages throughout the current–time transient has enabled the current–voltage characteristics of these surfaces electrochemical reactions to be determined, indicating Tafel behaviour. These data show this analysis to be a powerful methodology for understanding and measuring ECM characteristics under realistic ECM conditions.

List of symbols

A	area of electrode (both tool and workpiece)
f	tool feed rate
t	time
z	gap between the electrodes (perpendicular to planar electrode surfaces)
I	current
κ	electrolyte conductivity
ρ	density of the workpiece material
V	applied voltage
V_0	portion of the applied voltage required at the electrode interfaces to drive the machining process
y	thickness of erosion of the workpiece (perpendicular to workpiece surface)
dy/dt	erosion rate
n	valency or number of electrons transferred per dissolving metal atom
F	faradaic constant
M	average molecular mass of the workpiece
I_0	the exchange current for electrochemical reaction
E	potential
b	Tafel slope

Subscripts

∞	value as time approaches infinity
i	initial value (value at time designated as initial time for fitting purposes)
0	value at time zero
1	value at a designated time
2	value at an alternative designated time
C	calculated value

1. Introduction

The conventional milling or turning of high strength, low-weight, metallic and intermetallic alloys can be problematic in cases where the required high cutting forces exceed a tooling capability or are uneconomic because of high tool wear and low machining rates. Electrochemical machining (ECM), a process in which metal is removed by the electrochemical dissolution of a workpiece material, is a technology that has many

potential advantages for the machining of these advanced alloys. Unlike many competing metal shaping processes, ECM is able to machine a material irrespective of hardness and is able to produce complex shapes with high surface integrity at high metal removal rates [1–5]. ECM is carried out by passing an electric current through an electrolyte flowing in the gap between an electrode tool and workpiece. This causes electrochemical dissolution of the workpiece at current densities of the order of 1×10^6 A m^{-2}. As dissolution of the workpiece material occurs the tool electrode is moved, at a controlled rate, to remove material as required. In order to understand, model and control this process, it is important that the physicochemical parameters that control the dissolution are identified. Traditional electrochemical voltammetric [6] measurements have given some insight into the electrochemical dissolution processes occurring at low current densities (below 10^4 A m^{-2}). However, it is extremely unlikely that parameters obtained from these measurements can generally be applied to the high current dissolution region, as the reaction may be affected by the increased voltage and local ion depletion. This means that in the absence of experimental observations, traditional methods for analysing current-voltage data cannot be applied with confidence.

At high currents, parameters which are important in ECM are the electrolyte conductivity (controlled by the concentration and type of ions in the gap between the workpiece and the tool), the valency and the distribution of the applied voltage [7–11]. This is expected to vary with the nature of the workpiece and the current. Previous workers have demonstrated how values of these parameters can be obtained by experimental measurements. For example, Tipton [12] has shown that the 'effective overvoltage' (the portion of the applied voltage used to drive the surface electrochemical reactions) and conductivity can be determined from a plot of the relationship between the applied gap voltage and the gap size when machining at a constant current with no tool feed. The valency is then determined by comparing the mass of material dissolved with the charge passed, assuming constant valency throughout the measurement. However, such simple measurements are a long way from the conditions which are imposed for any practical geometry during electrochemical machining, and in particular where there is a complex interdependence of process parameters over the electrode surface. If such 'static' techniques were to be used, then extensive repeated measurements would be required to check for interparameter sensitivities. To date, there is no analytical method for the dynamic measurement of these parameters during machining [9, 13]. In this paper a novel electrochemical methodology for analysing current–time transients and obtaining these parameters during ECM is reported. The applicability of this method is also demonstrated for Titanium 6/4 (Ti6/4) and Inconel 718 (In718), two commercially important aerospace materials [14, 15].

2. Theory

The system under consideration is a planar tool (cathode) moving at a constant feed rate towards a planar parallel workpiece (anode) of the same area, with electrolyte between the two electrodes (Figure 1). It is assumed that the current is governed by migration (an essential assumption for stable machining). A further assumption is that the electrolyte is being pumped through the interelectrode gap at high enough flow rate that the build-up of machining products and/or the loss of ions from the electrolyte does not significantly affect the electrolyte conductivity, which can be assumed to remain constant throughout the experiment. This is the case for the experimental results presented herein. The current across the electrolyte is given by:

$$I = \frac{\kappa(V - V_0)A}{z} \tag{1}$$

Assuming that this all leads to electrode dissolution, this current is also the dissolution current of the workpiece, and therefore

$$I = \left[\frac{nFA\rho}{M}\right]\frac{dy}{dt} \tag{2}$$

The change in the interelectrode distance is given by (Figure 1(a))

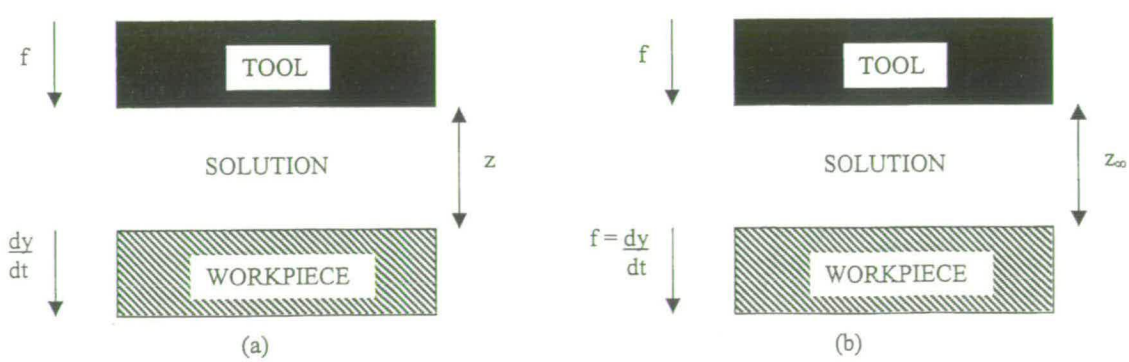

Fig. 1. Schematic representation of the planar tool/planar workpiece configuration (a) before steady-state (b) at steady-state. Relative movement of the tool and workpiece are shown by the arrows, and distance between the electrodes by the double headed arrows.

$$\frac{dz}{dt} = \frac{dy}{dt} - f \tag{3}$$

and hence, combining Equations 1, 2 and 3

$$\frac{dz}{dt} = \frac{k}{z} - f \tag{4}$$

where

$$k = \left[\frac{\kappa(V - V_0)M}{nF\rho}\right] \tag{5}$$

Now at the equilibrium current, I_∞, (I when $t \to \infty$), when a steady-state current has been reached, z remains constant at z_∞ and $dz/dt = 0$ (Figure 1(b)); hence $f = k/z_\infty$ and

$$\frac{dz}{dt} = k\left[\frac{1}{z} - \frac{1}{z_\infty}\right] \tag{6}$$

This equation can be integrated from $t = 0$, $z = z_0$ to $t = t$, $z = z$, to give

$$\ln\left[\frac{z_\infty - z_0}{z_\infty - z}\right] + \frac{z_0 - z}{z_\infty} = \frac{kt}{z_\infty^2} \tag{7}$$

Substituting the appropriate values of I_0, I and I_∞, the currents at $t = 0$, t and ∞ (the equilibrium current time), respectively, from Equation 1 gives

$$\ln\left(\frac{1 - I_\infty/I_0}{1 - I_\infty/I}\right) + (I_\infty/I_0 - I_\infty/I) = \frac{kt}{z_\infty^2} \tag{8}$$

or

$$\ln\left(\frac{1 - I_\infty/I_0}{1 - I_\infty/I}\right) + (I_\infty/I_0 - I_\infty/I) = \frac{f^2 t}{k} \tag{9}$$

Using Equation 9, a series of theoretical curves have been produced for the dimensionless current transients which would be obtained at different values of I_0/I_∞ (corresponding to different values of starting interelectrode distance with respect to the equilibrium machining distance) as a function of dimensionless time, f^2t/k. Figure 2 shows theoretical relationships both when $I_0 < I_\infty$ and when $I_0 > I_\infty$. It is clear that these two sets of transients are very different in shape. When $I_0 > I_\infty$, the dz/dt term dominates the f term in Equation 3 and from Equations 1, 3 and 4, I varies with $t^{-1/2}$ initially, showing a steep decrease in current until the equilibrium current is reached. However, when $I_0 \ll I_\infty$ (the starting interelectrode gap is large), the dissolution current is relatively low and remains so until the feed rate ensures that the gap approaches the equilibrium interelectrode gap, when a sharp rise in current to the equilibrium current is seen, producing S-shaped curves. Although the approach of the current (and gap) is asymptotic to I_∞ (and z_∞), for all practical purposes I reaches the value of I_∞ within experimental error well within the timescale of these plots. For any given value of f, the low dissolution current region becomes more pronounced as I_0 is decreased, since more time is required to reach the equilibrium interelectrode gap.

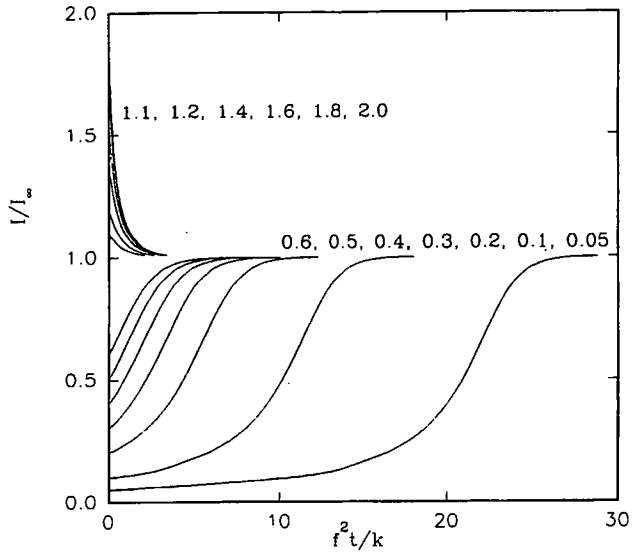

Fig. 2. Theoretical normalised current (I/I_∞) – normalized time (f^2t/k) curves for electrochemical machining using Equation 9. Values of the normalized initial currents (I_0/I_∞) for each series of curves are given on the diagram.

Usually, electrochemical machining experiments involve ensuring that $I_0 < I_\infty$, as this ensures a large starting interelectrode gap and precludes the possibility of shorting or electrolyte breakdown and sparking. Thus, generally rising current transients are observed. However, falling current transients are observed under pulsed voltages, conditions which have recently become of considerable interest [16, 17]. This will be the subject of a future publication. Furthermore, at any given value of I_0, Equation 9 shows that it is k/f^2 which is the characteristic time constant for these transients; thus increasing f or V_0 or decreasing κ or V will decrease the observed transient time for a given system.

3. Experimental details

ECM studies were performed using a Transtec electrochemical machine, (Figure 3). This was combined with a RDOA 100/240/415 regulating transformer (Bonar Brentford Electric) and a 600 A transformer (Goodyear). The solution flow was controlled by means of a Hydriacell D25 pump (Wanner Engineering Inc.); the flow sensor was a type FT 13 (Platon Instrumentation) and the current transducers were of type HT (RS Components). The data were collected using an Intelligent Instruments (Burr–Brown) PC data logging system combined with the Visual Designer software (Intelligent Instruments). The planar cathode (the tool) was a copper–tungsten alloy of length (parallel to the direction of solution flow) 4.00×10^{-2} m and width

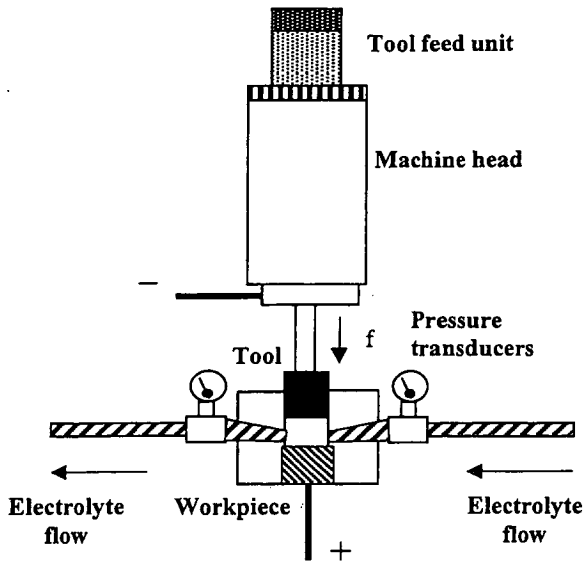

Fig. 3. Schematic diagram of the apparatus used to carry out the electrochemical machining experiments.

(perpendicular to the solution flow) 1.20×10^{-2} m. This gives an area for each electrode of $A = 4.80 \times 10^{-4}$ m^2.

The two electrolytes used were 60 litres of 15.0% w/v solution of sodium chloride or of 21.7% w/v solution of sodium nitrate (Anderson, Gibb and Wilson) as appropriate, maintained at 30 °C throughout. These percentage concentrations were chosen to ensure that the ions in solution were of the same molarity (2.56 mol dm^{-3}). The workpiece materials studied were Ti6/4 (Titanium International Ltd) and In718 (Haynes International Inc.). The certified compositions of these alloys were as given in Table 1.

For these data, the initial electrode gap, controlled by inserting a feeler gauge between tool and workpiece, was set at 0.8 mm. The voltage referred to for each experiment is held constant and is the voltage measured between the workpiece and the tool. The electrolyte flow rate and feed rate, f, were maintained at 20 dm^3 min^{-1} and 1.04 mm min^{-1}, respectively. Under these conditions, assuming that one electron results in the consumption or production of one anion or cation in the electrolyte and using this flow rate and an upper limit to I_∞ of 370 A for these experiments, this corresponds to a change in ion concentration of 1.1×10^{-2} mol dm^{-3}. From this the calculated change in electrolyte concentration is 0.4%. These conditions therefore ensure that the assumption of constant electrolyte concentration is applicable, which is confirmed by the observation of a constant equilibrium gap along the flow path for these experiments. Fitting of the current time transients was achieved by iteratively fitting the results to Equation 9, using the SigmaPlot plotting program (Jandel Scientific).

4. Results and discussion

Figures 4 and 5 show representative examples of typical current–time data for Ti6/4 in nitrate electrolyte and chloride electrolyte respectively. Figures 6 and 7 show comparable data for In718. Also shown are the iterative fits obtained using Equation 9. It is clear that good theoretical fits are obtained. To fit these data, a value of I_0/A was obtained from the starting current and the iterative fitting method was used to obtain values of I_∞/A and f^2/k. Values of I_∞/A and f^2/k are reported for these fits in Table 2.

From these and other data it is clear that I_∞/A remains constant at $(59 \pm 3) \times 10^4$ A m^{-2} for Ti6/4 for both types of electrolyte between 10 and 20 V. From Equations 2 and 3 when $dz/dt = 0$,

$$\frac{I_\infty}{A} = \frac{nF\rho f}{M} \tag{10}$$

This predicts a constant I_∞/A for any given material, as long as n and f remain constant. It is of course possible that products from the tool and the workpiece reaction could meet in the solution and react, generating species which could return to the electrodes and react further, thereby reducing the efficiency of the machining process. In this case and in contrast to these observations, it is likely that the number of electrons passed in the reaction would change as the workpiece and tool approach each other and good iterative fits to the current–time data would not be expected. Using the measured values of $\rho = 4.413$ g cm^{-3} and the average atomic weight of Ti6/4 (from Table 1), $M = 45.80$ g mol^{-1} in Equation 10 gives a value of $n = 3.5 \pm 0.2$. For In718, the corresponding values are $I_\infty/A = (70 \pm 2) \times 10^4$ A m^{-2}, $\rho = 8.228$ g cm^{-3}, $M = 59.79$ g mol^{-1} and $n = 3.0 \pm 0.2$. These values of n, the average valencies for the alloy, are the important valency parameters for the ECM process.

In principle it is possible to use these values of n to produce values for the valency of each constituent element in these alloys. For example, electrochemical dissolution of Al will be likely to produce Al(III) species, so one possible explanation of these data is that the dissolution of Ti6/4 involves a mixture of Ti(III) and Ti(IV) species, with n for Ti of approximately 3.5 ± 0.2. The observed value for In718 is also consistent with Fe

Table 1. Composition in weight percent of Ti6/4 and In718 alloys

Alloy	C	Fe	N	Al	V	O	Mn	Co	Cr	Cu	Mo	Ni	Si	Ti
Ti6/4	0.01	0.17	0.02	5.89	3.76	0.15	–	–	–	–	–	–	–	89.91
In718	0.05	23.50	–	0.48	–	–	0.22	0.17	18.16	0.02	2.96	53.32	0.10	1.02

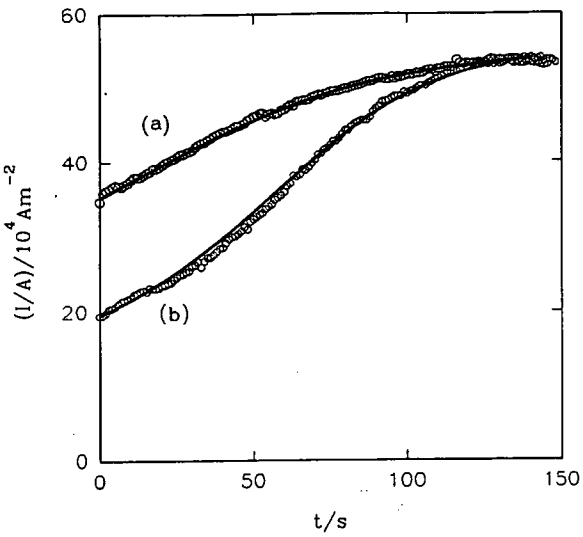

Fig. 4. Typical experimental data (O) for the electrochemical machining of Ti6/4 in nitrate electrolyte at applied voltages, V, of (a) 24 V (b) 18 V. Solid lines show the iterative fits obtained by fitting data to Equation 9.

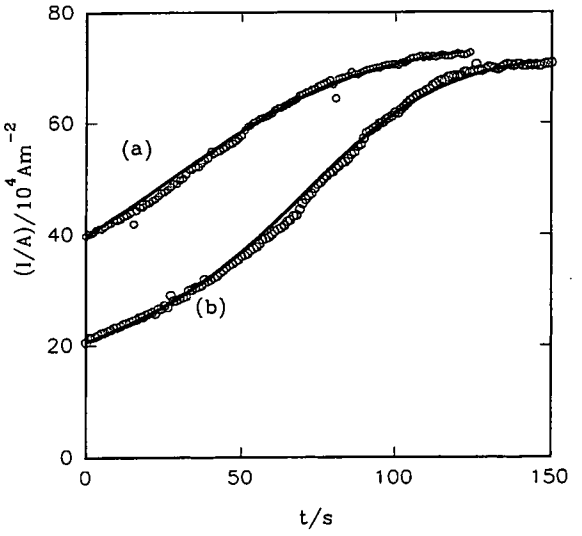

Fig. 6. Typical experimental data for the electrochemical machining of In718 in nitrate electrolyte at (a) 24 V (b) 16 V, plotted in same manner as Figure 4.

dissolving as Fe(III), Cr as Cr(III) and Ni as Ni(III). It is reassuring that these individual elemental valencies are chemically reasonable; however considerable caution must be exercised in assigning individual valencies. For example, previous work on nickel in nitrate electrolyte has suggested that dissolution occurs via Ni(II). Although this observation cannot simply be applied to In718 measurements, as the data were collected at lower current densities and from the pure metal, both of which may cause a change in the elemental valency [18], it is possible that the same mean valency could be achieved by balancing a lower valency for one element (e.g., Ni) with a higher valency for another (e.g., Cr). Thus careful measurements under a variety of elemental compositions close to the alloy composition would be necessary to establish these elemental valencies.

Once these values of n and I_∞ have been obtained from these experiments, it is not necessary to collect the full current time transient, as iterative fitting can be achieved whilst fixing I_∞ at its known value. Thus if I_∞ (or n) is known, values of f^2/k can be obtained experimentally with the consumption of less material or when I_∞ is not attained; for example at relatively small gaps or after the build up of products on recycling of the electrolyte or at lower flow rates, when a passivating surface layer can start to form [19]. However, care must be taken to ensure that the solution flow rate is large enough to ensure that the value of I_∞ is

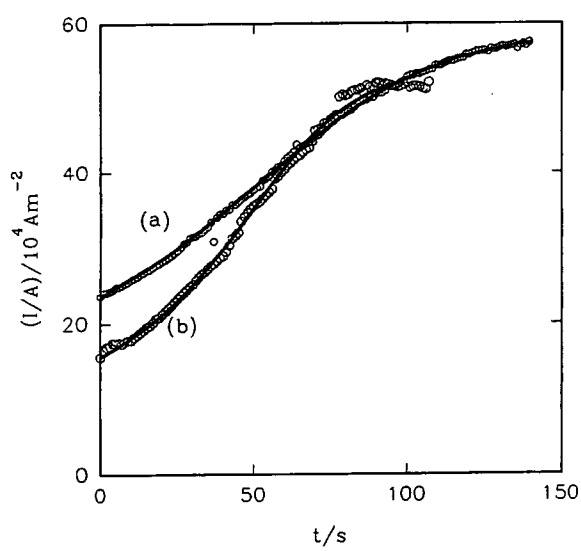

Fig. 5. Typical experimental data for the electrochemical machining of Ti6/4 in chloride electrolyte at (a) 16 V (b) 12 V, plotted in same manner as Figure 4.

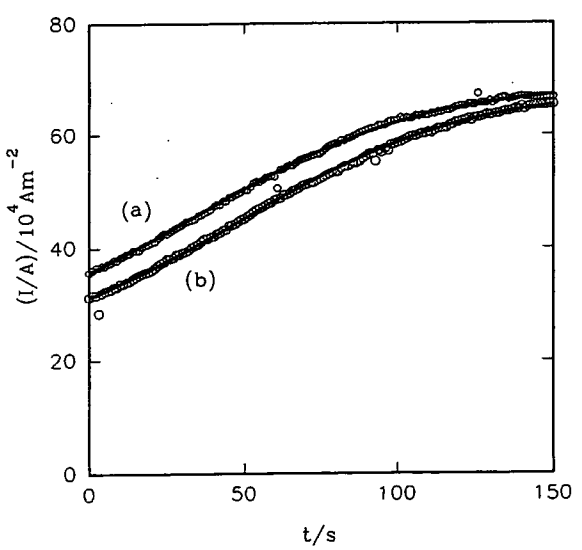

Fig. 7. Typical experimental data for the electrochemical machining of In718 in chloride electrolyte at (a) 24 V (b) 20 V, plotted in same manner as Figure 4.

Table 2. Values of f^2/k and I_∞ obtained from the iterative fits to the experimental current time transients

Electrode	Voltage/V	I_∞/A (/10^4 A m^{-2}) nitrate	f^2/k (/10^{-2} s^{-1}) nitrate	I_∞ /A (/10^4 A m^{-2}) chloride	f^2/k (/10^{-2} s^{-1}) chloride
Ti6/4	10	–	–	57.0 ± 0.1	7.80 ± 0.04
	14	55.7 ± 0.6	7.0 ± 0.1	58.9 ± 0.4	4.83 ± 0.05
	18	55.3 ± 0.1	4.40 ± 0.03	59.5 ± 0.1	3.44 ± 0.03
	20	53.7 ± 0.1	4.34 ± 0.05	61.7 ± 0.1	2.06 ± 0.03
	24	54.2 ± 0.1	3.96 ± 0.04	–	–
In718	12	74.4 ± 0.2	7.36 ± 0.03	71.1 ± 0.6	5.07 ± 0.08
	16	72.4 ± 0.1	5.02 ± 0.02	68.7 ± 0.2	3.41 ± 0.03
	20	70.7 ± 0.1	3.61 ± 0.02	67.9 ± 0.1	3.03 ± 0.01
	24	74.7 ± 0.2	3.51 ± 0.02	69.1 ± 0.1	2.96 ± 0.02

applicable under these conditions. From these iterative fits, the values of f^2/k and I_0/A can be used to determine V_0. From Equation 5,

$$\frac{k}{f^2} = \left[\frac{\kappa(V - V_0)M}{nF\rho f^2}\right] \propto (V - V_0) \tag{11}$$

and, from Equation 1,

$$\frac{I_0}{A} = \frac{\kappa(V - V_0)}{z_0} \propto (V - V_0) \tag{12}$$

since z_0, the starting interelectrode gap is constant in these experiments. Figure 8 shows that for Ti6/4, when k/f^2 and I_0 are plotted against V for these data, straight-line graphs are obtained, consistent with Equations 11 and 12. This indicates that V_0 has a constant value within experimental error under these conditions. In accord with Equations 11 and 12, both the k/f^2 and the I_0 plots show the same V-axis intercept within experimental error. These graphs therefore indicate that $V_0 = 5.4 \pm 0.1$ V and $V_0 = 9.8 \pm 0.5$ V for Ti6/4 in chloride and nitrate electrolyte respectively. Figure 9 shows the corresponding data for In718. As with Ti6/4, both the k/f^2 and I_0 data show a common V-axis intercept, giving values of $V_0 = 5.4 \pm 0.4$ V and $V_0 = 3.0 \pm 0.4$ V for chloride (the low voltage data) and nitrate electrolytes, respectively.

From the gradients of these lines in Figures 8 and 9 and Equations 11 and 12, four independent values for κ for each electrolyte can be obtained. These are all $\kappa = 20 \pm 1$ S m^{-1}, in very good agreement. These values, which have been obtained from the shape of the transients (all t) and the starting current ($t = 0$), respectively, are identical to those measured previously for these electrolyte systems [19]. This good agreement confirms that the products of the electrochemical machining process do not significantly alter the conductivity of the solution as machining progresses, further confirming an assumption of this theoretical treatment.

It is noted that the values of V_0 obtained are lower for chloride than nitrate. This can be explained by the increase in ligating ability when switching from nitrate to chloride. Chloride tends to form relatively strong complexes with the dissolving species at the workpiece

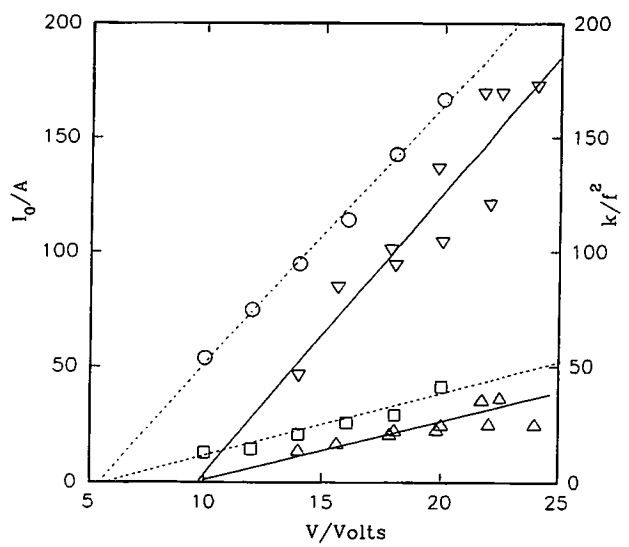

Fig. 8. Plots of I_0 against V for Ti6/4 in (○) chloride (▽) nitrate electrolyte and k/f^2 against V for Ti6/4 in (□) chloride and (△) nitrate electrolyte.

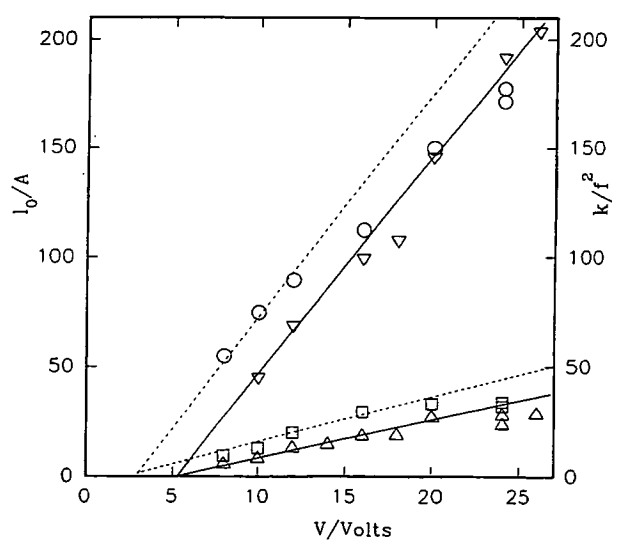

Fig. 9. Plots of I_0 against V for In718 in (○) chloride (▽) nitrate electrolyte and k/f^2 against V for In718 in (□) chloride and (△) nitrate electrolyte.

and this would lead to a decrease in the free energy of the dissolution process and hence a decrease in the oxidation potential. Also, V_0 varies with the nature of the alloy. There are potentially two different types of surface process occurring. If the reaction were simply the oxidation and dissolution of the metals as ions from the metal surface, then the observed values of V_0 would be expected to be less for Ti6/4 than In718, as the oxidation of both Titanium and Aluminium metal are thermodynamically favoured over Iron, Chromium and Nickel [20]. In fact V_0 for In718 is consistently lower than V_0 for Ti6/4, which indicates that the dissolution reaction involves the expulsion of the metal ions from the surface oxide, as the free energies of formation of titanium and aluminium oxides are much higher than those of iron, nickel and chromium oxides [21, 22]. This will lead to an increase in the energy required to expel metal ions from the Ti6/4 oxide with respect to In718 and hence to an increase in the value of V_0.

At higher applied voltages (16 V and above) for In718 in chloride both the k/f^2 and the I_0 data show systematic deviation from this line. This is consistent with an increase in the value of V_0 at these voltages, so that V_0 approaches the value observed for nitrate. Two possible explanations for this effect are also a decrease in the electrolyte conductivity and an increase in the resistance of an insulating surface layer on the workpiece. However, these can be rejected since a decrease in conductivity would cause an increase in the equilibrium gap and significant resistive IR drop due to a surface film would cause a current dependent deviation in the value of V_0 and result in a poor iterative fit to the current–time data. Neither of these effects is observed.

The most likely explanation is a change in the surface dissolution reaction mechanism, which would correspond to a plateau in the anodic current–voltage curve for this electrode. Similar behaviour has been previously observed for nickel in nitrate electrolyte [23], and was attributed to a change in nature of the surface oxide film inducing a change in the reaction. This is at present the subject of further investigation.

The apparent insensitivity of the observed values of V_0 with current is worthy of discussion. V_0 corresponds to that part of the applied voltage at the electrode surfaces, driving the electrochemical reactions. It is extremely difficult to produce a general theory for the quantitative analysis of I, V_0 characteristics, but the reactions that need to be considered are

$$M(s) \rightarrow M^{n+} + ne^-$$

at the workpiece (where M is the metal and n is its valency) and

$$H_2O + e^- \rightarrow \frac{1}{2}H_2(g) + OH^-(aq)$$

at the tool. At each electrode, the experiment is carried out under conditions of efficient mass transport, and at high currents, where the back reactions can be neglected. In this case Tafel behaviour should be observed. This is supported by the few experimental measurements which have been performed on different materials under similar conditions [24, 25]. In this case, the following general equation should apply

$$V_{0.2} - V_{0.1} = b \ln(I_2/I_1) \tag{13}$$

where b is the Tafel slope. Thus, at first sight, from Equation 13, V_0 would be expected to be dependent on current rather than independent of current as is found in the experimental data. The observed independence indicates that the change in V_0 with I is small and within experimental error for these data. In this case, the effect would only seen at applied voltages, V, sufficient to enable machining but sufficiently small that significant changes in $(V - V_0)$ occur during the time course of the current transient. This can be seen in the data collected at the lowest applied voltages, as shown in Figures 10(a) and 11(a), where calculated values of time, t_C, obtained by using the parameters from the iterative fit of the experimental data to Equation 9 are plotted against the experimental values of time, t, for two applied voltages, 11 and 12 V respectively. The data in Figure 10(a) show a systematic deviation of this line from a line of unity gradient and zero intercept at higher values of t, which is consistent with an increase in V_0 with increasing current. A similar deviation is also observed in Figure 11(a), although this is not as marked, due to the decrease in the relative change in $(V - V_0)$ brought about by the increase in V. This plot demon-

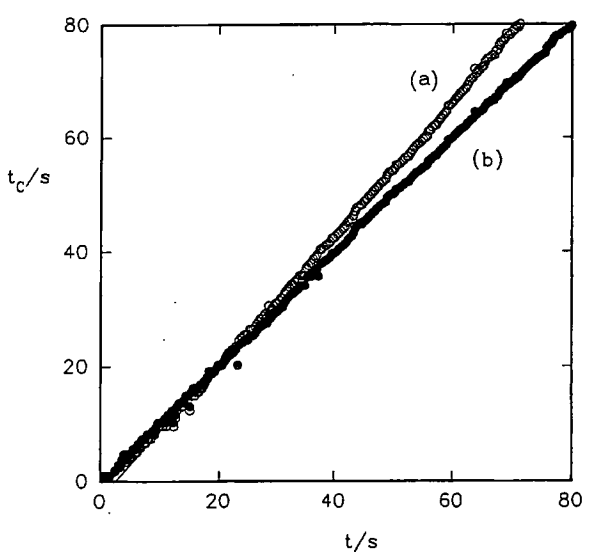

Fig. 10. Plots of t_C (calculated time) against t (experimental time) for electrochemical machining of In718 at an applied voltage of $V = 11$ V in nitrate electrolyte. (a) Iterative fit to the whole data set using Equation 9, with t_C being calculated from the resulting parameters and the observed current values. Equation of straight line is $t_C = 1.158\,t - 2.854$; correlation coefficient, $r = 0.9927$. (b) Fits to Equation 17 using successive iterative fits to 9 s portions of the data, followed by calculation of t_C values as in (a). Equation of straight line is $t_C = 1.004\,t - 0.198$; correlation coefficient, $r = 0.9998$.

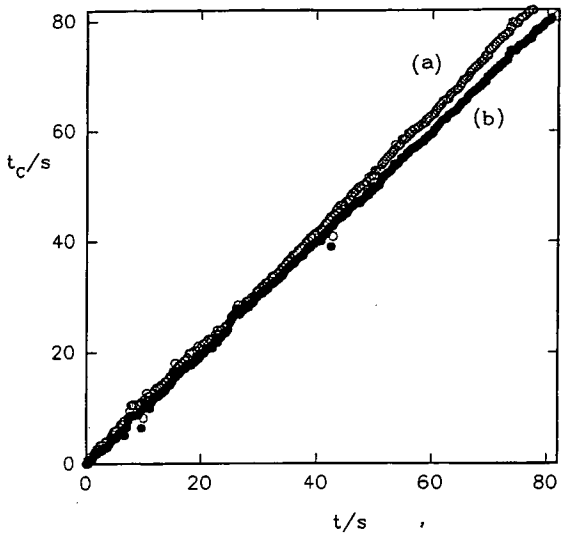

Fig. 11. Plots of t_C (the calculated time) against t (the experimental time) for electrochemical machining of In718 at an applied voltage of $V = 12$ V in nitrate electrolyte. (a) Iterative fit to the whole data set using Equation 9, with t_C being calculated from the resulting parameters and the observed current values. Equation of straight line is $t_C = 1.058\,t - 0.166$; correlation coefficient, $r = 0.9996$. (b) Fits to Equation 17 using successive iterative fits to 9 s portions of the data, followed by calculation of t_C values as in (a). Equation of straight line is $t_C = 1.003\,t - 0.241$; correlation coefficient, $r = 0.9998$.

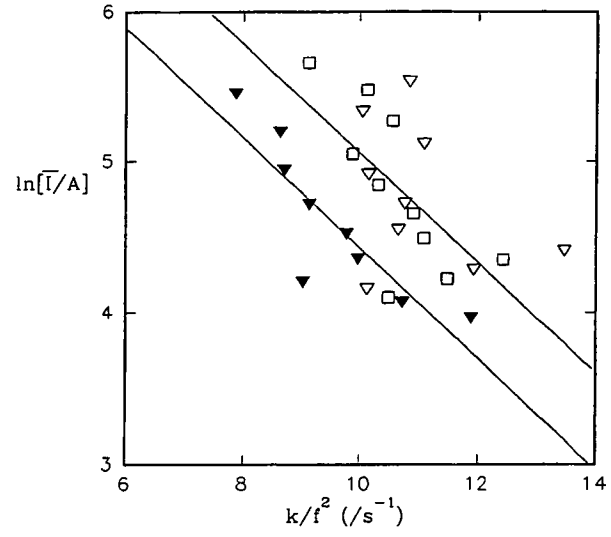

Fig. 12. Plot of $\ln(\bar{I})$, the logarithm of the mean current for each 9 s portion against the corresponding value of k/f^2 obtained from the iterative fits in Figures 10(b) and 11(b) for In718 in nitrate electrolyte at an applied voltage, $V = 11$ V (solid points), $V = 12$ V (open points). Straight line through the 11 V data is the regression line. Line through the 12 V data is that expected from Figure 9 if the same $\bar{I}$, V_0 behaviour were observed in each case.

strates why the iterative fits presented previously show a reasonable fit to the data, as when the voltage, V, applied to the system is increased above 12 V the change in the magnitude of $(V - V_0)$ throughout the transient becomes sufficiently small that the approximation of a constant value of $(V - V_0)$ is applicable.

For the 11 and 12 V data, it is possible to determine how V_0 varies throughout the transient. In this case, Equation 6 can be integrated from $t = t_i$, $I = I_i$ to $t = \infty$, $I = I_\infty$ to give

$$\ln\left(\frac{z_\infty - z_i}{z_\infty - z}\right) + \frac{z_i - z}{z_\infty} = \frac{k(t - t_i)}{z_\infty^2} \tag{14}$$

and hence,

$$\ln\left(\frac{1 - I_\infty/I_i}{1 - I_\infty/I}\right) + (I_\infty/I_i - I_\infty/I) = \frac{f^2(t - t_i)}{k} \tag{15}$$

where $t > t_i$ and the equation is referenced to an initial measurement of t_i, I_i. Since I_∞ is known from previous measurements at higher applied voltages, this equation can be applied over a range of $(t - t_i)$ values, as long as the change in I is sufficiently small to ensure that V_0 (and hence f^2/k) can be assumed to be constant. Iterative fits of the data to Equation 17 have been obtained at various values of t_i, with $(t - t_i) \leqslant 9$ s. This ensures that V_0 is constant, as the variation in I is 5% or less of I_∞. Figures 10(b) and 11(b) show the resulting values of t_C, which show the fits to be much improved compared with Figures 10(a) and 11(a).

Using these fits, a graph of the variation of k/f^2 with $\bar{I}$, the mean current of the section of data used for each fit, can be plotted, as shown in Figure 12. From Equation 11, the variation in k/f^2 in this case is due to changes in $-V_0$ and a graph of $\ln(\bar{I})$ against k/f^2 should be a straight line with a negative gradient if Tafel behaviour is observed. This is indeed the case. From the gradient of the k/f^2 plot in Figure 9 and since this variation in I with V_0 should be independent of the applied voltage (assuming no change in reaction mechanism) the equivalent data for an applied voltage of 12 V should fall on a parallel line, displaced by 2.0 s^{-1} on the k/f^2 axis. Despite the increased scatter, consistent with the increase in the error associated with measuring these data as V becomes the dominant term in $(V - V_0)$, there is reasonable agreement between these data and this line, which confirms Tafel behaviour (Equation 13). These lines each produce a value of $b \approx 1.4$ V.

This method of analysing portions of the current–time transient applies not only where there are changes in $(V - V_0)$, but also when there are changes to any of the constituent parameters of k. Thus changes in κ, due to the formation of bubbles, or to changes in the nature and concentration of ions in the gap can be measured by systematic variation of electrolyte flow rate in the latter case, and the inlet and outlet pressure of the electrolyte flow in the former, even in situations where an equilibrium machining current is not achieved.

5. Conclusions

The results presented in this paper clearly demonstrate that analysis of chronoamperometric electrochemical

machining data using a planar tool/planar workpiece geometry can be used to characterise the dissolution process of Ti6/4 and In718 under conditions (current density, flow velocity, voltage and feed rate) applicable to machining. In these cases, dissolution occurs with little significant resistance from surface layers, and values can be obtained which allow the voltage required to initiate significant machining to be obtained and the nature of the dissolution process to be probed, as well as the conductivity of the electrolyte and the valency of the reaction to be measured. Furthermore, current–voltage characteristics of the surface electrochemical reactions can be also obtained under conditions relevant to ECM.

It is clear that this approach has wide applicability in the study of electrochemical machining as it allows dynamic parameterization of the machining process and thereby gives insight into the electrochemistry of the dissolution process. Furthermore, it should also be invaluable in probing changes in such variables as electrolyte conductivity and V_0 (from fits to the shape of the curve) and valency (from changes in the value of I_∞ during machining) under conditions where these effects are important. Finally, this treatment can be extended to the analysis of the current–time transients of multiple electrodes which can be used to probe the spatial variation of these effects. This approach is being exploited in extending our studies of electrochemical machining to other alloys.

Acknowledgement

We wish to thank the Materials Initiative, Faculty of Science, University of Edinburgh for the summer studentship for KLE on which much of this work was done.

References

1. D.G. Risco and A.D. Davydov, *J. Am. Soc. Mech. Eng.* **64** (1993) 701.
2. M.A. El Dardery, *Int. J. Machine Tool Design Res.* **22**(3) (1982) 147.
3. B. Kellock, *J. Machinery and Product. Eng.* **140**(3604) (1982) 40.
4. O.V.K. Chetty and R.V. Murthy Radhakrishan, *Trans. ASME J. Eng. Ind.* **103**(3) (1981) 341.
5. A.R. Mileham, S.J. Harvey and K.J. Stout, *J. Wear* **109** (1986) 207.
6. M. Datta, *J. Res. Dev.* **37**(2) (1993) 207.
7. A.K. Karimov, *J. Sov. Aeronautics* **28**(3) (1985) 105.
8. A.G. Makie, *J. Math. Anal. Appl.* **117**(2) (1986) 548.
9. J. Kozak, L. Dabrowski, K. Lubkowski and M. Rozenek. Proceedings of the 13th International CAPE Conference, Warsaw (1997), p. 311.
10. H. Tipton, Proceedings of the 5th International Confererence on 'Advances in Machine Tool Design and Research' (1964) p. 509.
11. A.D. Davydov and V.D. Kanshcheev, *Elektronnaya Obrabotka Materialov* (1985) 80.
12. H. Tipton, *Machine. & Prod. Eng.* (1968) 325.
13. V.K. Jain and K.P. Rajurkar, *Precision Eng.* **13**(2) (1991) 111.
14. M. Atkey, *Indust. Robot* **12**(4) (1985) 231.
15. D.J. Jones, *Chem. Brit.* (1988) 1135.
16. B. Wei and J. Kozak, *Trans. NAMRI/SME* **22** (1994) 147.
17. M. Datta and D. Landolt, *Electrochim. Acta.* **26**(7) (1981) 899.
18. A.D. Davydov, E.N. Kiryak, A.N. Ryabova, V.D. Kashcheev, B.N. Kabanov, *Elektronnaya Obrabotka Materialov* **5** (1979) 19.
19. C.N. Larsson, *in* 'Electrochemical. Machining' edited by A.E. De Barr, D.A. Oliver (MacDonald, London, 1968), p. 108.
20. 'CRC Handbook of Chemistry and Physics', 74th edn, edited by D.R. Lide (CRC Press, Florida, USA, 1993).
21. R.D. Harrison (Ed.), 'Book of Data', Nuffield Advanced Science. (Penguin Books, Harmondsworth, UK, 1972).
22. F.J. DiSalvo and S.J. Clarke, *Current Opinion Solid State & Mater. Sci.* **1** (1996) 241.
23. M. Datta and D. Landolt, *J. Electrochem. Soc.* **122** (1975) 1466.
24. D. Landolt, R.H. Muller, C.W. Tobias, *J. Electrochem. Soc.* **118** (1971) 40.
25. J. Hives and I. Rousar, *J. Appl. Electrochem.* **23** (1993) 1263.

ELSEVIER

Journal of Materials Processing Technology 108 (2001) 338–348

Journal of Materials Processing Technology

www.elsevier.com/locate/jmatprotec

Electrochemical machining of gamma titanium aluminide intermetallics

D. Clifton[a,*], A.R. Mount[b], D.J. Jardine[b], R. Roth[b]

[a]*Department of Mechanical Engineering at Edinburgh University, The Kings Building, Edinburgh EH9 3JL, UK*
[b]*Department of Chemistry at Edinburgh University, Edinburgh EH9 3JL, UK*

Accepted 14 August 2000

Abstract

Characteristics of low density, high stiffness, good creep resistance and high strength at a wide range of temperatures make titanium aluminide a potentially important material in respect of weight savings in high performance components operating at high temperatures. Some work has already been carried out to examine properties of the machining of this alloy using mechanical stock-removal techniques such as, turning. Such methods are found to have limitations in terms of surface integrity defects and the formation of surface hardened layer. In this paper the electrochemical machining (ECM) characteristics of titanium aluminide are examined. Conditions under which reproducible ECM is viable for this material have been established and parameterised in terms of machining parameters generated from chronoamperometric analyses for both chloride and perchlorate electrolyte systems. Stable dissolution has been shown to be limited by surface passivation, in case of the chloride system, and choking in case of the perchlorate system. In case of the perchlorate surface there is evidence of an increased amount of cross-colony attack when compared to surfaces machined using chloride. Chronoamperometric analysis has indicated that this form of attack can be correlated to differences in the valency (2.4 for the perchlorate system and 3.0 for the chloride system) and the overpotential (3.8 V for the perchlorate system and 4.3 V for the chloride system). These differences have been related to measured differences in the surface dissolution characteristics of the microstructural phases of this material. Surface hardness of the ECM TiAl has been shown to have decreased by 46% with respect to conventionally machined surfaces.

Keywords: Electrochemical machining; Titanium aluminide; Dissolution stability; Surface hardness

1. Introduction

A continuing challenge in aircraft gas turbine design/manufacture is the achievement of greater fuel economy and operational efficiency through improvements in thrust/weight ratios. The most direct way of achieving this is through replacement of existing components with lighter materials without incurring a significant reduction in performance criterion, particularly high temperature and high strength characteristics [1].

Titanium aluminide intermetallic alloys offer low density, high stiffness, good creep resistance and high strength at a wide range of temperatures [2]. These alloys also offer good oxidation and hot corrosion resistance [3]. Such characteristics make titanium aluminide a potentially important material in respect of weight savings in high performance components operating at high temperatures. Although low temperature ductility and fracture toughness have been considered as a drawback in the use of these alloys (particularly for components that undergo heating/cooling cycles), continuing developments are expected to lead to an improved balance of properties in this respect [4]. The alloy is therefore, of particular interest in aerospace applications as a replacement to heavier nickel and iron based alloys [5]. There has already been considerable interest in applying this material to compressor casings and combustion chambers and nozzles, in aeroengine manufacture [1]. These and other potential applications have led to an increasing requirement to define the overall processing route for such alloys. As part of this route, forging and casting methods will enable initial production of components to pre-form shape. More accurate, secondary operations will then be required to produce the finally required component accuracy. Some work has already been carried out to examine properties of the machining of this alloy using single point cutting [6,7] grinding [8] and high speed machining [9]. However, such mechanical techniques are often limited in terms of surface integrity effects [6] and the formation of subsurface hardened layers [8] and a reduction in fatigue resistance [7]. Work has also been carried out to characterise the machinability of this alloy using electrical discharge machining

* Corresponding author. Tel.: +44-131-650-5693.
E-mail address: david.clifton@ed.ac.uk (D. Clifton).

0924-0136/01/$ – see front matter
PII: S0924-0136(00)00739-1

(EDM), a thermal process which unlike conventional mechanical techniques, is essentially forceless [10]. This process was found to produce microcracking, due to thermal recasting and white layers on the machined surface. Electrochemical machining (ECM), a process in which the workpiece material is removed by electrochemical dissolution, is a technique that potentially offers several improved characteristics over EDM and mechanical machining techniques. The process is able to machine a material irrespective of hardness and has the potential to produce complex shapes at high metal removal rates and with a high quality surface finish without producing residual stresses, surface hardening (through thermal recasting) or imparting microfracture damage to the material surface [11]. There is also no tool wear during ECM. Given these characteristics, it is suggested that ECM may become an important part of the overall processing route for these alloys.

In this investigation, the ECM dissolution characteristics of an γ-TiAl-based intermetallic are examined, using chronoamperometric analysis, for two different types of electrolyte systems. The conditions leading to the limits of stable dissolution are established. The investigation includes an examination of the machined surface characteristics and integrity for ECM of γ-TiAl. Some examples of conventionally machined (turned) surfaces have also been produced for comparisons to ECM.

2. Background and theory

ECM is carried out by applying an electric potential across an electrolyte flowing in the gap between an electrode tool (biased as the cathode) and workpiece (biased as the anode). This arrangement forms an electrochemical cell through which electric charge, flowing as a result of the applied potential, causes electrochemical dissolution of the workpiece anode in the immediate region of the cathode tool. For general background and theoretical overview on the ECM process see [11,12].

Parameterising electrochemical machinability for any given system (i.e. electrolyte/material combination) involves determining the relationship between the primary process parameters. These are feed rate, f, and applied machining voltage, V. Other parameters that characterise machinability are the current density, J, and the gap size, z. The inter-relation of these parameters determine the surface finish and the upper limit of dissolution stability, when the gap becomes too small in relation to the rate of dissolution, which is known as the choking limit. For some systems the limit of dissolution stability is also determined by these parameters, but involves formation of an insulating and passivating layer adhering to the workpiece surface. Whichever of the two conditions occur first is considered as the upper limit of dissolution stability for that system. Thus, the electrochemical machinability of a material is defined in terms of the relationship between machining parameters, just below this upper limit, and the resulting surface characteristics and volumetric removal rate.

In the following, basic ECM theory [13] and chronoamperometric theory [14] are briefly reviewed. The tool-workpiece configuration being considered is in the form of a plane parallel geometry as shown in Fig. 1. The tool and workpiece surfaces are of equal area (A), and the tool is fed in a direction which is perpendicular to both surfaces. The electrolyte solution passes in a plane parallel to the tool and workpiece surfaces. This is considered as a standard test arrangement for determining electrochemical machinability.

It is assumed that the current is governed by migration (an essential assumption for stable machining). In this case, the electrolyte is being pumped through the inter-electrode gap at high enough flow rate that the build up of machining products and/or the loss of ions from the electrolyte does not affect the electrolyte conductivity (ideally, in a practical machining situation, the tooling/flow configuration should be such that this condition is also satisfied). Conductivity is therefore, assumed to remain constant throughout the experiment. If the gap between the electrodes is z, the current across the electrolyte, I, will be given by

$$I = \frac{L(V - V_0)A}{z} \tag{1}$$

where V is the applied voltage, V_0 the voltage required at the two electrodes to drive the reaction and L the conductivity of the electrolyte (so that the current density, $J = I/A$). This

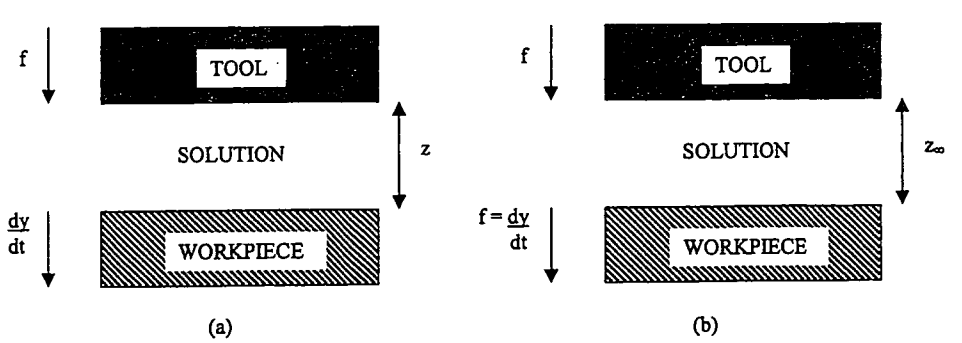

Fig. 1. Schematic representation of the planar tool/planar workpiece configuration showing model notation.

current is also the dissolution current of the workpiece, and therefore

$$I = \left[\frac{nFA\rho}{M}\right]\frac{dy}{dt} \tag{2}$$

where n is the number of electrons transferred per dissolving atom (the "valency"), M average molar mass of the workpiece, F Faraday's constant (96,485 C mol^{-1}), ρ density of the workpiece material and dy/dt thickness of workpiece removed per unit time. The change in the interelectrode distance, z, is given by

$$\frac{dz}{dt} = \frac{dy}{dt} - f \tag{3}$$

Now at the equilibrium current, I_∞, (I when $t \to \infty$), z remains constant at z_∞ and $dz/dt = 0$ hence $f = dy/dt$ and

$$\frac{dz}{dt} = k\left[\frac{1}{z} - \frac{1}{z_\infty}\right] \tag{4}$$

where

$$k = \left[\frac{L(V - V_0)M}{nF\rho}\right] \tag{5}$$

Integrating Eq. (4) from $t = 0$ to $t = t$, assuming that k is a constant under the experimental conditions, and substituting the appropriate values of I_0, I and I_∞, the currents at $t = 0$, t and ∞ (the equilibrium current time), respectively [14], gives

$$\ln\left[\frac{1 - (I_\infty/I_0)}{1 - (I_\infty/I)}\right] + \left[\frac{I_\infty}{I_0} - \frac{I_\infty}{I}\right] = \frac{f^2 t}{k} \tag{6}$$

This treatment assumes a constant value of $(V - V_0)$, with V_0 independent of I. Although a dependence of V_0 on I would generally be expected, it has already been shown that at large values of V this is insignificant, as $(V - V_0)$ has been found to be constant throughout the current–time transients for Ti6/4, within experimental error, except at very low values of V near V_0 [14]. In this case, variation in the value of V_0 for different electrolyte types will indicate variation in the surface machining process.

The machinability of any given system (material/electrolyte) can be characterised in terms of the machining constant, k as formulated from the determination of the stoichiometric parameters of n, L and V_0 according to (5). The value of k obtained when using a particular electrolyte system is then used to determine the equilibrium gap as a function of the primary process parameters of f and V, at the condition that $z_\infty = k/f$ (from Eq. (1–4)), which can be written to express the planar equilibrium gap function z_∞, as follows:

$$z_\infty(V,f) = \frac{L(V - V_0)M}{\rho F f n} = \frac{k}{f} \tag{7}$$

Together with the Cos θ system [13] for approximating equilibrium gaps from planar equilibrium gaps, or more accurately with the aid of recently developed numerical ECM tool design systems [15,16], this surface function can be used to estimate parameter selection (V, and f for a required z_∞). In particular it can be used to estimate the dissolution stability limits (the choking or passivation conditions).

3. Experimental

3.1. Material and ECM equipment

The material studied was Howmet's XD^{TM} γ-TiAl-based intermetallic Ti-45Al-2Mn-2Nb (at.%) + 0.8 vol.% TiB_2. This material was in the form of a 25 mm × 75 mm × 180 mm cast slab, HIPed at 1260°C, 170 MPa for 4 h and then heat treated at 1010°C for 50 h. The microstructure was lamellar with a colony size of approximately 80 μm. Prior to carrying out the ECM tests the slab was sliced, using electrode discharge wire machining, into test pieces having dimensions of 12 mm × 40 mm × 22 mm.

All chemicals used to make up electrolytes were of AnalaR quality. Machine trials were carried out using many different electrolyte solutions. However, the dissolution characteristics of this material, in respect of electrolyte type, can be grouped into two different families, electrolytes that produce a oxide residual adherence and those electrolytes that produce no noticeable oxide adherence. It could be expected that the dissolution characteristics and the condition of the machined surface would be different when using electrolytes from each of these groups. Therefore, a detailed study undertaken using one electrolyte has been selected from each of these groups. That is, a 20.0% w/v aqueous NaCl electrolyte known to produce a surface oxide adherence and a 31.4% aqueous sodium perchlorate electrolyte which does not produce any oxide.

The tooling was designed to machine across the full 12 mm × 40 mm face of the workpiece within a fully enclosed flow cell that acted to direct and confine the electrolyte along the line of the workpiece surface.

In all ECM trials, the initial electrode gap was held constant at 0.80 mm. The voltage referred to for each experiment is the voltage measured directly between the workpiece and the tool (i.e. so that possible significant voltage losses in power cables need not be considered). The electrolyte flow rate and feed rate, f, were also held constant throughout at 20 dm^3 min^{-1} and 1.04 (chloride experiments) and 0.98 mm min^{-1} (perchlorate), respectively. A customised Transtec ECM machining system was used for all trials. The experimental current–time data were recorded using PC data acquisition (Intelligent Data Acquisition (Burr–Brown) using Visual Designer software). These data were iteratively fitted to Eq. (6), as appropriate, using SigmaPlot (Jandel Scientific).

A polyether impression material (Permadyne) was used to cast the flow channel for each trial to enable measurement of the equilibrium gap. The gap dimensions were then obtained

Table 1
Comparison of mocrohardness for ECM turned and cast surfaces

Process	Microhardness ($HV_{0.2}$)
FCM	369
Turning	689
Cast outer skin	535

by measuring the solidified casting using a micrometer. Repeated measurements showed that the error using this technique is ±0.02 mm.

To make a comparison with the ECM surface of titanium aluminide, a series of reference single point turning tests were carried out. These tests used a tungsten carbide (CCMT060204-TP15) tool tip on a Colchester 2000 series lathe which ran at a speed of 600 rpm using a feed rate of 3 mm min^{-1}.

Surface roughness measurements were made using a Rank-Taylor-Hobson Talysurf-4 set with a cut-off length of 0.8 mm using a sample length of 6 mm. Surface finish values in relation to dissolution current density (achieved by increasing the feed rate according to Eq. (7)) were obtained for surfaces machined using both 15% w/w NaCl and 31% w/w $NaClO_4$ electrolytes. Surface finish values are given in Fig. 16 as the average of five readings taken at 1 mm intervals across the machined surface parallel to the direction of electrolyte flow. Error bars illustrate an average deviation over the five readings of 6%. Surface mircohardness measurements were carried out using a Leitz Miniload II with a 200 g load (Table 1).

A Carl–Zeiss photomicroscope II was used to produce optical surface micrographs. Polishing of surfaces for micrograph studies were carried out using a sequence of 12, 6 and 3 μm diamond polishing pastes. This was followed by surface etching carried out using a solution as per [6] as follows, 3% HF, 6% HNO_3, 91% H_2O. All surfaces were etched for a duration of 6 s.

Transverse cross-sections of the ECM surfaces were photographed after first using EDM wire erosion to produce the section before mounting the section in Bakelite. Transverse surface preparation was then carried out in the same way as the machined surface preparation. Surface scanning profiles were carried out using a Zygo Newview 100 scanning white light interferometer fitted with a 40× mirau objective. The scans made using this system have a area of 0.7 mm × 0.7 mm, a spatial sampling of 0.28 μm and a lateral resolution of 0.73 μm.

4. Results and discussion

4.1. Chronoamperometric measurements

4.1.1. Machining with chloride electrolyte

Figs. 2–4 show examples of typical chronoamperometric data for TiAl, and the iterative fit to these data obtained using

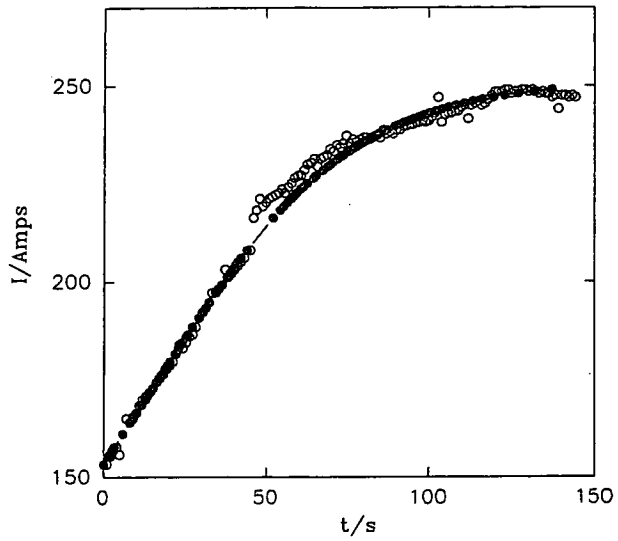

Fig. 2. Typical experimental current–time data (○) for the electrochemical machining of TiAl in chloride electrolyte at an applied voltage, V, of 16.0 V. The solid line and solid data points (●) in this and future plots also show the iterative fits obtained by fitting the data to Eq. (6).

Eq. (6) for 16, 17 and 18 V. It is clear that good theoretical fits to the data are obtained. In order to fit these data, a value of I_0 was obtained from the experimental starting current. Each observed value of I was then used in Eq. (6) to obtain a corresponding calculated value of time, t. Iterative fitting was then used to obtain values of I_∞ and f^2/k that minimised the difference between the calculated and observed values of t for the data. In the course of this fitting process, it became clear that I_∞ remained constant at 253 ± 1 A for all the data between 10 and 20 V. This is consistent with the value of I observed as $t \rightarrow \infty$, and this constancy is explicable as [14]

$$I_\infty = \frac{nFA\rho f}{M} \tag{8}$$

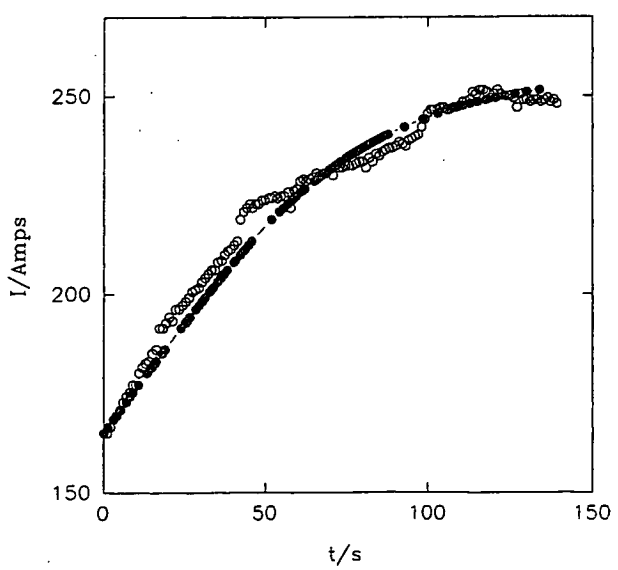

Fig. 3. Analogous data to Fig. 2 for a current–time experiment performed at V = 17.0 V.

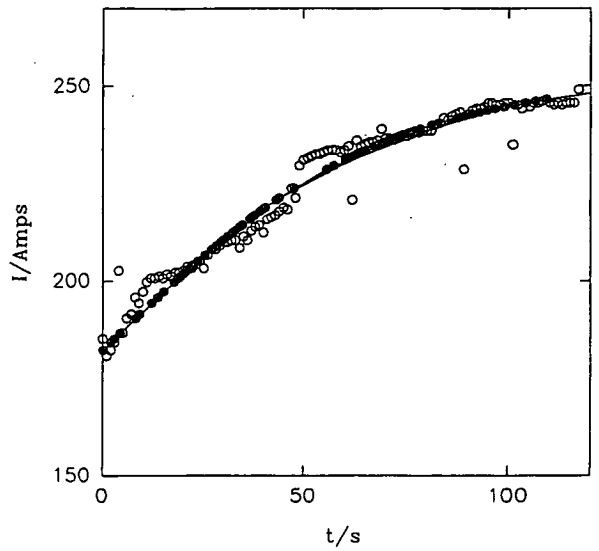

Fig. 4. Analogous data to Fig. 2 for a current–time experiment performed at $V = 18.0$ V.

This predicts a constant I_∞ for any given material at a constant f, as long as n remains constant. Using measured values for ρ of 3.90 g cm^{-3}, $A = 4.80$ cm^2 and M (the average atomic weight of γ-TiAl) = 37.45 g mol^{-1}, this gives $n = 3.03 \pm 0.05$, consistent with Al and Ti both being oxidised to their (III) oxidation state.

In contrast, this value of I_∞ is not found experimentally as $t \rightarrow \infty$ for transients obtained at $V = 10$, 12, 14 and 20 V. Fig. 5 shows a typical transient for an applied voltage of 20 V, along with the iterative fit obtained. It is clear that this iterative method produces a very poor fit to this transient. This is not surprising, as the current does not increase steadily, but rather shows a sharp change in its rate of increase with time. However, if the value of I_∞ is constrained to be 253 A and the data is iteratively fitted to obtain a value of f^2/k, it is clear that the fit to the short time data, before the break in slope, is very good. This is also the case for the 10, 12 and 14 V data. This can be understood if the change in slope is due to some change in the machining process at this time for example, due to passivation of the TiAl surface or choking, which inhibits reproducible machining. Under these applied voltages prolonged machining is not possible, and when the voltage is disconnected and the surface of the TiAl is examined, a grey deposit can clearly be seen (an example of this phenomenon can be seen later in Fig. 12), indicating the presence of an insulating oxide layer. The point of departure of the experimental current–time data from the theoretical transient therefore, indicates the onset of passivation.

From these iterative fits to the early time data before the onset of passivation and the initial current, values of f^2/k and I_0 have been obtained, which can be used to parameterise machinability. From reference [14]

$$\frac{k}{f^2} = \left[\frac{L(V - V_0)M}{nF\rho f^2}\right] \propto (V - V_0) \tag{9}$$

and

$$I_0 = \frac{L(V - V_0)A}{z_0} \propto (V - V_0) \tag{10}$$

since z_0, the starting inter-electrode gap is constant at 0.8 mm in these experiments. Fig. 6 shows that when k/f^2 and I_0 are plotted against V for these data, straight-line graphs are obtained, which is predicted by Eqs. (9) and (10). This indicates that V is sufficiently large at these applied potentials that V_0 can be considered to be essentially constant. Furthermore, it is satisfying that both lines have the

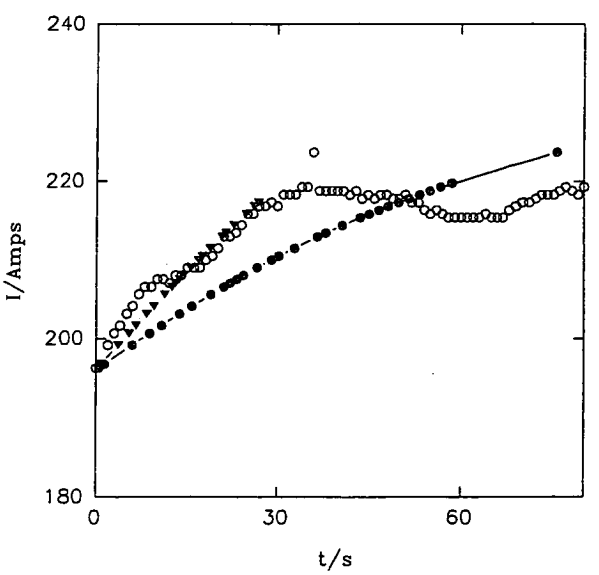

Fig. 5. Analogous data to Fig. 2 for a current–time experiment performed at $V = 20.0$ V. (●) The iterative fit to all the data using Eq. (6). (▼) The iterative fit to the early data (up to $t = 30$ s) using a fixed value of I_∞ of 253 A.

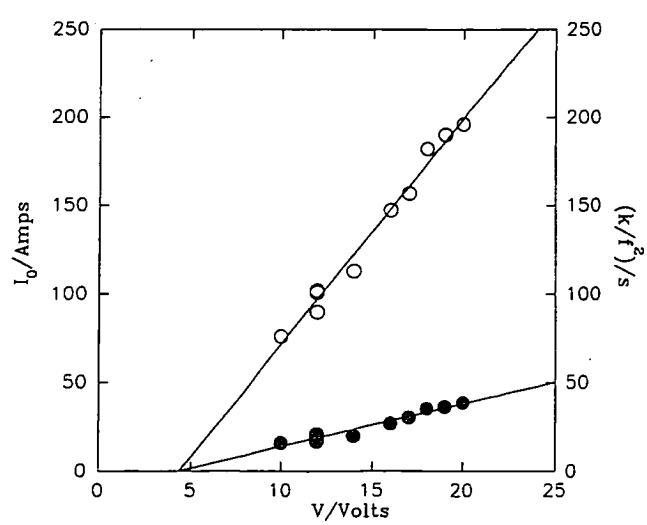

Fig. 6. Plots of the values of (○) I_0 and (●) k/f^2 obtained from the iterative fits against V in chloride electrolyte. The lines shown are the best-fit regression lines for the data.

same x-axis intercept within experimental error, namely 4.37 and 4.29 V, respectively consistent with the estimation that $V_0 = 4.3 \pm 0.1$ V. From the gradients of these two lines and Eqs. (9) and (10), two independent values for L can be obtained. These are $L = 0.219 \pm 0.010$ and 0.212 ± 0.010 S cm^{-1}, respectively consistent with the estimation that $L = 0.215 \pm 0.004$ S cm^{-1}.

4.1.2. Machining with perchlorate electrolyte

Figs. 7–9 show equivalent fits to the chronoamperometric data for TiAl/sodium perchlorate electrolyte to those in Figs. 2–4. It is clear from these data that good fits are obtained. This is again consistent with the value of $(V - V_0)$ remaining approximately constant for the TiAl/perchlorate system. At lower applied voltages (12 V or less), sharp decreases in the gradient of the rising current–time transient were found, possibly indicative of choking at the low inter-electrode gaps required under these conditions. However, as with chloride the early portion of the current–time transient fits well to Eq. (6) if a value of I_∞ is prescribed, equal to the value obtained where a fit to the full transient is possible (Fig. 9). This indicates that stable machining occurs prior to this choking event. The values of I_0 and I_∞ obtained from the full fits are consistently lower than those found for chloride. In fact the value of I_∞ observed was always in the range 192 ± 3 A and so a fixed value of 192 A was used for the partial fits. This would indicate that the valency of the electrode reaction is different for perchlorate than for chloride. From Eq. (8), a value of the valency can be calculated, giving $n = 2.4 \pm 0.1$. Fig. 10 shows the equivalent plot for perchlorate to Fig. 6 for chloride. Again, good agreement is observed for these data, with both lines having an x-axis intercept of $V_0 = 3.8 \pm 0.2$. As with chloride, the gradients of the two lines, from Eqs (9) and (10) can be used to produce independent values of L for the perchlorate system, these are $L = 0.131 \pm 0.010$ and $L = 0.140 \pm 0.010$ s cm^{-1}, respectively from the two equations giving an average estimate for L of 0.135 ± 0.005 s cm^{-1}.

The value of n observed for TiAl is indicative of a significant change in the oxidation state(s) of the dissolving metal species in the presence of perchlorate. It is noted that the observed value of $n = 2.4 \pm 0.1$ would indicate the presence of metal ions with mixed oxidation states. Due

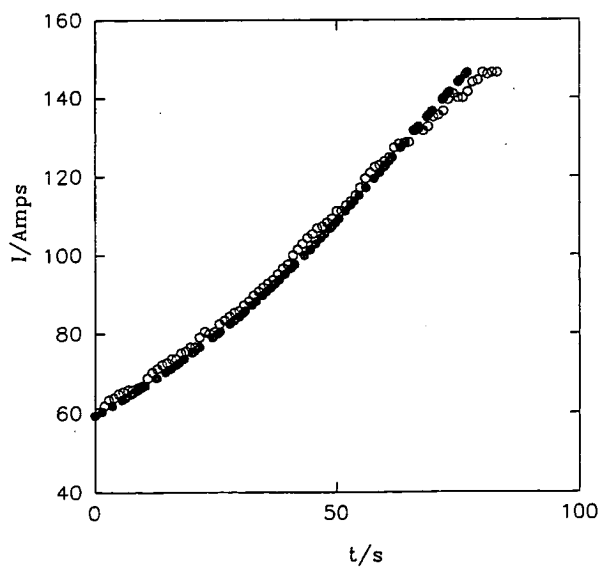

Fig. 7. Typical experimental current–time data (○) for the electrochemical machining of TiAl in perchlorate electrolyte at an applied voltage, V, of 12.0 V. The solid line and solid data points (●) show the iterative fits obtained by fitting the data to Eq. (6) with a fixed value of I_∞ of 192 A. The experiment was terminated near $t = 80$ s as the current was observed to fall rapidly at this point.

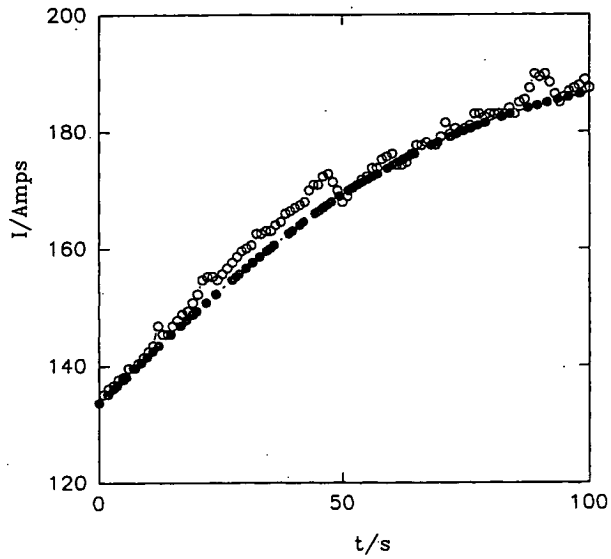

Fig. 8. Analogous data to Fig. 7 for a current–time experiment performed at $V = 18.0$ V. The full iterative fit to the data was performed in this case in order to obtain values for f^2/k and I_∞.

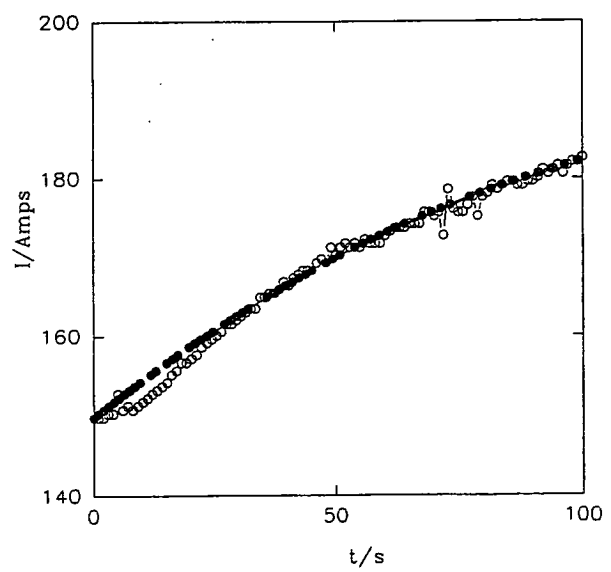

Fig. 9. Analogous data to Fig. 8 for a current–time experiment performed at $V = 22.0$ V.

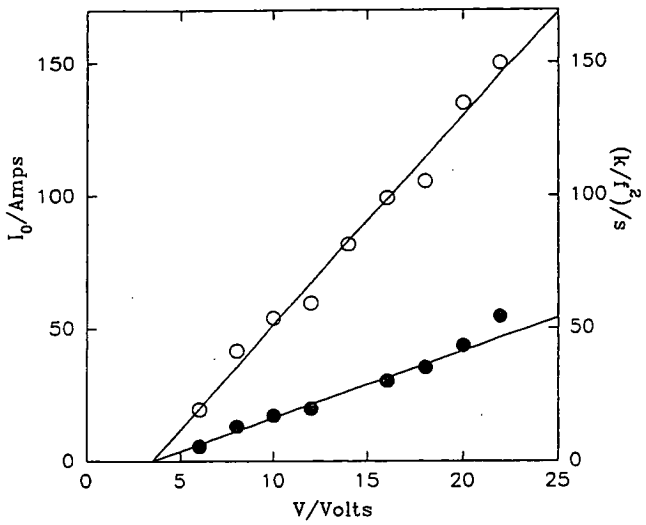

Fig. 10. Plots of the values of (○) I_0 and (●) k/f^2 obtained from the iterative fits to the perchlorate experiments against V. The lines shown are the best-fit regression lines for the data (with the data point for 22 V for k/f^2 being omitted from the regression line due to its large error limit).

to its reactivity, aluminium is most likely present after machining as a metal ion with a valency of 3. These results therefore, indicate (within experimental error) that machining in sodium perchlorate under these conditions produces approximately equal amounts of titanium with valency (or oxidation state) $n = 2$ and 3, as compared to machining in NaCl which produces titanium exclusively with a valency of $n = 3$.

4.2. Parameterisation of electrochemical machinability

From the analysis described above, the stoichiometric parameters of n, L and V_0, for the two systems studied can summarised as given in Table 2. In addition, computed values of the machining constant k, according to Eq. (5), are given for a typical set of machining voltages.

A machinability database for a particular tooling design can then be generated for each electrolyte system. Depending upon production requirements, this can be done either at a selected machining voltage with the feed rate adjusted for the required gap (according to the $\cos\theta$ technique or numerical computational methods of tool design), or at a selected feed rate with the required equilibrium gap determined by setting the voltage, according to Eq. (7). The machining parameters in Table 2 have been used to plot the gap-voltage relationship, shown in Fig. 11, for both the chloride and Perchlorate electrolyte systems. Measured machining gaps from the machining trials have been added to this plot. The reasonable closeness of fit of these data to the generated gap-voltage relationship is seen as a validation of the chronoamperometric measurements.

Table 2
Microhardness measurements for titanium aluminide, comparing single point turned, ECM and cast surfaces

Stoichiometric machinability Parameter for γ-TiAl	Chloride system	Perchlorate system
n	3.03	2.4
L	0.215 S cm^{-1}	0.13 S cm^{-1}
V_0	4.3 V	3.8 V
k at 14 V	4.25×10^{-2} s^{-1}	6.59×10^{-2} s^{-1}
k at 16 V	3.52×10^{-2} s^{-1}	5.42×10^{-2} s^{-1}
k at 18 V	3.00×10^{-2} s^{-1}	4.59×10^{-2} s^{-1}
k at 20 V	2.63×10^{-2} s^{-1}	3.99×10^{-2} s^{-1}
k at 22 V	2.33×10^{-2} s^{-1}	3.52×10^{-2} s^{-1}

4.3. Machining stability, surface condition and integrity

A lightly adhering surface oxide was observed for all surfaces machined using 20.0% NaCl electrolyte solution. No oxide adherence was noted in the case of surfaces machined using electrolyte 31.4% $NaClO_4$. Machining was limited by, severe surface passivation, shown in Fig. 12, occurring as the equilibrium machining gap was reduced to 0.32 mm (by lowering the voltage to 12 V at a constant feed rate of 1.04 mm min^{-1}) when using chloride electrolyte solution. The form of this passivation was a white/grey deposit, characteristically of circular form and always occurring at the far end of the electrolyte flow field.

When machining using perchlorate electrolyte, the surface was observed to be free from oxide. Dissolution stability was limited in this case only by the onset of choking as the equilibrium gap was reduced down to ~0.18 mm.

Surface microhardness measurements for surfaces machined by turning, ECM and as a reference, the surface from the supplied cast slab, are given in Table 2. The hardness values shown have a ±3% sigma value (S.D.) from the mean of five readings for each of the three surface types. Note that the ECM surfaces were found to have the same hardness values, within the 3% S.D., irrespective of which of the two electrolytes were used. These measurements are therefore, grouped into a single ECM surface hardness measurement.

As would be expected the hardness of the turned surface is significantly increased above that of the original cast specimen. A similar increase was also reported by [6] who attributed this to strain hardening and suggested that the consequential reduction in ductility would be expected to cause a reduction in fatigue life. The mircohardness of the ECM surface is seen to be 46% lower than that of the turned surface (similar values for the hardness of turned surfaces were also given by [6]). This is explicable due to the absence of strain hardening in the ECM process. The apparent reduction in surface hardness relative to the original cast surface is probably just an indication as to the hardness of the outer skin of the casting. The hardness value for the ECM surface is probably a better guide as to the bulk hardness of the casting.

Fig. 13(a) shows the transverse cross-section of a typical ECM surface. As would generally be expected when using

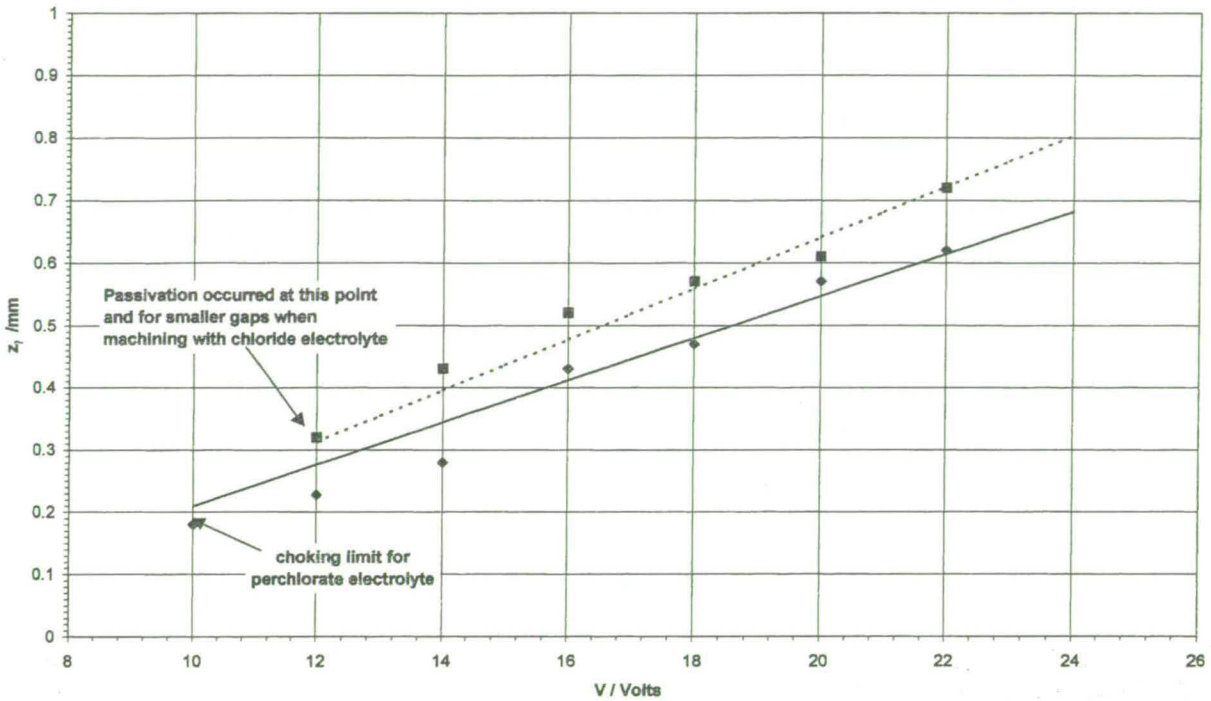

Fig. 11. Predicted and experimental planar equilibrium gap plotted against gap-voltage for perchlorate and chloride data. The dotted line (···) for chloride and solid line (—) for perchlorate show the function predicted from the current–time analysis and using Eq. (7). For validation experimental measured gaps are plotted for perchlorate (◆) and chloride (■).

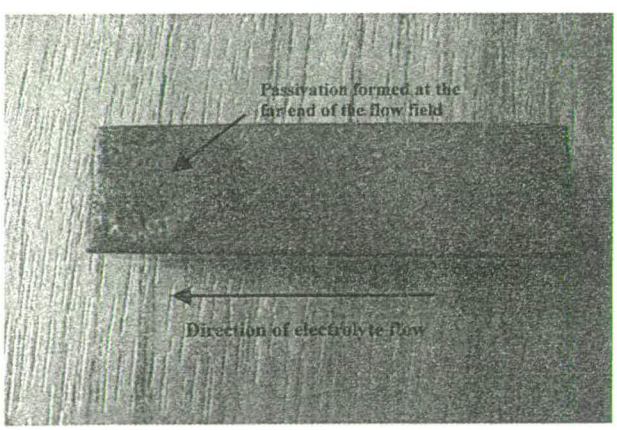

Fig. 12. General view of ECM surface condition showing passivation and oxide adherence in the case of the surface machined using chloride.

the ECM process, this surface exhibits no damage to the microstructure in terms of surface cracking, surface drag, or any change in lamellae spacing and formation. Close examination of Fig. 13 shows that lamella colony sites have been "sliced" by the ECM dissolution process. As a comparison, an example of mechanical damage which commonly occurs for turned surfaces is shown in Fig. 13(b). This is a representative example of such a surface showing grain pullout and plastic deformation leading to flow of lamella around the pullout sites. Similar forms of damage to surface integrity have also been reported for other mechanical machining processes for TiAl [6,7,9].

Fig. 14(a) and (b) show micrographs of the etched ECM formed surface in the cases when using chloride and perchlorate electrolytes, respectively. As would be expected for

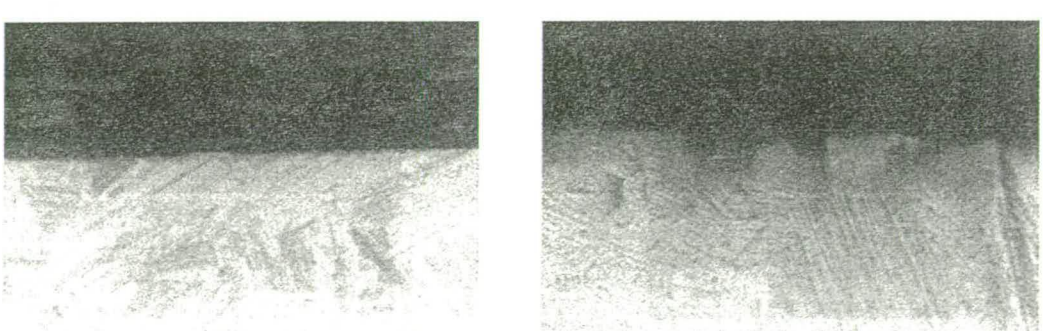

Fig. 13. Transverse micrographs cross-sections of machined surfaces comparing (a) with ECM surface exhibiting through grain attack with (b) turned surface exhibiting pullout and lamellar deformation/drag.

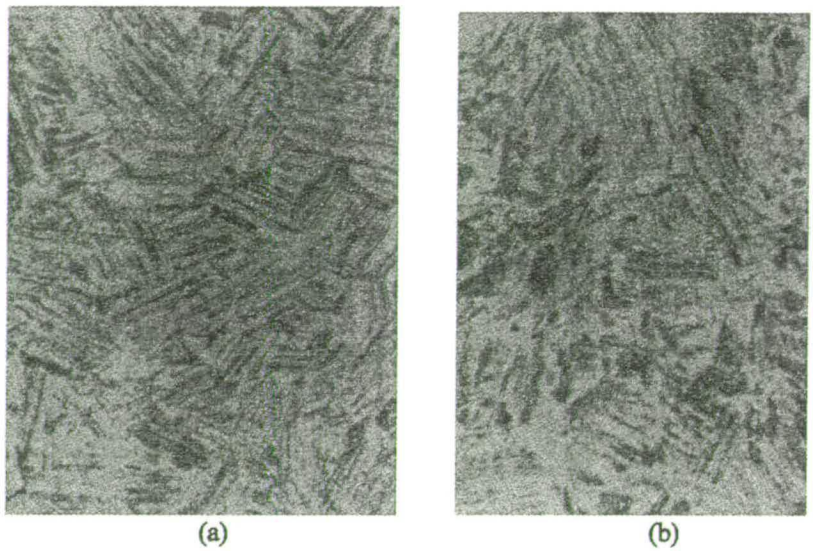

Fig. 14. Micrographs of etched ECM surfaces revealing lamellar structure for both (a) chloride and (b) perchlorate systems.

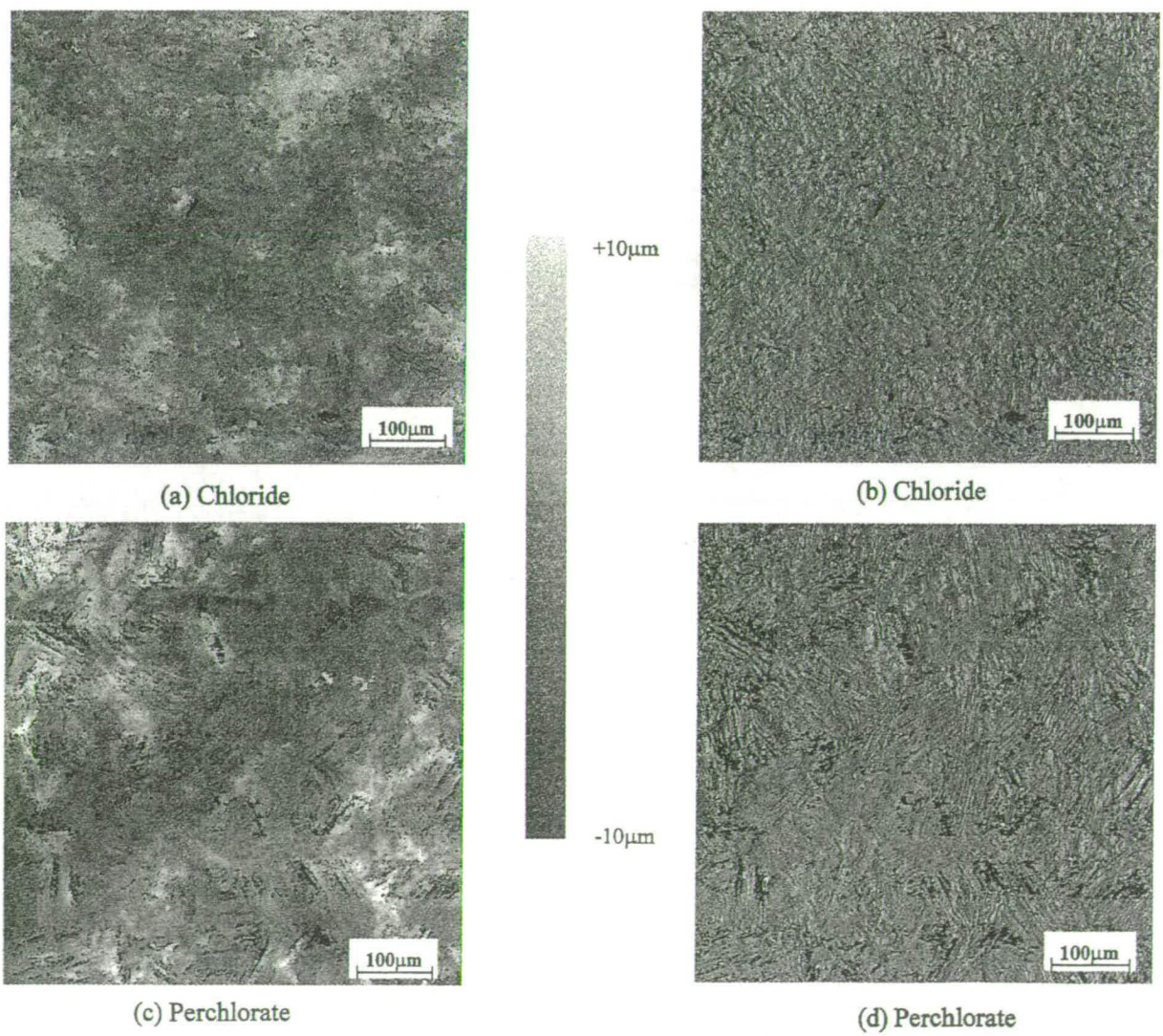

Fig. 15. Surface optical interferometry plots showing height profiles for (a) chloride and (c) perchlorate surfaces represented in ±10 μm greyscale, and (b) and (d) surface scans (*x*-slope profiles) for the same (b) chloride and (d) perchlorate surfaces.

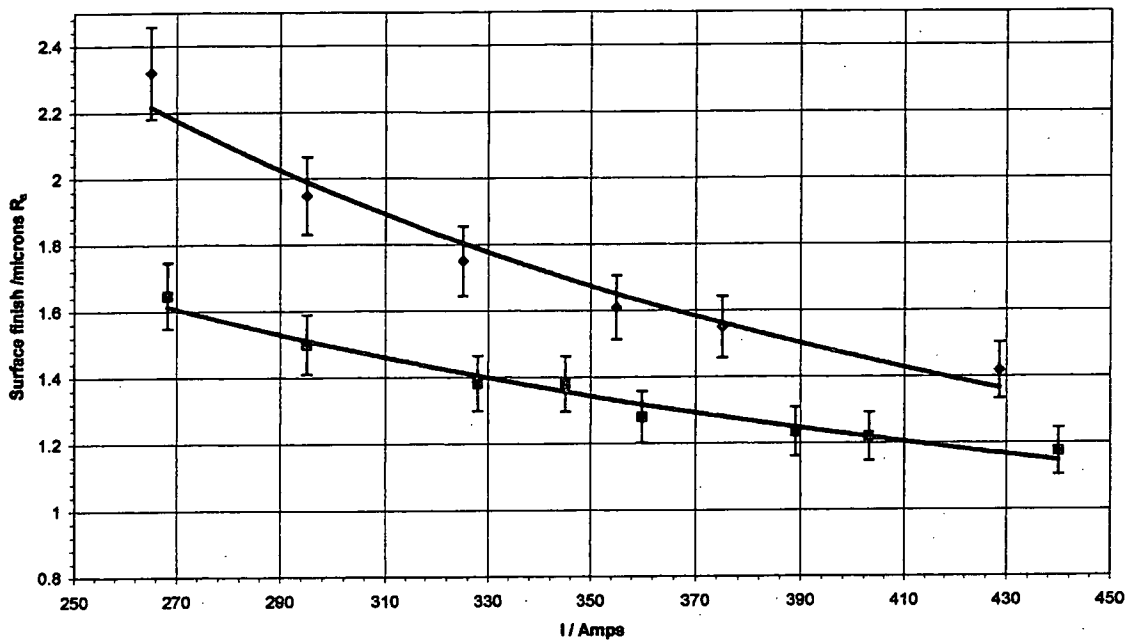

Fig. 16. Surface roughness (μm R_a) as a function of dissolution current (Amps) for surfaces machined using chloride (■) and perchlorate (◆) electrolyte.

the ECM process, these surfaces are seen to be of high integrity with no evidence of structural defects. The lamella grain structure is clearly visible in both cases. In the case of the Perchlorate surface there appears to be some evidence of an increased amount of cross-colony attack, observed as an increased density of darkened etched sites. In order to examine the degree of cross-colony attack further, optical interferometry scans have been made on these surfaces. Fig. 15 shows representative optical interferometry plots of the surface of TiAl after ECM with perchlorate (Fig. 15(c and d)) and chloride (Fig. 15(a and b)) electrolytes. In both cases, machining was carried out until the equilibrium machining current, I_∞, had been established. Both surface scan and height profile information is displayed for each system for the same representative portion of these surfaces. In contrast to the surface machined with chloride (Fig. 15(c)), the lamellar structure of γ-TiAl [4] is clearly seen after ECM with perchlorate (Fig. 15(d)). Furthermore, the variation in height across the surface for the perchlorate data (Fig. 15(c)) is much larger than that found for chloride (Fig. 15(a)) and this variation is closely correlated with the lamellar structure. This is indicative of a difference in the dissolution characteristics with perchlorate between gamma TiAl (about 90 vol.%) and Ti_3Al α-2 phase (about 10 vol.%), the constituents of the lamellar structure. For chloride, this difference is much less. The chronoamperometric measurements (detailed in Section 4.1 above) have demonstrated that machining with perchlorate produces a valency of 2.3. This has been attributed to a difference in valency for the dissolving Ti and Al species when performing ECM under these conditions. It is therefore, suggested that the observed difference in the dissolution characteristics of γ-TiAl and α-2 TiAl could arise from the difference in the proportion of Ti and Al in these two phases (TiAl and Ti_3Al, respectively [4]). It is reasonable to suggest that this would give rise to differences in the overpotential for dissolution at the surfaces of these phases. This would produce the variation in the equilibrium machining distance, z_∞, which would produce the variation in height across the surface observed in these measurements. In contrast, the data for chloride indicate that the Ti and Al species both dissolve with a valency of 3 and with an increased mean overpotential. This suggests that there is less difference in the dissolution characteristics of Ti and Al, and hence less difference in the dissolution characteristics of the γ and α-2 phases. This explains the decreased variation in height obtained with chloride compared to perchlorate. Further evidence of this effect is provided by the typical R_a measurements collected for these surfaces and displayed in Fig. 16. These data show significantly increased R_a values for the perchlorate surfaces.

It is suggested that the increased inhomogeneity of dissolution observed for perchlorate would lead to larger areas of exposed grain boundaries. Since, it is well established that grain boundaries are crucial in determining the fracture characteristics, the differences in surface form observed when using perchlorate compared with chloride is likely to lead to decreased fracture resistance. This is currently being investigated.

5. Conclusions

- Conditions under which reproducible stable ECM are viable have been established and parameterised in terms

of stoichiometry machining parameters generated from chronoamperometric analyses. This has shown that stable dissolution is limited by surface passivation, in the case of the chloride system, and choking in the case of the perchlorate system. The limit of stable dissolution has been extended using the perchlorate system.

- Significant differences have been observed between the ECM characteristics of γ-TiAl with perchlorate and chloride electrolytes. In the case of the perchlorate surface there is evidence of an increased amount of cross-colony attack (also measured as an increased surface roughness for perchlorate surfaces). Chronoamperometric analysis has indicated that this form of attack can be correlated to differences in the valency and the overpotential of the dissolution process. These differences have been related to measured differences in the surface dissolution characteristics of the microstructural phases of this material. These affect surface condition and potentially surface integrity.
- Using the ECM process, the surface of TiAl is seen to be, in general, of high integrity with no evidence of structural defects.
- Surface hardness of the ECM TiAl has been shown to have decreased by 46% with respect conventionally machined (turned) surfaces.

Acknowledgements

We would like to thank the EPSRC/DTI innovative manufacture initiative and Roll-Royce plc for funding the work. We would also like to thank John Horrocks at Rolls-Royce, Derby for advice and supplying the titanium aluminide alloys, and Alan Cannon at Rolls-Royce, Bristol for technical advice on ECM and Dr. Jonathan Muhl for helping with surface analysis.

References

[1] J.A. Peters, M. Blank-Bewersdorff, Sulzer Technical Review 1 (1991) 6–9.
[2] J.M. Larsen, B.D. Worth, S.J. Balsone, J.W. Jones, TiAl applications, Minerals, Met. Mater. Soc. (1995) 821–834.
[3] Z. Yoa, M. Marek, TiAl corrosion, Mater. Sci. Eng. (1995) 994–1000.
[4] M. Yamaguchi, H. Inui, K. Kishida, Gamma Titanium Aluminide Alloys, Mat. Res. Soc. Symp. Proc. 364 (1995) 3–16.
[5] G. Golvin, M. Cianci, B. Kleyn, Minerals, Met. Mater. Soc. (1991) 361–369.
[6] A.L. Mantle, D.K. Aspinwall, Surface integrity and fatigue life of turned gamma titanium aluminide, J. Mater. Process Tech. 72 (3) (1997) 413–420.
[7] P.E. Jones, D. Eylon, Material science and engineering A: structural properties, Microstruc. Process. 263 (2) (1999) 296–304.
[8] S.A. Bentley, N.P. Goh, D.K. Aspinwall, in: Proceedings of the International Conference on Advances in Materials and Processing Technologies, AMPT, 1999.
[9] S.A. Bentley, A.L. Mantle, D.K. Aspinwall, Intermetallics 7 (1999) 967–969.
[10] A.L. Mantle, D.K. Aspinwall, M.L.H. Wise, in: Proceedings of the 3rd International Conference on Behaviour of Materials in Machining, Institute of Materials, UK, 1994, pp. 244–255.
[11] J.F. Wilson, Practice and Theory of Electrochemical Machining, Wiley, New York, 1971.
[12] A.E. DeBarr, D. Oliver, Electrochemical Machining, Macdonald, London, 1968.
[13] H. Tipton, in: Proceedings of the 5th International Conference on Advancement in Machine Tool Designing and Research, 1964, p. 509.
[14] A.R. Mount, K. Eley, D. Clifton, J. Appl. Electrochem. 30 (4) (2000) 447–455.
[15] H. Hardesty, A.R. Mileham, H. Shirrani, Proc. Inst. Mech. Eng. Part B 211 (1997) 197–210.
[16] O.H. Narayanan, S. Hinduja, C.F. Noble, Int. J. Mach. Tool Des. Res. 26 (3) (1986) 323–338.

The Use of Ultrasound for in-line Measurement of the Inter-electrode Gap in Electrochemical Machining

D Clifton, G.M Alder, A.R. Mount* and D. Jardine
University of Edinburgh, School of Mechanical Engineering, King's Buildings, Edinburgh EH9 3JL, UK
*Except * Department of chemistry, University of Edinburgh*

Abstract

An estimate of the nominal equilibrium gap function, for specified process conditions, can be obtained through process characterisation trials carried out prior to determining the tool design. However, the complex nature of process interdependencies means that such gap data may only be valid for a limited range of process conditions. If greater process understanding and control is to be achieved then it is suggested that direct in-line measurement of the gap data dependencies would be required. Any gap dependency can then be compensated by the in-line adjustment of process parameters based on reducing the errors in the gap measurement parameter. A novel approach to achieve this, using an ultrasound device to measure the gap value at any specified point, is presented. In this approach the ultrasound device is clamped directly to the workpiece to measure its change in thickness during ECM. A real-time measurement of the gap value is then computed by subtraction of the tool position from the workpiece thickness. It is shown how the gap data, together with a measurement of current-time data, is used to probe ECM parameters dependencies, such as the sensitivity of the electrolyte conductivity to current density.

Keywords: electrochemical machining, characterisation, ultrasound

1. Introduction

Electrochemical machining (ECM) is a process in which metal is cut and shaped through anodic dissolution. The process is commonly applied to the production of complex shapes in hard materials. Application of the process often incurs high costs due to the need to develop process parameter relationships and tool designs through empirical trials. Such trials often need to be repeated for different machining systems (i.e. electrolyte composition and anode/ cathode material). The process currently finds applications for specialist part production in high technology industries such as aerospace and medical where the high cost of production associated with ECM can often be offset against the high costs already incurred in these industries.

This paper is directed to the development of a methodology by which process descriptions can be readily generated based on directly measurable characterisation relationships. Ultimately such developments would enable ECM system characterisation to be achieved without the need for extensive iterative trials. The primary feature of this methodology is the novel use of ultrasound applied to in-line dynamic measurement of the machining gap. It is shown how this measurement together with other process parameters can be used to develop a detailed understanding of ECM dynamics. The paper also includes a description of the possibility for use of applying in-line gap measurements to maintaining and achieving a specified workpiece profile for a given tooling design.

2. Background

A simplifying assumption commonly made in studies into tool / workpiece transfer characteristics in ECM is that the inter-electrode gap (IEG) is a medium with a constant effective conductivity and that the overpotential values and valency of dissolution are constant and insensitive to process conditions. When these conditions are valid dissolution dynamics can be said to be ideal such that tool design can then be computed by application of Faraday's laws and by solving the Laplace field equation for the required geometry. However, many authors have provided experimental data and developed analytical models to show that assumptions of ideal conditions are only valid for a limited range of process conditions. For example, Hopenfeld and Cole [1] have shown that the effective conductivity of the electrolyte decreases along the axis of the flow direction due to the accumulation of void fraction. Thorpe and Zerkle [2] have carried out a detailed analytical study into the effects of both void fraction and temperature. According to this study the accumulation of void fraction causes a decrease of the effective conductivity along the direction of flow which at equilibrium results in a decrease in the IEG width (gap size). This effect is compensated by the electrolyte temperature increasing, due to a Joule heating, which increases the conductivity (and therefore the gap size) in proportion to position along the length of the flow path. Thus either a decrease or increase in the gap can result depending on which condition dominates. Other non-ideal effects in ECM are less commonly reported but can in some cases be significant. Sensitivity of the overpotential with machining

voltage and also with the type of electrolyte used in the dissolution process has been reported [[2]]. Also, Moir and Harvey [3] report a valency transition when machining stainless steel with dependency correlated to the electrolyte flow velocity and flow path length. Some analysis of how process conditions correlate to these non-ideal effects has been made however, as is generally acknowledged, an improvement of the models and measurements made is still required if a detailed resolution of IEG dependency is to be attained.

The set-up commonly used to develop models and for the study of ECM dynamics is that of a parallel/ planar cell configuration. The dynamics for such a system was first developed in detail [4] and also extended to describe current-time solutions [5]. The basis of this process description is a non-linear dynamic equation, relating the rate of change in gap, *dz/dt*, to the feed rate, *f*, as follows:

$$\frac{dz}{dt} = \frac{k}{z} - f \qquad (1)$$

k is a machinability parameter defined by:

$$k = \frac{\kappa\varepsilon(V - V_0)}{\rho F} \qquad (2)$$

Where κ is the conductivity of the electrolyte, ε is the electrochemical equivalent of dissolution, V is the applied machining voltage, V_0 is the sum of anodic and cathodic overpotentials, ρ is the workpiece density and F is Faraday's constant. During ECM the value of V is usually held constant, ρ is a constant for most practical workpiece materials and F is a constant by definition. The value of the parameter *k* will therefore define overall machinability in terms of the constituent values of electrolyte conductivity, overpotential and valency. Ideal ECM conditions can be defined as existing when this parameter is constant and independent of process parameters. The sensitivity of k, or its constituent parameters, to ECM process conditions can therefore be used to quantify non-ideal conditions.

A direct measurement of the parameter *k* can be provided by developing a gap-time solution to equation 1 (see [5] for details) in the form of:

$$\frac{z_0}{z_\infty} - \frac{z}{z_\infty} + \ln\frac{1 - \frac{z_0}{z_\infty}}{1 - \frac{z}{z_\infty}} = \frac{f^2 t}{k} \qquad (3)$$

Where z_0 and z_∞ are the initial (at time = 0 occurring at the initiation of machining) and equilibrium gap (occurring when both the gap and machining current are effectively constant, for a constant *f*) respectively. z is the gap measured at time t and *k* is the machinability parameter defined by equation 2.

The values of I, I_0, and I_∞ corresponding to the values of z, z_0, and z_∞ respectively in equation 3, can be obtained by use of the simple ohmic relationship, as follows:

$$I = \frac{\kappa(V - V_0)A}{z} \qquad (4)$$

Substitutions into equation 3 gives the current-time solution of the form:

$$\ln\left[\frac{1 - \frac{I_\infty}{I_0}}{1 - \frac{I_\infty}{I}}\right] + \left[\frac{I_\infty}{I_0} - \frac{I_\infty}{I}\right] = \frac{f^2 t}{k} \qquad (5)$$

It can be seen that the machining parameter *k* can be measured using a fit of experimental data to either equation 3 (for gap-time data) or equation 5 (for current-time data). Obtain both current-time and gap-time data would enable a dynamic measurement of conductivity (assuming constant V_0) according to equation 4.

3. Experimental

An initial set of trials to demonstrate and assess the technique has been carried out using the nickel based alloy In718. Electrolyte was made up of a solution of 21.7% wt/wt $NaNO_3$ in water (this concentration was chosen since it corresponds to the molarity of a commonly used reference solution containing 15% NaCl). The tooling has been designed to machine across the full 12mm x 40mm face of the workpiece giving an area, A, of 4.8 cm^2, in a plane configuration, with the flow directed along the tool/workpiece gap in a plane perpendicular to the direction of tool feed. This has enabled the flow regime to be accurately specified and current densities to be accurately determined (since there is no generated surface).

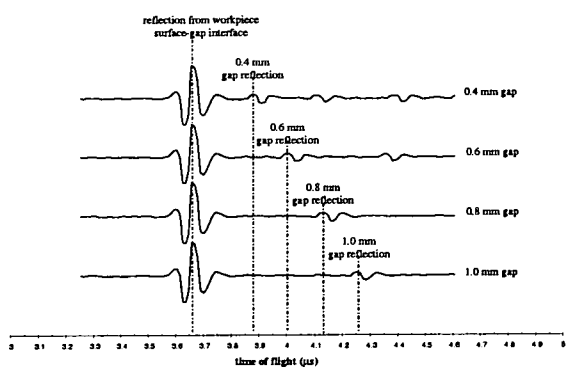

Fig. 1:Time-of-flight traces for ultrasound pulses received from equilibrium gaps set at 0.4, 0.6, 0.8 and 1.0mm

The ultrasound probe, a CLF4 (Buehler Krautkramer Ltd) piezoelectric / perspex delayline system operating at a frequency of 15 MHz, is sprung

loaded against the lower face of the workpiece to be ECM'ed. The ultrasound probe has been positioned to record data at the centre (20 mm from the flow inlet) of the 40 mm flow path length. The upper face of the workpiece is machined in a direction towards the probe and orthogonal to the acoustic axis of the ultrasound beam. The probe operates in a pulse-echo mode (with a pulse repetition frequency of 500 Hz) such that the piezoelectric device producing the ultrasound pulse is automatically energised (during the pulse-off period) into receive mode whereby it converts the reflected sound energy into an electrical signal.

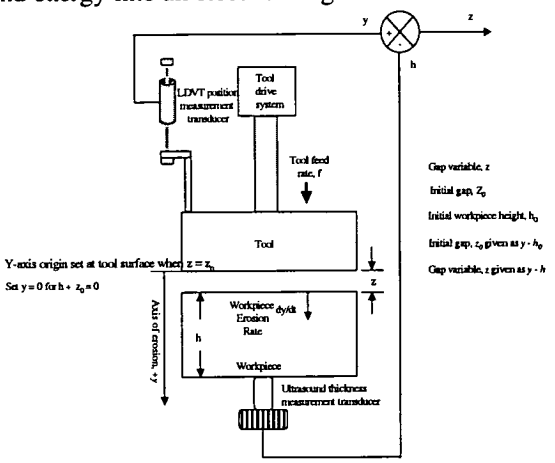

Fig. 2. Tool and workpiece configuration and arrangement used for gap measurement

A USPC2100 (Buehler Krautkramer Ltd) PC based ultrasonic thickness/flaw system has been used to display and analyse the echo from the surface undergoing machining. Thickness computation requires that a series of calibration tests are made using a known thickness of the material to be tested. This enables the ultrasonic propagation velocity to be determined for the workpiece material and/or the electrolyte in the gap. The USPC2100 uses an autocorrelation computation to compute the ultrasound pulse return time (twice the time-of-flight to the interface being measured) and hence calculates the distance to the interface using the predetermined medium velocity.

The machining voltage, measured directly between the workpiece and the tool (i.e. so that possible significant voltage losses in power cables need not be considered), is held at a constant value throughout the machining trial, using the servo controlled motorised rheostat. Electrolyte flow rate and feed rate were also held constant throughout at 15 dm^3 min^{-1} and 1.00 mm min^{-1} respectively. The temperature control system within the electrolyte tank maintains the electrolyte temperature at 30±1°C. Thus, although the electrolyte at the exit from the machining gap will be at a variable temperature, depending mainly on the current density passing for particular conditions, the electrolyte entering the gap will be at a constant 30°C. For further details of the machining apparatus see [5].

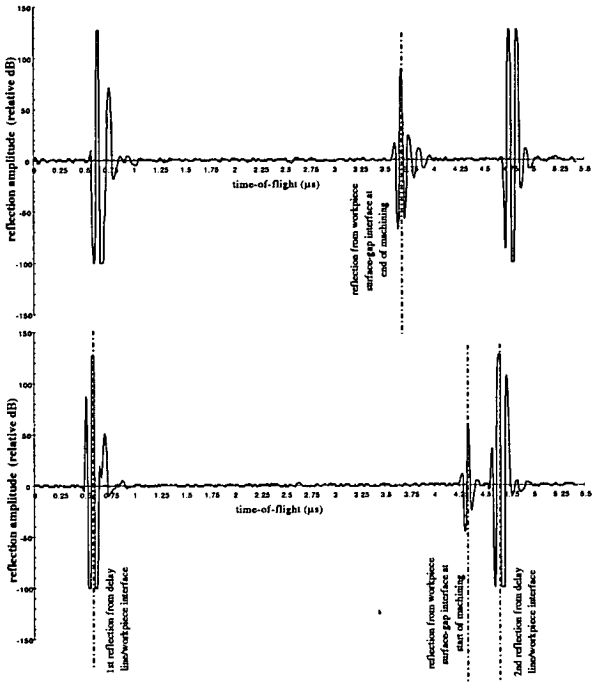

Fig. 3. Shows time-of-flight measurements corresponding to the start of machining (lower trace) and the end of machining (upper trace)

The experimental current-time data, measured using a Hall effect probe, and gap-time data, fed from the USPC2100, were recorded using PC data acquisition (Burr-Brown Visual Designer data acquisition software). Fitting of current-time and gap-time data was carried out using Mathcad's *Genfit* algorithm.

An initial series of ultrasound set-up trials was carried out in which there was no tool feed, only stagnant electrolyte was contained within the gap (i.e. the electrolyte flow was not activated) and the gap power was not energised. A series of time-of-flight plots, obtained from these trials, for ultrasound pulses received from equilibrium gaps set at 0.4, 0.6, 0.8 and 1.0 mm intervals, are shown in figure 1. During these measurements the dominant ultrasound reflection is that received from the upper workpiece surface to gap interface. In this case the ultrasound has passed through only the workpiece material at a velocity of 5720 m/sec (determined by prior calibration through a 10 mm reference sample of In718). The time of flight for this reflection is measured at 3.66 µs corresponding to a workpiece thickness of 20.93 $x10^{-3}$ m. A second reflection, resulting from the ultrasound passing through the electrolyte and rebounding from the lower tool surface, can also be seen in figure 1. This reflection is attenuated by about 26dB relative to the main deflection from the workpiece surface. The velocity of the ultrasound through the electrolyte has been measured using a calibration gap of 1 mm giving a sound velocity through the electrolyte of 1605 m/sec. From figure 1 it can be seen that each increment of gap reduction by 0.2 mm reduces the time-of-flight across the gap in 0.125 µs intervals. When the ECM dissolution power is activated the gap reflection signal is attenuated further (probably due to non-homogeneity in electrolyte density once

dissolution begins) and can no longer be resolved effectively from the noise level of the measurement. The signal can therefore not be used directly for gap measurement. The reflection from the workpiece surface however remains unchanged during dissolution. Thus in order to implement an in-line gap measurement system, during dissolution, the workpiece surface/gap interface reflection has been used together with a continuous direct measurement of the tool position. This arrangement, illustrated in figure 2, incorporates the combined use of linear differential voltage transducer (LDVT), to measure the tool face position, y, and an ultrasound thickness probe to measure the workpiece height, h. The gap, z, being computed as $z = y - h$ for the initial condition that $z_0 = y - h_0$.

4. Results

Figures 3,4,5 and 6 show measurements made from a trial with the gap voltage set at 16 V, a feed rate of 1.0mm/min and an initial electrode gap of 0.8mm. Machining was carried out until equilibrium conditions (constant gap and constant current) were achieved. Figure 3(a) shows the ultrasound time-of-flight measurement corresponding to the start of machining when the workpiece thickness was 20.93mm. Figure 3(b) shows the time-of-flight measurement at the end of the machining run indicating a workpiece thickness of 17.49mm. The machining duration for this run was 234 seconds corresponding to the tool moving a distance of 3.54 mm. This gives a calculated machining gap of 0.26mm. The machining gap-time data measured using the arrangement as shown in figure 2 and recorded at intervals of one second, is shown in figure 4. This data confirms the gap at equilibrium to be in the region of 0.26mm. Figure 5 shows the current time data for the same machining run. The numerical fitting of theoretical relationships for the current-time trend (equation 5) and the gap-time trends (equation 3) to these data (shown in figure 4 and five respectively) produce values for the machining parameter k (defined by equation 2) of $k = 0.0039$ mm^2 sec^{-1} for the gap time data and $k = 0.0038$ mm^2 sec^{-1} for the current time data. Close correspondence between these values confirms the accuracy of the gap measurement data as an average throughout the duration of the machining run.

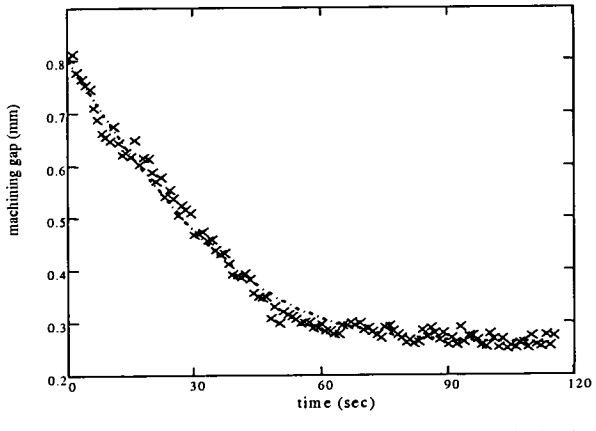

Fig. 4. gap-time measured data (x x x) and plot of theoretical solution according to equation 3(----)

As an example of how parameter interdependency can now be analysed, using the current-time and gap-time data, the effective gap conductivity as a function of current density has been computed, according to equation 4. This has been computed using a value of overpotential of V = 3.0 [5]. Although Tafel behaviour will cause some dependency of V_0 with current density [5], this effect is small (in the region of 0.1V per 100A) and has therefore been neglected. From figure 6 it can be seen that the conductivity shows a general trend indicating an increase from in the region of 16 S m^{-1} to in the region of 21.5 S m^{-1} as the dissolution current increases from 100 A at the start of machining, to 365 A at equilibrium. This increase can be attributed to the increase in available ionic products with current density and also the increase in conductivity as the result of increased Joule heating as the dissolution current increases. A decrease in conductivity, that has previously been observed to occur due to the accumulation of a void fraction [1], is not the dominant effect under these conditions. Such an effect is more likely to be observed at lower flow velocities.

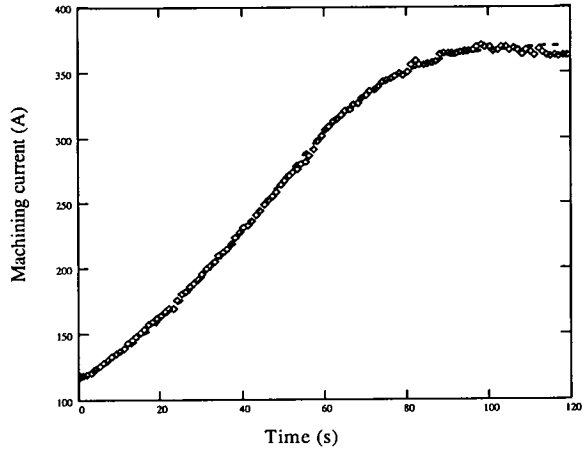

Fig. 5. Current-time measured data (x x x) and plot of theoretical solution according to equation 5(----)

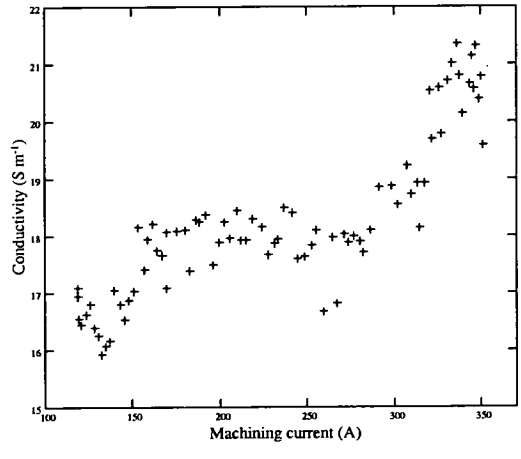

Fig. 6. Dependency of the effective gap conductivity with machining current for In718 /nitrate system at 16 V

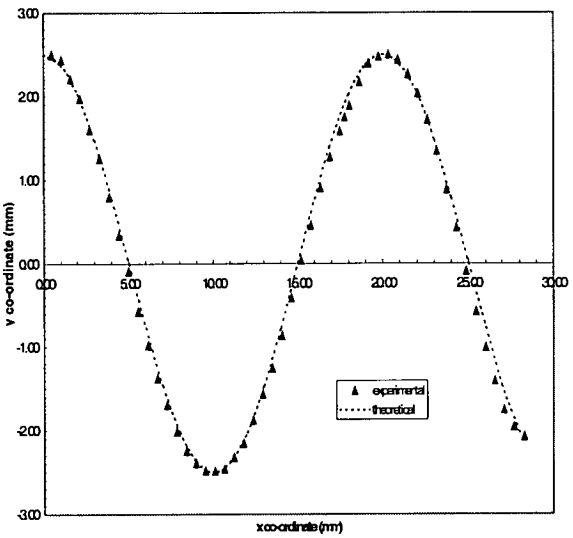

Fig. 7. Comparison between measured and theoretical workpiece profile for single sinusoidal component at nominal gap of 1.0 mm

5. Geometric control using in-line gap measurement

The development of a methodology for monitoring and control of machining gaps makes possible the use of tools designed for operation at larger nominal gaps. The potential advantages are higher electrolyte flow rates and lower cell pressures, but tool design requires more attention because of the significant differences between tool and workpiece geometry. Recent work on two-dimensional tool design [6] has developed a direct analytical relationship between a desired workpiece geometry, and the corresponding tool shape. The workpiece profile, $y_W(x_W)$, is decomposed into N harmonic components defined by:

$$\frac{y_W}{L} = \sum_{r=0}^{r=N} a_r \cos\frac{r\pi x_W}{L} \qquad (6)$$

where x_W and y_W are the workpiece coordinates; L is the profile length; and a_r (r = 1,N) is the amplitude of component r. The corresponding tool profile, $y_T(x_T)$, was shown to be:

$$\frac{y_T}{L} = \frac{z_\infty}{L} + \sum_{r=0}^{r=N} a_r \cosh\frac{r\pi z_\infty}{L}\cos\frac{r\pi x_W}{L}$$
$$\frac{x_T}{L} = \frac{x_W}{L} + \sum_{r=1}^{r=N} a_r \sinh\frac{r\pi z_\infty}{L}\sin\frac{r\pi x_W}{L} \qquad (7)$$

where x_T and y_T are the tool coordinates; and z_∞ is the nominal equilibrium machining gap. Experimental verification of this approach to tool design is shown in Figure 7 in this case to generate a single sinusoidal workpiece surface using a tool designed to operate at a nominal equilibrium gap of 1mm. The theoretical method also allows tolerance bounds to be established on tool manufacture and gap control, so as to achieve given workpiece precision. For example, in the case of the tool used to machine the profile in Fig. 7, it has been shown that the maximum local error in the workpiece profile is of the same order as gap control errors.

Because the flow velocity used to produce the workpiece shown in figure 7 was high (>60m/sec) and the flow path length was small (40mm along the flow axis), non-ideal effects are not likely to cause significant distortion in the IEG. Close correspondence between the theoretical and experimental workpiece surface is therefore observed. Thus for ideal conditions in-line gap measurement can be used as a means of achieving a required tolerance. When non-ideal effects are significant (usually at high flow path lengths, high current densities and/or low flow rates) then dynamic gap measurement can be used to parameterise such effects. Parameterisation by this method can then be used to develop correction functions for appropriate modification to tool designs.

6. Conclusions

The application of ultrasound for dynamic gap-time measurement in electrochemical machining has been successfully demonstrated. Close correlation between the theoretical model and experimental gap-time data has been observed. Furthermore, correspondence of the gap-time data with the current-time data has provided validation as to the accuracy of the gap values over a range of conditions as equilibrium is approached. The use of gap-time data has been shown to provide direct measurement of the sensitivity of conductivity with dissolution current.

Further work will now be undertaken to extend the application of dynamic gap measurement towards more general characterisation of ECM machinability. For example, work is currently underway with the aim of integrating a series of ultrasound gap measurement sensors within a segmented cathode arrangement. The segmented cathode assembly enables dissolution currents to be resolved at pre-defined intervals along the axis of the flow path. The system will enable a study to be made of the relationship between the effective electrolyte conductivity (and in more generally the value of k) and process parameters correlated to flow field co-ordinates. Ultimately the work is intended to lead to a method for the generation of the complete empirical data function describing all non-ideal gap dependencies. Input of this data function into tool design systems of the type described above (section 6) will provide compensation for non-ideal effects.

Acknowledgements

The authors would like to thank the British government funding body, EPSRC, Rolls-Royce plc and Doncasters plc for funding this work.

References

[1] Hopenfield, J., Cole, R. R. *J. Engineering for Industry,* 1966, **88**(4), 455-461

[2] Thorpe J. F., Zerkle, R.D. Analytic determination of the equilibrium gap in electrochemical machining *Int. J. Mach. Tool Des and Res.*, 1969, **9**, 131-144

[3] Moir, P. G., Harvey, J. 16th *MATADOR Conf.* 1976, 257-281

[4] Tipton, H. *Proc. 5th Int. Conf. Machine Tool Design and Research* . 1964, 509-522

[5] Mount, A.R., Eley K., Clifton, D. *J. Applied Electrochem,* 2000, **30**(4) 447-455

[6] Alder G.M., Clifton, D, Mill, F.G. *ImechE, J of Eng. Manuf.* 2000 **214** (B), 754-749

An Integrated Strategy for Materials Characterisation and Process Simulation in Electrochemical Machining

A.R. Mount[a], D. Clifton[b], P. Howarth[a], A. Sherlock[b]
[a] *Department of Chemistry and* [b] *Department of Mechanical Engineering*
King's Buildings, West Mains Road, Edinburgh EH9 3JJ, UK

Abstract

The analysis of current transients during electrochemical machining (ECM) at a planar workpiece planar tool configuration results in the determination of the important parameters for the ECM process. These can be used in finite difference simulation of the ECM process, which allows simulation of the current transients and tool and workpiece configurations at any time for non-planar configurations more applicable to industrial ECM. Small differences in the simulated and experimentally observed current transients are often observed, which can be attributed to variation of the ECM parameters with current and electrolyte flow path length. Measurement of these variations can be achieved by current transient analysis of experimental data obtained from the ECM of a planar workpiece planar segmented tool configuration. This information can then be used to improve the finite difference simulation. Together, this forms an integrated strategy for materials characterisation and process simulation in ECM.

Keywords: electrochemical machining, characterisation, finite difference, process simulation

1. Introduction

Recent technological advances have lead to an increasing number of applications for high strength, low-weight, metallic and intermetallic alloys. This has in turn led to an increasing requirement for metal cutting and forming processes able to cope effectively with such materials. Conventional milling or turning procedures can be problematic, as the necessarily high cutting forces often result in imperfections in shape and/or structure. They can also be uneconomic due to high tool wear and low machining rates. In electrochemical machining (ECM), the metal alloy (the anode or **workpiece**) is removed by electrochemical oxidation and dissolution, by applying a voltage which induces a current between the workpiece and a counterelectrode (the cathode or **tool**). During this process the tool is advanced towards the workpiece at a controlled rate in an electrolyte solution, and control of the resulting workpiece form is achieved by ensuring migrational mass transport and using an appropriately shaped tool. For these advanced alloys, this has the advantages over many shaping processes of being able to machine efficiently despite their hardness and being able to produce complex shapes at high metal removal rates. Also, as the process involves controlled oxidation and dissolution of the metal from all points on the surface, with little increase in surface temperature, a high quality surface is produced without residual stresses or surface damage to the microstructure [1-5]. However, despite these advantages, ECM has yet to become the manufacturing process of choice for these systems. This is due in large part to the difficulty in predicting the tool shape and machining parameters necessary to produce a given workpiece profile. This problem can be considered in two parts; the generation and measurement of machining parameters for a particular workpiece-electrolyte system and the development of a simulation or modeling procedure into which these parameters can be input in order to produce the required tool form for any given workpiece shape. In this paper, a method for determining ECM machining parameters by current transient measurements using a planar workpiece-planar tool system is presented. The application of these parameters to the machining of more complicated shapes is also considered by comparing simulated data obtained using a finite difference technique with data obtained experimentally.

2. Theory of Current Transients in the Planar Machining Configuration

The theory for the analysis of current transients obtained using a planar workpiece-planar tool configuration has been detailed elsewhere [6]. For this system, the schematic set-up is as shown in Fig. 1.

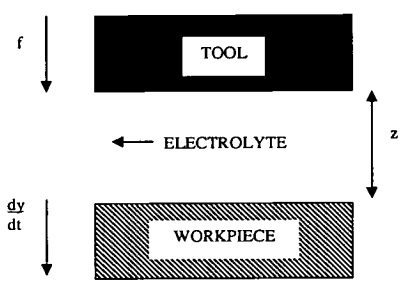

Fig. 1. The configuration for electrochemical machining. The planar tool is fed at a feed rate, f, towards the workpiece, which is machining at a rate dy/dt. Electrolyte flows rapidly through the tool-workpiece gap. At long times or $t \rightarrow \infty$ (equilibrium), the separation of the electrodes, z, is z_∞ and $f = dy/dt$.

The planar tool is of area A and moves at a constant feed rate, f, towards a planar parallel workpiece, also of area A. It is assumed that the current is governed by migration (an essential assumption for stable machining). The simplest case is where the electrolyte is being pumped through the interelectrode gap (IEG) at high enough flow rate that the build up of machining products and/or the loss of ions from the electrolyte does not significantly affect the electrolyte conductivity, which can therefore be assumed to remain constant across the tool and workpiece throughout the experiment. Since the gap between the electrodes is z, and the applied voltage is generally sufficient for the establishment of field lines perpendicular to the electrodes, the migrational current across the electrolyte, I, is given by:

$$I = \frac{\kappa(V - V_0)A}{z} \tag{1}$$

where V is the applied voltage, V_0 is the voltage required at the two electrodes to drive the reaction and κ is the conductivity of the electrolyte. Assuming that this current produces solely workpiece dissolution, this current is also the dissolution current of the workpiece, and therefore

$$I = \left[\frac{nFA\rho}{M}\right]\frac{dy}{dt} \tag{2}$$

where n is the number of electrons transferred per dissolving atom (the "valency"), F is the Faraday (96,487 C mol^{-1}), ρ is the density of the workpiece material, dy/dt is the thickness of workpiece removed per unit time and M is the average molecular weight (the mass of one mole of the workpiece material with the workpiece composition). The change in the interelectrode distance, z, is given by

$$\frac{dz}{dt} = \frac{dy}{dt} - f = \frac{k}{z} - f \tag{3}$$

where

$$k = \left(\frac{\kappa(V - V_0)M}{nF\rho}\right) \tag{4}$$

For I_∞, (I when $t \rightarrow \infty$) a constant current is reached and z remains constant at z_∞ as dz/dt = 0; hence $f = dy/dt = k/z_\infty$. Thus

$$\frac{I_\infty}{A} = \frac{nF\rho f}{M} \tag{5}$$

and

$$\frac{dz}{dt} = k\left[\frac{1}{z} - \frac{1}{z_\infty}\right] \tag{6}$$

This equation can be integrated from t = i, $z = z_i$ to t = t, z = z, to give

$$\ln\left[\frac{z_\infty - z_i}{z_\infty - z}\right] + \frac{z_i - z}{z_\infty} = \frac{k(t - t_i)}{z_\infty^2} \tag{7}$$

or from eqn. (1),

$$\ln\left[\frac{1 - \frac{I_\infty}{I_i}}{1 - \frac{I_\infty}{I}}\right] + \left[\frac{I_\infty}{I_i} - \frac{I_\infty}{I}\right] = \frac{k(t - t_i)}{z_\infty^2} = \frac{f^2(t - t_i)}{k} \tag{8}$$

where I_i, I_∞ and I are the initial current, the equilibrium current and the current at $t = t_i$, ∞ and t respectively. Judicious choice of these currents allows analysis of ECM parameters to obtain values of f^2/k and I_i.

3. Experimental

The experimental apparatus used in these measurements is as detailed in reference 6. The solution flow was controlled by means of a Hydriacell D25 pump (Wanner Engineering Inc.); the flow sensor was a type FT 13 (Platon Instrumentation) and the current transducers were of type HT (RS Components). The data were collected using a 486 PC (Viglen) and Intelligent Instruments (Burr-Brown) in house data logging system combined with the Visual Designer software (Intelligent Instruments). The experimental set-up involved a reservoir of 60 litres of electrolyte, thermostatically controlled at 30°C. The planar anode, or workpiece, was of width 1.20 cm and length (along the electrolyte flow path) 4.00 cm, giving a total area of 4.80 cm^2. The planar single tool was a copper-tungsten alloy of the same dimensions and area. Experimental feed rates, f, were set at 1.00 mm min^{-1} throughout unless otherwise stated.

4. Electrochemical machining

Fig 2 shows typical current transient data for the machining of In718 alloy. Also shown are theoretical fits to the current-time data produced by iterative fitting to eqn. (8). This procedure involves selecting a suitable initial value of t_i (and hence I_i) from the early experimental current transient data and for all experimental currents, I, to iteratively minimise the error in the calculated values of t from eqn. (8) with respect to the experimental times, t.

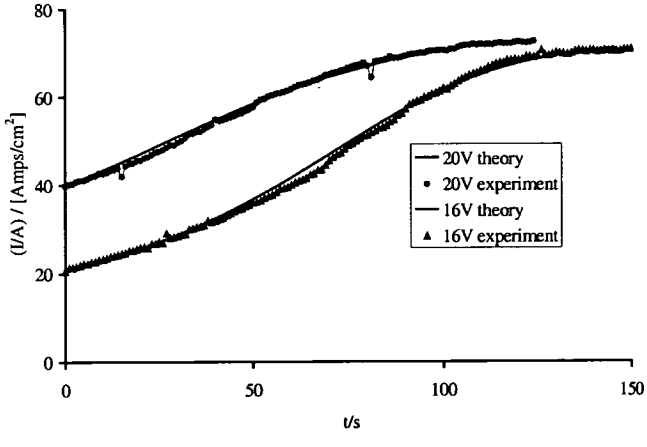

Fig. 2. Comparison of typical theoretical and experimental current transients for the ECM of In718 at applied voltages of 16 V and 20 V, with an electrolyte of 21.7% w/v of aqueous sodium nitrate, flowing at 20 l min^{-1} and f = 1.0 mm min^{-1}. Currents are

reported as current densities, I/A. The initial gap between tool and workpiece was 0.80 mm. Theoretical data were produced by iterative fitting to eqn. (8), with values of t = i and I_i being fixed at the experimental values as close to the application of the machining voltage as possible, when stable machining started to occur. As with all other ECM current transients in this paper, time, t, is measured with respect to this chosen value of t_i.

It is clear that this process produces close agreement between experiment and theory. Furthermore, values of I_∞ and f^2/k are produced for each iterative fit. As expected from eqn. (5), for a constant feed rate (in this case f = 1.0 mm min^{-1}) I_∞/A was found to be independent of applied voltage at 70 ± 2 A cm^{-2} for In718. As ρ = 8.228 g cm^{-3} and M = 59.79 g mol^{-1} in this case, this gives a constant value for the valency of n = 3.0 ± 0.2.

The values of the parameters f^2/k and I_i are also important, as they can be used to determine a value for V_0. This is shown by Fig. 3, where k/f^2 and I_i have been plotted as a function of the applied voltage, V, for both chloride and nitrate electrolytes.

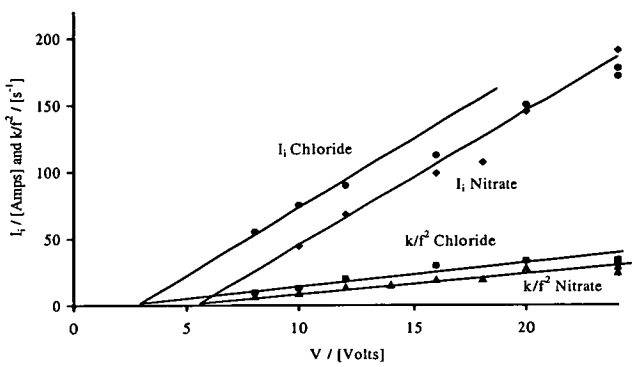

Fig. 3. Plot of I_i and k/f^2 against the applied voltage V for 21.7% w/v aqueous sodium nitrate and 15% w/v aqueous sodium chloride electrolyte. Each of these electrolyte concentrations is equivalent, at 2.56 mol dm^{-3}. t_i was chosen to be as close as possible to the onset of stable machining, to ensure that z_i = 0.80 mm (the initial gap) in each case.

From eqns. (1) and (4), both k/f^2 and I_i should be proportional to $(V - V_0)$. Thus for each electrolyte, as V_0 is relatively insensitive to changes in V [6], if there is no change in surface reaction, both lines should intercept at a common V-axis intercept of V_0. This is clearly the case for the nitrate electrolyte, where an intercept of V_0 = 5.4 ± 0.4 V is obtained. The low V data for chloride also show similar behaviour, with an intercept of V_0 = 3.0 ± 0.4 V. The gradients of each of the lines can be used to determine a value for the conductivity of the electrolyte, κ, which was found to be 20 ± 1 S m^{-1} for both the nitrate and chloride electrolytes. This is consistent with previous measurements on these electrolytes [7]. However, at high V, both the k/f^2 and I_i data for chloride show systematic deviations from their lines, which indicates a significant increase in V_0. This can be attributed to a change in the nature of the anodic dissolution reaction.

5. Finite Difference Simulation of Non-Planar ECM Configurations

It is important to assess whether these ECM parameters obtained from a planar machining configuration can be generalized to more typical non-planar configurations and other tool feed regimes. A 2D simulation of the ECM process was therefore undertaken using a time-stepped finite difference approach. It is assumed that changes in the electric field distribution within the gap occur much faster than any changes in the geometry. Thus the Laplace field equation can be solved using the finite difference method for a fixed tool and workpiece geometry. The tool and workpiece geometries are represented by interpolation splines. At each node of the workpiece spline the derivative of the potential in the direction normal to the surface is calculated. From this the current density and hence the removal rate according to Faraday's laws is calculated. Thus the change in the workpiece geometry for a small time-step Δt can be calculated. The workpiece spline is then reformed for the new geometry ready for the next time-step. This can be repeated for as long as necessary, often until equilibrium machining occurs (as evidenced by the attainment of a constant current and the invariance of the workpiece shape with time). This process simply requires the input of the ECM parameters V_0, n, κ obtained from the planar ECM configuration experiments, plus the appropriate values of z_i, V, A and f for the experiment. Fig. 4 shows as an example the calculated and experimentally observed current transients obtained for ECM of a planar In718 workpiece in 15% w/v aqueous sodium chloride electrolyte using a stepped tool. In this example the feed rate, f was also increased from 0.5 mm min^{-1} to 0.8 mm min^{-1} during the transient.

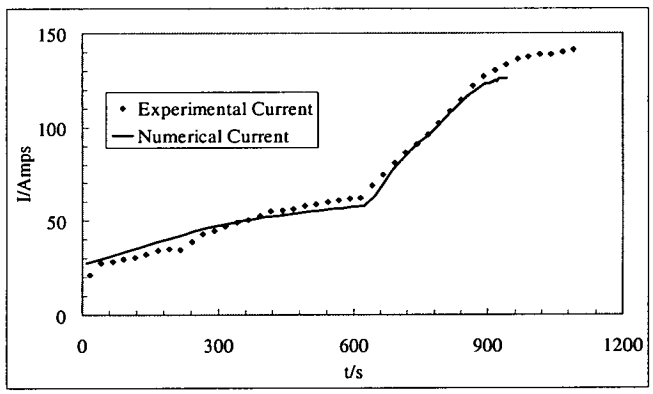

Fig. 4. Comparison of experimental and numerical current transients for a planar In 718 workpiece using 15% chloride electrolyte and a stepped tool with an applied voltage of 16 V.

The reasonable agreement between the numerical and experimental current transients demonstrates the success of this approach. Furthermore, this procedure allows comparison between the numerical and experimental workpiece shapes at equilibrium machining. This is shown in Fig. 5, along with the tool shape used in these experiments. Again, reasonable agreement between numerical simulation and experiment can be seen. The small deviation observed between theory and experiment seen in Figs. 4 and 5 is most likely attributable either to changes in V_0 or κ with ECM current or to changes in these parameters along the electrolyte flow path length. Improved simulation would therefore require measurement of these parameters as a function of these variables. The former effect has been measured by iterative fitting of small sections of the current transient (for which V_0 and κ can be assumed to be constant) to eqn. (8) [6]. The latter has been studied by the use of a segmented tool (section 6).

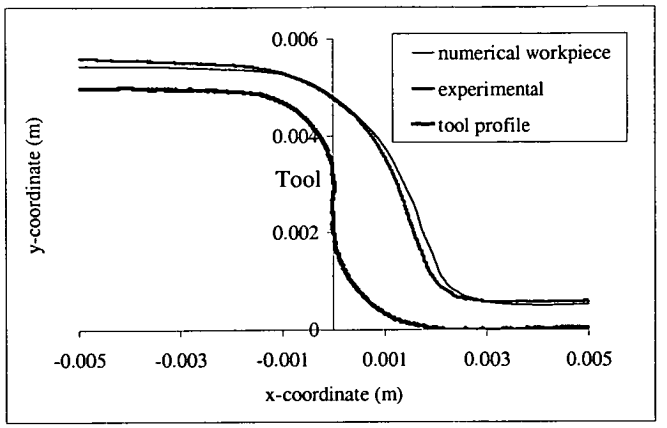

Fig. 5. Tool profile and numerical and experimental workpiece profiles for the In 718 ECM experiment in Fig. 4.

6. Planar segmented tool planar workpiece ECM system

At slower flow rates and higher ECM currents, the consumption and production of ions during ECM would be expected to change significantly the composition of the electrolyte, which may result in variation in the ECM parameters along the flow path. In order to study this, a planar segmented tool system has been constructed, as shown in Fig. 6 [8]. Here the planar tool is divided into seven distinct segments of similar area along the flow path length, each separated by a relatively thin insulating gap.

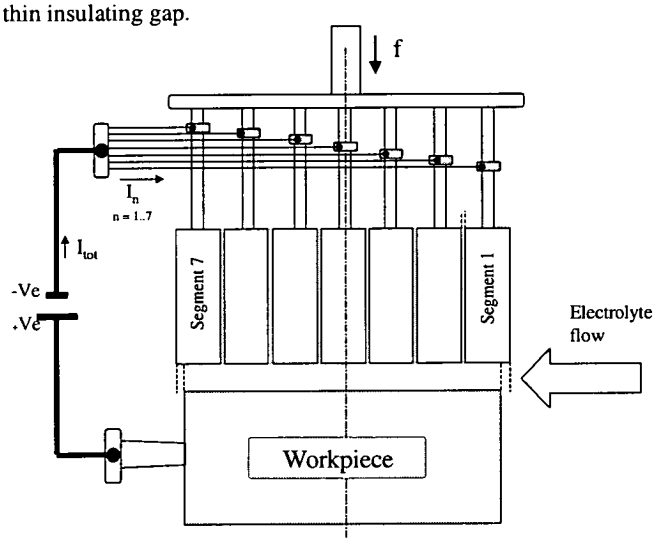

Fig. 6. The planar segmented tool planar workpiece system.

The ECM current through each segment, I_n, is measured individually during the experiment, with n having values from 1 to 7 for the seven segments. Segment 1 corresponds to the most upstream segment in the electrolyte flow and segment 7 the most downstream. Fig. 7 shows a typical response for the ECM of In 718 in 21.7% sodium nitrate using this system.

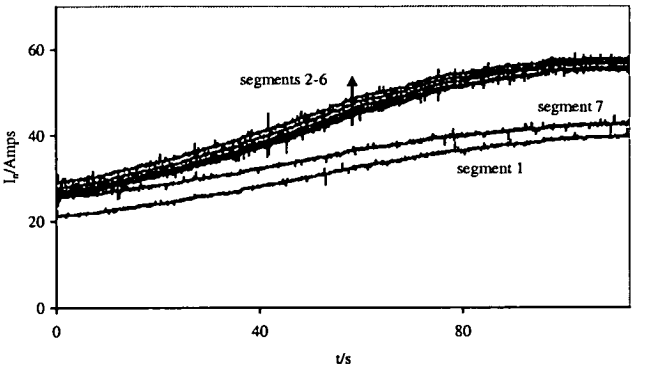

Fig. 7. Segment current transients for the ECM of a planar In 718 workpiece in 21.7% electrolyte using the segmented tool. The applied voltage, V was 20 V, the starting gap was 0.8 mm and the electrolyte flow rate was 16 l min^{-1}.

As expected, segments 2-6 all produce current transients that can be fitted to eqn. (8), using the appropriate value of the area, A, of each segment, and each gives the same value of I_∞ within experimental error, indicating no significant change in valency across the workpiece surface. However, the values of I_i (and k/f^2 produced from the iterative fits) can be seen to show a small but significant increase with increasing segment number, indicative of an increase in the value of k. This is most likely due to a small but significant increase in κ, which can be attributed to the production of soluble ionic products (metal ions at the workpiece, hydroxide ions at the tool) along with a small increase in the electrolyte temperature along the path length in the IEG due to resistive heating [9, 10]. In this case these effects clearly outweigh the decrease in κ which would be expected if the hydrogen gas evolved at the tool produced a significant accumulated void fraction in the electrolyte [11]. It should be noted that segments 1 and 7 produce different current transients. This is because they overlap the workpiece edges (Fig. 6). This produces a lower effective area and hence equilibrium current for these two segments compared to segments 2-6. Furthermore, there is significant contribution from non perpendicular field lines between the overlapping portion of segments 1 and 7 and the workpiece edge at larger values of z. As a result, the workpiece edges become rounded during machining and the current transients for segments 1 and 7 show a different form from eqn. (8), which has been considered elsewhere [8]. Despite this difference in form, the increased value of I_i for segment 7 compared with segment 1 can still clearly be seen in Fig. 7, which confirms the increase in k measured for the other segments along the flow path length.

The segmented tool can also be used to study ECM under conditions where a change in valency occurs along the electrolyte path length. A good example is the ECM of the stainless steel SS316 (EN 58J) in sodium chloride electrolyte. Previous measurements [12,13] have shown that a valency change, attributed to a change in dissolution valencies from Fe(III), Cr(VI) to Fe(II), Cr(III) occurs and that under suitable conditions of electrolyte flow, feed rate, and applied voltage, equilibrium machining can produce two different zones of stable ECM machining, each with their own characteristic valency and surface finish. Fig. 8 shows typical current transients obtained for ECM of an SS 316 workpiece using the planar segmented tool under conditions where this occurs.

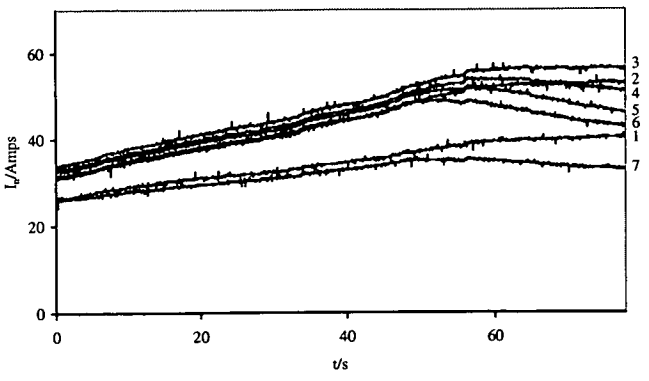

Fig. 8. Segment current transients for the ECM of a planar SS 316 workpiece in 15% w/v sodium chloride electrolyte using the segmented tool. The applied voltage, V was 25 V, the starting gap was 0.8 mm and the electrolyte flow rate was 16 l min^{-1}. The segment numbers for each transient are shown to the right of the diagram.

As for In 718, a small increase in κ is observed along the electrolyte path length at early times. However, as machining progresses and the current increases and the value of z decreases, a critical point is reached for segments further down the flow path where the valency decreases, as evidenced by the decrease in the machining current. This is consistent with previous observations [12]. It is clear from these data that this decrease occurs earliest on segment 7 and progressively later with decreasing segment number, with little discernible change in valency for segment 1 throughout its transient. This suggests that this change in valency is as a result of the change in electrolyte composition along the path length as a result of machining. Furthermore, the change can be seen to be progressive, with the valency decreasing smoothly, rather than stepping from one limiting value to another. Such observations allow the valency to be determined as a function of electrolyte path length and ECM current across the workpiece.

Conclusions

The use of a planar workpiece planar tool configuration to measure and analyse current transients allows the determination of the parameters important in ECM. Segmentation of the tool allows the dependency of these parameters on electrolyte flow length to be determined. Using finite difference process simulation, it has been shown that these parameters can then be used in the simulation of non-planar configurations applicable to practical ECM. Together, this forms an integrated stategy for ECM characterisation and process development.

Acknowledgements

The authors would like to thank the British government funding body, EPSRC, Rolls-Royce plc and Doncasters plc for providing the funding for this work. Thanks also go to Mikel Agirre for carrying out some of the experiments on the stepped tool.

References

[1] D.G. Risco and A.D. Davydov, J. American Soc. Mech. Eng., 64 (1993) 701.
[2] M.A. ElDardery, Int. J. Machine Tool Design and Research, 22 (1982) 147.
[3] B. Kellock, J. Machinery and Production Engineering, 140(3604) (1982) 40.
[4] O.V.K. Chetty and R.V. Murthy Radhakrishan, Trans. of the ASME J. Engineering for Industry, 103(3) (1981) 341.
[5] A.R. Mileham, S.J. Harvey and K.J. Stout, Journal of Wear, 109 (1986) 207.
[6] A.R. Mount, K. Eley and D. Clifton, J. Applied Electrochem., 30 (2000) 447.
[7] C.N. Larsson in "Electrochemical Machining" ed. A.E. De Barr, D.A. Oliver, (MacDonald, London) (1968) p. 108.
[8] A.R.Mount, P. Howarth and D. Clifton, J. Applied Electrochem., (2000) submitted for publication.
[9] W.G. Clark and J.A. McGeough, J. Applied Electrochem., (1977) 277.
[10] J.F. Thorpe and R.D. Zerkle, J. Mach. Tool Des. and Res., 9 (1969) 131.
[11] J. Hopenfield and R.R. Cole, J. Engineering for Industry, 88 (1966) 455.
[12] P.G. Moir and J. Harvey, Proc. of 16th MATADOR conference, (1976) 275.
[13] A.R. Mileham, R.M. Jones and S.J. Harvey, Prec. Eng., 4 (1982) 168.

A direct analytical solution to the tool design problem in electrochemical machining under steady state conditions

G M Alder, D Clifton* and **F Mill**
School of Mechanical Engineering, University of Edinburgh, Scotland, UK

Abstract: A method for the direct computation of two-dimensional electrochemical machining tool designs is described. The required workpiece geometry is represented by a Fourier series. Conformal transformation is then used to express the tool shape in series form, each term being a direct analytical function of the corresponding workpiece harmonic. Tool designs are thus achieved without numerical iteration. The model has been experimentally validated for a required workpiece geometry consisting of two harmonics, for which a tool was designed and manufactured. An In 718–15 per cent NaCl workpiece–electrolyte system was used to produce a machined surface, whose Fourier transform was obtained. The measured and predicted harmonic amplitudes agree closely. This harmonic design method is also shown to give insight into the relationship and limitations between tool design and achievable workpiece detail.

Keywords: electrochemical machining, tool design, conformal transformation

NOTATION

a_r	coefficient of Fourier series
E	applied electrode potential
F	Faraday's constant
h	nominal equilibrium gap
j_n	normal component of current density
j_x, j_y	current density components in the coordinate directions
J_{eq}	nominal equilibrium current density
k	electrochemical equivalent of the work material
L	width of tool and workpiece surface
r	an integer denoting harmonic in series
u	electric field potential
U	potential driving the dissolution current
U_0	total overpotential at the electrode surfaces
V_f	tool feed velocity
x, y	physical coordinates
Z	complex function
η	current efficiency
θ	local angle that the machined surface makes with the x axis
κ	electrolyte conductivity
ρ	density of the work material
ϕ	dimensionless electric potential
ψ	dimensionless electric flux

The MS was received on 23 December 1999 and was accepted after revision for publication on 9 February 2000.
**Corresponding author: School of Mechanical Engineering, University of Edinburgh, King's Buildings, Mayfield Road, Edinburgh, Scotland EH9 3JL, UK.*

1 INTRODUCTION

Electrochemical machining (ECM), in which metal is removed by electrochemical dissolution of a workpiece material, is a process that has the potential to produce complex shapes at high metal removal rates. A significant constraint in attaining improved manufacturing effectiveness in ECM applications is that of achieving the correct tool design for a specified workpiece profile. In this short communication a method for a new direct analytical approach to tool design is outlined.

Much work has been reported on the problem of ECM process simulation [**1**, **2**], where the tool geometry is specified and the resulting workpiece geometry generated. The basis of these approaches is a solution of the field equations using finite difference, finite element or boundary element methods. The design problem, which is addressed here, is the inverse of simulation, attempting to determine the tool profile needed for a given workpiece surface. Previous workers addressing the design problem [**3–5**] have employed computational iteration to satisfy boundary conditions at both tool and

workpiece surfaces. The new approach is analytical and computationally very efficient when compared with the numerical optimization methods.

The method presented is applicable for two-dimensional tool design, in the case of equilibrium machining along a singe axis. This is a common configuration in ECM applications. The method starts with a Fourier transform of the required two-dimensional workpiece shape. Conformal transformation is then used to express the tool shape analytically as a direct function of the harmonics of the Fourier transform. Although conformal transformation has previously been applied to ECM by, for example, Nilson and Tsuei [3], in this case the transformation was determined numerically. The present analysis is particularly applicable when the nominal equilibrium gap is known in advance (for specified machining conditions) or can be measured during machining. In this short communication the concept is described and then applied to a test shape for experimental validation.

2 THEORY

The two-dimensional configuration considered is shown in Fig. 1a. The tool surface AB moves downwards, parallel to the y axis with a steady feed velocity V_f. The coordinates x and y are non-dimensionalized by the width of both surfaces, L. The machined surface CD lies below the tool. The analysis relates to the electric field in the inter-electrode gap. The boundary conditions are

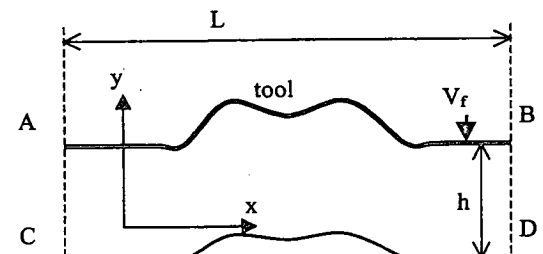

(a)

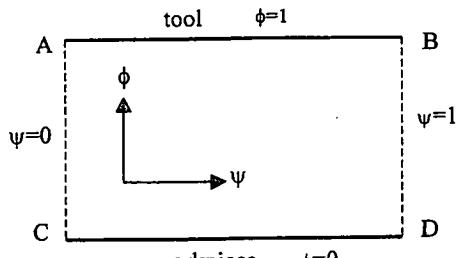

(b)

Fig. 1 The two coordinate systems: (a) physical coordinates; (b) ψ–ϕ coordinates

constant potentials at the tool surface and the machine surface. The boundaries AC and BD are insulated.

The spacing between the two surfaces is expressed i terms of the nominal equilibrium gap h defined as

$$h = \frac{\eta k \kappa E}{\rho V_f} \qquad (1$$

where η is the current efficiency, κ is the electrolyte co ductivity, ρ and k are the density and electrochemic equivalent of the work material, defined as $k = nA/F$ where n is the valency, A is the atomic number and F Faraday's constant. E is the potential difference betwee the surfaces which can be decomposed as the differenc between, U is the potential driving the dissolution cu rent and U_0 is the total overpotential at the electroc surfaces. The definition of h is the nominal gap an would exist in the case where both the tool and the worl piece are planes normal to the feed direction.

The analysis below uses the dimensionless potenti $\phi = (u/E)(h/L)$, where u is the electric potential at an point in the field, and the dimensionless flux ψ is define as

$$\frac{j_x h}{\kappa E} = \frac{\partial \psi}{\partial y}, \qquad \frac{j_y h}{\kappa E} = -\frac{\partial \psi}{\partial x} \qquad (2$$

where j_x and j_y are the current density components in th coordinate directions. The current density componen can also be derived from the potential:

$$\frac{j_x h}{\kappa E} = \frac{\partial \phi}{\partial x}, \qquad \frac{j_y h}{\kappa E} = \frac{\partial \phi}{\partial y} \qquad (3$$

Thus, the following relationships can be obtained fro equations (2) and (3):

$$\frac{\partial \psi}{\partial y} = \frac{\partial \phi}{\partial x}, \qquad \frac{\partial \psi}{\partial x} = -\frac{\partial \phi}{\partial y} \qquad (4$$

The analysis follows the approach of Nilson and Tsu [3], in which it is noted that ψ and ϕ are orthogon (because lines of flux are normal to lines of equi pote tial), and that they constitute an alternative coordina system (Fig. 1b). Equations (4) are the Cauchy Rieman equations of complex variable theory an mean that the relationship between the two coordina systems can be written

$$Z = Z(W) \qquad (5$$

where Z is an analytic function relating the compl numbers $Z = y + ix$ and $W = \phi + i\psi$. Of the ma possible functions Z, it is proposed here that lettin $Z = W + e^W$ provides a particular basis for the EC configuration of Fig. 1. This choice can be generalize as follows:

$$Z = W + \sum_{r=1}^{r=N} a_r (e^{r\pi W} + e^{-r\pi W}) \qquad (6$$

where the integer r is the wave number of a harmonic series and a_r is the corresponding constant coefficient. Application of equation (5) then leads to a direct analytical relationship between a desired machined surface and the tool required to make it.

At the machined surface, the rate of removal of material is related to the current density normal to the surface by Faraday's law:

$$V_n = \frac{\eta}{\rho} k j_n \tag{7}$$

where V_n is the velocity at which the surface erodes (normal to the surface) and j_n is the normal component of current density at the surface. In steady state ECM, the local shape is maintained with corresponding points moving in the y direction at the tool feed velocity. Thus

$$\frac{V_n}{\cos\theta} = \frac{(\eta/\rho)kj_n}{\cos\theta} = V_f \tag{8}$$

where θ is the local angle that the machined surface makes with the x axis. Using equation (1) leads to

$$\frac{j_n h}{\kappa E \cos\theta} = 1 \tag{9}$$

The vertical component of current density is $j_y = j_n \cos\theta$ so that, with substitution from equation (3), equation (9) becomes

$$\frac{j_y h}{\kappa E \cos^2\theta} = \frac{1}{\cos^2\theta}\frac{\partial\psi}{\partial x} = 1 \tag{10}$$

Equation (10) applies along the machined surface, which is a path of constant $\phi = 0$. By making a change in coordinates, it can be shown that:

$$\left(\frac{\partial\psi}{\partial x}\right)_y = \left(\frac{\partial\psi}{\partial x}\right)_\phi \cos^2\theta \tag{11}$$

where the subscripts denote the path of partial differentiation. Thus, the boundary condition at the machined surface [equation (10)] becomes

$$\left(\frac{\partial\psi}{\partial x}\right)_\phi = 1 \tag{12}$$

Equation (12) represents a uniform horizontal current distribution along the machined surface, which is consistent with the underlying model of steady state erosion.

When equation (6) is expanded, and real and imaginary parts equated, the following equations are obtained:

$$x = \psi + \sum_{r=1}^{r=N} a_r \sinh(r\pi\phi)\sin(r\pi\psi)$$

$$y = \phi + \sum_{r=0}^{r=N} a_r \cosh(r\pi\phi)\cos(r\pi\psi) \tag{13}$$

On the equipotential line $\phi = 0$, equations (13) become

$$x = \psi \tag{14a}$$

$$y = \sum_{r=0}^{r=N} a_r \cos(r\pi\psi) \tag{14b}$$

Equation (14a) satisfies equation (12), confirming that the line $\phi = 0$ represents the machined surface. The procedure thus starts with the decomposition of the desired machined surface profile into harmonic components, giving the coefficients a_r in equation (14b). Any other equipotential line $\phi =$ constant in equations (13) then represents a corresponding tool surface lying at a particular value of the equilibrium gap.

3 EXPERIMENTAL VALIDATION

In order to validate the model, the double cosine case with $a_1 = 0.5$ and $a_2 = -0.125$ in equation (14b) has been considered. These coefficients become $a_1 = 5 \times 10^{-3}$ m and $a_2 = -1.25 \times 10^{-3}$ m when expressed in physical dimensions for a tool of 40×10^{-3} m overall width, as shown in Fig. 2. Equations (13) were then applied to give the required tool profile for a nominal machining gap [as defined by equation (1)] of 0.6×10^{-3} m. This tool profile was then manufactured.

The workpiece material was the nickel-based alloy In 718. Electrolyte was made up as a solution of 15% w/w $NaNO_3$ in water. During machining the workpiece was fully enclosed within a flow cell that acts to direct and confine the electrolyte along the line of the workpiece surface (left to right in Fig. 2) . Flow conditions were set to pass a constant 20 l/min through the machining gap. This rate has been determined from previous work [6], to be sufficient that the geometric distortions caused by variations in effective electrolyte conductivity, thought to be due to the accumulation of machining products [7], are less than 0.01×10^{-3} m and can be neglected.

An initial set of calibration trials was undertaken to determine the nominal gap–voltage function according to

$$h(U) = \frac{(U - U_0)\kappa}{J_{eq}} \tag{15}$$

where J is the steady state current density.

From previous work [6] on the In 718–15 per cent NaCl system the constants $\kappa = 0.22 \times 10^2$ S/cm and $U_0 = 3.0$ V were obtained. At the fixed feed rate of 1.0 mm/min used in the experiments, $J_{eq} = 70.4 \times 10^4$ A/m^2. The nominal gap was then set, by adjusting the voltage, according to equation (15). The value of h used was $0.60 \pm 0.01 \times 10^{-3}$ m at a gap voltage of 20.0 ± 0.1 V. In order to characterize the sensitivity of

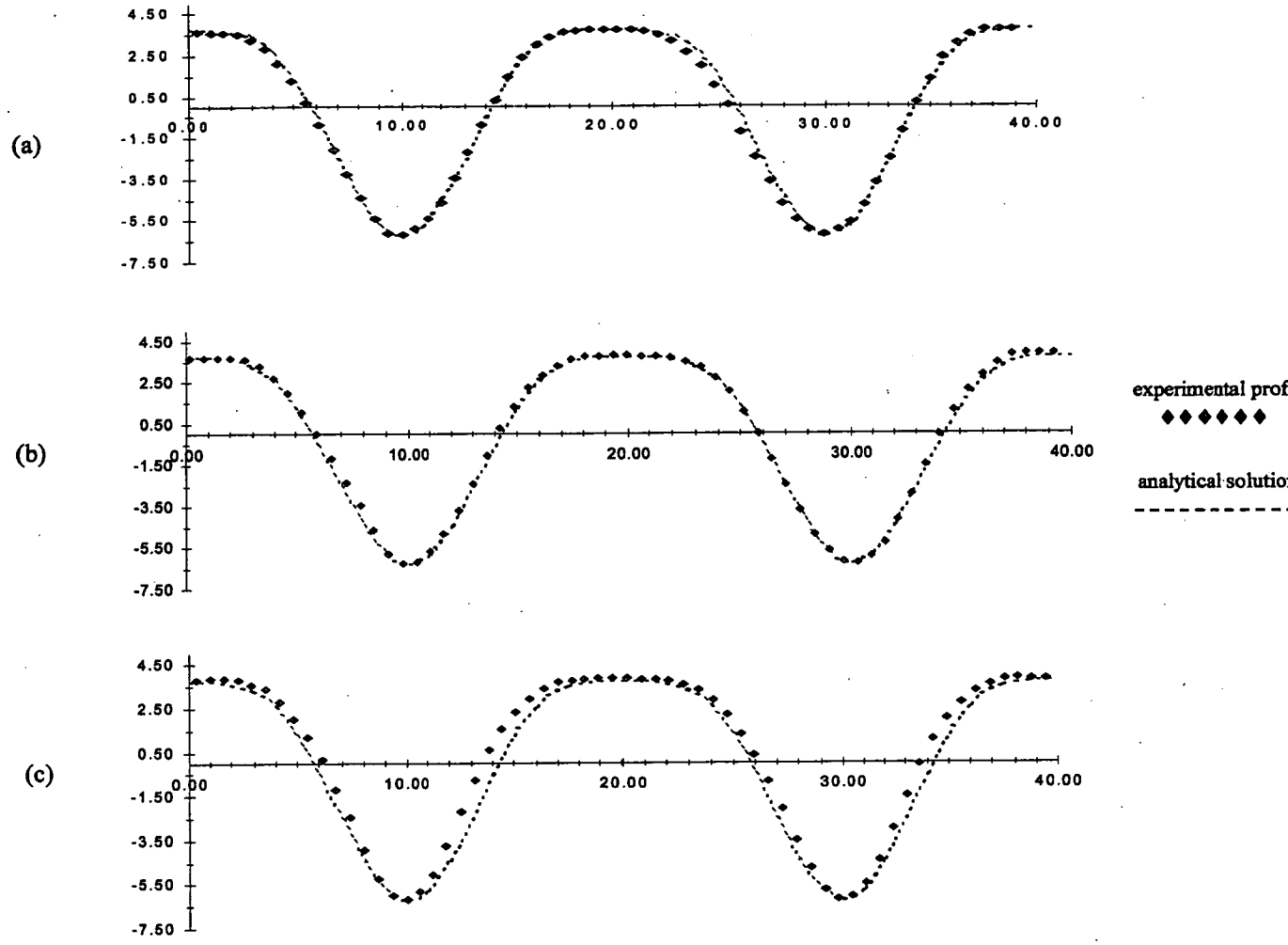

Fig. 2 Comparison between a theoretical workpiece profile and an experimental profile for $a_1 = 5 \times 10^{-3}$ m and $a_2 = -1.25 \times 10^{-3}$ m (all axes in $\times 10^{-3}$ m): (a) 0.8×10^{-3} m nominal gap; (b) 0.6×10^{-3} m nominal gap; (c) 0.4×10^{-3} m nominal gap

the analytical solution to deviations in the actual gap, additional machining operations were carried out at gaps slightly below and above the nominal value of $0.60 \pm 0.01 \times 10^{-3}$ m. These were $0.40 \pm 0.01 \times 10^{-3}$ m, using a voltage of 14.0 ± 0.1 V, and $0.80 \pm 0.01 \times 10^{-3}$ m using a gap voltage of 26.0 ± 0.1 V.

Machined profiles, plotted with the theoretical profile, for the computed nominal gap at 0.6×10^{-3} m and the additional profiles at gaps of 0.4×10^{-3} m and 0.8×10^{-3} m are shown in Fig. 2. A close spatial correspondence to the model workpiece shape can be seen at the set gap of 0.6×10^{-3} m while, as would be predicted, at the gap of 0.8 mm the machined profile is wider than the model shape and narrower for the 0.4 mm gap. However, because the convergence to conformity between the theory and machined profile is difficult to quantify in the spatial domain, a series of Fourier transforms has been applied to produce the coefficients a_1 and a_2 for the experimental profiles. Convergence is then quantified as the minimization of the difference $a_{1(\text{diff})} = a_{1(\text{theory})} - a_{1(\text{exper})}$ and $a_{2(\text{diff})} = a_{2(\text{theory})} - a_{2(\text{exper})}$. This gives $a_{1(\text{diff})}$ and $a_{2(\text{diff})}$ for th 0.4×10^{-3} m gap profile of 0.14 and 0.31 respectivel and for the 0.8×10^{-3} m gap profile of -0.13 and 0.2 respectively. This compares with the case of th 0.6×10^{-3} m gap, on which the actual tool design wa based, of 0.01 and 0.00 respectively. From these data close convergence to correspondence at the predicte gap of 0.6×10^{-3} m can be clearly seen.

4 DISCUSSION

The experiments described in Section 3 above succes fully demonstrate the application of the theory outline in Section 2. This success arises even though the theor uses an ideal model covering only the electric field wit assumption of uniform gap conductivity. This is in lin with the set experimental conditions that non-ide effects become small at high flowrates.

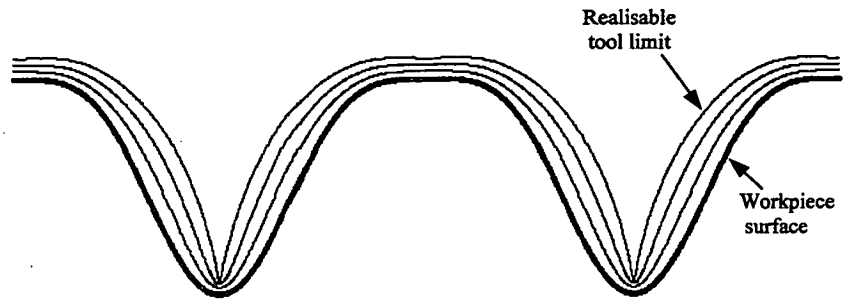

Fig. 3 Predicted tool profiles, showing the approach to the realizable limit as the gap increases

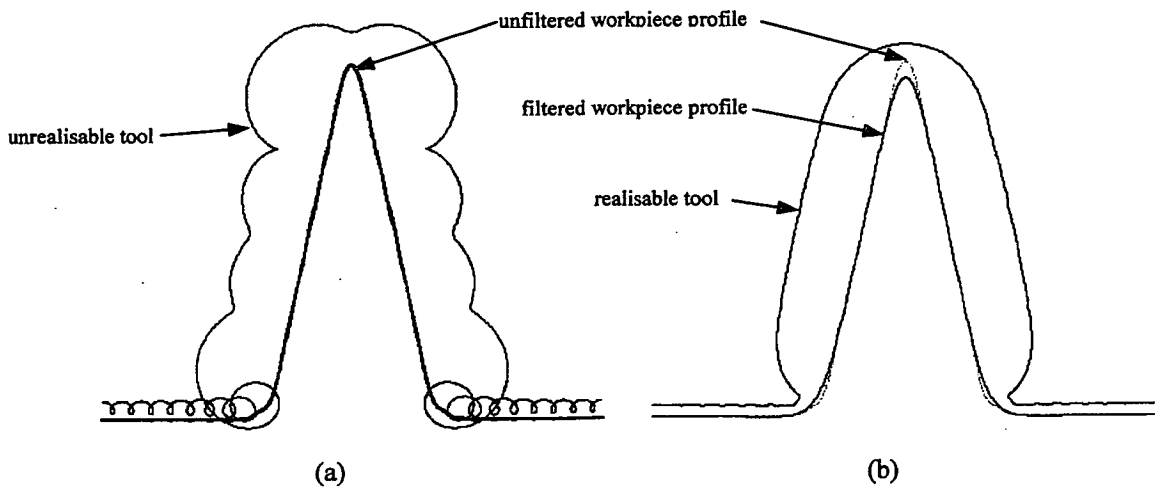

Fig. 4 Example showing the effect of filtering on workpiece profiles having high-order components: (a) unrealizable tool for an unfiltered profile; (b) realizable tool for a filtered profile

An important advantage of the design method described here is that larger machining gaps can be contemplated, allowing higher electrolyte flowrates, with consequent benefits with regard to the removal of gaseous and solid products. The harmonic design method also gives insight into the profile relationship between an ECM tool and the workpiece. For example, Fig. 3 shows a set of tool surfaces, generated by equations (13), for equilibrium gap values $h/L = 0.025$, 0.05 and 0.075. It can be seen that, as the gap is increased, the tool shape needed to generate the required profile becomes more distorted, eventually reaching a limiting state, beyond which physically realizable tools are not possible. This limit is in line with ECM experience, where it is well known that fine detail cannot be copied across significant machining gaps. Inspection of equations (13) shows that limiting cases arise when the sinh and cosh terms significantly distort the original harmonics of equation (14b). That happens at the larger gaps and/or higher wave numbers. The example in Fig. 4 shows a workpiece consisting of straight line and radius segments. The harmonic decomposition leads to a large number of high wave number components whose amplitudes, although initially small, are amplified and distorted by equations (13) when the tool shape is calculated (Fig. 4a). Filtering the workpiece surface leads to a feasible tool shape (Fig. 4b), but at the expense of some loss of workpiece detail. However, the example illustrates the ability of equations (13), not only to generate tool profiles, but also to provide information about how feasible it might be to machine a given geometry in the first place.

REFERENCES

1 **Hardisty, H., Mileham, A. R.** and **Shirvani, H.** Theoretical and computational investigation of the electrochemical machining process for characteristic cases of a stepped moving tool eroding a plane surface. *Proc. Instn Mech. Engrs, Part B, Journal of Engineering Manufacture*, 1997, 211(B3), 197–210.

2 **Narayanan, O. H., Hinduja, S.** and **Nobel C.F.** The prediction of workpiece shape during electrochemical machining by the boundary element method. *Int. J. Mach. Tool Des. Res.*, 1986, **26**(3), 323–338.

3 **Nilson, R. H.** and **Tsuei, Y. G.** Free boundary problem for the Laplace equation with application to ecm tool design. *Trans. ASME, J. Appl. Mechanics*, 1976, **8**(4), 54–58.

4 **Shuvra, D. A. S.** and **Ambar, K. M.** Use of boundary element method for the determination of tools shape in electrochemical machining. *Int. J. Numer. Meth. Engng*, 1992, **35**(5), 1045–1054.

5 **Zhou, Y.** and **Derby, J. J.** The cathode design problem in electrochemical machining. *Chem. Engng Sci.*, 1995, **50**(17), 2679–2689.

6 **Mount, A. R.** and **Clifton, D.** Theoretical analysis of chronc amperometric transients in electrochemical machining an characterisation of titanium 6/4 and Inconel 718 alloy *J. Appl. Electrochemistry*, 2000, **30**(4), 447–455.

7 **Hopenfield, J.** and **Cole, R. R.** Prediction of the one-dimer sional equilibrium cutting gap in electrochemical machinin *Trans. ASME, J. Engng for Industry*, 1969, (B8), 755–765.

A2 Mathcad Worksheets.

Although around thirty Mathcad spreadsheets were used of throughout the work in this thesis, the following three spreadsheet provide an overview of the most significant computations which contain the basis of most of the other spreadsheets.

The three appended spreadsheets are as follows:

File: *ECM basic dynamics general:* This spreadsheet has been used for general computations and simulations based on the planar dynamics as described in chapter two.

File: *Current transient fit to segment currents*: The spreadsheet contains details of how current-time data was fitted to theoretical solutions to provide values of the k-parameter. A similar spreadsheet was used for the fitting of gap-time data.

File: *Flow path length interval solver*: This spreadsheet was used to discretise equal intervals of flow path length (corresponding to segment widths of the segmented tool) for the double cosine tool, as described in chapter 8.

File: ECM basic dynamics general

This worksheet can be used to caculate the theoretical equilibrium gap functions for the case of a plane parallel electrode arrangement. The system uses current transient data from which the erosion parameters of electrolyte conductivity, overpotential, and equlibrium current are used to caculate a series of characteristics relating the equilibrium gap to several machining variables.

Set machining parameters for run to be analysed are:

Machining area of: $area := 4.8cm^2$

feed rate $f := 1.00mm \cdot min^{-1}$

Machining voltage

Fixed process constants are:

The Faraday $Far := 96487C\,mole^{-1}$

Density and elemental composition for In718 alloy is as follows:

$Far = 9.649 \times 10^4\,s\,A\,mol^{-1}$

Density of material $\rho := 8.228gm \cdot cm^{-3}$

Composition constant computed as follows

NB Total in % column must equal 1(i.e. 100%): Use 0 in % column if element not in alloy

	Mass	Valency	%
Aluminium	M	z	%
Magenese(Mn)	27.0	3.0	0.0048
Carbon	54.94	3.0	0.0022
Chromium	12	3.0	0.0005
Coalt	52	3.0	0.1816
Iron	58.9	3.0	0.0017
Magnesium (Mg)	55.9	3.0	0.235
Molybdenum	24.3	3.0	0
Nickel	95.9	3.0	0.0296
Silicon	58.7	3.0	0.5332
Titanium	28.1	3.0	0.001
Vanadium	47.9	3.0	.0102
copper	50.9	3.0	0
Mn	63.55	3.0	0.00017
	0	3.0	0

$a :=$

check that % tot is equal to one $per\_tot := \sum_{c=0}^{13} a_{c,2}$ $per\_tot = 0.99997$

From the elemental composition above the average molecular mass, M_av and the electrochemical equivalent, ε can be calculated as follows:

Average molecular mass $M_{av} := \sum_{i=0}^{13} a_{i,0} \cdot a_{i,2}$

$M_{av} = 57.601$

give Mav units of gm per mol $M := M \cdot gm \cdot mol^{-1}$

Then Calculate the valency using the measured values of density average molecular mass as

Calculate electrochemical equivalent using valency as specified above

$$\varepsilon := \sum_{i=0}^{13} \frac{a_{i,0}}{a_{i,1}} \cdot a_{i,2}$$

$$\varepsilon = 1.92 \times 10^{4}\,\mathrm{mol\,kg^{-1}\,gm{\cdot}mol^{-1}}$$

From the axis intercept of the plot k/f^2 Vs $V\text{-}V_0$ and Io/A Vs $V\text{-}V_0$, the electrolyte conductivity,κ is determined as

$V_0 := 3.0V$ for chloride with error +/- 0.4V

From the axis intercept of the plot k/f^2 Vs $V\text{-}V_0$ and Io/A Vs $V\text{-}V_0$, the electrolyte conductivity,κ is determined as

$$\kappa := 0.2\mathrm{S{\cdot}cm^{-1}}$$

The measured equlibrium current is: $A_{eq} := 338{\cdot}A$ $J_{eq} := \frac{A_{eq}}{area}$ $J_{eq} = 70.4\,\mathrm{A{\cdot}cm^{-2}}$

According to Faraday's laws the thickness of material removed from unit area of the workpiece in time t, at equlibrium is given by:

Thus for $t := 1{\cdot}min$ $thickness := \frac{J_{eq}{\cdot}t{\cdot}\varepsilon}{\rho{\cdot}Far}$

Sinc the system is at equlibrium this will also equal the feed rate (distance travelled by tool in the same time) so that a value for the valency, n can be determined by assuming 100% dissolution effectivness, and writing ε as M_{av}/n, so that:

$$n := \frac{J_{eq}{\cdot}M_{av}}{\rho{\cdot}Far{\cdot}f} \qquad \text{eq1.1}$$

$volts := 25{\cdot}V$

$n := 3.0$

The current density through the electrolyte, J is given by: $J := E{\cdot}\kappa$ eq 1.2

Where E is the potential gradient in the electrolyte, given by:

$$E := \frac{(volts - V_0)}{z_{eq}}$$

Where Volts-Vo is the voltage available to drive the current through the electrolyte and zeq is the equlibrium gap

So that $z_{eq} := \frac{(V - V_0){\cdot}\kappa}{J_{eq}}$

And subsituting for Jeq from a rearrangement of eq 1.1., gives:

$$z_{eq} := \frac{(volts - V_0){\cdot}\kappa{\cdot}M_{av}}{n{\cdot}\rho{\cdot}Far{\cdot}f} \qquad \text{eq 1.3}$$

$z_{eq} = 0.638\,mm$

erosion constant can be formulated as : $k := \frac{(volts - V_0){\cdot}\kappa{\cdot}M_{av}}{n{\cdot}\rho{\cdot}Far}$ $k = 0.010641\,\mathrm{mm^2{\cdot}s^{-1}}$

$k = 1.064 \times 10^{-8}\,\mathrm{m^2\,s^{-1}}$

and $k2 := \frac{f^2}{k}$ $k2 = 0.026\,\mathrm{s^{-1}}$

For a varying voltage at a fixed feedrate the change in gap can be plotted by rearranging eq 1.21 as:

exp data from trials DC1NC* $X := (18 \;\; 20.3 \;\; 21 \;\; 22 \;\; 26 \;\; 28)$

$Y := (0.52 \quad 0.62 \quad 0.65 \quad 0.72 \quad 0.88 \quad 0.96)_i \qquad i := 0, 1 .. 5$

$\kappa := 0.25 \cdot S \cdot cm^{-1}$

$volts\_var := 10 \cdot V, 11 \cdot V .. 30 \cdot V$

$$z\_var(volts\_var, over\_var) := \frac{(volts\_var - over\_var) \cdot \kappa}{J_{eq}}$$

$z\_var(25. \cdot V, 5 \cdot V) = 0.71\ mm$

$z\_var(25. \cdot V, 4 \cdot V) = 0.75\ mm$

$z\_var(25. \cdot V, 6 \cdot V) = 0.67\ mm$

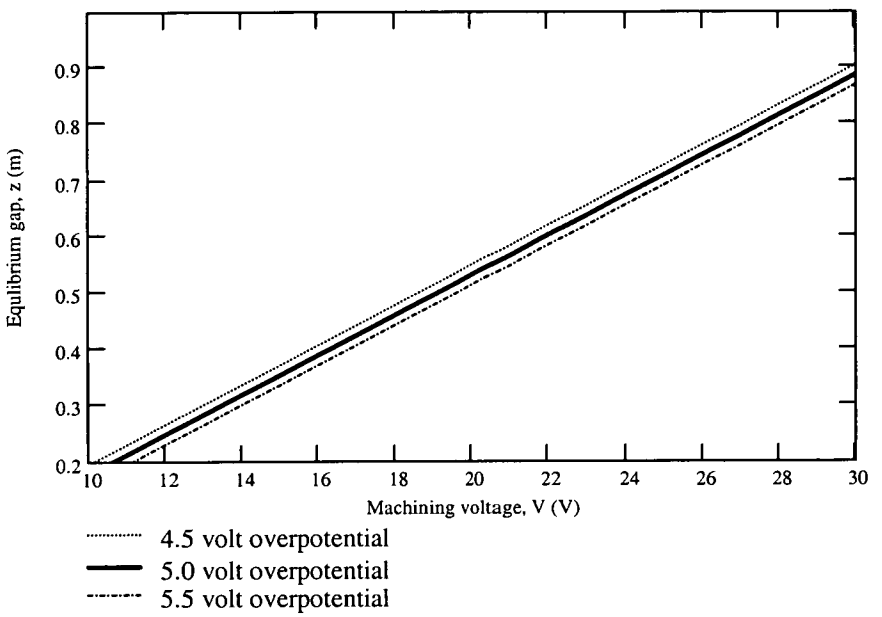

equation 1.3 can be used to examine the sensitivity of the IEG to feedrate,valency, conductivity and overpotential, as follows.

For feed rate range $f\_var := 1.0 \cdot mm \cdot min^{-1}, 1.1 \cdot mm \cdot min^{-1} .. 3.0 \cdot mm \cdot min^{-1}$

For valency variation range $n\_var := 2, 2.1 .. 4$

For conductivity range $\kappa\_var := 0.1 \cdot S \cdot cm^{-1}, 0.2 \cdot S \cdot cm^{-1} .. 0.3 \cdot S \cdot cm^{-1}$

and for overpotential range $V_{0\_var} := 2 \cdot V, 3 \cdot V .. 4 \cdot V$

Setup IEG/feedrate function

$$z_{eq}(f\_var, volts\_var) := \frac{(volts\_var - V_0) \cdot \kappa \cdot M_{av}}{n \cdot \rho \cdot Far \cdot f\_var}$$

$$z_{eq}\left(1.0 \cdot \frac{mm}{min}, 25 \cdot V\right) = 7.981 \times 10^{-4}\ m$$

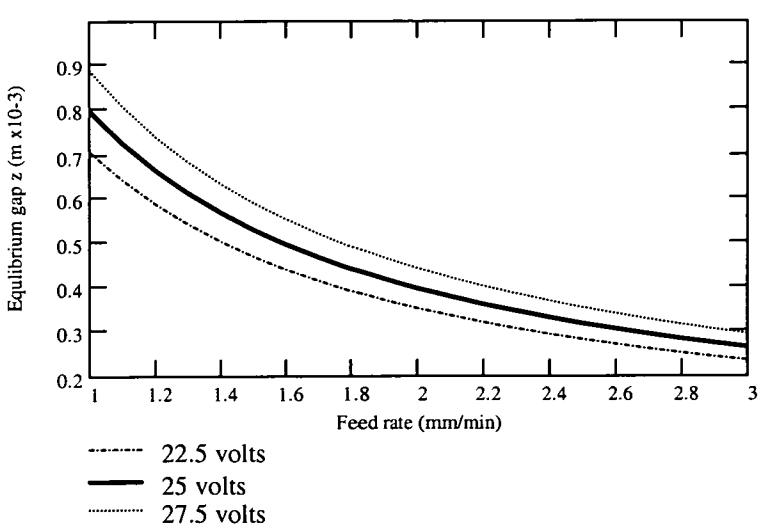

Setup IEG/valency function $z_{eq}(n\_var, volts\_var) := \frac{(volts\_var - V_0)\cdot\kappa\cdot M_{av}}{n\_var\cdot\rho\cdot Far\cdot f}$

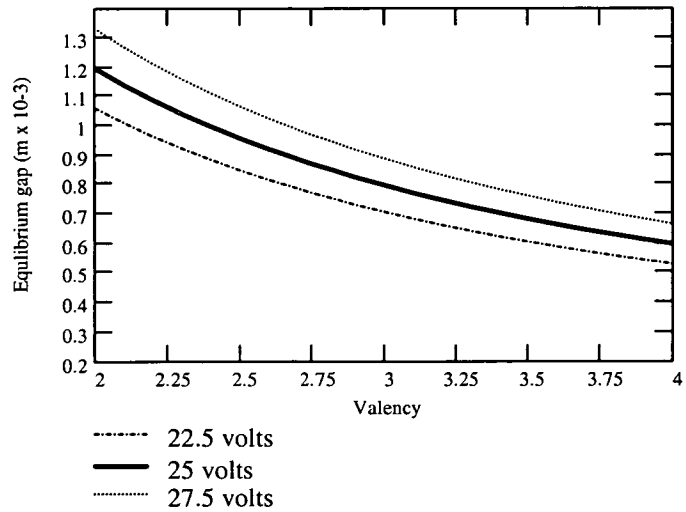

Setup IEG/conductivity function $z_{eq}(\kappa\_var, volts\_var) := \frac{(volts\_var - V_0)\cdot\kappa\_var\cdot M_{av}}{n\cdot\rho\cdot Far\cdot f}$

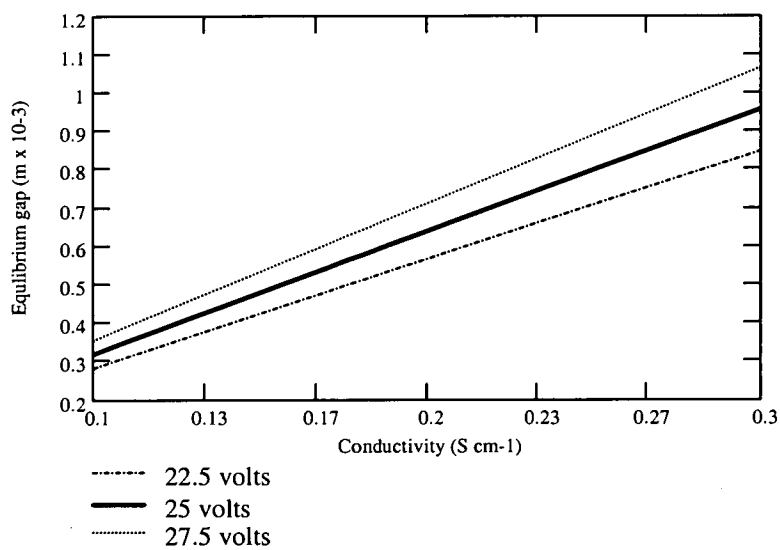

Setup IEG/overpotential function $z_{eq}(V_{0\_var}, volts\_var) := \frac{(volts\_var - V_{0\_var})\cdot\kappa\cdot M_{av}}{n\cdot\rho\cdot Far\cdot f}$

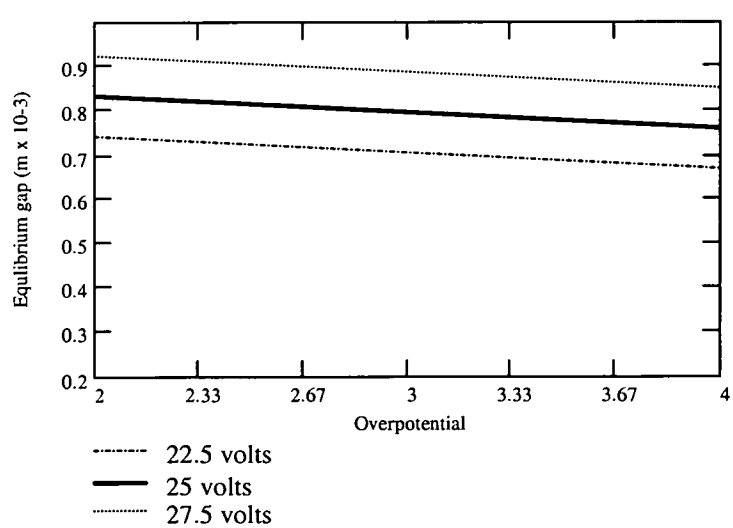

File: Current transient fit to segmented currents

Electrolyte conductivity $\kappa := 0.20 \cdot S \cdot cm^{-1}$

Machining voltage $Volts := 16 \cdot V$

Molecular Mass $M := 57.6 \cdot gm \cdot mol^{-1}$

Set voltage losses $V_0 := 3.0 \cdot V$

Set machining parameters for run to be analysed are:

feed rate $f := 1.00 mm \cdot min^{-1}$

Fixed process constants are:

The Faraday $Far := 96487 C\, mole^{-1}$

Density and elemental composition for In718 alloy is as follows:

Density of material $\rho := 8.228 gm \cdot cm^{-3}$

valency $n := 3.2$

$area := 4.8 \cdot cm^2$

Calculate Erosion constant $k := \frac{\kappa \cdot (Volts - V_0) \cdot M}{n \cdot Far \cdot \rho}$ $k = 0.00589\ mm^2 \cdot sec^{-1}$

Calculate equilibrium gap $zi := \frac{k}{f}$ $zi = 0.354\, mm$ $k = 5.895 \times 10^{-9}\, m^2 s^{-1}$

$\frac{k}{f^2} = 21.222\, s$ $\frac{f^2}{k} = 4.712 \times 10^{-2}\, s^{-1}$

data :=

	0	1	2
0	25.57	28.71	32.77
1	25.86	28.43	32.49
2	25.57	28.71	32.49
3	27.3	28.99	33.06
4	25.86	29.26	33.34
5	26.44	29.54	33.63
6	26.44	29.82	34.2
7	27.3	30.37	34.77
8	27.3	30.65	35.05
9	27.59	30.93	35.34
10	27.88	31.2	35.62

because units are difficult to handle for minerr redefine k and f without units

$f := 0.0166$ set series (i.e collumn) number $j := 0$

$k1 := 0.0057$

$\frac{f^2}{k1} = 4.834 \times 10^{-2}$ $\frac{k1}{f^2} = 20.685$ $equli\_curr := 72$

Set value for equilibrium current $Ji := equli\_curr$

$J := 0.5$ size of data series is $end := 140$

Given

Assign ECM current transient equality $\left(\frac{Ji}{J1o} - \frac{Ji}{J}\right) + \ln\left(\frac{1 - \frac{Ji}{J1o}}{1 - \frac{Ji}{J}}\right) = \frac{(f^2 \cdot t)}{k1}$

Minimise error in J based on above function $CurrTran(J1o, Ji, t) := Minerr(J)$

Set index count to number of data points to fit. $i := 0, 1 .. end$

Assign time variable to index to sync plot of data and function $t_i := i$

Assign start current variable $J1o := data_{1,j}$

Assign variable JJ to function CurrTran $JJ1_i := CurrTran(J1o, Ji, t_i)$

compute mean squared error $\sum_{i=0}^{end-1} (JJ1_i - data_{i,j})^2 = 59.341$

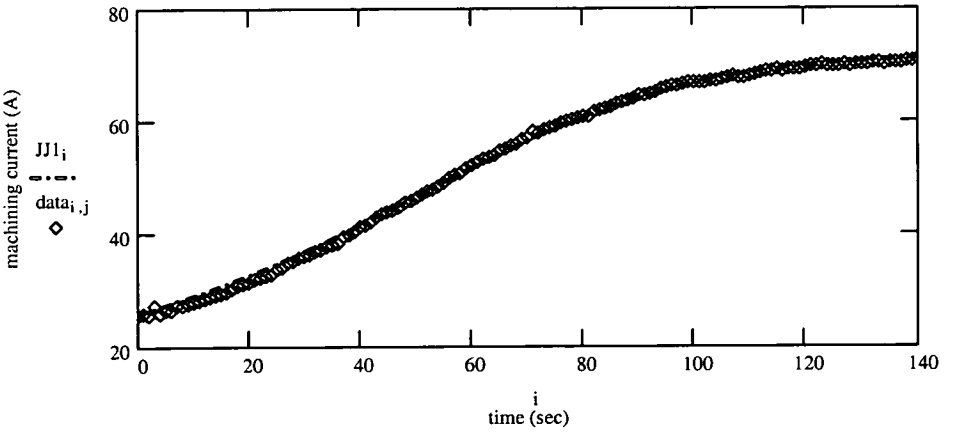

$k2 := 0.0055$ $\quad j := 1$ $\quad Ji := equli\_curr$

$\frac{f^2}{k2} = 5.01 \times 10^{-2}$

$\frac{k2}{f^2} = 19.959$

Given

Assign ECM current transient equality $\left(\frac{Ji}{J2o} - \frac{Ji}{J}\right) + \ln\left(\frac{1 - \frac{Ji}{J2o}}{1 - \frac{Ji}{J}}\right) = \frac{(f^2 \cdot t)}{k2}$

Minimise error in J based on above function $CurrTran(J2o, Ji, t) := Minerr(J)$

Set index count to number of data points to fit. $i := 0, 1 .. end$

Assign time variable to index to sync plot of data and function $t_i := i$

Assign start current variable $J2o := data_{1,j}$

Assign variable JJ to function CurrTran $JJ2_i := CurrTran(J2o, Ji, t_i)$

compute mean squared error $\sum_{i=0}^{end-1} (JJ2_i - data_{i,j})^2 = 33.9$

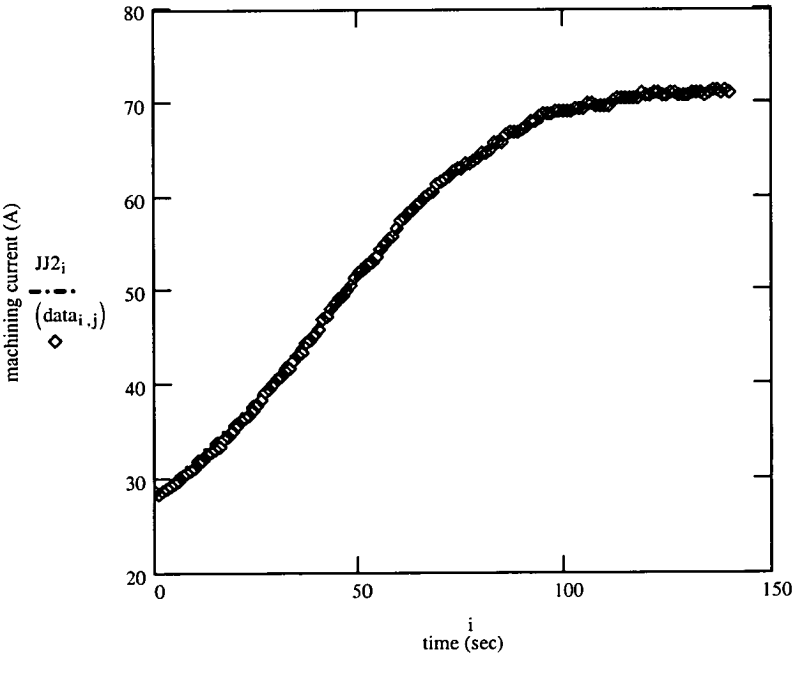

$k3 := 0.0054$ $j := 2$ $Ji := equli\_curr$

$\frac{f^2}{k3} = 5.103 \times 10^{-2}$

$\frac{k3}{f^2} = 19.596$

Given

Assign ECM current transient equality $\left(\frac{Ji}{J3o} - \frac{Ji}{J}\right) + \ln\left(\frac{1 - \frac{Ji}{J3o}}{1 - \frac{Ji}{J}}\right) = \frac{(f^2 \cdot t)}{k3}$

Minimise error in J based on above function $CurrTran(J3o, Ji, t) := Minerr(J)$

Set index count to number of data points to fit. $i := 0, 1 .. end$

Assign time variable to index to sync plot of data and function $t_i := i$

Assign start current variable $J3o := data_{1,j}$

Assign variable JJ to function CurrTran $JJ3_i := CurrTran(J3o, Ji, t_i)$

compute mean squared error $\sum_{i=0}^{end-1} (JJ3_i - data_{i,j})^2 = 101.268$

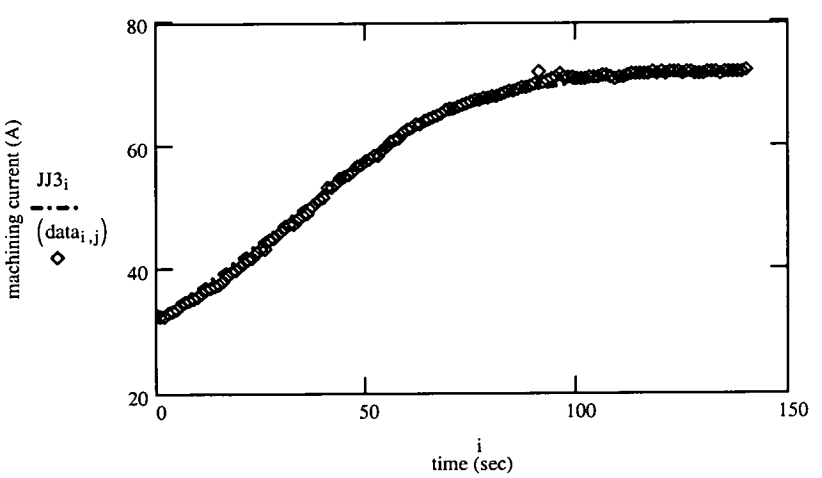

$k4 := 0.0054$ $j := 3$ $Ji := equli\_curr$

$\frac{f^2}{k4} = 5.103 \times 10^{-2}$ $\frac{k4}{f^2} = 19.596$

Given

Assign ECM current transient equality $\left(\frac{Ji}{J4o} - \frac{Ji}{J}\right) + \ln\left(\frac{1 - \frac{Ji}{J4o}}{1 - \frac{Ji}{J}}\right) = \frac{(f^2 \cdot t)}{k4}$

Minimise error in J based on above function $CurrTran(J4o, Ji, t) := Minerr(J)$

Set index count to number of data points to fit. $i := 0, 1 .. end$

Assign time variable to index to sync plot of data and function $t_i := i$

Assign start current variable $J4o := data_{1,j}$

Assign variable JJ to function CurrTran $JJ4_i := CurrTran(J4o, Ji, t_i)$

compute mean squared error $\sum_{i=0}^{end-1} (JJ4_i - data_{i,j})^2 = 119.36$

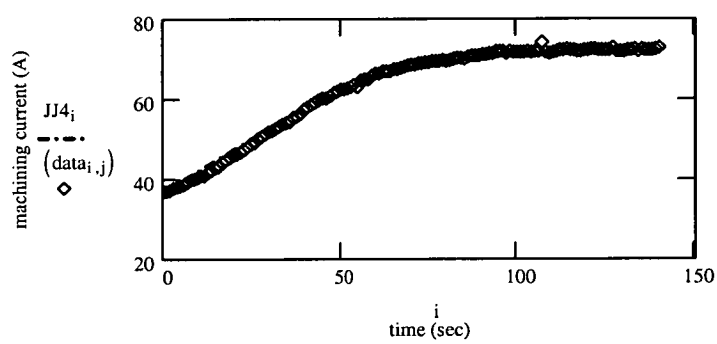

$k5 := 0.0054$ $j := 4$ $Ji := equli\_curr$

$\frac{f^2}{k5} = 5.103 \times 10^{-2}$

$\frac{k5}{f^2} = 19.596$

Given

Assign ECM current transient equality $\left(\frac{Ji}{J5o} - \frac{Ji}{J}\right) + \ln\left(\frac{1 - \frac{Ji}{J5o}}{1 - \frac{Ji}{J}}\right) = \frac{(f^2 \cdot t)}{k5}$

Minimise error in J based on above function $\text{CurrTran}(J5o, Ji, t) := \text{Minerr}(J)$

Set index count to number of data points to fit. $i := 0, 1 .. \text{end}$

Assign time variable to index to sync plot of data and function $t_i := i$

Assign start current variable $J5o := \text{data}_{1,j}$

Assign variable JJ to function CurrTran $JJ5_i := \text{CurrTran}(J5o, Ji, t_i)$

compute mean squared error $\sum_{i=0}^{\text{end}-1} (JJ5_i - \text{data}_{i,j})^2 = 154.23$

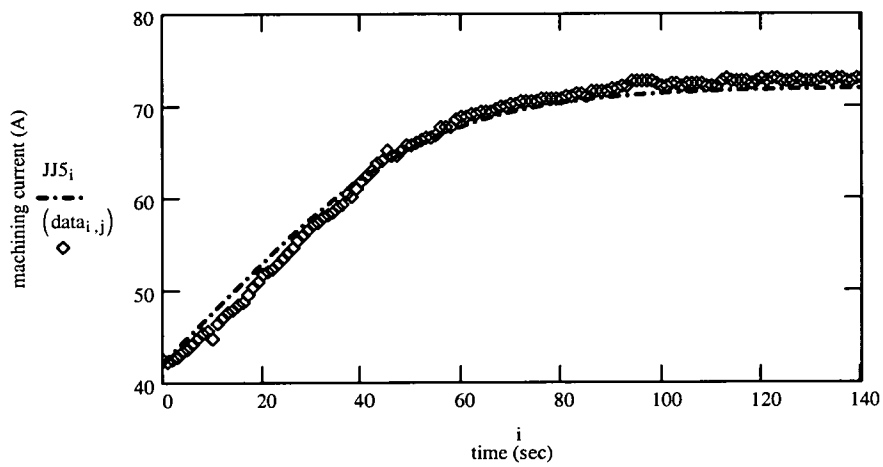

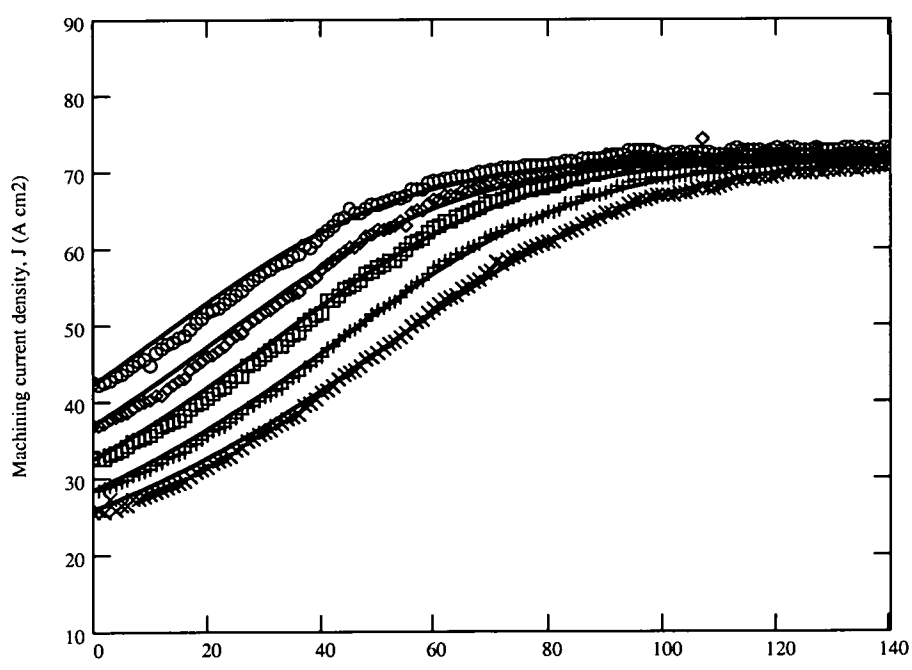

File: flow path length interval solver

Double cosine function is:

$$y(x) := 5\cdot\cos\left(\pi\cdot\frac{x}{10}\right) - 1.25\cdot\cos\left(2\cdot\pi\cdot\frac{x}{10}\right)$$

$$x := 0,1..40$$

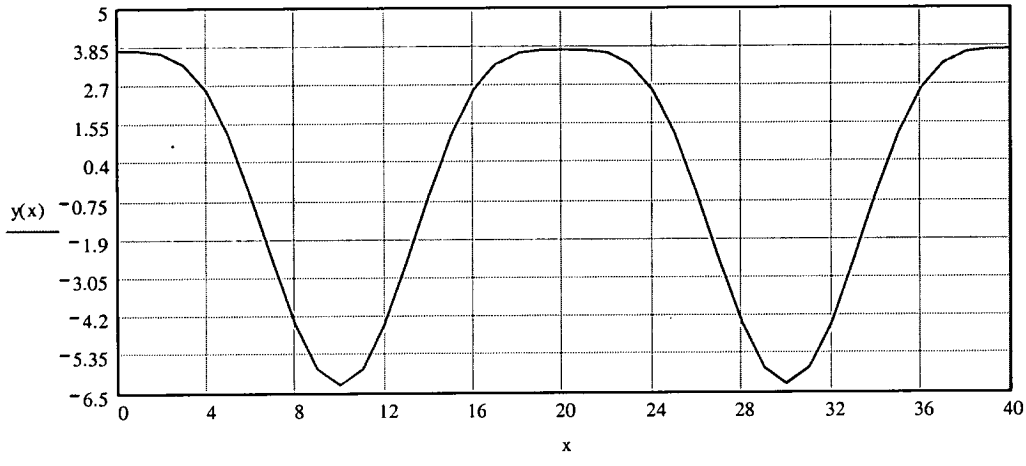

The following work sheet calculates incremental values moving along the x axis for a tool, described by the function f(x)l for a given arc length. The figure below shows the relationship between the variables used in this work sheet.

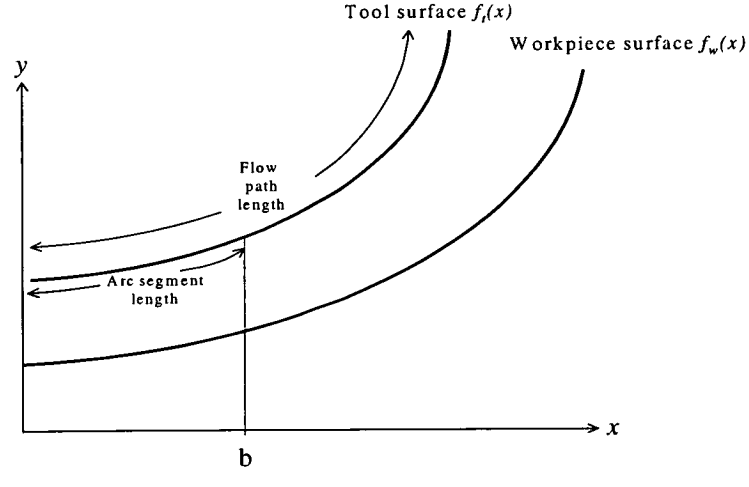

Input b := −5
c := 5
d := −5

Where b is is the initiation x co-ordinates from which the first segment length will be calculated and c is the x co-ordinates at which the last segment ends . For symmetrical tools, when the number of intervals is odd, then the start co-ordinate should have a negative offset by an amount of half the x segmented interval so that an interval index occurs at the centre of the function.

Assign tool shape function

$a := 0.8$

$f(x) := a \cdot x^2$

Assign required number of intervals within arc length

$N := 7$

The Arc length interval, between the limits b and c, for the function is given by:

$$\int_b^c \sqrt{1 + \left[\frac{d}{dx}\left(a \cdot x^2\right)\right]^2}\, dx$$

First find total arc length for given value of x-plane flow path length, by solving above integral:

$c := 20 \qquad b := 0$

$$total\_arc\_length := \int_b^c \sqrt{1 + \left[\frac{d}{dx}\left(5 \cdot \cos\left(\pi \cdot \frac{x}{10}\right) - 1.25 \cdot \cos\left(2 \cdot \pi \cdot \frac{x}{10}\right)\right)\right]^2}\, dx$$

$total\_arc\_length = 30.433$

$$total\_profie\_length := \frac{total\_arc\_length}{0.5}$$

$total\_profie\_length = 60.867$

The total_arc_length is then divided by the required number of intervals, N to give the arc length interval, ι

$$\iota := \frac{total\_arc\_length}{N} \qquad \iota = 4.348$$

A symbolic solution of the above integral will give a relationship between the required arc length interval ι x i, and the x co-ordinates interval vector x_interval_vector. i is the index for the required arc length. i.e. for the first interval length i=1, for the second interval length i=2, etc

Compute the value of ι as a vector using the index from 1 to N.

Given

$$\iota = \frac{1}{4 \cdot i} \cdot \frac{\left(2 \cdot \sqrt{1 + 4 \cdot a^2 \cdot c^2} \cdot \sqrt{a^2} \cdot c + \ln\left(2 \cdot \sqrt{a^2} \cdot c + \sqrt{1 + 4 \cdot a^2 \cdot c^2}\right)\right)}{\sqrt{a^2}} - \frac{1}{4 \cdot i} \cdot \frac{\left(2 \cdot \sqrt{1 + 4 \cdot a^2 \cdot b^2} \cdot \sqrt{a^2} \cdot b + \ln\left(2 \cdot \sqrt{a^2} \cdot b + \sqrt{1 + 4 \cdot a^2 \cdot b^2}\right)\right)}{\sqrt{a^2}}$$

$v(i) := \text{Find}(c)$ So that the first arc length interval is calculated over the x co-ordinate region from $b = 0$ to $v(1) = 2.118$

and the second arc length interval is calculated over the x co-ordinate region fror $b = 0$ to $v(2) = 3.126$

Etc intil $b = 0$ to $v(N) = 6.057$

Assign values of each X co-ordinates interval to a single vector, x_interval_vector, as follows:

$j := 1, 2 .. N \quad i_j := j$

$xt_j := v(i_j)$

$xt_j =$

2.118
3.126
3.889
4.527
5.088
5.593
6.057

Compute the equation for a normal at a selected interval point corresponding to the interval number, inc.

$inc := 5$

Thus the x-coordinate at which normal will be completed is $x := xt_{inc}$

Gradient of tangent is computed as:

$$m := \frac{d}{dx} f(x)$$

$x = 5.088$

$m = 8.141$

The normal y-axis intercept can be calculated for each point since each normal will pass through the point x.

Thus $y := f(x)$ $y = 20.709$

guess $c1 := 1$

Given

$$y = \frac{-x}{m} + c1$$

$intercept := Find(c1)$ $intercept = 21.334$

Equation of tangent is: $y_n(x2) := \frac{-x2}{m} + intercept$

equlibrium gap at that point is: $equlib\_gap := 0.4$

gradient of normal is: $mn := -m^{-1}$ $mn = -0.123$

$\phi := atan(mn)$

$\theta := 90 \cdot deg - \phi$

Thus length of normal $normal\_gap := \frac{equlib\_gap}{\cos(\theta)}$

$normal\_gap = -3.281$

length of equlibrium gap in x direction is: $x\_gap := equlib\_gap \cdot \tan(\theta)$ $x\_gap = -3.256$

Then need to compute the X and Y co-ordinates on the workpiece at the point of intersection of the normal, i.e xw and yw.

$xw := x - x\_gap$

$xw = 8.344$

$yw := y - equlib\_gap$

$yw = 20.309$

Plot Tangent over the equlibrium gap interval $x2 := x, x + 0.01 .. xw$

Plot function over the interval $x := d, d + 0.01 .. c$

C0_ordinates of flow path length intervals are:

$X := (-6.848 \quad -5.168 \quad -2.667 \quad 2.667 \quad 5.168 \quad 6.848 \quad 8.2)^T$

$Y := (13.547 \quad 7.543 \quad 1.716 \quad 1.716 \quad 7.543 \quad 13.547 \quad 19.6)^T$

A3 Mathematical derivations.

A3.1 ECM Planar dynamics

Starting from equation 4.1-1 in section 4.1 (main body of thesis), that is:

$$\left[\frac{z.z_{\infty}}{z_{\infty}-z}\right]dz = kdt$$

Equation 4.1-1

Integrating from t=0 to t=t for $z=z_0$ (at time t=0) to z=z (at time t=t)

yields for the RHS

kt.

By applying the following general integration formula:

$$\int \frac{ax+b}{cx+d}dx = \frac{ax+b}{c} + \frac{-ad+bc}{c^2}\ln(cx+d)+c$$

the LHS of 4.1-1 can be integtrated using the substitutions as follows:

$x=z$, $a=d=z_{\infty}$, $b=0$, and $c=-1$

Thus the integration of the LHS of 4.1-1 becomes:

$$\int_{z_0}^{z} \frac{z_{\infty}z}{-z+z_{\infty}}dz = \left|\frac{z_{\infty}z}{-1} + \frac{-z^2}{1}\ln(-z+z_{\infty})+c\right|_{z_0}^{z}$$

$$\Rightarrow \quad \left(-z_{\infty}z - z^2{}_{\infty}\ln(z_{\infty}-z)+c\right)-\left(-z_{\infty}z_0 - z^2{}_{\infty}\ln(z_{\infty}-z_0)+c\right)$$

$$\Rightarrow \qquad (z_\infty z_0 - z_\infty z) + z_\infty^2 \ln\left[\frac{z_\infty - z_0}{z_\infty - z}\right]$$

Combining the integrations of the LHS and the RHS of 4.1-1 gives:

$$(z_\infty z_0 - z_\infty z) + z_\infty^2 \ln\left[\frac{z_\infty - z_0}{z_\infty - z}\right] = kt$$

Which re-arranges to give:

$$\frac{z_0 - z}{z_\infty} + \ln\left[\frac{z_\infty - z_0}{z_\infty - z}\right] = \frac{kt}{z_\infty^2}$$

That is equation 4.1-3 in section 4.1 in main body of thesis

A3.2 Cylindrical erosion

The cylindrical current-time solution of Equation 4.1-6 in section 4.1 is obtained as follows:

The rate of metal removal at the workpiece surface is given by:

$$\frac{dr_{rc}}{dt} = \frac{\varepsilon J_{rc}}{F\rho} = \frac{k}{r_c \ln(r_c / r_t)} \qquad \text{equation A1}$$

Where k is the machinability constant as defined above.

Equation A1 can be solved, by integration, using the boundary condition that $r_c = r_t$ at t=0, and $r_c = r_w$ at time t=t, Thus:

$$\int_{r_t}^{r_w} r_c(\ln r_c - \ln r_t)dr_c = \int_o^t k dt$$

integrating gives:

$$\left[1/2\left(r_c^2 \ln r_c - \frac{r_c}{2}\right)\right]_{r_t}^{r_w} - \left[\frac{r_c^2}{2} \ln r_t\right]_{r_t}^{r_w} = kt$$

which expands to:

$$\frac{1}{2}\left[r_w^2 \ln r_w - \frac{r_w^2}{2}\right] - \frac{r_w^2}{2} \ln r_t - \frac{1}{2}\left[r_t^2 \ln r_t - \frac{r_t^2}{2}\right] + \frac{r_t^2 \ln r_t}{2}$$

simplifying gives Equation 4.1-6 in section 4.1, as follows:

$$\frac{1}{2} r_w^2 \ln \frac{r_w}{r_t} - \frac{r_w^2}{4} + \frac{r_t^2}{4} = kt$$

A4 Alloy compositions

The elemental breakdown of the alloys used throughout the trials in this thesis are given in the following three tables

Table A2-1: Elemental Composition of In718

Element	Fe	Al	Mn	Co	Cr	Cu	Mo	Ni	Si	C	Ti
% composition*	23.5	0.48	0.22	0.17	18.16	0.02	2.96	53.3	0.01	0.05	1.02

Table A2-2: Elemental Composition of Ti 6/4

Element	Fe	Al	V	O	N	Ti	C
% composition*	0.17	5.89	3.76	0.15	0.02	89.91	0.01

Table A2-3: Elemental Composition of TiAl

Element	Mn	Al	V	O	N	Ti	C
% composition*	0.17	5.89	3.76	0.15	0.02	45	0.01

The TiAl used during trials was Howmet's XDTM γ-TiAl-based intermetallic: Ti-45Al-2Mn-2Nb (at%)+0.8vol% TiB2. This material was in the form of a 25mm x 75mm x 180mm cast slab, HIPed @1260oC, 170 MPa for 4h and then heat treated @1010 °C for 50 hrs. The microstructure was lamellar with a colony size of approximately 80 μm. Prior to carrying out the ECM tests the slab was sliced, using electrode discharge wire machining.

In718 specification as per Haynes International material specification: AMS 5596H

Ti6-4 specification as per Titanium International specification: AMS 4911H

* all weight percentages and nominal composition

A5 Current and segmented transducers calibration

All data logged current monitoring was carried out using split-core LEM-HEME Hall effect current transducers (type RS 286-456 with a range of 0-200 A, for segmented current monitoring and type RS 286-513, with a range of 0 to 500 A, for monitoring of the total current). Both types of transducers are true r.m.s. types producing an output of 0-5 V d.c. over the full range output. The calibration accuracy is quoted as ± 1% gain and ±0.4% offset over the output range. Since the accuracy of parameterisation data is highly sensitive to current values, a series of current and segment transducer calibrations were carried out in order to improve on the quoted accuracy of these devices. These trials consisted of a sequence of machining runs in which the dissolution current is varied by adjustment of the machining gap. This current sweep been calibrated to provide accurate reference data by monitoring the voltage drop across a 0-1000A, 0.075 ohms reference current shunt. The output from the current shunt being calibrated using a 1030 (RS 610-348, Time Electronics Ltd) precision current/voltage source. Based on this data the total current transducer output is then re-calibrated and this calibration then used as a reference for gain and offset adjustment for each of the individual segmented current transducers referenced to segment number 4 transducer.

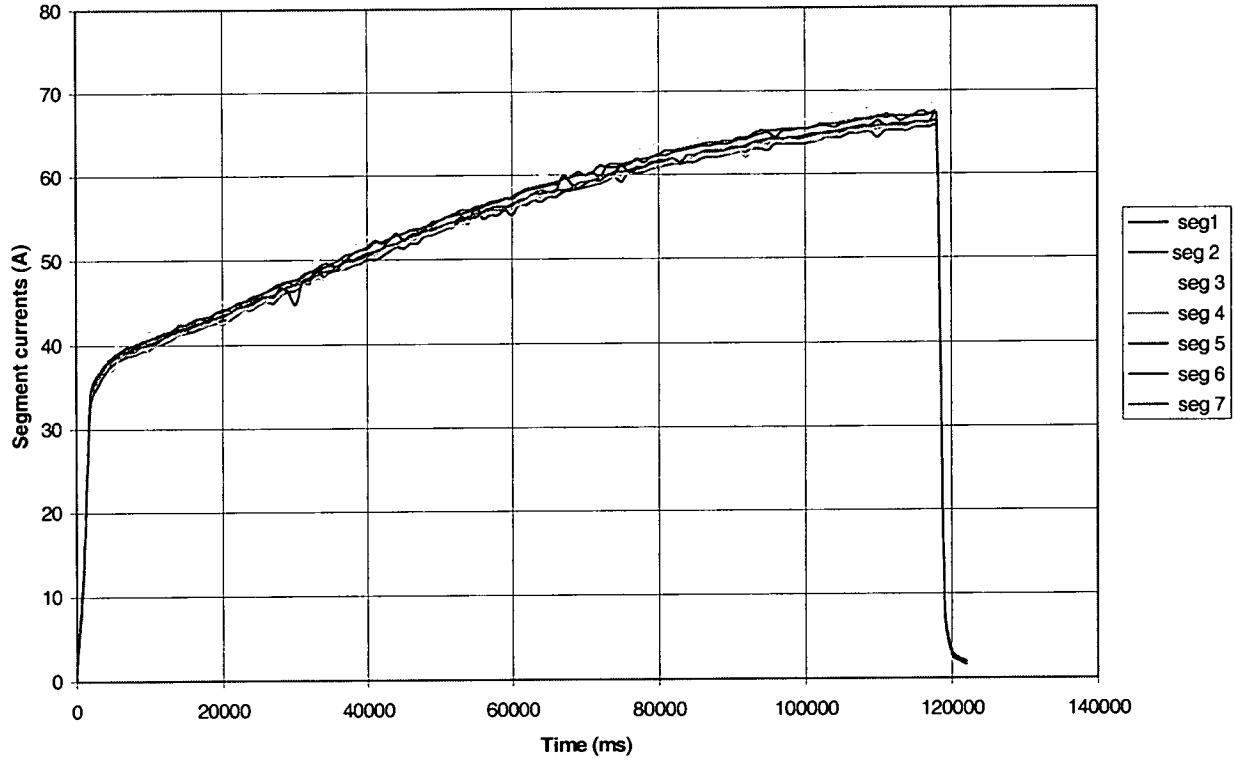

Figure A5-1: Raw data from segment transducers without offset and gain adjustments

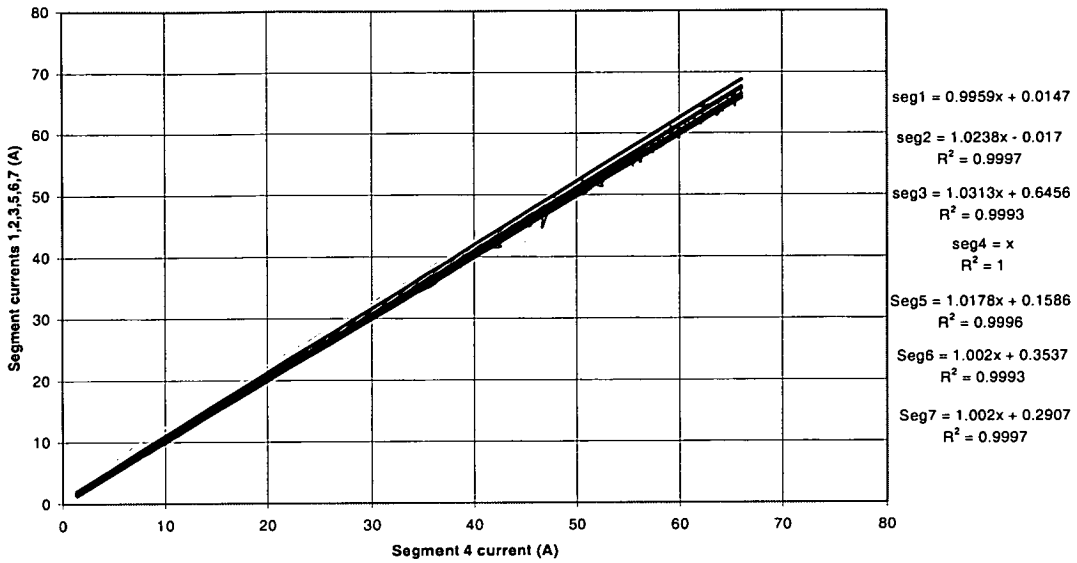

Figure A5-2: Linearity plot for segment 4 transducer plotted against all other segment transducers (gain and offset values shown to right of chart)

With a reference to the linearity plot shown in figure A5-2 adjustments were then made within the Visual Designer data-logging software to compensate for gain and offset errors for each of the transducers. For example segment 2 output is compensated with reference to segment 4 using gain = 1/1.0238 and offset = +0.017, etc according to transducers gain and offset values shown to right of chart in figure A5-2.

In order to check this re-calibration the current sweep trial is then repeated using these new values of gain and offset. The outputs from this trial are shown in figure A5-3. Close correspondence with a resolution of ±0.25A over of the full 0-200 A range of each transducer is noted.

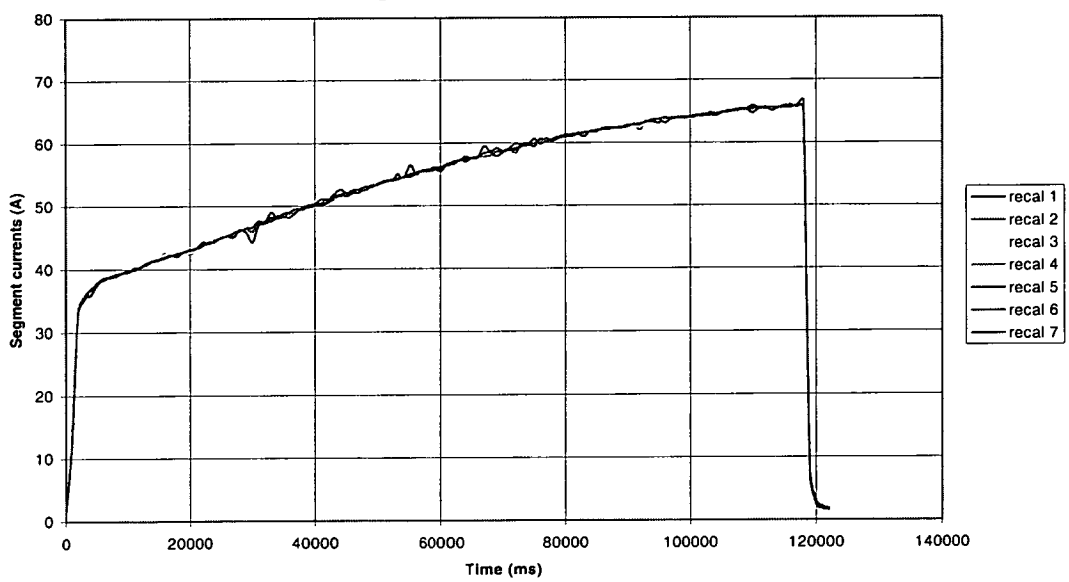

Figure A5-3: segment current outputs after re-calibration of gain and offset values

A6 Complete graphical data from C-function trials

The following 64 graphs contain raw data from the C-function trials as reported in chapter 8. These data are in the form of 8 individual plots for each of the 8 trial runs. The trials consisted of certain specified parameter sweeps as follows:

1. Titanium/chloride system at 20 volts with flow 16, 10, 8 and 4 l/min
2. Titanium/chloride system at 24 volts with flow 16 l/min
3. In718/nitrate system at 20 volts with flow 16, 10, 8 and 4 l/min
4. In718/nitrate system at 24 volts with flow 16 and 4 l/min
5. In718/chloride system at 20 volts with flow 16, 12, 8 and 4 l/min
6. In718/chloride system at 24 volts with flow 16, 12, 8 and 4 l/min
7. Titanium/nitrate system at 20 volts with flow 16 and 4 l/min
8. Titanium/nitrate system at 24 volts with flow 16 l/min

For each of these runs 8 graphs, labelled *a* to *h*, have been plotted as follows:

a) Inlet (seg 2) and outlet (seg 6) gap values, z, against time, t

b) Segment current density (1 to 7), J, against time

c) Main parameters and variables (total current density, J, voltage, V, feed rate, f, inlet pressure P, flow rate, U) against time.

d) C-function, C, against time, t

e) Workpiece thickness, h, against time

f) The ratio $z.J/V$, representing the gap conductivity according to equation 2.2-4 against current density, J

g) The ratio $z.J/V$, representing the gap conductivity according to equation 2.2-4 against time, t

h) Inlet gap, z_{in}, against inlet pressure, P.

Titanium/nitrate system at 24 volts with flow 16, 12, 8 and 4 l/min

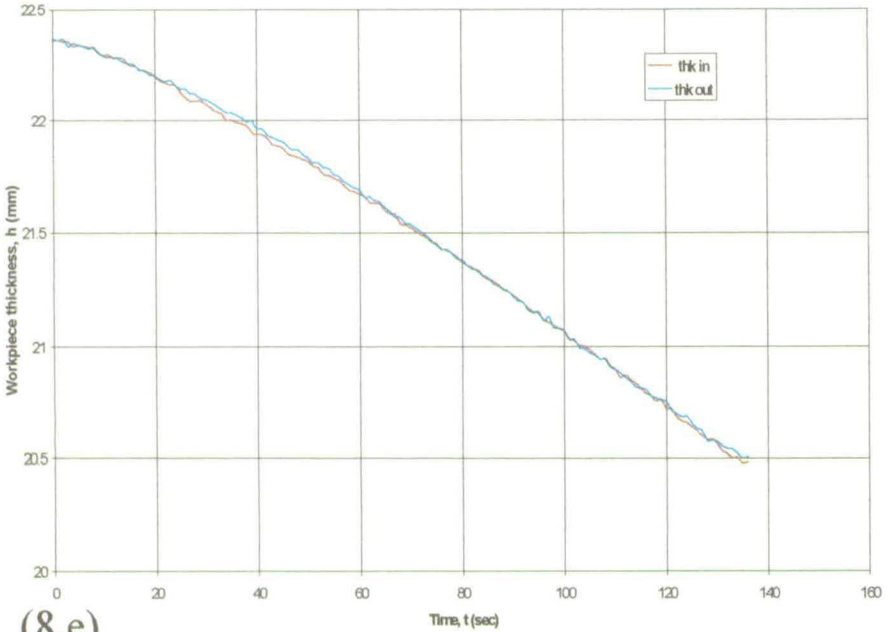

(8.e)

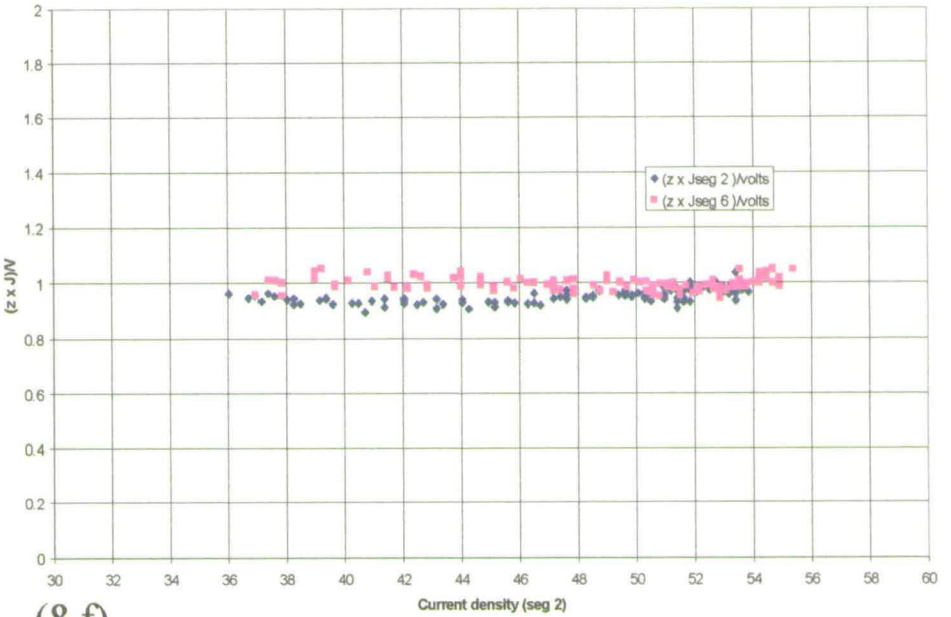

(8.f)

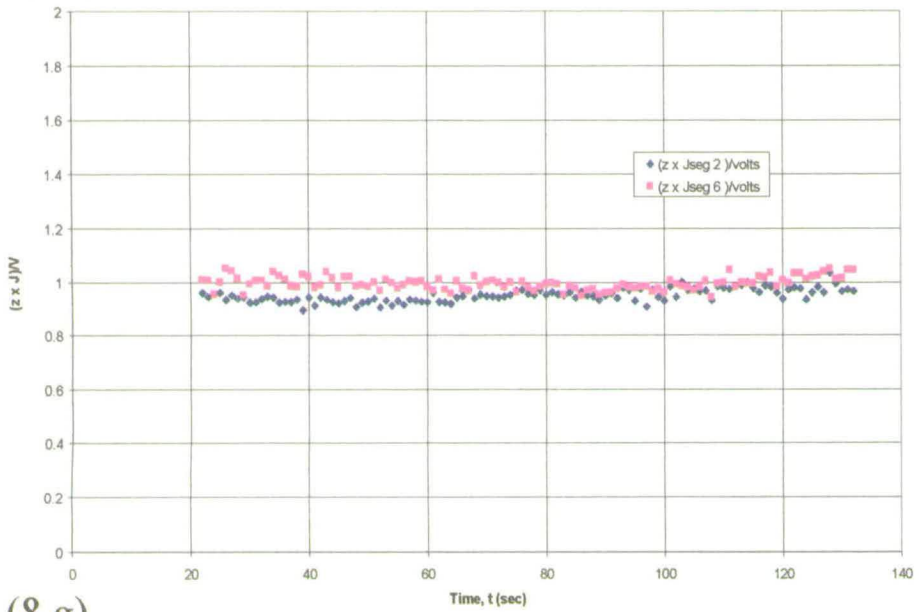

(8.g)

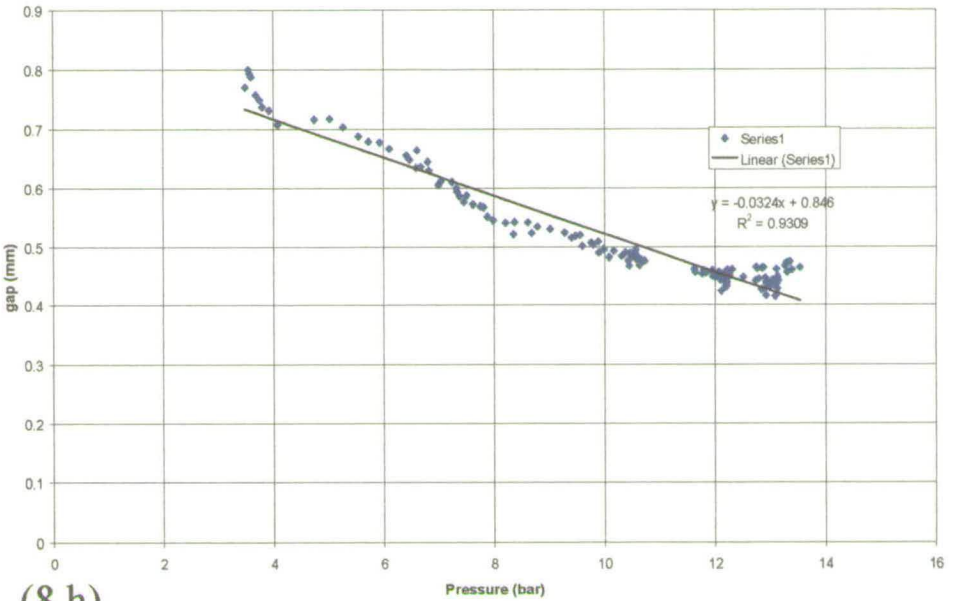

(8.h)

Titanium/nitrate system at 24 volts with flow 16 l/min

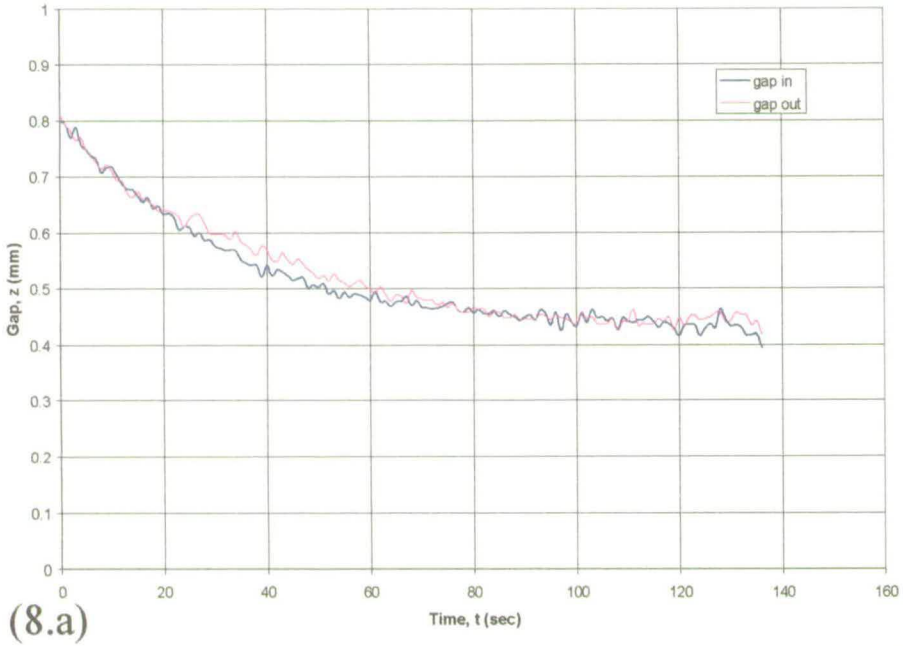

(8.a)

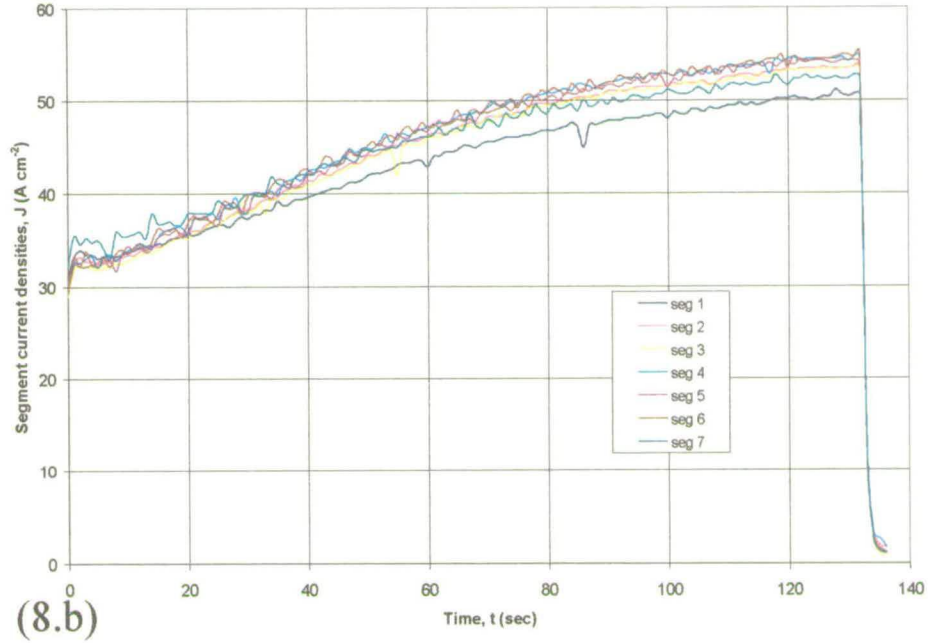

(8.b)

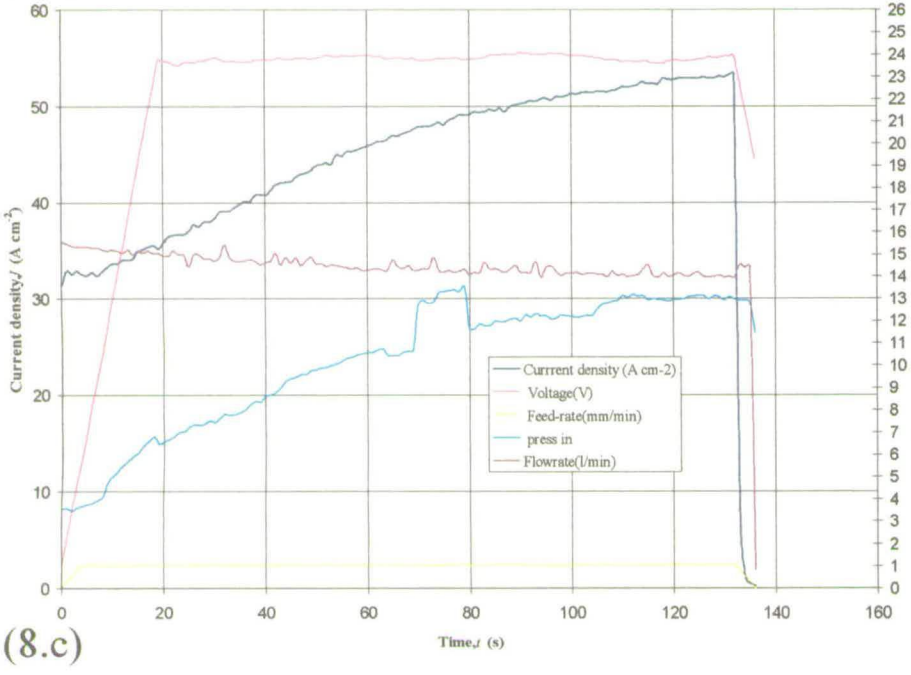

(8.c)

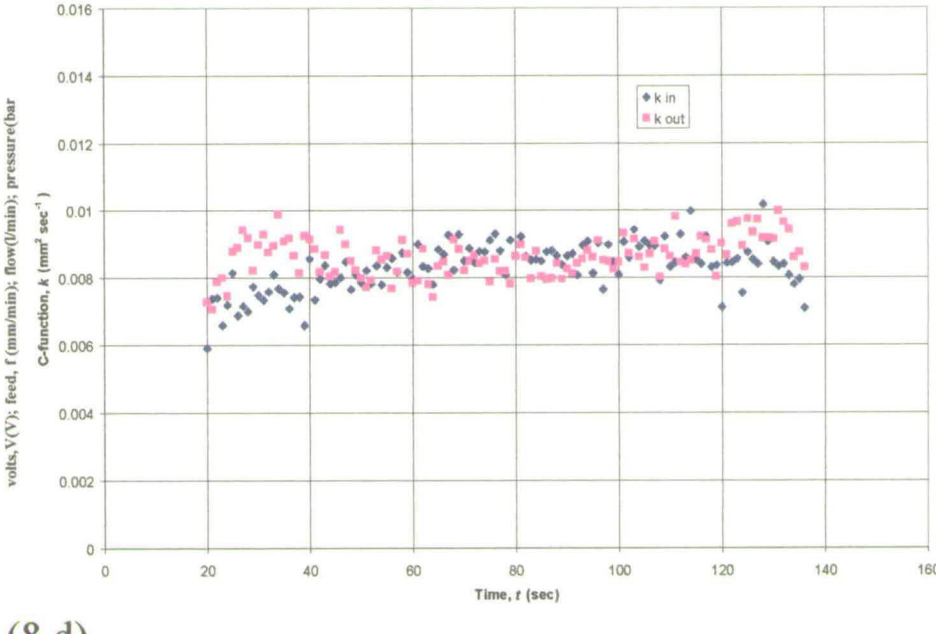

(8.d)

Titanium/nitrate system at 20 volts with flow 16 and 4 l/min

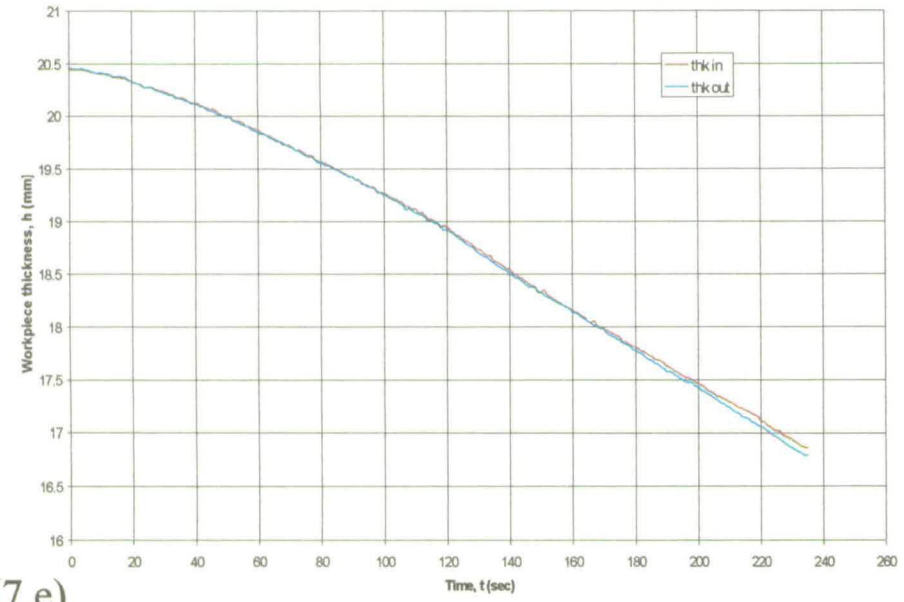

(7.e)

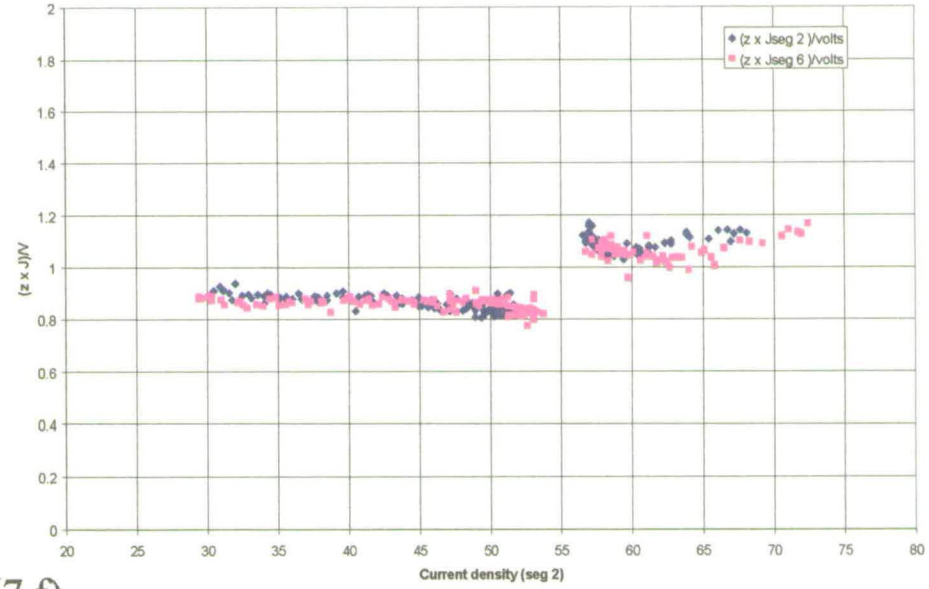

(7.f)

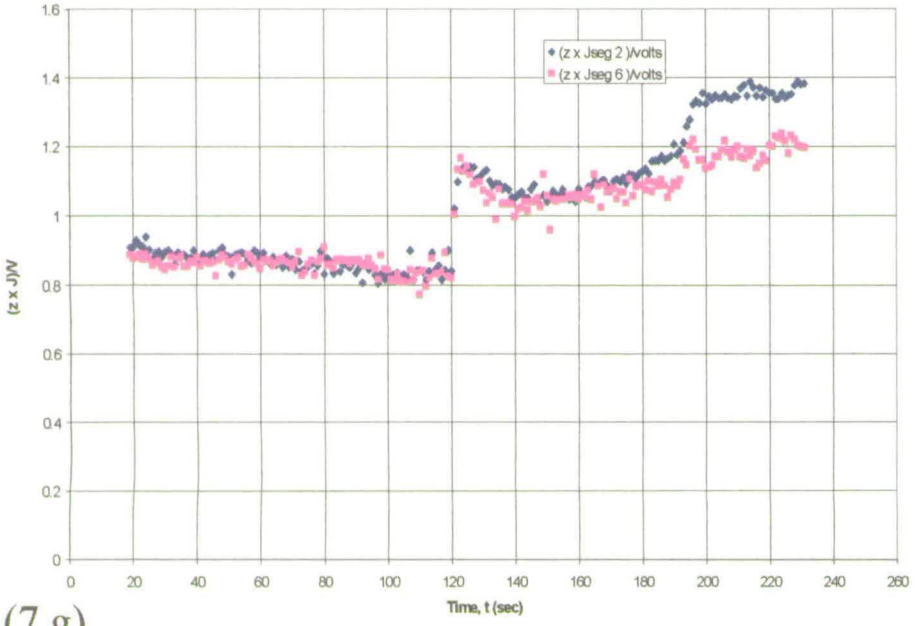

(7.g)

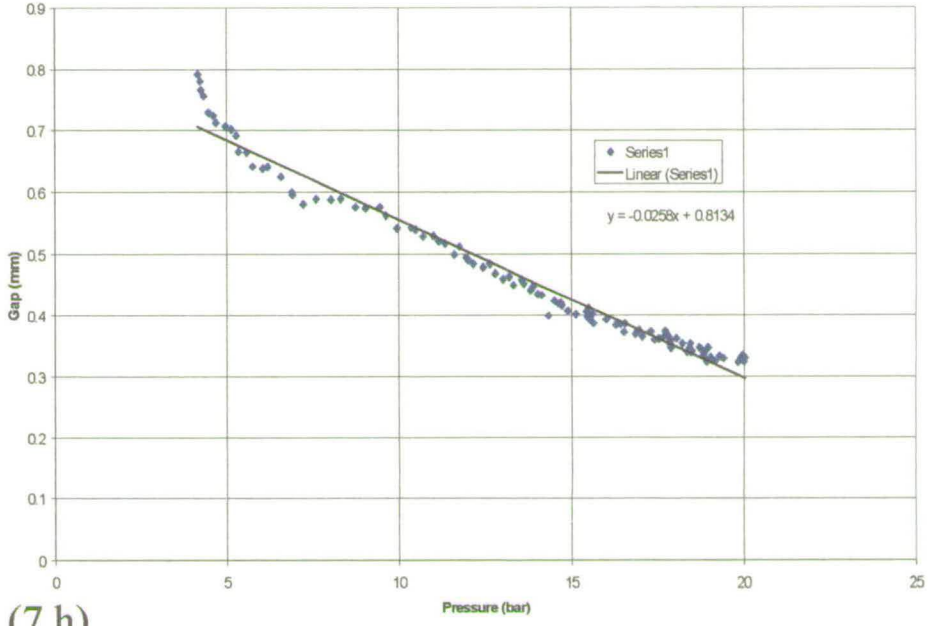

(7.h)

Titanium/nitrate system at 20 volts with flow 16 and 4 l/min

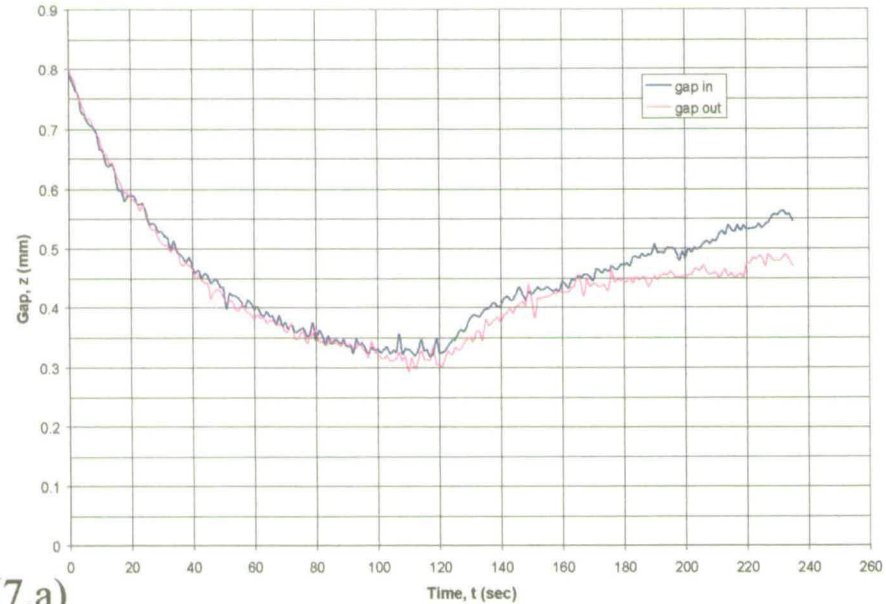

(7.a)

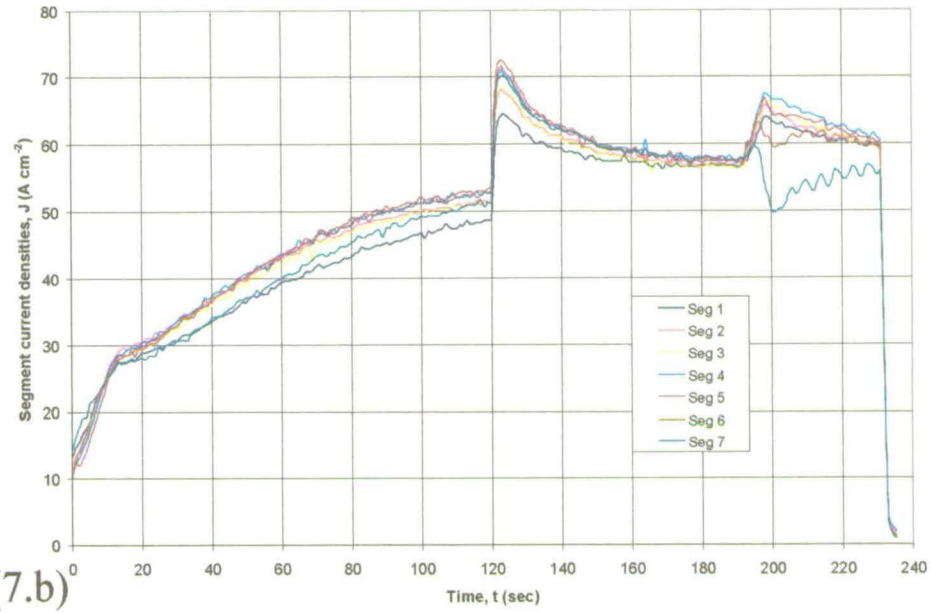

(7.b)

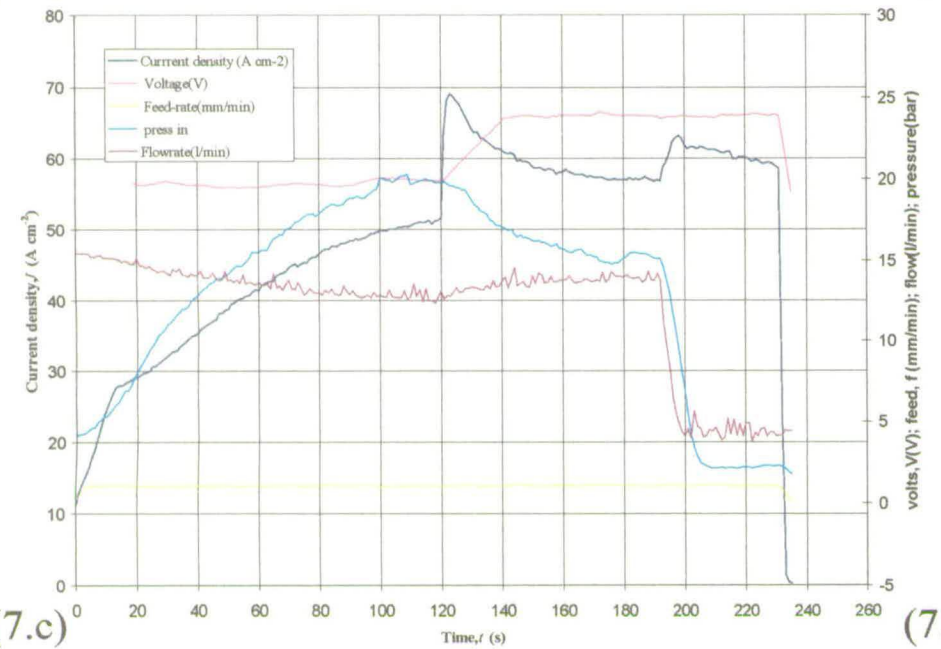

(7.c)

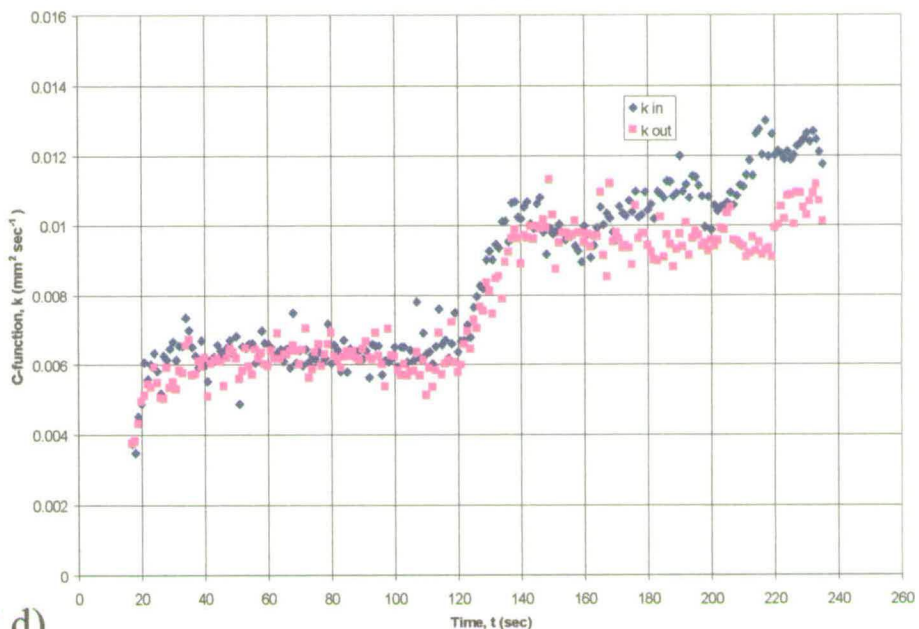

(7.d)

In718/chloride system at 24 volts with flow 16, 12, 8 and 4 l/min

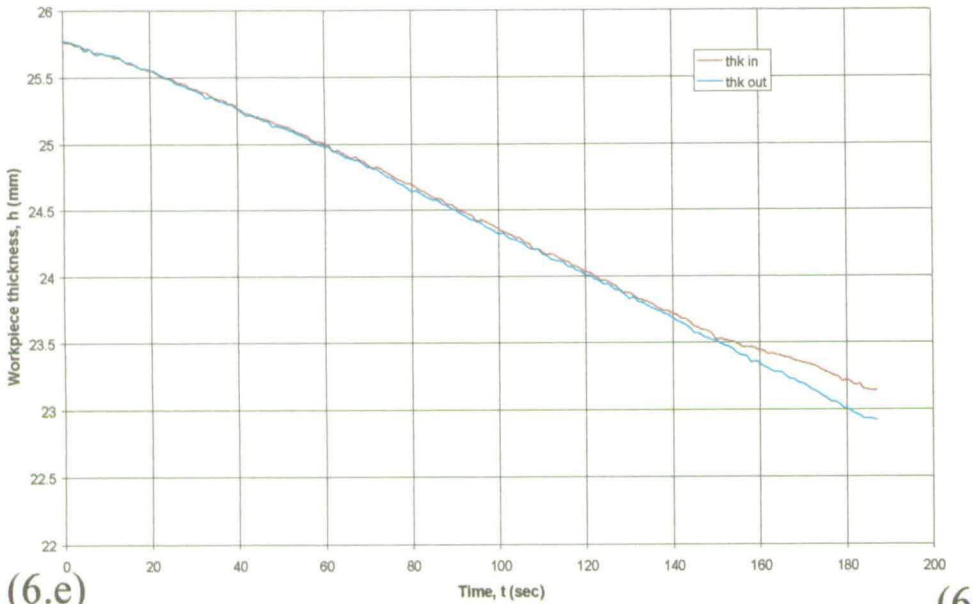

(6.e)

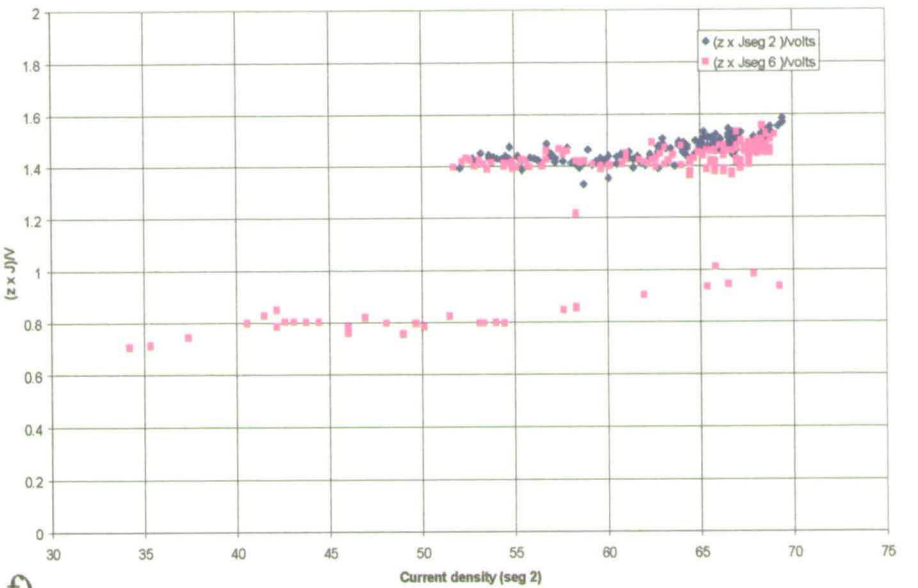

(6.f)

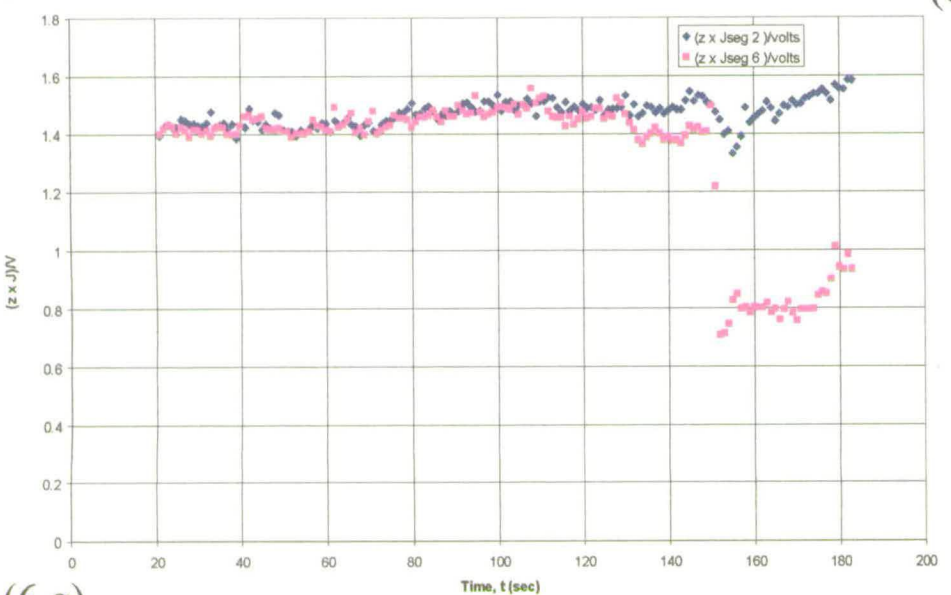

(6.g)

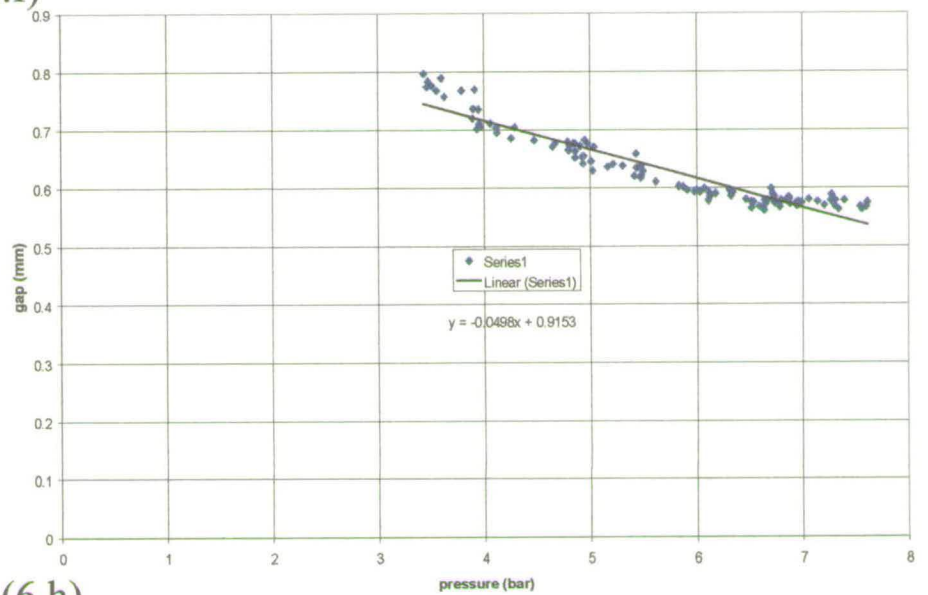

(6.h)

In718/chloride system at 24 volts with flow 16, 12, 8 and 4 l/min

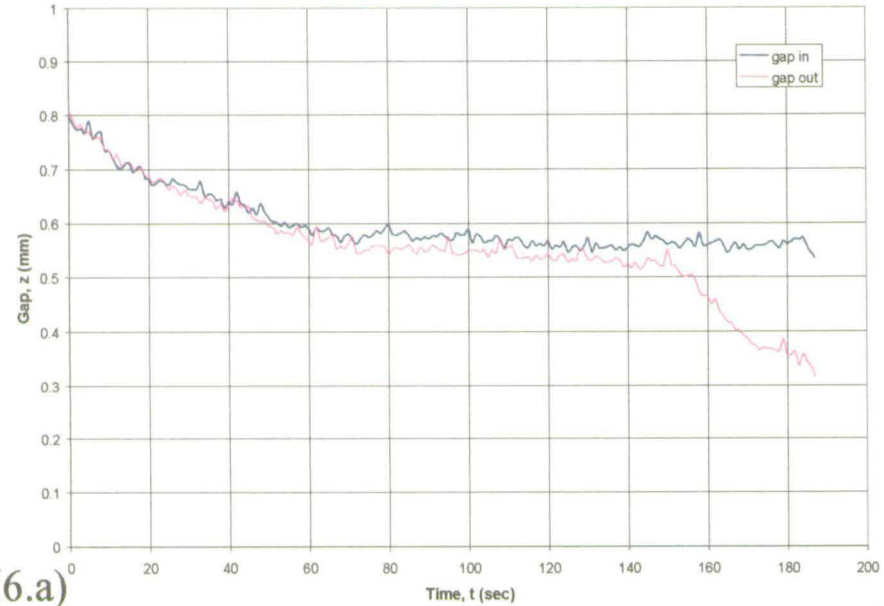

(6.a)

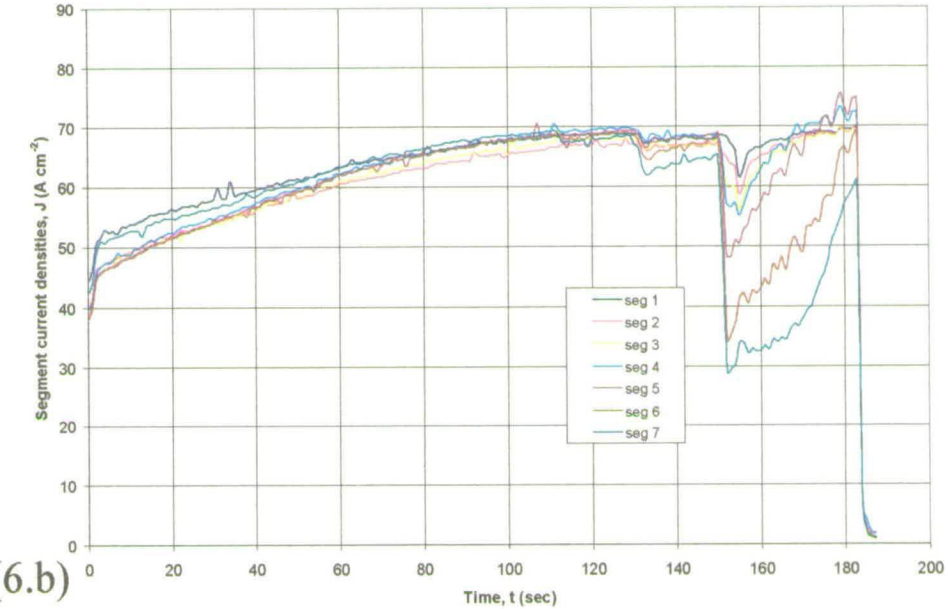

(6.b)

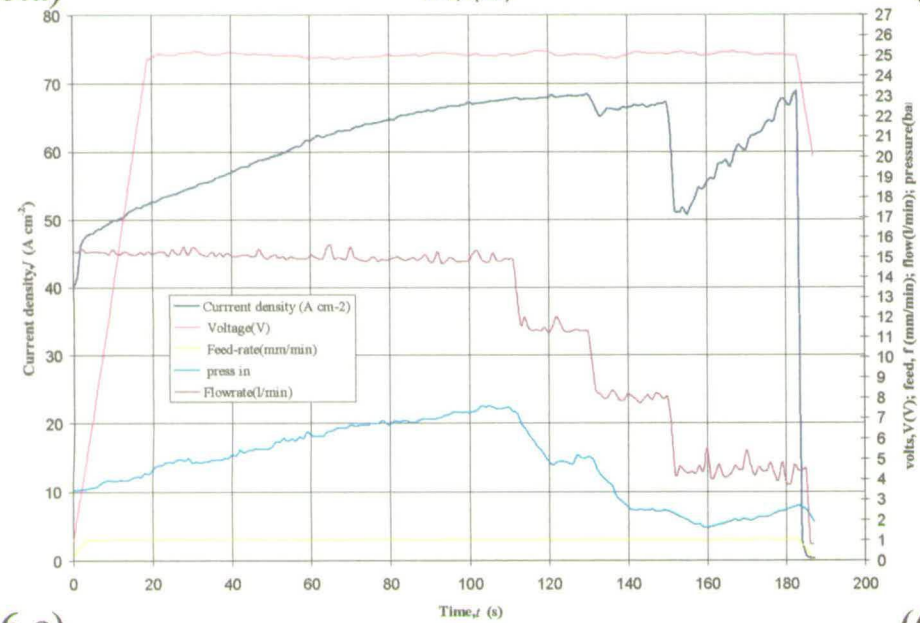

(6.c)

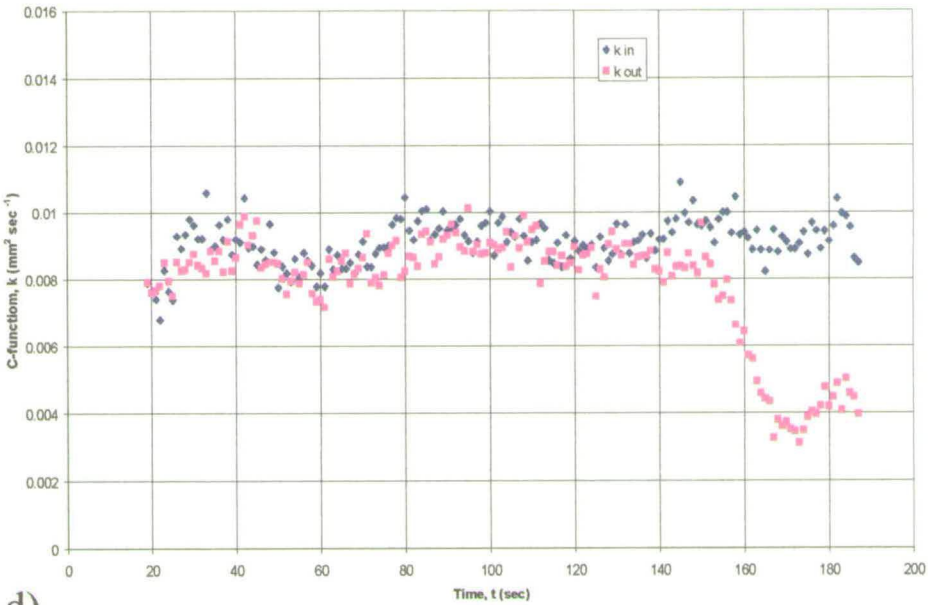

(6.d)

In718/chloride system at 20 volts with flow 16, 12, 8 and 4 l/min

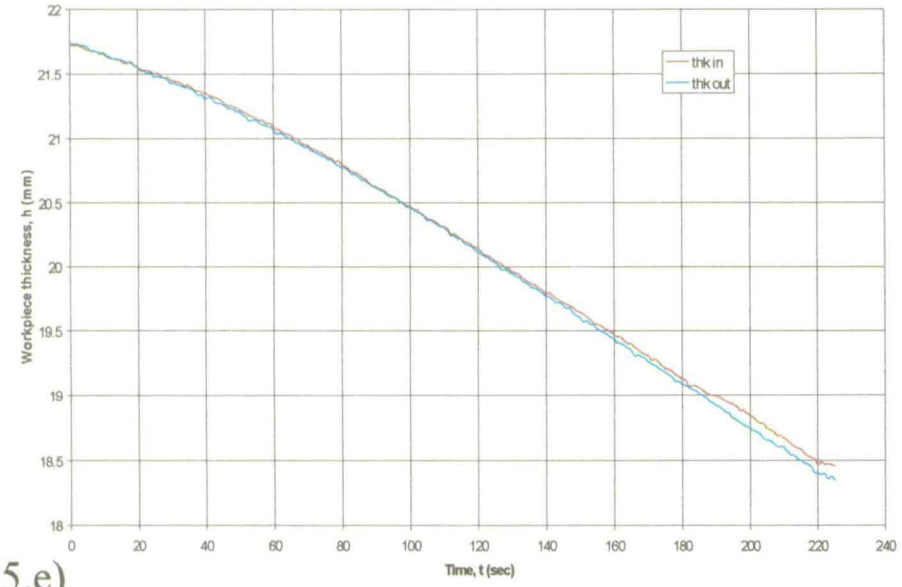

(5.e)

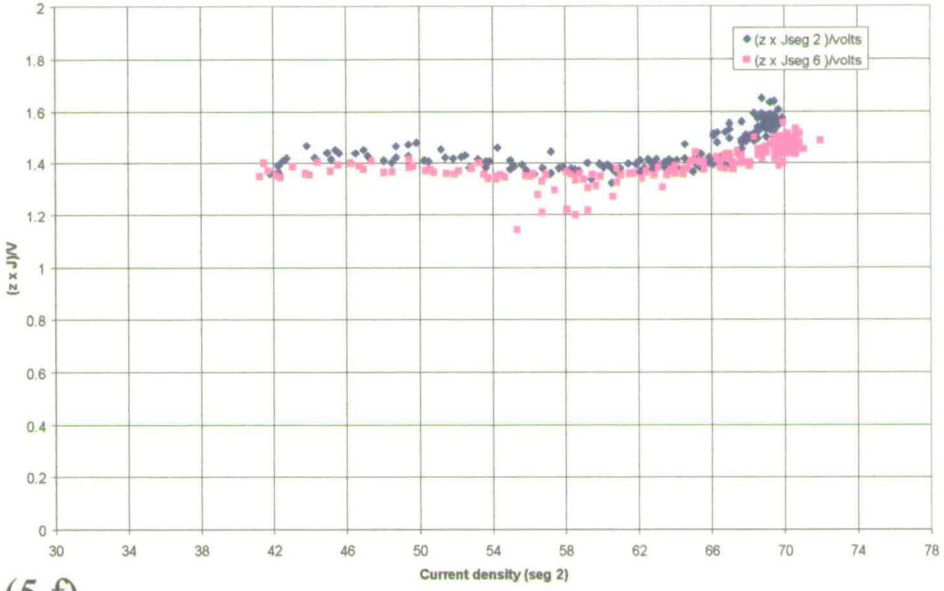

(5.f)

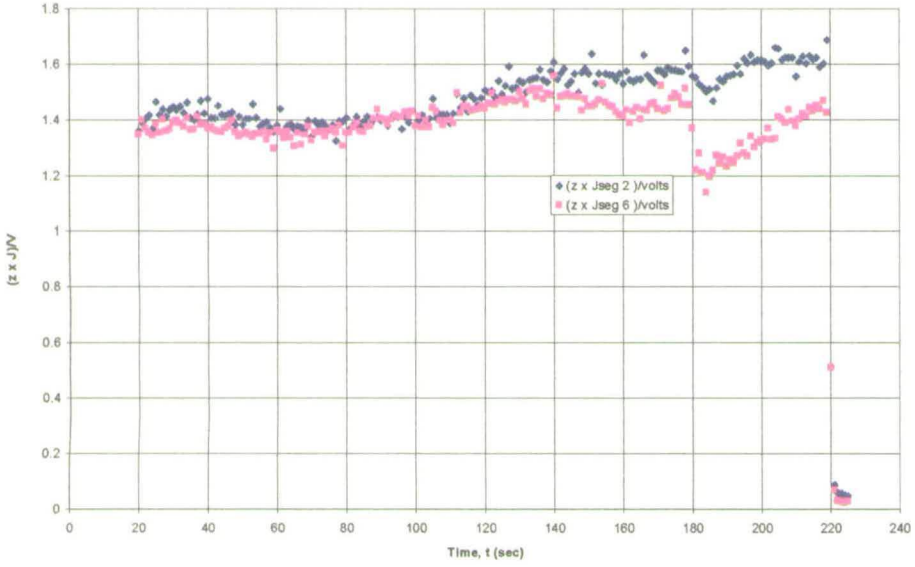

(5.g)

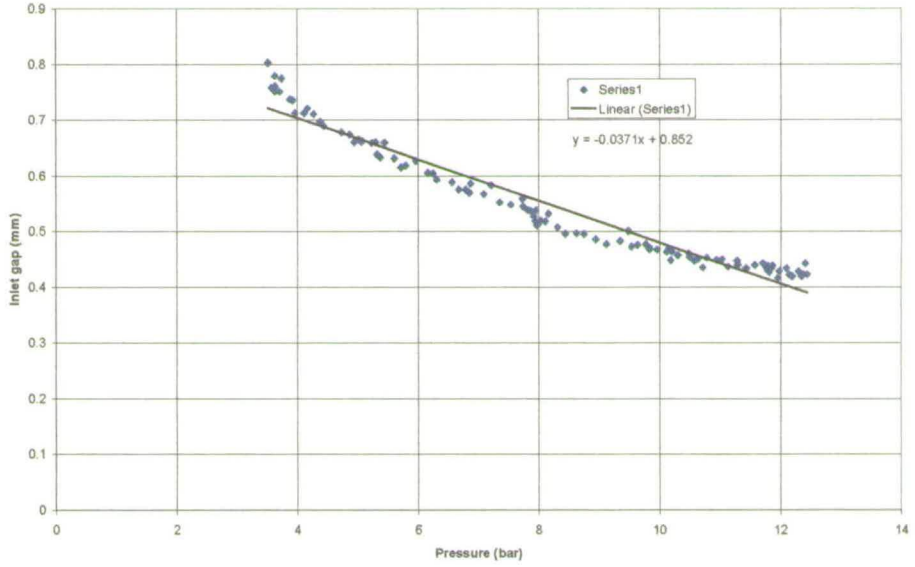

(5.h)

In718/chloride system at 20 volts with flow 16, 12, 8 and 4 l/min

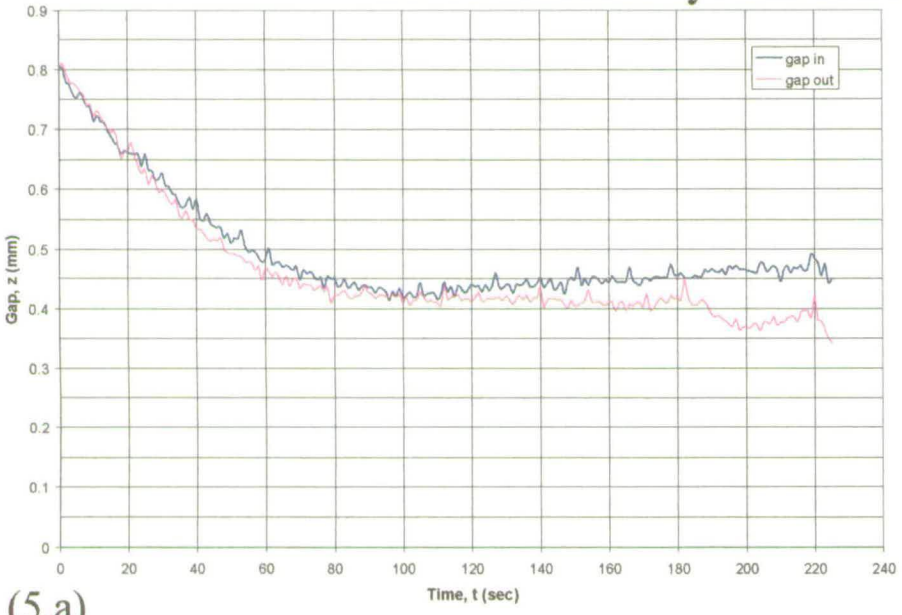

(5.a)

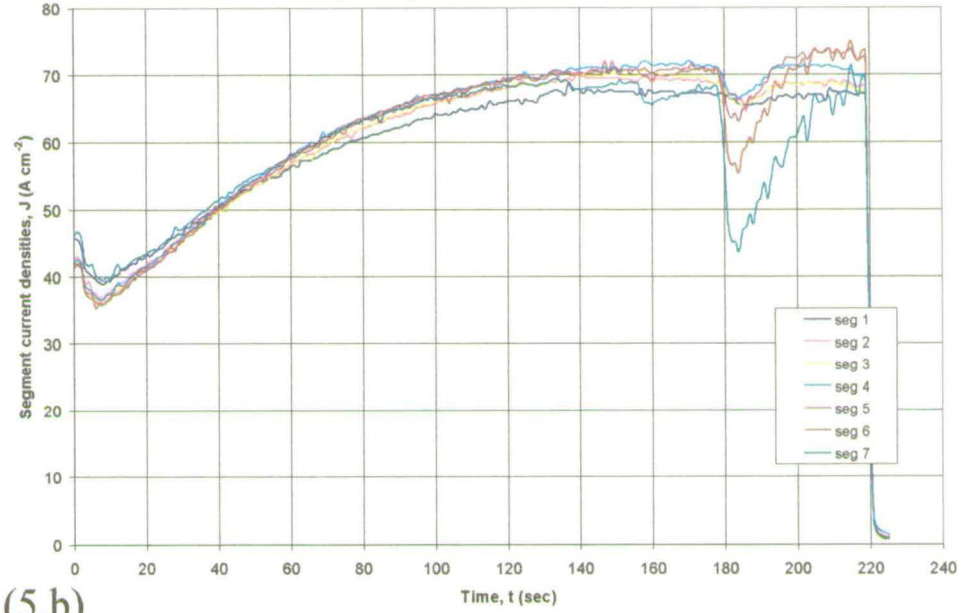

(5.b)

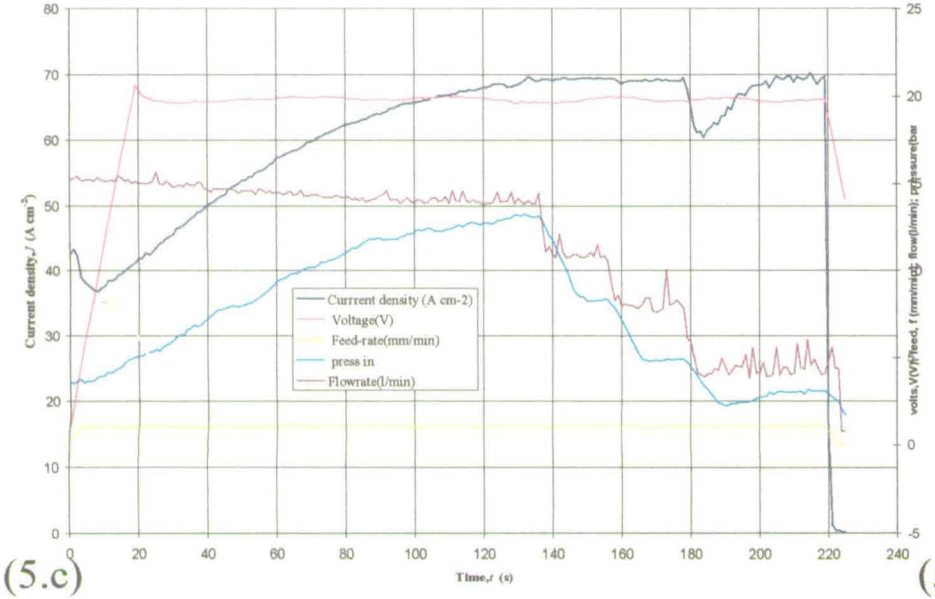

(5.c)

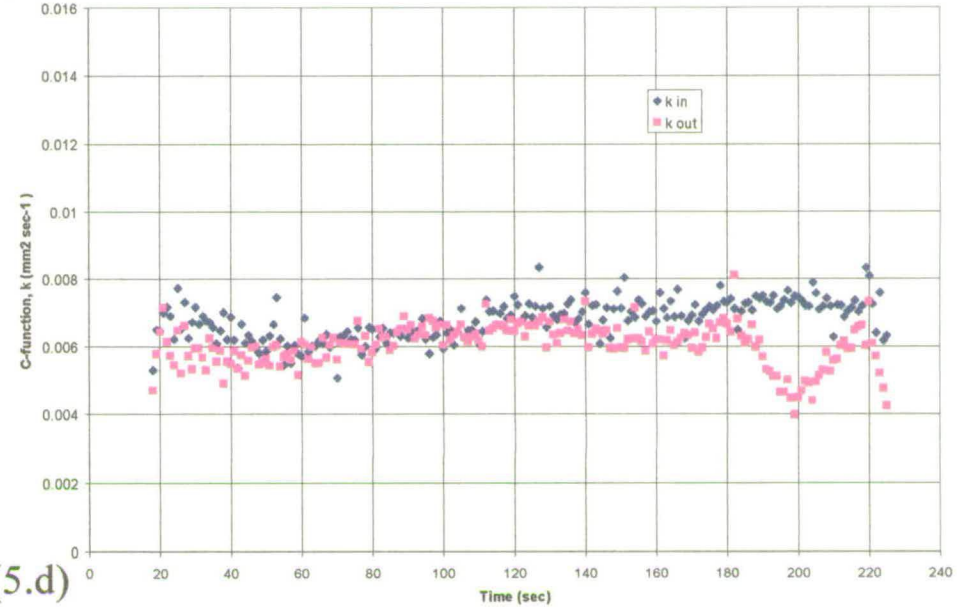

(5.d)

In718/nitrate system at 24 volts with flow 16 and 4 l/min

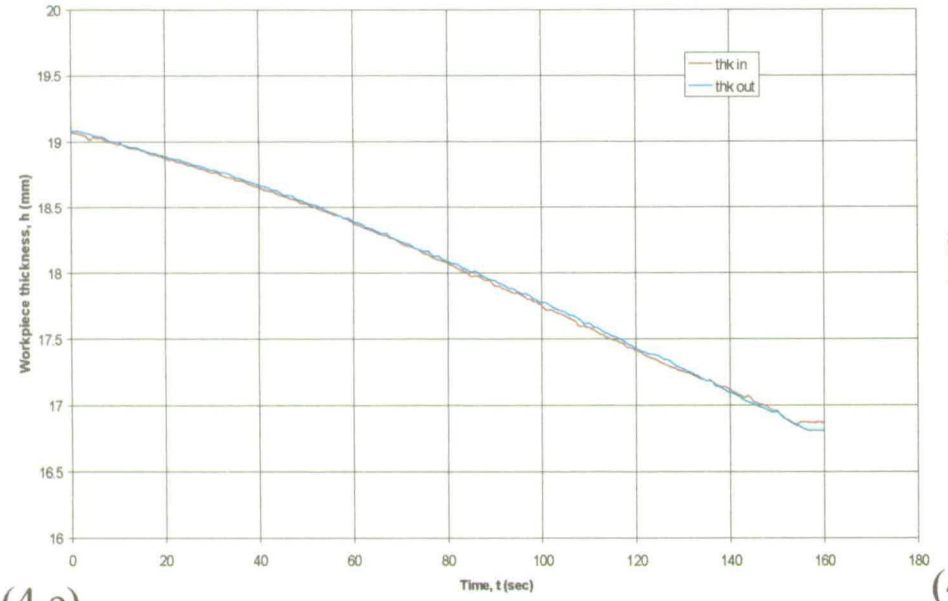

(4.e)

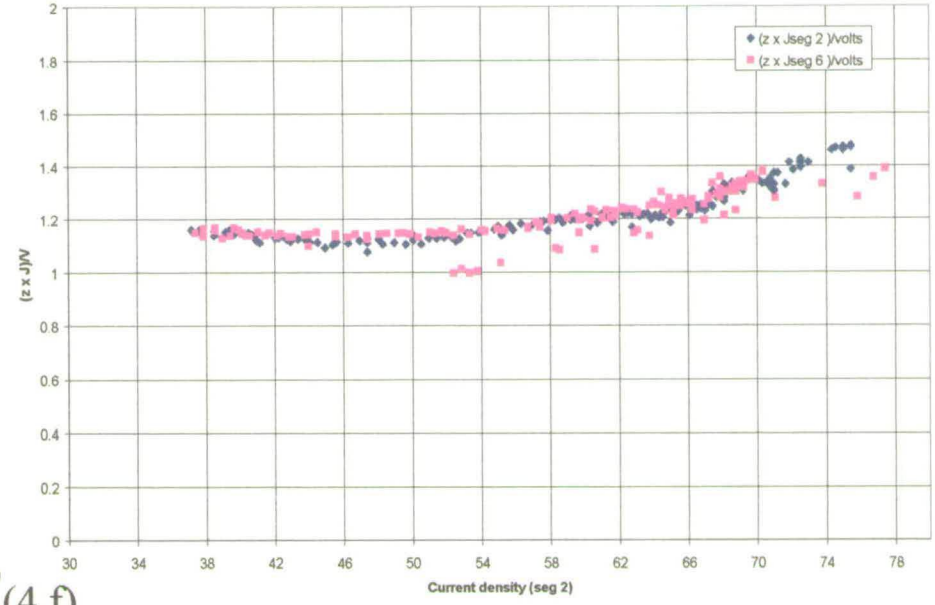

(4.f)

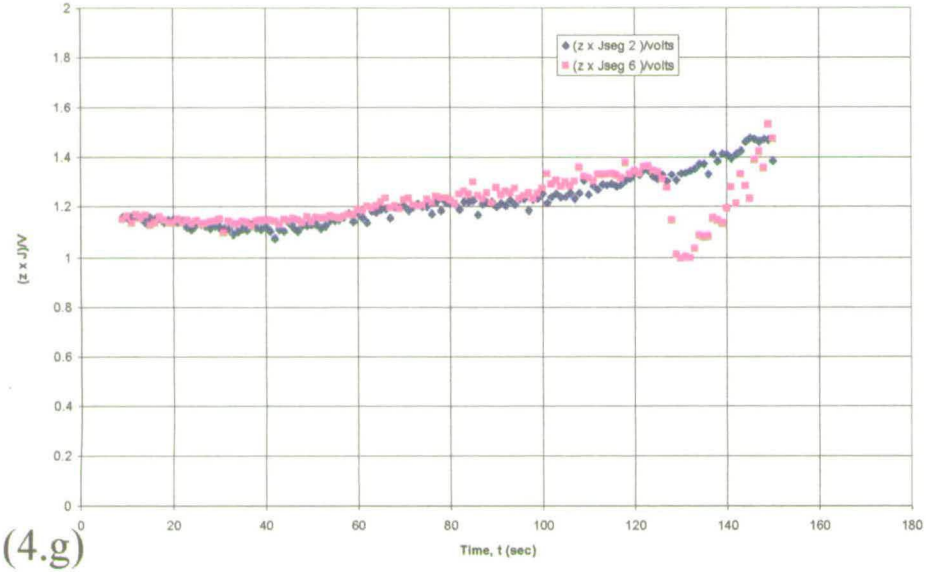

(4.g)

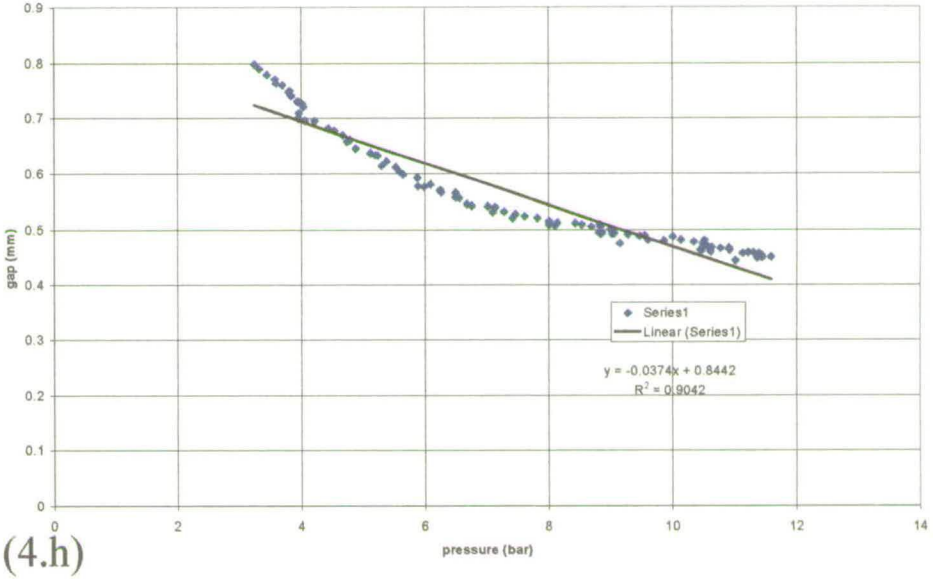

(4.h)

In718/nitrate system at 24 volts with flow 16 and 4 l/min

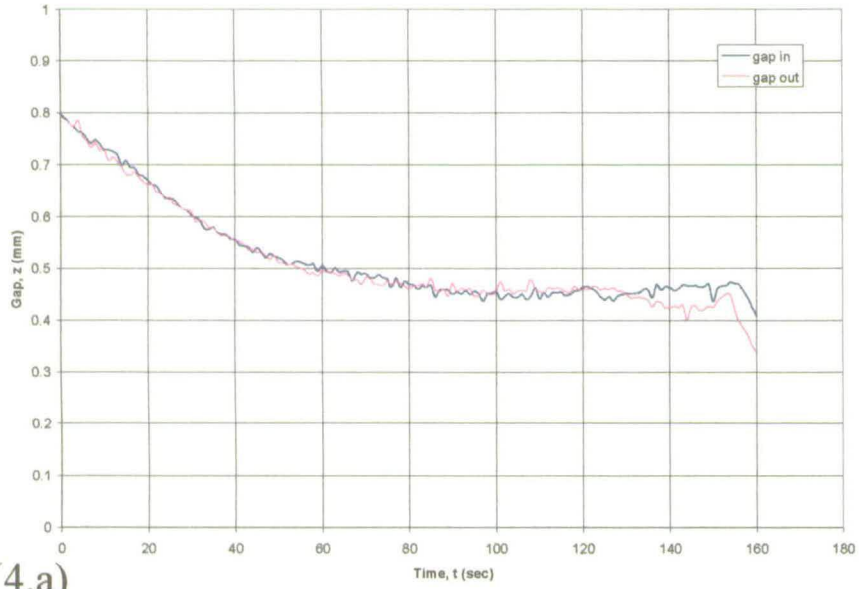

(4.a)

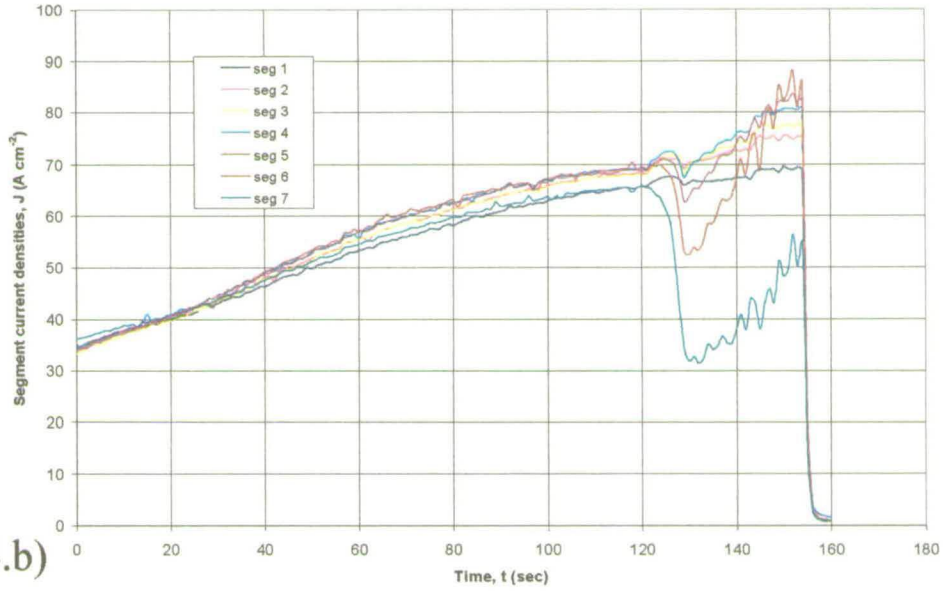

(4.b)

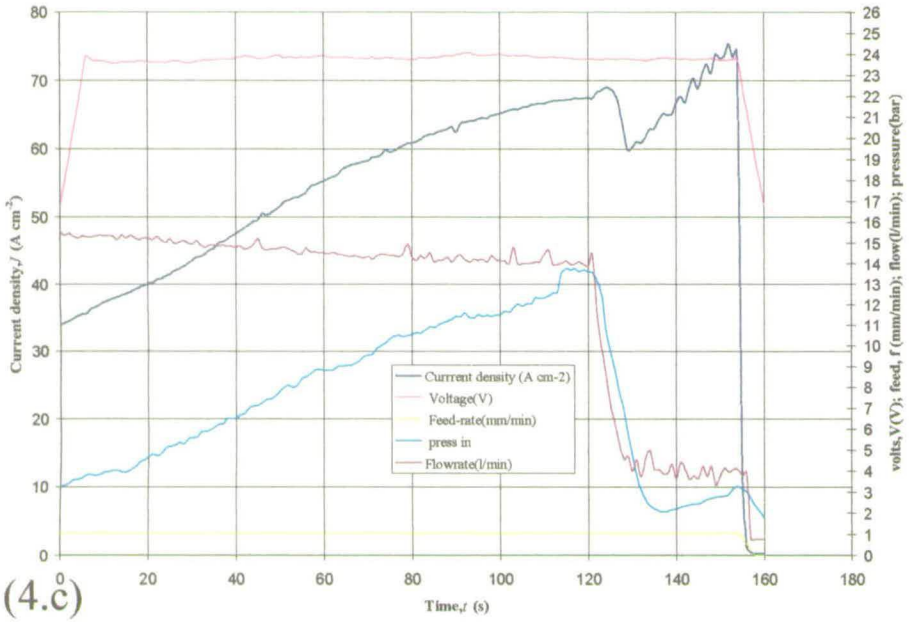

(4.c)

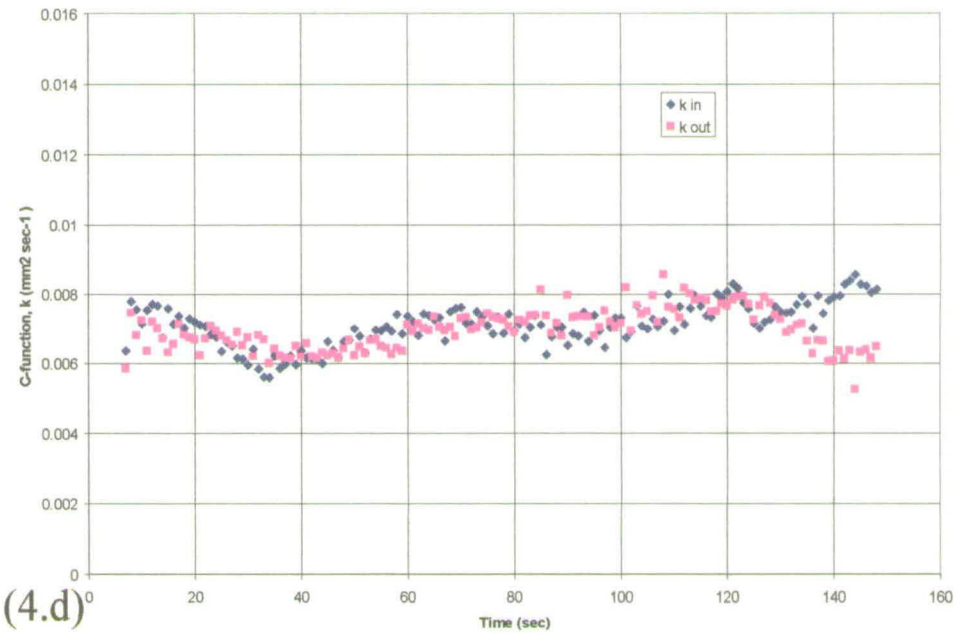

(4.d)

In718/nitrate system at 20 volts with flow 16, 10, 8 and 4 l/min

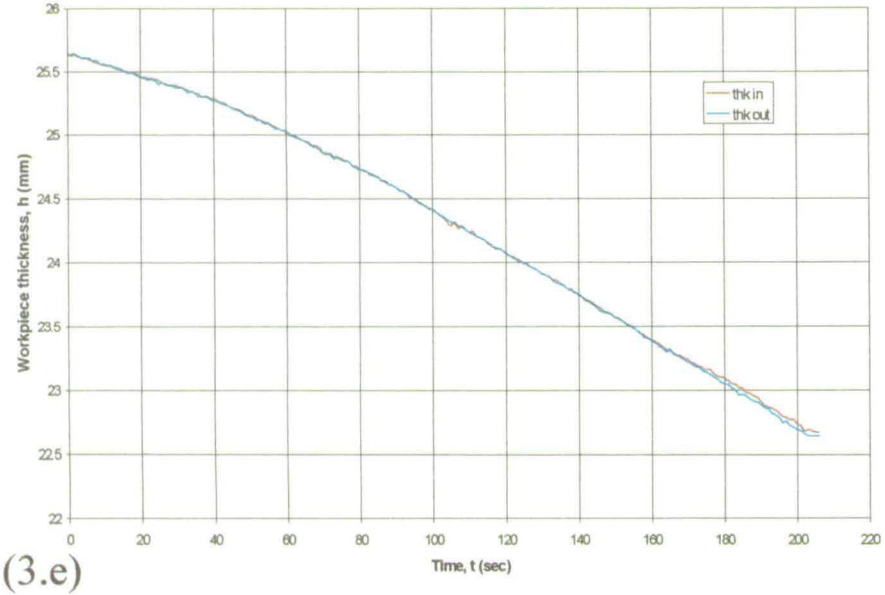

(3.e)

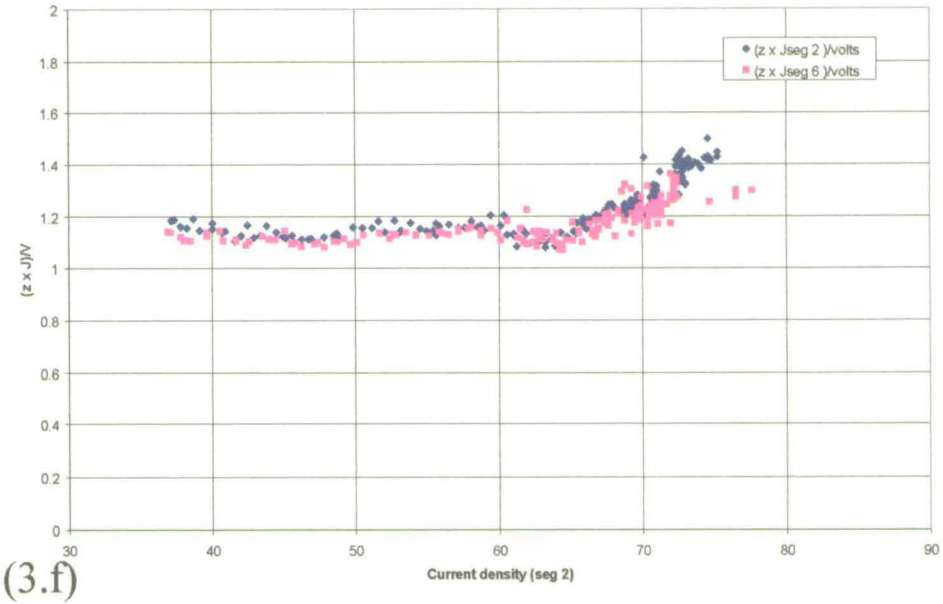

(3.f)

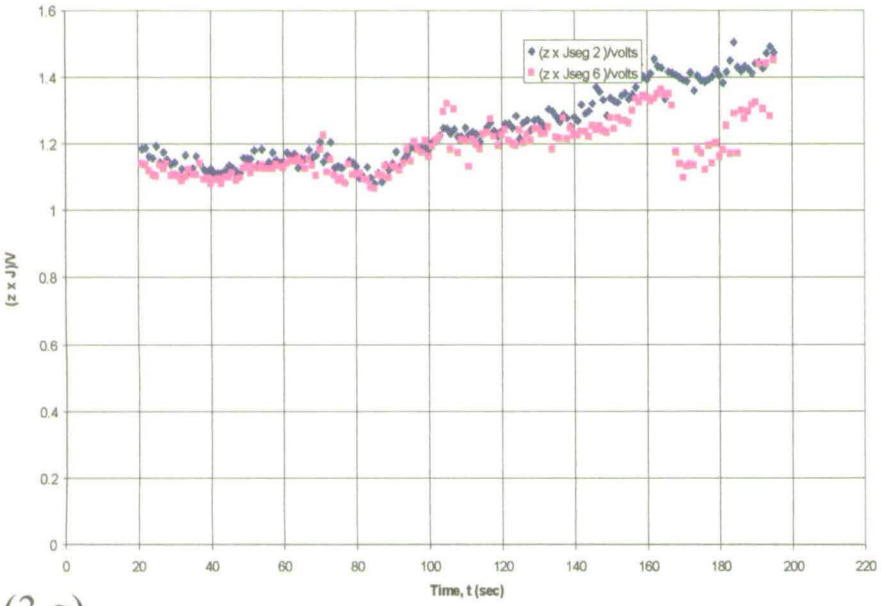

(3.g)

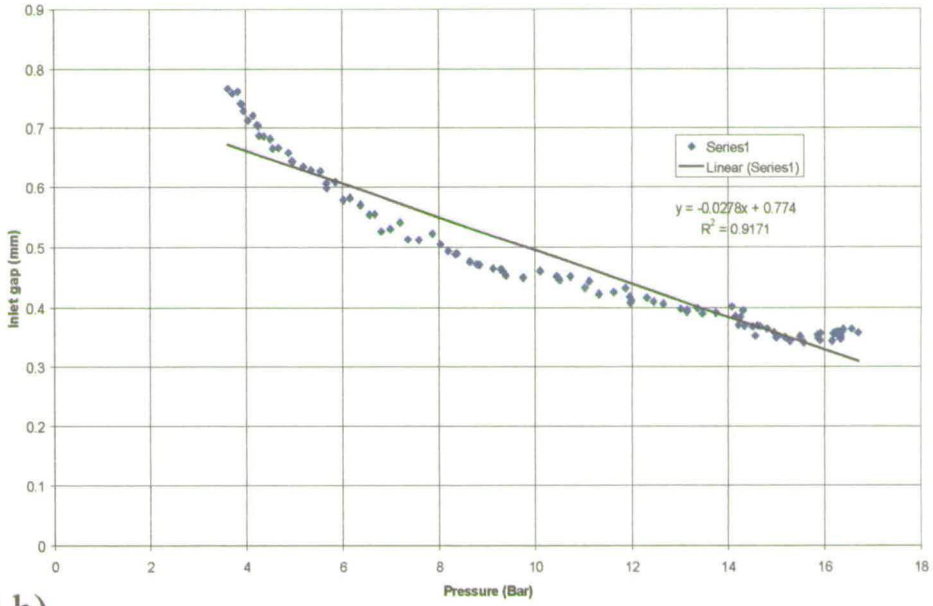

(3.h)

In718/nitrate system at 20 volts with flow 16, 10, 8 and 4 l/min

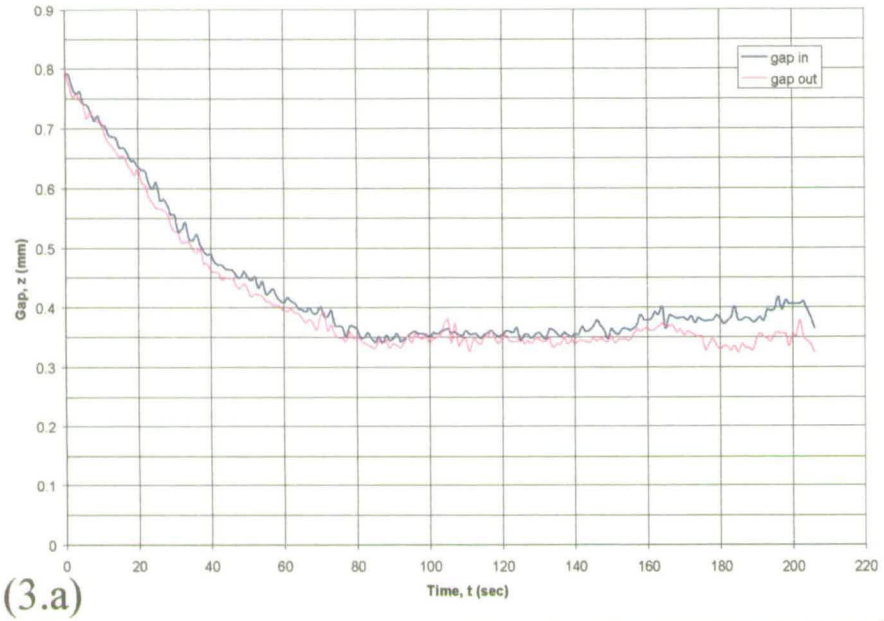

(3.a)

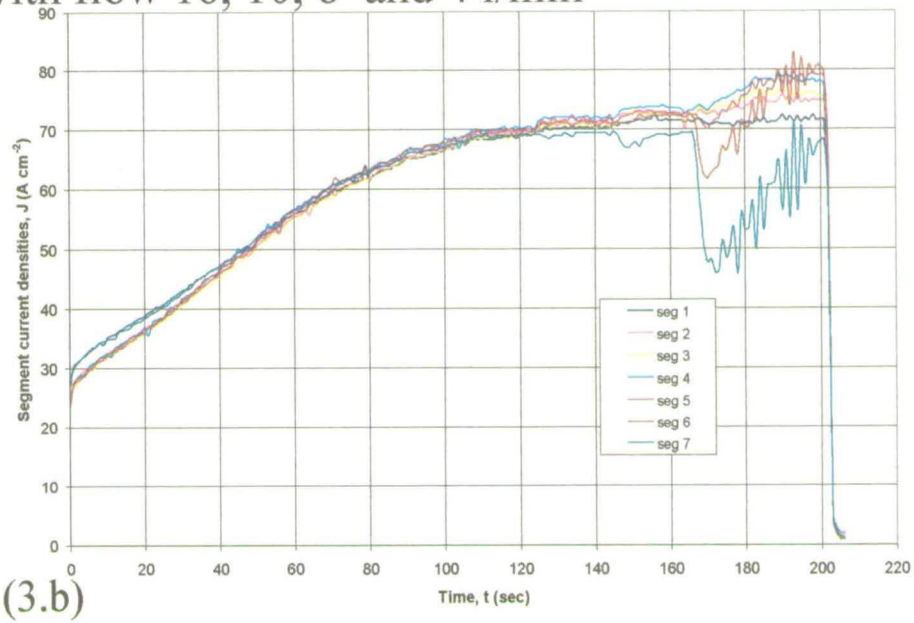

(3.b)

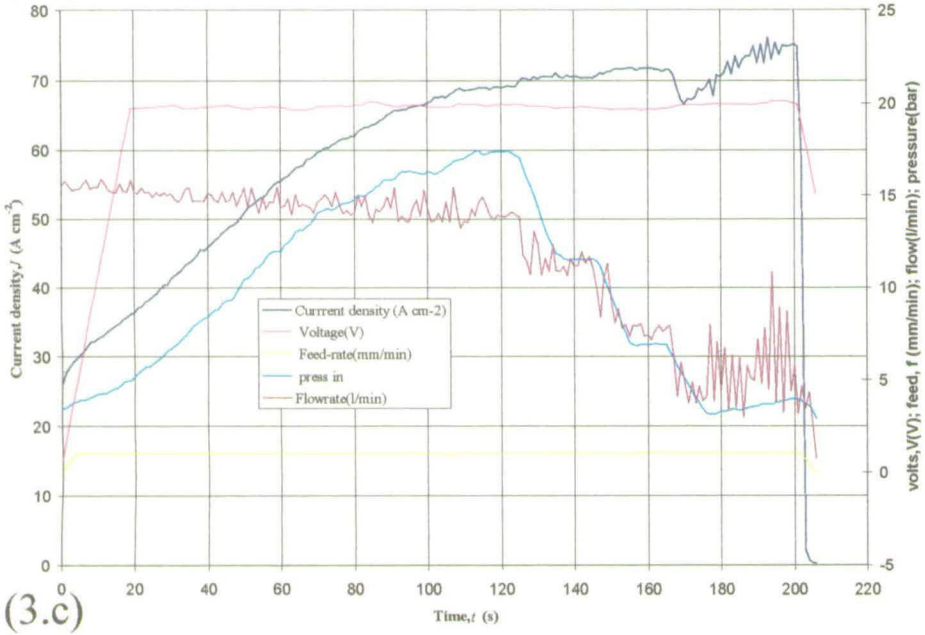

(3.c)

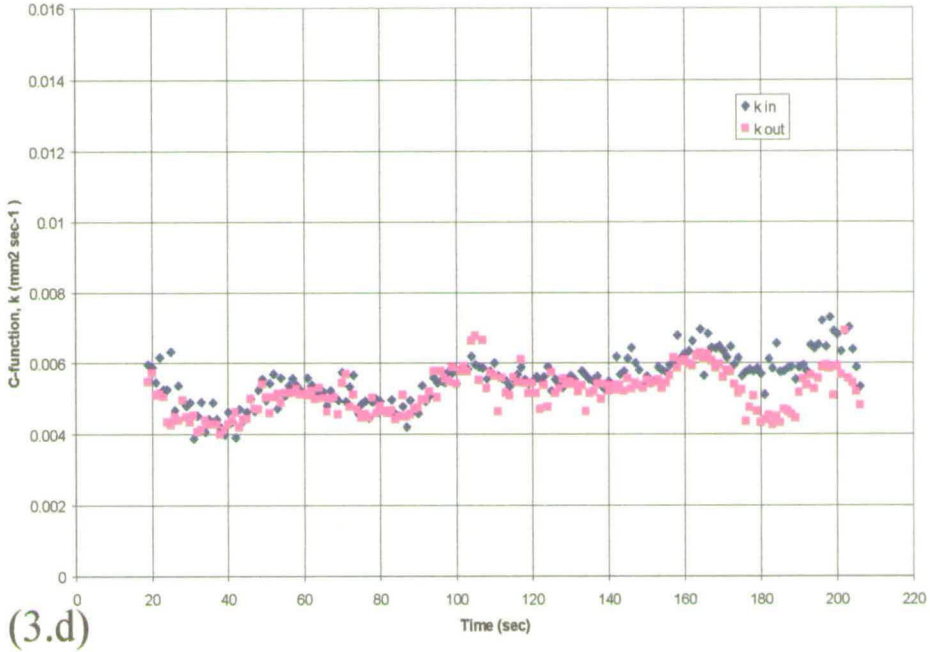

(3.d)

Titanium/chloride system at 24 volts with flow 16 l/min

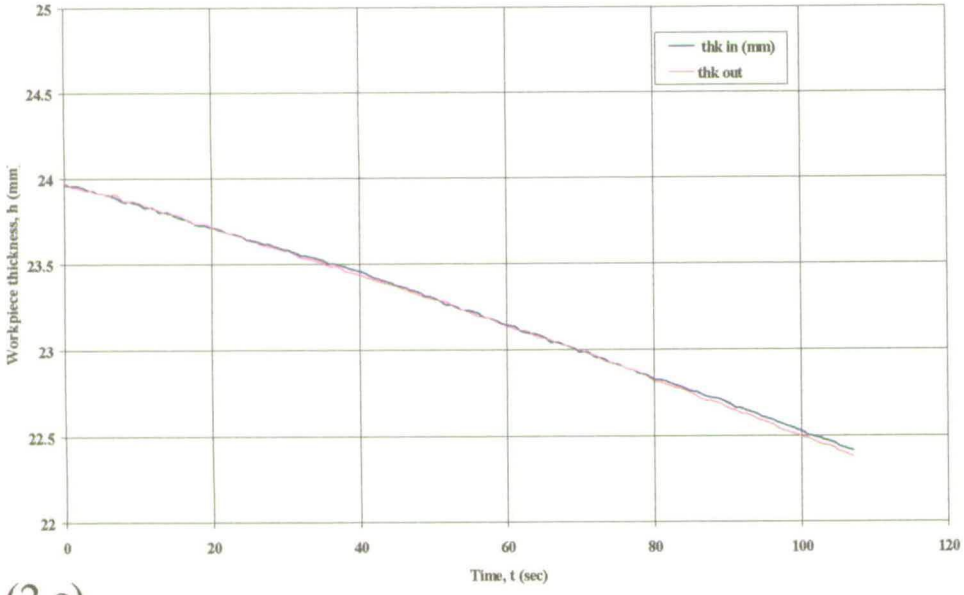

(2.e)

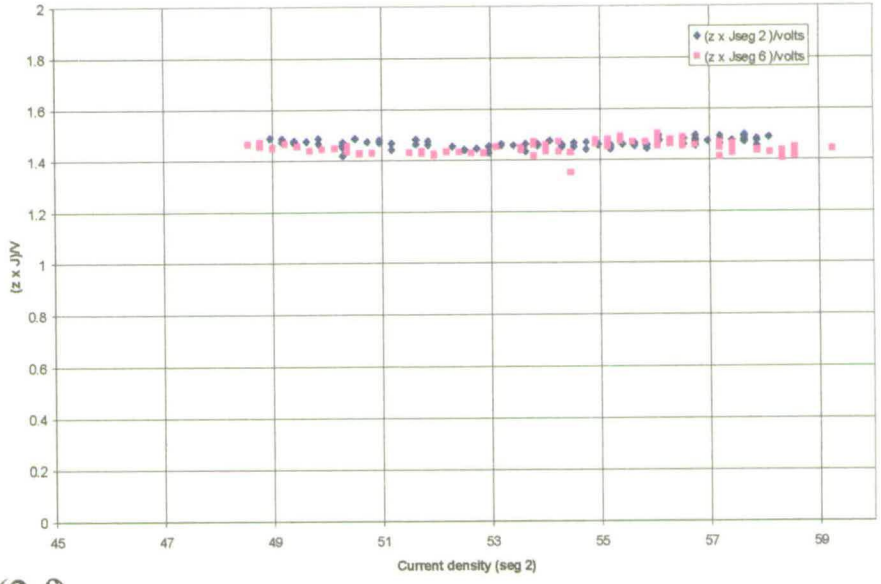

(2.f)

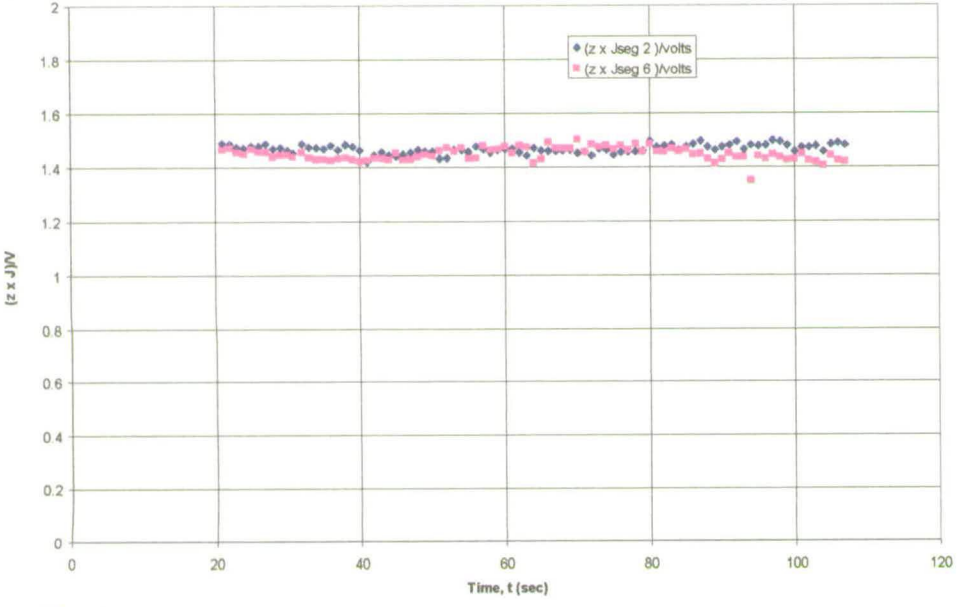

(2.g)

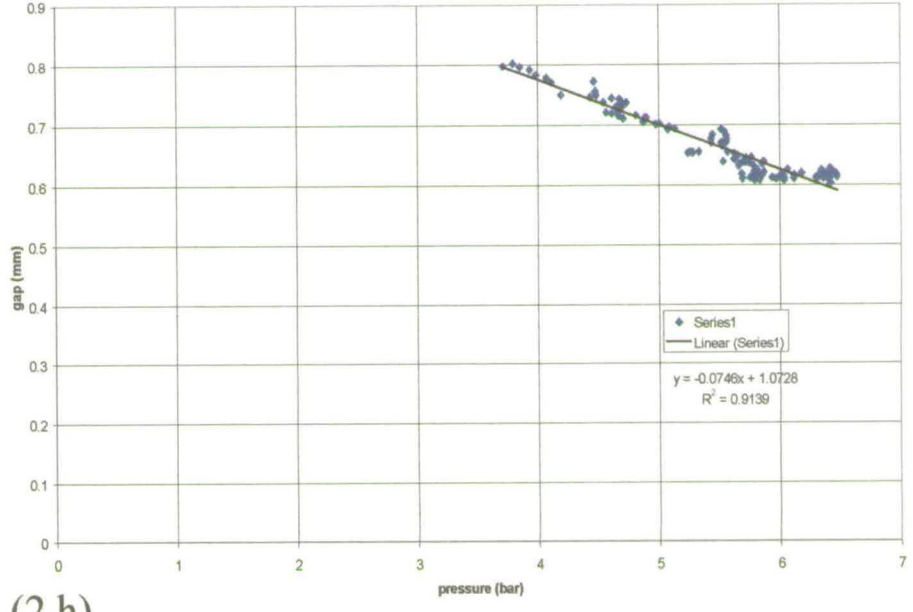

(2.h)

Titanium/chloride system at 24 volts with flow 16 l/min

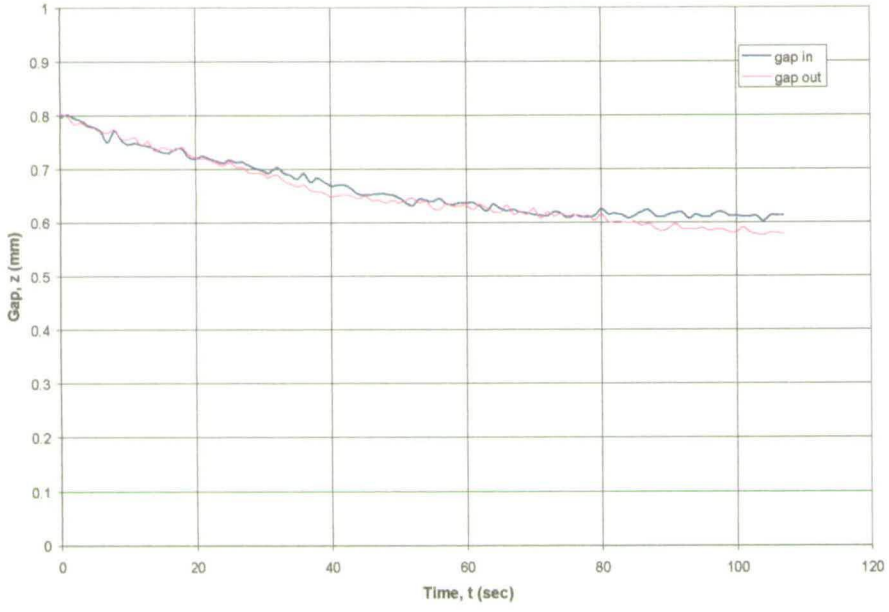

(2.a)

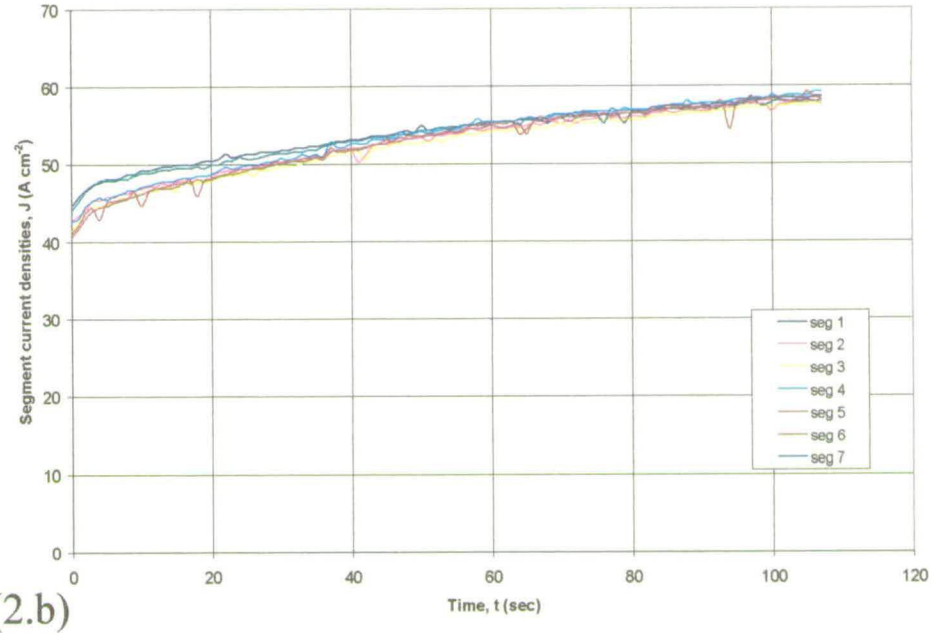

(2.b)

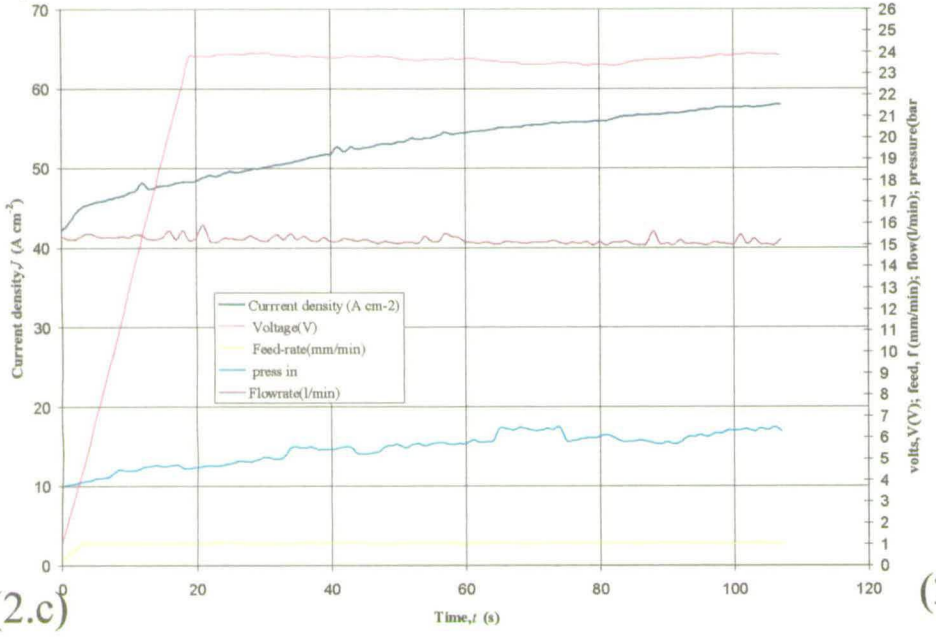

(2.c)

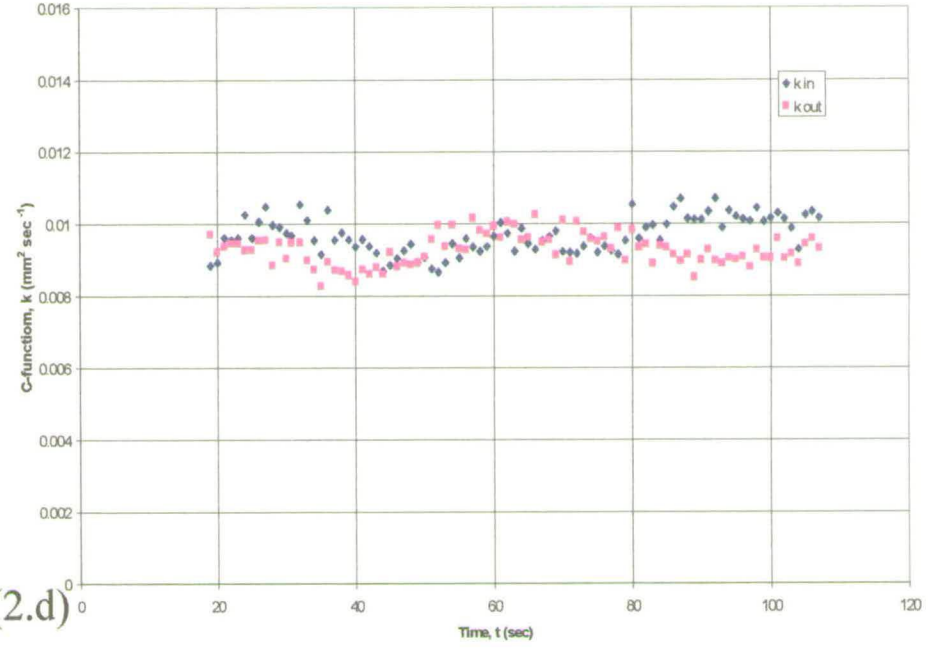

(2.d)

Titanium/chloride system at 20 volts with flow 16, 10, 8 and 4 l/min

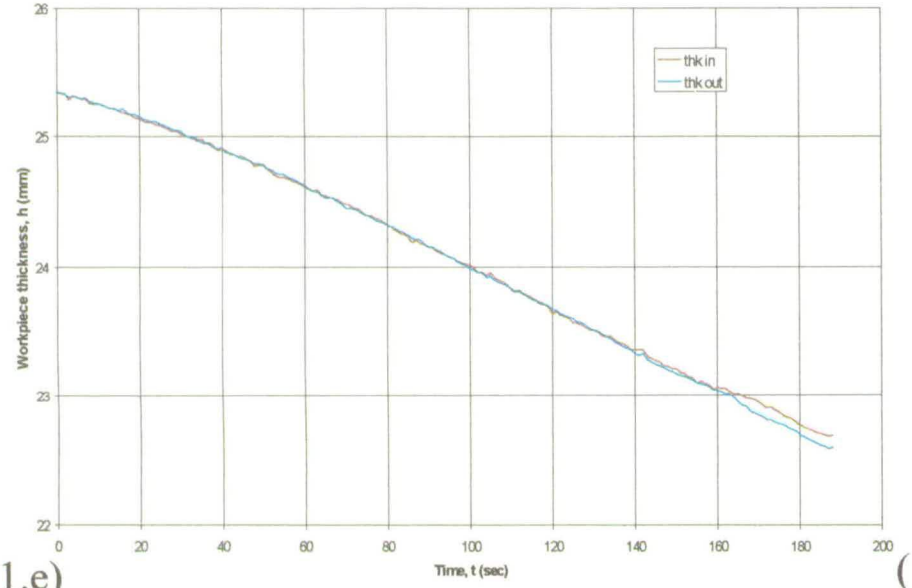

(1.e)

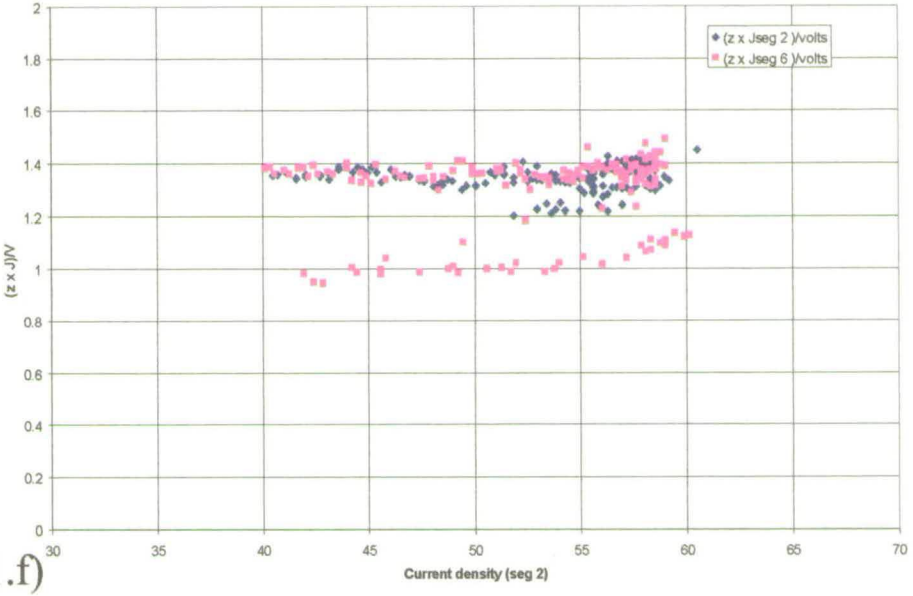

(1.f)

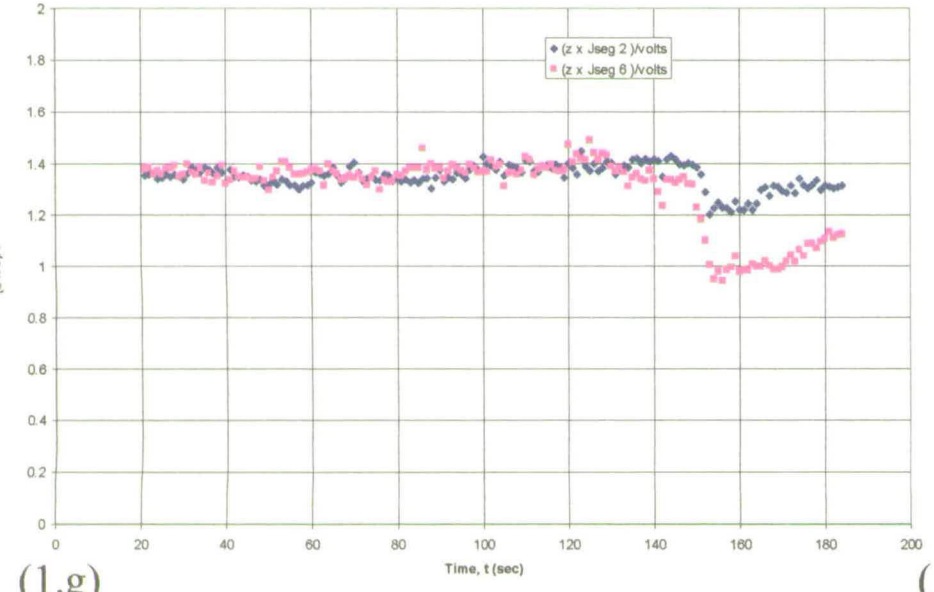

(1.g)

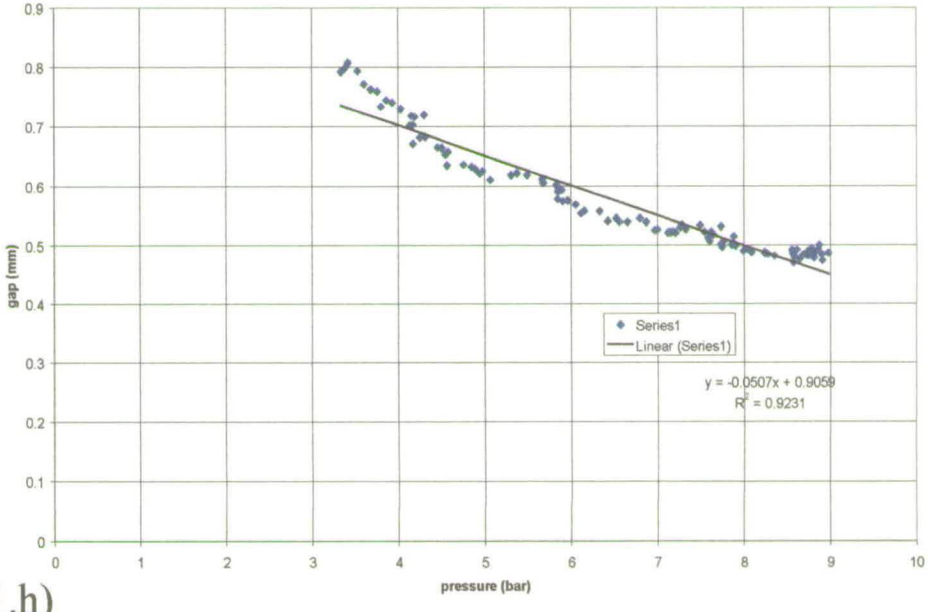

(1.h)

Titanium/chloride system at 20 volts with flow 16, 10, 8 and 4 l/min

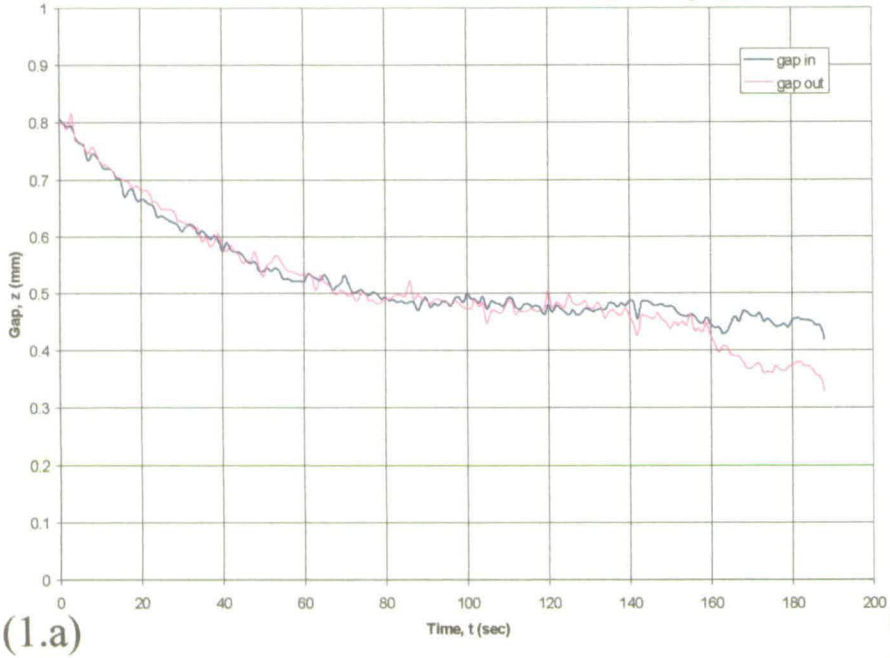

(1.a)

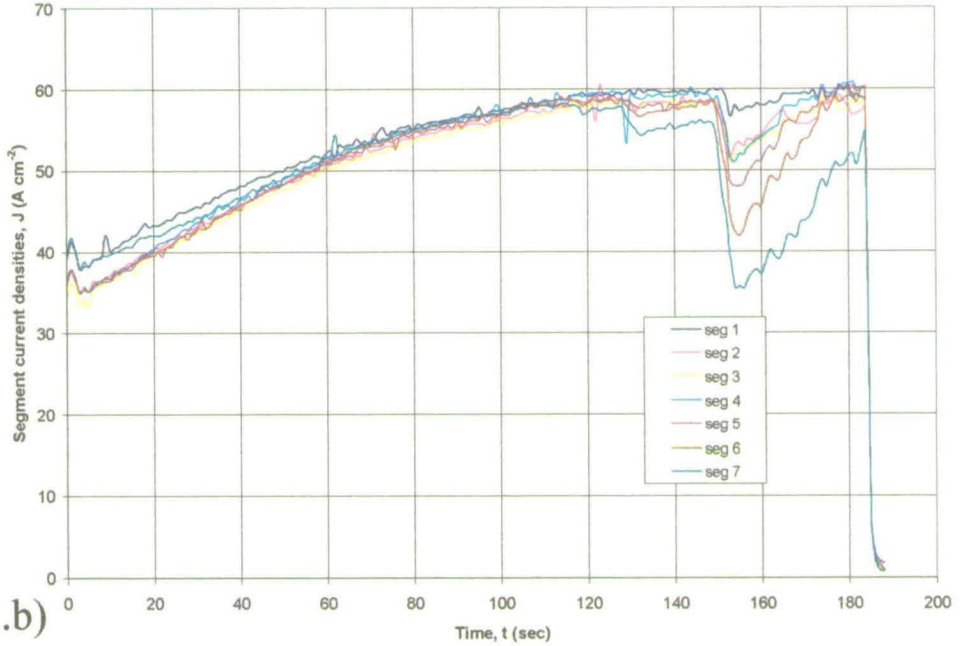

(1.b)

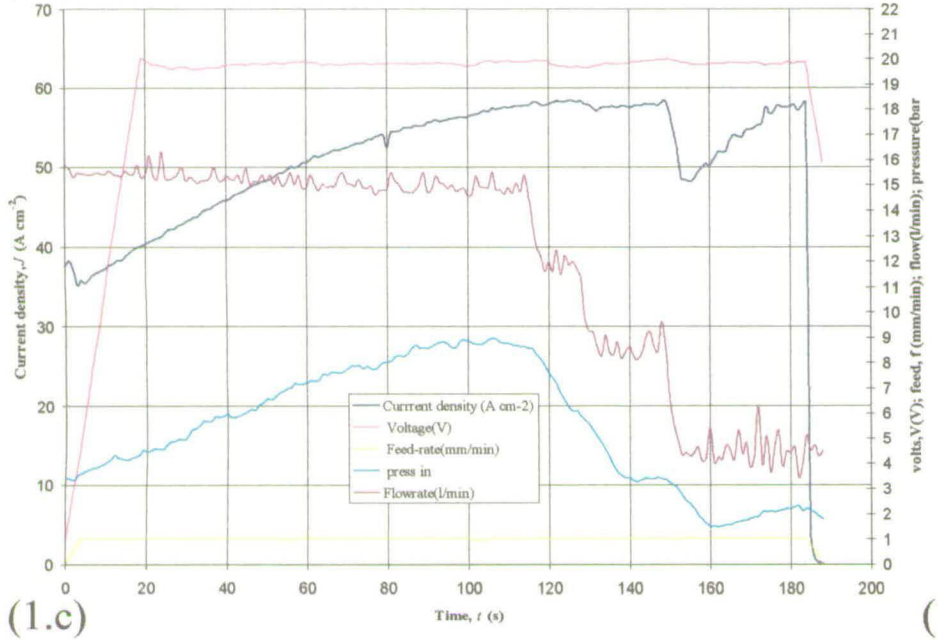

(1.c)

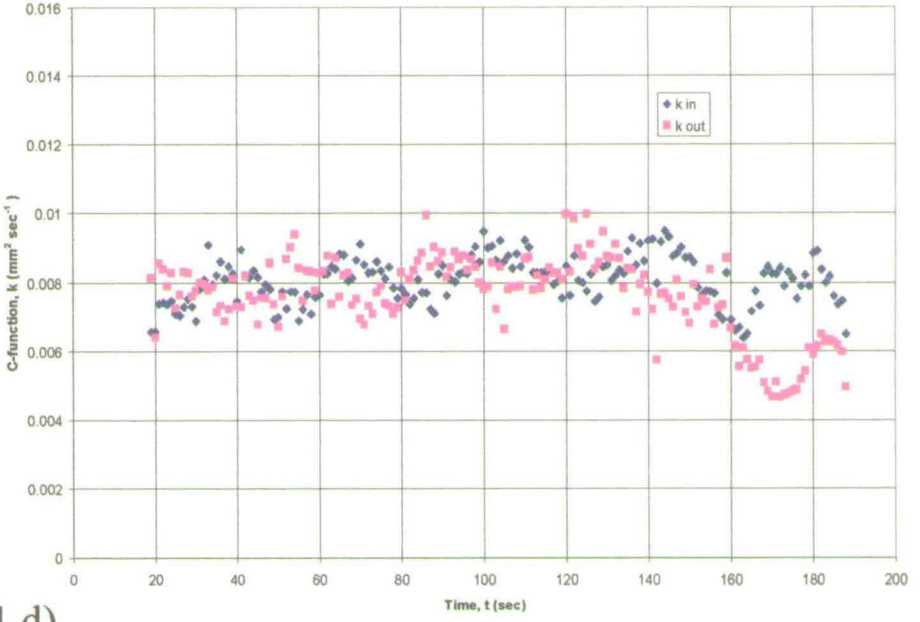

(1.d)